THE OXIDATION OF A 1.5 PERCENT SILICON-IRON ALLOY

THE OXIDATION OF A 1.5 PERCENT SILICON-IRON ALLOY IN CARBON DIOXIDE - CARBON MONOXIDE ATMOSPHERES

By

RAMESH CHANDRA LOGANI, B.Sc., B.Tech.

A Thesis
Submitted to the Faculty of Graduate Studies
in Partial Fulfilment of the Requirements
for the Degree
Doctor of Philosophy

McMaster University
October 1969

DOCTOR OF PHILOSOPHY (1969)
(Metallurgy)

McMASTER UNIVERSITY
Hamilton, Ontario.

TITLE: The Oxidation of a 1.5 Percent Silicon-Iron Alloy in Carbon Dioxide - Carbon Monoxide Atmospheres

AUTHOR: Ramesh Chandra Logani, B.Sc. (Andhra University)
B.Tech. (Indian Institute of Technology, Kharagpur)

SUPERVISOR: Professor W. W. Smeltzer

NUMBER OF PAGES: xvi , 194.

SCOPE AND CONTENTS:

The oxidation kinetics of a 1.5 $^{w}/o$ silicon-iron alloy in atmospheres of carbon dioxide - carbon monoxide at 890°C and 1000°C have been determined with a gravimetric balance as a function of gas composition. The reaction was observed to proceed in three stages.

In the initial stage simultaneous growth of wustite-fayalite nodules and an amorphous silica film on different regions of the specimen was observed and this mixed reaction continued until complete coverage by a uniform scale was achieved. A model involving both lateral and vertical growth of the oxide nodules and vertical growth of the silica film has been proposed to rationalize these kinetics.

A second stage involving fluctuations in the reaction rate was observed in atmospheres of low oxidizing potential. These fluctuations were associated with the formation of massive fayalite bands, brought about by silicon supersaturation of the wustite and alloy. At high oxidizing potentials, this stage was not observed.

At long times, a third stage consisting of linear reaction kinetics was observed. A model based on gas-oxide interfacial reaction control, involving the dissociation of carbon dioxide and incorporation of the chemisorbed oxygen into the wustite lattice has been advanced to describe these kinetics. The observed gas pressure dependence of the linear rate constants is consistent with the model.

ACKNOWLEDGMENTS

Grateful acknowledgment is made to Dr. W. W. Smeltzer for suggesting the problem and for his continuing direction and guidance throughout all stages of this project.

The author is indebted to Dr. J. S. Kirkaldy for his help in interpreting the precipitation phenomena and to Dr. J. D. Embury for his help in interpreting the electron microscopy results.

The author also wishes to thank the staff and graduate students of the McMaster Metallurgy Department for their help and stimulating discussions. In particular, thanks are due to Mr. R. Foster for his help with the construction of the apparatus; to Mr. R. Jarochowicz for his assistance in electron microscopy; and to Mr. H. Walker for his assistance in electron probe microanalysis.

The alloy used in this investigation was obtained through the courtesy of Dr. G. R. Purdy from Ford Research Laboratory, Dearborn, Michigan.

This project was supported by grants from the American Iron and Steel Institute to Dr. W. W. Smeltzer, and a National Research Council of Canada Graduate Studentship awarded to the author.

TABLE OF CONTENTS

LIST OF ILLUSTRATIONS

LIST OF TABLES

CHAPTER 1

INTRODUCTION

The advancement of science and technology has necessitated the production of better materials to withstand the rigors of aggressive gaseous environments. Therefore, alloys have been developed to overcome the inadequacies of pure metals. This causes diverse problems requiring understanding in the field of metal oxidation. Since the oxidation mechanisms of pure metals are not even completely understood, it is extremely difficult to obtain an understanding of the more complex oxidation mechanisms of alloys. Despite these complexities a large number of oxidation mechanisms have been postulated for alloys but not on a mathematical basis.

One of the major alloys in use today is steel, especially mild steel. An understanding of the oxidation properties of this steel can be gained by learning in detail the oxidation behaviour of the simpler systems: iron, iron-carbon alloys, iron-silicon alloys, iron-manganese alloys. Studies on the oxidation of iron have been conducted in recent years with the result that this process is well understood. However, the features of iron-alloy oxidation are poorly understood.

In this study, the oxidation properties of a 1.5% silicon-iron alloy wereunder investigation. In previous investigations, Pettit and Wagner(42, 43) and Smeltzer(44, 50) have advanced models to account for formation of oxide on iron in carbon dioxide-carbon monoxide at elevated temperatures. Since the diffusive flux of iron in wustite under these conditions was extremely rapid, it was possible to show that the reaction was controlled by a surface reaction at the external wustite surface. Morris and Smeltzer(46) found that iron-nickel alloys wherein nickel is more noble than iron behaved in a similar manner, though large amounts of subscale were observed below the surface wustite layer. It was hoped that on exposure of iron-silicon alloys to carbon monoxide atmospheres at elevated temperatures, wustite would form as the external scale layer and also that a layer of fayalite would form between the alloy and wustite layer. Thus the oxidation rate of the alloy would be drastically reduced since fayalite, a ternary oxide of iron and silicon, has very low diffusive properties for iron compared to the iron binary oxides.

Preliminary experiments revealed the formation of an external wustite scale and a two-phase fayalite-wustite layer between the alloy and the external scale. The alloy was found to oxidize at a linear rate after an initial period of slowly increasing rate. A dispersed fayalite layer was observed in the two-phase layer. In the light of this evidence experiments were designed to quantitatively determine the reaction rates and scale structures to help suggest mechanisms to account for these phenomena.

In the following sections, the results of these experiments are presented. The constant uptake of oxygen from the gas phase is theoretically described in terms of a rate limiting phase boundary reaction. The initial stage of accelerated rate is described in terms of an original model for growth of oxide nodules on the alloy surface. These sections are preceded by a review of oxidation theory and publications pertinent to this study.

CHAPTER II

REVIEW OF THE LITERATURE

2.1 Introduction

A metal or alloy in a gaseous environment constitutes a very complex chemical reaction system and in most cases an interpretation of the reaction behaviour can only be achieved with great difficulty. The total chemical equation for the reaction between oxygen gas and metal to form metal oxide may be written as,

$$a\,Me + b0 \rightarrow Me_a0_b \qquad 2\text{-}1$$

However, the reaction mechanism and oxidation behaviour of a metal depends upon a large number of variables, and the reaction mechanisms as a result prove to be quite complicated. The initial step in the metal-oxygen reaction involves the adsorption of the gas on the metal surface. As reaction progresses, oxygen may dissolve in the metal; then oxide is formed on the surface either as a film or as discrete oxide nuclei. Both adsorption and the initial oxide formation are functions of surface orientation, crystal defects on the surface, impurities in the metal and gas and surface preparation.

The surface oxide frequently appears as a compact phase with the metal and oxygen gas being spatially separated from each other, and further reaction is then only possible through solid state diffusion of the reactants through the film. In such a situation, the course of the reaction is no longer determined by equation (2-1), but by diffusion processes and phase boundary processes, for which the mechanism can be quite complex. In general, one must consider the several partial processes listed below. Of these, one is generally the slowest and hence the rate determining step:

1. Phase-boundary reactions involving chemisorption of oxygen molecules with subsequent formation of oxide by transfer of oxygen into metal or of the metal into the adsorbed oxygen layer. This formation stage involves nucleation and crystal growth processes.
2. Diffusion of cations, anions and electrons through the oxide film or layer. The driving force for the above processes being the chemical or electrical potential gradients in the oxide layer.
3. Predominant transport processes in a space charge boundary layer in case of thin films, especially at low temperatures where electrical potential gradients are the major driving forces.

Two other factors are also important for the formation, composition and structure of the oxide film or scale: the thermodynamic stability of the oxide that is formed and the crystal structure of the oxide layer and of metal or alloy, which determines the adhesion between the oxide layer and underlying metal.

It is the purpose of this chapter to present a summary of metal and alloy oxidation principles incorporating properties of oxides, general concepts of gas-metal reaction, reaction rates and rate equations and theories of alloy oxidation. A complete description is to be found in one of the standard works in this field(1-5).

2.2 Initial Oxide Formation and Growth

2.2.1 Adsorption

The accumulation of gas molecules on a solid surface is the initial process in the reaction between metal or alloy and gas. On the basis of kinetic theory of gases, it can be estimated that if all the impinging molecules of gas on a solid surface are adsorbed, then a monolayer of gas molecules would form in about 2 seconds at room temperature at a pressure of 10^{-6} torr. Since the rate of impingement of molecules is proportional to the gas pressure, pressures much lower than 10^{-6} torr are necessary to prevent surface contamination of a clean surface. Because of these requirements of the vacuum necessary to prevent contamination, most oxidation studies reported in literature have been made on contaminated surfaces. Only recently with the advance of ultrahigh vacuum technology has it become possible to study gas-metal interaction with truly clean surfaces.

Clean surfaces on various metals like nickel, tungsten, platinum, silicon and germanium have been prepared by either of two techniques: flash melting or positive ion bombardment with gases like argon and neon(6-9). Low energy electron diffraction studies of nickel surfaces suggest that the topmost layer of atoms of both (111) and (110) are displaced normally away from the next atomic layer with the mean square vibrational amplitude of the surface atoms being greater than the bulk material(10). However, in the case of silicon and germanium, this surface asymmetry leads to the formation of surface structures different from the bulk material.

The adsorption process results in a decrease in surface free energy but since there is also a loss of some degree of freedom, this implies a decrease in entropy. Hence there is a net decrease in the enthalpy during the adsorption process, thus adsorption is normally an exothermic process.

In considering adsorption on metal surfaces, there are essentially two types, physical and chemical. In physical adsorption, gases are bound to the surface through van der Waal's forces and a process similar in nature to condensation of vapour on its liquid surface. Consequently, the heat of physical adsorption is of the same order as heat of condensation and normally less than 10 kcal/mole(13, 14). Also physical adsorption takes place at low temperatures and usually below the boiling point of the adsorbed gas.

In chemisorption, on the other hand, the adsorbed species forms a chemical bond with surface atoms and also involves a transfer of electrons. Since chemical bonds are quite strong, the heat of chemisorption is usually quite large and may be as high as 100 kcal/mole (13, 14). Chemisorption takes place at elevated temperatures as compared to physical adsorption. Chemisorption may also involve activated rate processes, and may proceed slowly if thermal activation is over a high energy barrier. However, experiments with clean metals have shown very rapid chemisorption, the process apparently proceeding without barrier inhibition(11, 13, 14). Chemisorption is also very specific in nature since the adsorption sites on a surface depend on its crystallographic orientation and defect structure. It is generally considered that chemisorption proceeds only until a monolayer of the adsorbent is formed on the surface.

Low energy electron diffraction studies by Farnsworth and co-workers(15, 16) and Germer, MacRae, and co-workers(17-19) have established that adsorbed gases may form a large variety of structures on solid surfaces depending on adsorbent and adsorbate, crystal faces exposed, temperature, surface coverage, impurity atoms and defects. The adsorbed layer ranges from amorphous, like that found in the adsorption of oxygen on silicon(20), to regular order structures of adsorbed atoms which cause no detectable effects on the substrate as in the case of oxygen on the (100) face of nickel(21). The adsorption may also be accompanied by a rearrangement of the surface atoms in the substrate, as observed for adsorption on the (110) nickel surface.

2.2.2 Initial Oxide Nucleation

Due to the difficulties of obtaining clean metal surfaces and of maintaining them, most studies on the oxidation of metals in the initial stages are of recent date. All previous studies involved the oxidation of metals with at least an adsorbed layer of oxygen and most often with a thin oxide film on the surface when the experiments were started.

Germer and MacRae(19), Sewell and Cohen(22) were able to study the initial oxide formation taking place after the surfaces had become covered with chemisorbed oxygen. An important feature of the initial oxide formation is that isolated oxide nuclei nucleate at what appear to be random positions on the substrate. These observations were made on nickel and iron reacting with oxygen. Similar observations have also been made for other metals.

After the formation of oxide nuclei, oxidation proceeds through growth of the individual crystallites until the whole surface is covered with oxide. Wagener(23), Bloomer(24), Cohen(25) and Orr(26) studied the initial oxide formation on barium and magnesium and found that the rate of reaction increased with time. Bloomer(24) proposed a model for this increasing reactivity as due to an initial oxide formation at preferred sites and subsequent reaction by lateral surface growth of nuclei.

In his model it is assumed that the surface is heterogenous and the oxide nucleation occurs at certain sites whilst the rest of surface is comparatively inert. If the nuclei grow laterally and if only the surface or edge of oxide nuclei are active, then the sticking probability will increase with oxidation. On this basis, the sticking coefficient s and the oxygen uptake w can be related by the generalized expression

$$s = Aw^{1/n} \qquad 2\text{-}2$$

The values of n are determined by the geometry of oxide nuclei and the rate determining process during the oxide formation and growth. Bloomer concluded that n = 2 if the oxide islands were cylindrical disks one monolayer high and the active region is an annulus 1 atom wide around the circumference, and n = 3/2 when the islands were hemispherical caps and the entire surface is active for oxygen uptake. Orr(26) further elaborated on the model by taking into account and analysing the importance of the various partial processes involved, for example, adsorption, nucleation rate of oxide, surface diffusion and capture of oxygen. Orr concluded in the case of hemispherical caps where only edges were active that n=3.

Bardolle and Benard(27) studied the nucleation and growth of iron oxide nuclei during the oxidation of iron and found that discrete oxide nuclei growth was important even after a thin base film of oxide has been formed. Harris(28) in the study of oxide nuclei on copper observed the formation of two types of nuclei, the crystalline base film and oxide polyhedra. These two types were found to grow at different rates. The density of base film nuclei varied with time whilst the polyhedra density was independent of time.

For the above types of nucleation phenomena it is difficult to estimate the kinetics and relative importance of different modes of oxide growth, and consequently few studies are available concerning these features. Nucleation and growth phenomena may give rise to an unusual pressure dependence of the oxidation. For example, Boggs(29) found that in the oxidation of iron at low temperatures, and at low pressures (0.1 torr), the rate of nucleation of Fe_2O_3 was low and relatively thick films of Fe_3O_4 and high oxidation rates result. At high oxygen pressures (100 torr), however, the rate of nucleation and growth of Fe_2O_3 is high, the surface is rapidly covered with Fe_2O_3 and low rates result.

The details of nucleation and growth mechanisms are still a matter of conjecture. It has been suggested that dislocations, impurities, surface defects serve as nucleation sites. Rhead(30) has developed a detailed model of oxide nuclei growth and particle density. The rate of growth of oxide nuclei is assumed to occur by surface diffusion to the nuclei edges. A radial concentration gradient of diffusing atoms is assumed to surround each oxide nuclei. If the atom concentrations are C in the particle, C_s at particle edge and C_∞ at large distances from a particle and if $C - C_s >> C_\infty - C_s$, the particle radius R and the circular cross section of the particles, A, can be expressed by

$$R = 2\lambda (D_s t)^{1/2} \qquad 2\text{-}3$$

and

$$\frac{dA}{dt} = 4\pi\lambda^2 D_s \qquad 2\text{-}4$$

where D_s is the surface diffusion coefficient, t is time and λ is given by the equation

$$\lambda^2 \ln (e^{0.577}\lambda^2) + (C_\infty - C_s)/(C - C_s) = 0 \qquad 2\text{-}5$$

Equation 2-4 predicts that the area of particles will increase uniformly with time and at a rate proportional to the surface diffusivity. Rhead interpreted in terms of "Ostwald ripening" the fact that the particle density remains constant and the fast growing particles are widely spaced. As a general rule and in accordance with the general theory of nucleation the formation of discrete oxide particles will become increasingly marked and important the higher the temperature and the lower the partial pressure of oxygen.

2.2.3 Growth of Oxide Nuclei

Evans(3) has considered oxidation processes involving lateral growth of three-dimensional oxide crystals on the surface. A similar lateral growth of oxide crystals may also be considered for large oxide crystals growing on an oxide base film. For such lateral growth the fraction f of total surface area covered at time t is given by

$$f = \left[1 - \exp(-kt^n)\right] \qquad 2\text{-}6$$

where n is given by the nucleation rate. If the nuclei appear simultaneously and density is constant, n = 2; if nucleation rate is constant, n = 3. Bartlett(31) has proposed a detailed model for lateral oxide growth coupled with linear and parabolic vertical growth rate processes. When the vertical growth rate is linear, the reaction rate will initially increase and eventually become linear when the surface is fully covered. On the other hand, if the vertical growth rate is parabolic, the reaction rate will initially increase and eventually decreases according to a parabolic rate. The latter type of kinetics is described by a sigmoid curve. Bartlett has applied this type of model to describe the nucleation and growth of crystalline γ-alumina in an amorphous oxide film. Dignam et al(32, 33) and Beck et al(34) have also developed models for combined lateral growth of γ-alumina crystals in an amorphous oxide film based on similar concepts to those outlined above. The above authors obtained good agreement with their models in their investigations of the oxidation of aluminum in oxygen at 200 - 600°C.

2.3 Scale Formation

This section concerns films greater than 10000Å in thickness. These films are assumed to be electrically neutral when formed rapidly at high temperatures and after extended periods of time at intermediate temperatures. In most cases, scales exhibit parabolic growth behaviour but other growth relationships like linear, asymptotic and logarithmic are also observed. These growth relationships can be attributed to phase boundary control, breakdown and spalling of oxide film, and short circuit diffusion.

Wagner(35) formulated a quantitative theory for the parabolic growth of thick oxide films which has since been tested and verified by numerous investigators. He postulated that ions and electrons, which migrate independently of one another, are the only diffusing species. The prerequisite for an ionic species to be mobile is that its sublattice contain point defects such as interstitial ions and vacancies. Reactions at interfaces are considered to be sufficiently rapid for local equilibria to exist at both interfaces. On the basis of these assumptions, an expression was derived for the reaction rate utilizing ion mobilities, namely,

$$K_r = C_i \int_{a_x^{(m)}}^{a_x^{(s)}} (D_C \frac{Z_c}{Z_x} + D_x) \, d\ln a_x \qquad 2\text{-}7$$

where $C_i = Z_c C_c = Z_x C_x$ is the concentration of metal or non-metal ions in the oxide in equivalents per cubic centimeter, a_x is the thermodynamic activity of the non-metal, and D_c and D_x are the self diffusion coefficients of the metal and non-metal respectively.

In Wagner's parabolic oxidation theory, it was assumed that the oxide was homogenous and does not contain structural irregularities such as pores, grain boundaries or dislocations. Investigations on oxide films by electron microscopy, X-ray techniques and studies of nucleation of oxide on metal surfaces showed that this assumption may be an oversimplification. Furthermore, diffusion in polycrystalline materials have shown that such structural defects act as low resistance paths and may be an important mode of transport, especially at intermediate temperatures.

Evans(3) and Davies et al(36) have proposed models whereby transport of reactants is assumed to take place preferentially along pores or low resistance paths. Two cases were considered. In the first, fresh oxide results in self-blockage of pores and an asymptotic oxidation rate; in the second case, mutual blockage occurs due to compressive stresses and a logarithmic rate is observed. Harrison(37) recently has derived an expression which accounts for self and mutual blockage occurring simultaneously.

Smeltzer et al(38) proposed a theory to describe the non-parabolic oxidation kinetics of titanium, hafnium and zirconium. In this theory, lattice diffusion and diffusion along low resistance paths, which decrease in density with time, were assumed to occur simultaneously. Irving(45) proposed a model for non parabolic oxidation based upon a combination of diffusion along grain boundaries and lattice diffusion. The contribution of the grain boundary diffusion to the effective diffusion coefficient was weighted according to the grain size. More recently, Perrow and Smeltzer(39) have employed the above concepts based upon short-circuit diffusion of reactants to explain the non-parabolic oxidation kinetics of nickel.

It has been shown by Fishbeck(40) that the oxidation reaction can occur by phase boundary control at the oxide/gas interface when experimental conditions are chosen to satisfy the condition that diffusion of reactants through the scale is much more rapid than the surface reaction steps. In more recent years, Hauffe et al(41), Pettit et al(42, 43) and Smeltzer(44, 50) have shown that this condition applies to the oxidation of iron in carbon dioxide-carbon monoxide atmospheres at high temperatures. These authors have been able to advance a fairly detailed mechanism for this behaviour involving dissociation of the reactant gas and incorporation of oxygen into the wustite lattice. In this investigation, these concepts will be extended to account for the oxidation behaviour of iron-silicon alloys.

2.4 Oxidation of Alloys

2.4.1 General Features

Although it is not possible to quantitatively predict the effects on the oxidation behaviour of a metal by the addition of an alloying element, several distinct possibilities can be defined. The alloying element may:

(i) be completely inert and serve only to dilute the oxidizing metal at the metal/oxide interface,

(ii) be completely inert, but improve the lattice fit at the metal/oxide interface and defer the onset of scale breakaway by oxide cracking and spalling,

(iii) be inert and become mechanically entrained in the oxide product as a second phase distribution,

(iv) dissolve to some extent in oxide scale and possibly modify its mechanical properties as well as its atomic defect concentrations,

(v) cause the formation of a two-phase scale layer and as above modify the mechanical properties and defect concentrations of both phases,

(vi) cause the formation of a single phase compound scale, whose structure differs from that of the solvent metal oxide,

(vii) be a strong oxide former that forms only its own oxide on the alloy.

Some of these cases have been considered in detail by several investigators(47-71), in particular, cases (i), (iii), (iv), (v) and (vii). As will be obvious from the cases described above, the spatial distribution of the components and oxide phases depends on the various modes of oxidation behaviour. Some insight may be gained on the distribution of phases if the ternary phase diagram for the system of binary alloy and oxygen is known for the conditions of diffusive growth of phases and rapid interface reactions as described by Clark and Vines(47) and Kirkaldy(48). Moreau and Benard(49) have presented a very general classification of these different modes of oxidation and the spatial distribution of phases based on experimental observations.

2.4.2 Alloy Oxidation Rates

The empirical reaction rate relationships found in the case of pure metals, that is, linear, parabolic, logarithmic etc., are also applicable in the case of alloys. However, in alloys the kinetic data obtained from oxidation experiments often deviate from these idealized relationships and a series of rate transitions may be observed.

In particular, the conditions necessary for the parabolic relationship to hold in alloy systems are as follows. The sequence of reaction layers must not change with time and alterations in oxide structure due to cracking and phase transformations must not occur. Interface reactions must be quite rapid to ensure local thermodynamic equilibrium. In order to obtain tractable mathematical expressions with appropriate boundary conditions, it has been necessary to assume that the composition of the alloy at some point must be the initial composition and that the diffusion constants of the species must not be a function of composition. The composition at the metal/oxide interface under these conditions is then time independent.

It is clear from the overall number of kinetic factors to be considered, as well as the mechanical and adhesion properties of scales on alloys, that a theoretical description of alloy oxidation by a unified theory is virtually impossible. Nevertheless, several attempts have been made to theoretically describe the oxidation mechanisms for a few limiting cases.

2.4.3 Alloy Oxidation Mechanisms

Iron-silicon alloys exhibit extremely complex reaction behaviour upon their exposure to atmospheres containing oxygen at high temperatures. Several of the general alloy oxidation features outlined above are found for these alloys and require discussion in greater detail.

2.4.3 (a) Ternary Metal Oxides

In this case, ternary metal oxide solid solutions are formed by the dissolution of solute metal into the base metal oxide. This situation was treated by Wagner and Hauffe(1) in detail and only the basic principles will only be described here. The rate of growth of these oxides depends upon their defect concentration, which according to this mechanism may be increased or decreased by the addition of solute ions.

Consider for example, the extensively studied metal-deficit oxide Ni0, and the equilibrium,

$$\frac{1}{2}\,0_2 = \mathrm{Ni}_{\square} + 2\oplus + \mathrm{Ni0} \qquad 2\text{-}8$$

where the mass action constant is given by

$$\left[\mathrm{Ni}_{\square}\right]\left[\oplus\right]^2 = \text{constant}\left[\mathrm{P}_{0_2}\right]^{1/2} \qquad 2\text{-}9$$

Here $\mathrm{Ni}_{\square}$ represents a nickel cation vacancy and $\oplus$ a positive hole consisting of a nickel ion in the higher tri-valent state. If a solute atom of higher valency than 2 is added, it will substitute for nickel ions in the oxide lattice in a higher valence state than nickel and decrease the concentration of positive holes. The concentration of vacancies increases, and since the oxide grows by diffusion via vacant cation sites, the rate of oxidation is expected to increase. On the other hand, with the substitution of a solute of lower valency, the oxidation rate will decrease. These effects have been experimentally verified. Similarly, it can be shown for metal excess oxides, additions of ions of higher valency decreases the rate of oxidation, whereas addition of ions of lower valency increases the rate. Arguments such as these also apply to wustite formed on iron alloys but only qualitatively since this oxide has a much larger concentration of iron vacancies. Neutron diffraction studies have shown that these defects are not randomly distributed in the oxide lattice but form ordered clusters in wustite(51).

2.4.3 (b) Selective Oxidation of Alloys

In selective oxidation the less noble constitutent of an alloy is selectively oxidised to form an outer, often protective layer, and thus the scale often consists of only one oxide. Selective oxidation takes place in alloys for which the oxides of the alloying components show great differences in stability, for example, iron alloys with silicon, aluminum or chromium and copper alloys with beryllium or silicon. The occurrence of preferential oxidation is dependent not only on the alloying element but also on the composition of alloy and reaction atmosphere and temperature.

Wagner(52-54) has shown that under certain conditions, selective oxidation will take place above a critical concentration of active alloy component in a binary alloy and has derived a mathematical expression for this concentration. He considered an alloy A-B in which B is the less noble metal and A and B do not react to form a double oxide or spinel. Under conditions of compact scale formation, three main cases for oxidation of alloy A-B were considered.

1. At low concentrations of B, only the A oxide is formed and B will diffuse into the alloy from the alloy/oxide interface (Fig. IV-1). As oxidation proceeds, the concentration of B in the alloy will increase, and formation of B oxide will take place when the concentration of B at the interface reaches the equilibrium concentration, N_B^*, for the mixture (alloy + A oxide + B oxide). The concentration of B in bulk alloy N_B', is originally smaller than N_B^*.
2. For sufficiently high contents of B in the alloy, N_B'', only B oxide will be formed and A will diffuse into the alloy from the alloy/oxide interface (Fig. IV-2). Formation of A oxide will take place only when the concentration of A at the interface reaches the critical concentration, $N_A^* = 1 - N_B^*$ corresponding to the equilibrium (alloy + A oxide + B oxide).
3. At concentrations ranging from N_B' to N_B'', both A oxide and B oxide will be formed simultaneously. A possible reaction scheme for this case, assuming that cations are the mobile species and AO grows more rapidly than BO is shown in Fig. IV-3.

Based on the premise that the oxidation reaction is controlled by diffusion processes, Wagner showed that the critical concentration N_B'', above which only B oxide is formed is given by,

$$N_B'' = \frac{V}{Z_B M_o} \left(\frac{\pi k_p}{D}\right)^{1/2} \qquad 2\text{-}10$$

where V is the molar volume of alloy, Z_B is valence of B atoms, M_o is the atomic weight of oxygen, D is the diffusion coefficient of B in alloy and k_p is the parabolic rate constant for exclusive formation of B oxide. Rapp(55) found agreement with theory in his investigation of the silver-indium system whereas Maak(56-58) did not find agreement

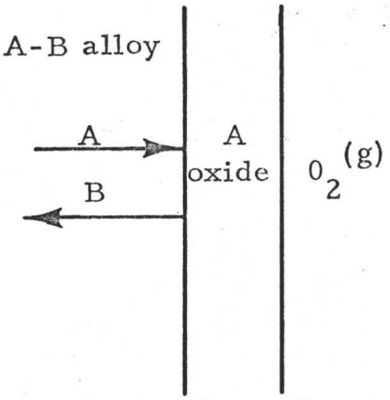

Fig. IV-1: Exclusive formation of A oxide ($N_B < N'_B$)

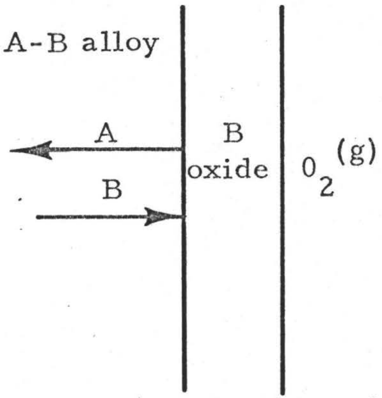

Fig. IV-2: Selective oxidation of Boxide ($N_B > N''_B$)

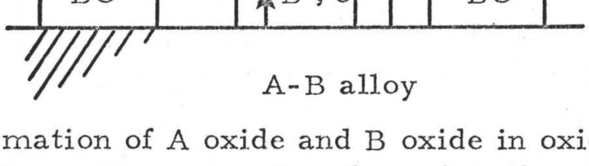

Fig. IV-3: Simultaneous formation of A oxide and B oxide in oxidation of A-B alloy assuming cation migration through both oxides. B oxide grows according to the displacement reaction $AO + B^{2+} = A^{2+} + BO$.

for copper-beryllium alloys due to the fact that the scales developed were porous and simultaneous internal oxidation of beryllium in the alloy phase occurred.

2.4.3 (c) Complex Oxides

One of the primary disadvantages of using the pure less-noble oxide as the protective layer as discussed above, lies in the fact that depletion of the alloy by the oxidation process causes the system to have poor self-healing properties in the case of mechanical rupture of the protective film. Therefore the situation where a complex oxide containing both alloying components forms on the alloy may be desirable. Diffusion rates in complex oxides are very often appreciably lower than in the single oxides(5).

The best known examples of complex oxides are 'spinels' consisting of compounds with the general formula $A0. B_2 0_3$ where A-B is the alloy. Generally spinels have a cubic structure. For example, Schmahlzried and Wagner(59) have studied lattice defect phenomena in iron-nickel spinels and demonstrated that the diffusion parameters are smaller than in single oxides. However, the elementary steps in the diffusion mechanism in spinel lattices are not very well understood. On iron-chromium alloys the spinel $Fe\ Cr_2 0_4$ is formed, whilst $Ni\ Cr_2 0_4$ is formed on nickel-chromium under certain experimental conditions.

2.4.3 (d) Internal Oxidation

When oxygen dissolves in the alloy phase during oxidation, the less noble alloy component may form oxide within the alloy. In this manner, oxide may be formed below the alloy surface-scale interface. This is often termed subscale formation.

Internal oxidation takes place in numerous alloy systems and detailed analyses of internal oxidation have been made for alloys of copper, silver, nickel, etc. with small concentrations of less noble alloying elements such as aluminum, silicon, chromium etc.(54-58, 60-69). For internal oxidation to occur, the diffusion rate of oxygen in the alloy must be much faster than the alloying element. If this among other conditions is satisfied, an oxygen gradient is established in the alloy and the dissolved oxygen will react to form oxide of the less noble oxidizing element in a zone below the alloy surface. The internally oxide zone extends to the depth at which the concentration of dissolved oxygen becomes too low to support oxide formation.

Various features of this type of reaction behaviour have been described by Rhines et al(62, 63), Darken(65), Meijering et al(66), Wagner(54), Rapp et al(55, 67, 68) and Bohm and Kahlweit(69). Following Wagner(54) and assuming that no surface scale is formed and that the internal oxidation is diffusion controlled, the thickness of the internally oxidized zone may be expressed by

$$\xi = 2\gamma\,(D_o t)^{1/2} \qquad 2\text{-}11$$

where D_o is self-diffusion coefficient of oxygen in alloy, t is time and γ is a dimensionless parameter.

Using Fick's second law, Wagner derived the following equations for the concentration profiles of oxygen and alloying addition B,

$$N_o = N_o^{(s)} \left\{ \frac{1-\mathrm{erf}\left[(x/2)(D_o t)^{1/2}\right]}{\mathrm{erf}\ \gamma} \right\} \quad \text{for } x \leq \xi \qquad 2\text{-}12$$

$$N_B = N_B^{(o)} \left\{ \frac{1-\mathrm{erfc}\left[(x/2)(D_B t)^{1/2}\right]}{\mathrm{erf}\ (\theta^{1/2}\gamma)} \right\} \quad \text{for } x \geq \xi \qquad 2\text{-}13$$

where x is distance from the outer surface of the alloy, N_o is the mole fraction of oxygen at x and $N_o^{(s)}$ at the outer surface, N_B is the mole fraction of B in alloy and $N_B^{(o)}$ in the unoxidized alloy. D_M is the self diffusion coefficient of B in the alloy, and $\theta = \frac{D_o}{D_B}$.

Since the flux of oxygen is equal to the flux of B atoms at the front of the internally oxidized zone:

$$D_o\left(\frac{\partial N_o}{\partial x}\right)_{x=\xi} = -\nu \; D_B\left(\frac{\partial N_B}{\partial x}\right)_{x=\xi} \qquad 2\text{-}14$$

where ν represents the number of oxygen atoms per B atom in precipated oxide, it can then be shown that

$$\frac{N_o^{(s)}}{\nu \, N_B^{(o)}} = \frac{\exp(\gamma^2 \text{ erf } \gamma)}{\theta^{1/2} \exp(\theta\gamma^2) \text{erfc}(\theta^{1/2}\gamma)} \qquad 2\text{-}15$$

from which γ can be determined.

A very common situation in solids is described by $\gamma << 1$ and $\theta^{1/2} >> 1$, whence

$$\xi = \left(\frac{2 N_o^{(s)} D_o t}{\nu N_M^{(o)}}\right)^{1/2} \qquad 2\text{-}16$$

Rapp(55) has shown that the above approximations and equation 2-16 are valid for internal oxidation of Ag-In during exposure to air at 550°C.

Similar treatments for simultaneous scale formation and internal oxidation have been given by Rhines et al(63) and Maak(57) for parabolic growth of scale. Rapp(70) has treated the situation when scale growth is linear. Bohm and Kahlweit(69) have made detailed analysis of oxide formation at the internal oxidation front. They studied the number of oxide particles precipitating per unit volume, Z(x), as a function of distance from the surface, x, in the oxidation of Ag-Cd alloy at 850°C.

Their theoretical treatment predicts that

$$Z(x) = \beta\, a_o^{3}\ x^{-3} \qquad 2\text{-}17$$

where a_o is the concentration of dissolved oxygen in the alloy at the surface, and β is a parameter which is a function of diffusion coefficients of cadmium and oxygen, initial concentration of cadmium in alloy, solubility product and critical concentration product of the precipitated oxide. The experimental results for Ag-Cd system agreed with the equation 2-17.

All of the above analyses involving diffusion theory for a description of the internal oxidation phenomena have been based on mathematical treatments assuming that the ternary system consisting of a binary alloy and oxygen behaves as a psuedo-binary system. That is, ternary diffusion parameters are approximated to binary parameters. These approximations are valid for the alloys studied to this time. Recently, Kirkaldy(71) has generalized these relationships to oxidation conditions for alloys where ternary diffusion theory must be invoked to describe the phenomena.

CHAPTER III

OXIDATION PROPERTIES OF IRON, SILICON AND IRON-SILICON ALLOYS

3.1 Oxidation of Iron

The oxidation properties of iron have been studied extensively under different conditions of reactant gas pressures and temperatures because of the technological importance of this metal.

There are certain features in the iron-oxygen system, shown in Fig. III-1, which should be considered. At temperatures above 570°C, three oxides, namely, wustite, magnetite and hematite are stable whilst below 570°C, bulk wustite is unstable. The above oxides lead to the formation of multilayered scales on iron and excellent examples of these scale are given by Paidassi(72).

Marker studies, radiotracer diffusion studies and electrical conductivity measurements, along with phase equilibria studies have enabled the establishment of the defect structures for these oxides. Wustite is a p-type oxide of a large composition range. The defects consist of vacant cation sites and positive holes and diffusion occurs via cation vacancies. Magnetite contains an excess of oxygen, but much smaller than wustite, and the corresponding defect concentration is smaller. Birchenall(75) originally found by tracer studies that both anions and cations diffuse in this oxide but more recent investigations have shown that diffusion is mainly cationic. Hematite exists with an excess of cations, and diffusion is anionic via anion vacancies.

The oxidation rate has been observed to obey a parabolic relationship above 200°C when oxidized in air or oxygen. These results indicate that the mechanism of oxidation is associated with diffusion processes, but the scales form in a complex manner. Simnad, Davies and Birchenall(73,74) determined the oxidation rates of iron at sufficiently high temperatures

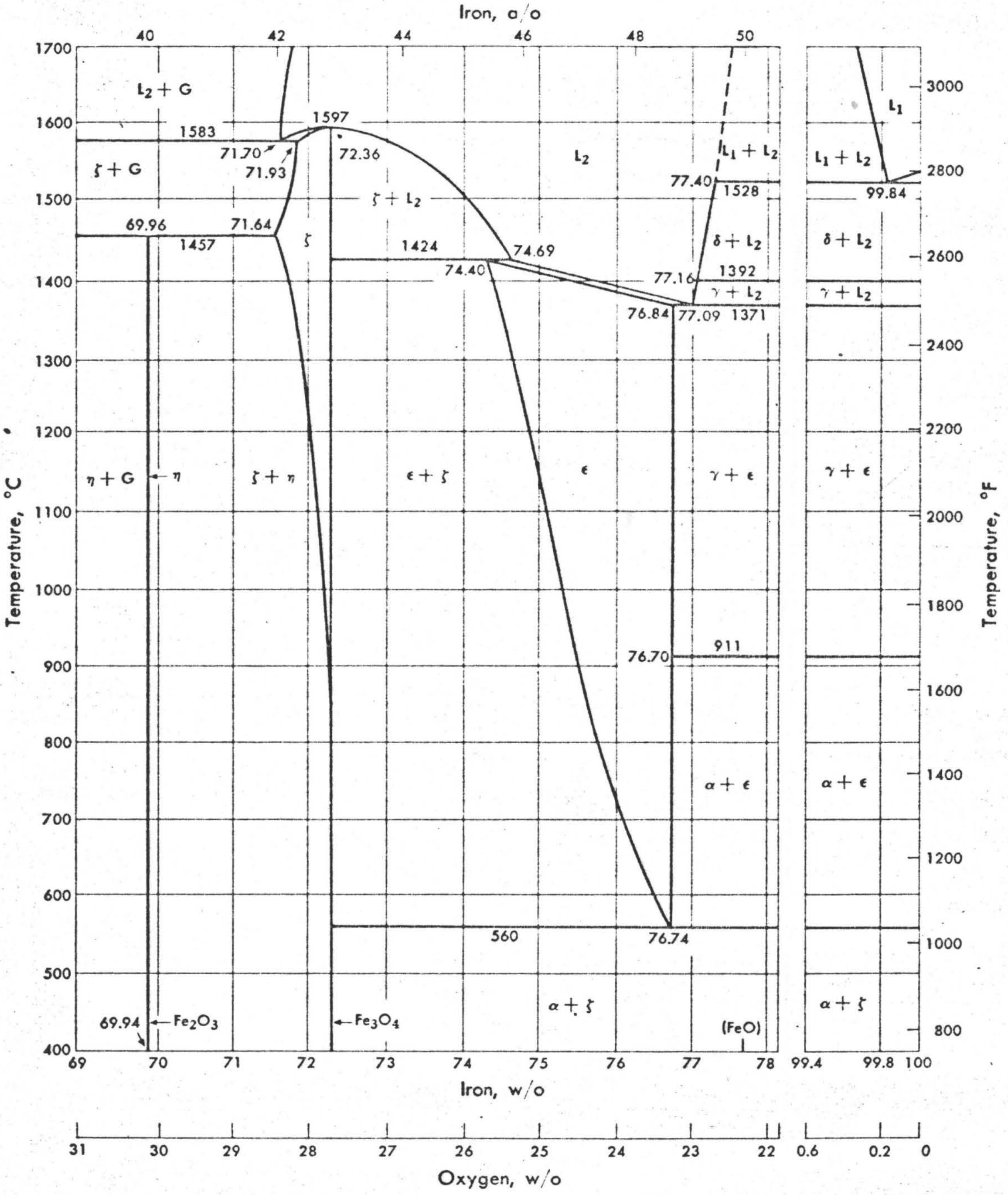

Melting point: Iron, 1536°C

Fig. III-1: Iron-oxygen phase diagram.

to form wustite, magnetite and hematite and found that the parabolic relationship was obeyed. The self diffusion coefficients of iron in the three oxides were determined by Himmel, Mehl and Birchenall(75) and the experimental oxidation rates were compared with the rates calculated from Wagner's theoretical parabolic equation. The agreement was good. Paidassi(72) has also shown metallographically that the three oxides thicken at a parabolic rate at temperatures above 700°C. The relative thickness of the layers was approximately 100:5:1 for $t_{FeO} : t_{Fe_3O_4} : t_{Fe_2O_3}$ and these values are independent of time. Smeltzer(44, 50), and Pettit and Wagner(42, 43) determined the oxidation rates of iron in carbon dioxide in the temperature range 600-1100°C and observed linear rates at short times and parabolic rates at long times.

As mentioned above, in atmospheres of low oxidizing potential like carbon dioxide-carbon monoxide atmospheres and hydrogen-water vapour, iron oxidizes at a linear rate and compact scales are obtained. Fishbeck et al.(40) initially observed this linear reaction behaviour on oxidation of iron in carbon dioxide. Since studies on the oxidation of iron in atmospheres of low oxidizing potential are of specific interest to the work in this investigation, published results will be reviewed in some detail.

In order to obtain more detailed knowledge on the reaction mechanism responsible for linear reaction rates, Hauffe and Pffeiffer(41) oxidized iron in carbon dioxide-carbon monoxide atmospheres at 900-1000°C. Wustite was the only oxide formed and it was found that the oxygen uptake was proportional to the time suggesting interface reaction control. Since the linear reaction rate, K_L, could be shown to depend on the gas pressure as follows,

$$K_L = \text{const} \left(\frac{P_{CO_2}}{P_{CO}}\right)^{0.71} \tag{3-1}$$

the authors suggested that the overall rate controlling step was the dissociation of carbon dioxide on the wustite surface producing chemisorbed oxygen ions.

That is,

$$CO_2 = 0^-_{ad} + CO + \oplus \tag{3-2}$$

followed by incorporation of the adsorbed species into the wustite lattice,

$$0^-_{ad} = Fe0 + Fe''_{\square} + \oplus \tag{3-3}$$

where $\oplus$ denotes an electron hole and $Fe''_{\square}$ a vacant cation site in the wustite lattice.

Pettit, Yinger and Wagner(142) were unsatisfied with this interpretation of the empirical relation 3-1. Accordingly they studied the oxidation of iron in carbon dioxide - carbon monoxide atmospheres of widely different oxidizing potentials at temperatures in the range 925-1075°C. A chemisorption reaction was assumed to be rate controlling, namely,

$$CO_2 \rightarrow CO + 0_{ads} \tag{3-4}$$

They then represented the number of equivalents of oxide formed per unit area per unit time, $\overset{o}{n}$,

$$\overset{o}{n} = k' P_{CO_2} - k'' P_{CO} \tag{3-5}$$

where k' and k" are the reaction rate constants for the forward and backward reaction, respectively, in 3-5. According to Kobayashi and

Wagner(76), the rate of dissociation of carbon dioxide is a function of the concentration of electron defects in the oxide. Since the decomposition reaction is assumed to be rate controlling, the iron/oxygen ratio in the wustite layer is that in equilibrium with the metallic iron due to rapid equilibration of iron by diffusion of cation vacancies in wustite. Therefore the concentration of electron holes is fixed and does not appear in equation 3-5.

At equilibrium, $\overset{o}{n} = 0$ and

$$\frac{k''}{k'} = \left(\frac{P_{CO_2}}{P_{CO}}\right)_{eq} = K \qquad 3\text{-}6$$

where k is defined by the equilibrium,

$$Fe + CO_2 = Fe0 + CO \qquad 3\text{-}7$$

Substitution into equation 3-5 and expressing P_{CO_2} in terms of the total pressure P of reacting gas, Pettit et al(42) obtained,

$$K_L = k'\ P(1+K)\ (N_{CO_2} - N_{CO_2\ (eq)}) \qquad 3\text{-}8$$

where N_{CO_2} is the mole fraction of CO_2 in the reacting gas and the subscript (eq) denotes the mole fraction of CO_2 in atmosphere in equilibrium with iron and wustite.

Smeltzer(50) also investigated the mechanism of oxidation of iron to wustite in carbon dioxide-carbon monoxide atmospheres assuming that the reaction kinetics were controlled by an interface reaction. Furthermore, it was assumed that carbon dioxide was adsorbed irreversibly to form chemisorbed oxygen and carbon monoxide. The elementary steps for the oxidation reaction are as follows:

$$CO_{2(g)} \rightarrow 0^{=}_{ads} + 2\oplus_{(o)} + CO_{(g)} \qquad 3\text{-}9$$

$$0^{=}_{ads} \rightarrow Fe0 + Fe_{\square(o)} \qquad 3\text{-}10$$

$$Fe_{\square(o)} + 2\oplus_{(o)} \rightleftharpoons Fe_{\square(i)} + 2\oplus_{(i)} \qquad 3\text{-}11$$

$$2\oplus_{i} + Fe_{(i)} + Fe_{\square(i)} \rightleftharpoons Nil \qquad 3\text{-}12$$

$$0^{=}_{ads} + 2\oplus_{(o)} \rightarrow \frac{1}{2}\, 0_{2\,(g)} \qquad 3\text{-}13$$

The subscripts (g), (o), (i) refer to the gas phase and lattice defect structure at the oxide-gas interface and metal oxide interface respectively. Nil refers to the annulment of lattice defects by solution of iron into oxide.

Oxidation rates would obey a parabolic relationship if the concentration of vacancies and electron holes equalled their equilibrium values. Since linear rates were observed, equation 3-9 and 3-10 were assumed to represent the rate controlling processes. Considering that the surface coverage of adsorbed oxygen, θ_o, is constant during oxidation and that lattice defects in the oxide are equilibrated with the metal phase, Smeltzer derived the following expression for the surface coverage,

$$\theta = \frac{k_2}{k_3 + k_6 K}\left(P_{CO_2} - P^*_{CO_2}\right) \Big/ \left\{1 + \frac{k_2}{k_3 + k_6 K}\left(P_{CO_2} - P_{CO_2}{}^*\right)\right\} \qquad 3\text{-}14$$

where k_2, k_3, k_6 are rate constants for oxygen chemisorption during wustite formation, and oxygen desorption, respectively; K is defined by the equilibrium of equation 3-8.

Two approximations to equation 3-14 were considered; namely, that θ approaches zero and that the rate controlling step was the incorporation of chemisorbed oxygen into wustite. The relationships for the linear rate constants are:

$$K_L = k_2 (P_{CO_2} - P_{CO_2}*) \qquad 3\text{-}15$$

where the dissociation of carbon dioxide is the rate controlling step as θ approaches zero, and

$$K_L = \frac{k_3 k_2 (P_{CO_2} - P_{CO_2}*)}{k_3 + k_6 K} \qquad 3\text{-}16$$

where $0 < \theta < 1$ and $k_2 << k_3 + k_6 K$ respectively. Since the partial pressures of carbon dioxide are proportional to the mole fraction of carbon dioxide and total pressure of reacting gas, equations 3-15 and 3-16 are of same form as equation 3-8.

An interface reaction control mechanism has also been adapted by Turkdogan(77) to describe the initial rates of oxidation of iron in water-hydrogen atmospheres by applying Eyring's theory of absolute reaction rates. A chemisorption reaction was assumed and the overall phase boundary reaction was represented by,

$$H_2 0_{(g)} + 2e \longrightarrow 0^{=}_{ad} + H_{2\ (g)} \qquad 3\text{-}17$$

It was possible to derive an expression for the linear reaction rate under conditions of a constant number of available sites on the wustite surface, the rate of oxidation being determined by the dissociation of an activated complex. The reaction rate constant was,

$$K_L = k' \ \theta_o \left(\frac{1}{a_o} - \frac{1}{a_o''}\right) P_{H_2 0} \ e^{-E/RT} \qquad 3\text{-}18$$

where $k' = \frac{RT}{nh} K_+ \frac{k_3}{k_4}$, E is heat of activation and a_o'', a_o are the activities of oxygen at the oxide-gas interface in equilibrium with gas phase and oxide-iron interface, respectively, P_{H_2O} is the partial pressure of water vapour in the atmosphere and K_+ is the equilibrium constant for $H_2O = [H_2O]_+$. 3-19

If θ_o is assumed constant at fixed temperatures,

$$K_L = k'' \left(\frac{1}{a_o} - \frac{1}{a''_o}\right) P_{H_2O} \qquad 3\text{-}20$$

An analagous expression can be derived for oxidation kinetics in carbon dioxide-carbon monoxide atmospheres. By suitable substitution for a_o and a''_o in the above expression, it can be shown to be similar in form to each of the equations, 3-8, 3-15, and 3-16.

As the wustite scale grows in thickness greater than 10^{-2} cm., diffusion through the oxide eventually becomes the rate controlling process. A transition from linear to parabolic kinetics was found in carbon dioxide-carbon monoxide and water-hydrogen atmospheres. By taking into account the interplay between the phase boundary reaction and diffusion through the scale, Pettit and Wagner derived and experimentally confirmed an expression for the change from linear to parabolic oxidation(43).

3.2. Oxidation of Silicon

The oxidation behaviour of silicon can be classified under two types: the active and the passive types. The particular type of oxidation is dependent on the temperature and oxygen potential of the reaction atmosphere. The oxidation of silicon has been principally studied under conditions where passive oxidation occurs. Passive oxidation occurs when a stable film of protective oxide SiO_2, formed on the silicon surface, causes the reaction rates to become very slow. In addition to the very low rate of oxygen diffusion in the oxide, the specific volumes of the three crystallographic forms of silica, quartz, cristobalite and tridymite, as well as the amorphous form, are greater than those of silicon which permits formation of an adherent oxide which serves to explain the very slow oxidation rate, even at elevated temperatures. Active oxidation occurs at high temperatures above 1000°C, and atmospheres of low oxidizing potential. A volatile oxide, Si0, forms at the silicon surface but does not accumulate as a protective film in the boundary gas layer. If the resulting partial pressure p_{Si0} at the surface is less than the equilibrium partial pressure $p_{Si0}*$ for the reaction

$$\frac{1}{2}\,Si_{(s)} + \frac{1}{2}\,Si0_{2(s)} \rightleftharpoons Si0_{(g)} \qquad 3\text{-}21$$

the silicon surface will remain bare. At higher oxygen potentials, however, p_{Si0} will reach p_{Si0}^{*} and accordingly a protective $Si0_2$ layer may be formed. Consequently, the transition from the active to passive state is expected to occur if

$$p_{Si0} = p_{Si0}^{*} \qquad 3\text{-}22$$

Wagner(78) has theoretically predicted the maximum oxygen partial pressure in bulk gas $p_{0_2}^{o}$ (max) at which a bare silicon surface can be maintained as,

$$p_{0_2}^{o}\,(\text{max}) \simeq \frac{1}{2}\left(\frac{D_{Si0}}{D_{0_2}}\right)^{1/2} p_{Si0}^{*} \qquad 3\text{-}23$$

Both Kaiser and Breslin(79) and Gulbransen et al(80) have experimentally confirmed the validity of equation 3-23 for liquid and solid silicon, respectively.

Owing to the importance of planar silicon device technology, the formation of silicon dioxide layers by thermal oxidation of single crystal silicon has been studied very extensively in the past several years. On the basis of these studies, Deal and Grove(81) were able to formulate a simple paralinear model involving interface reaction control at short times and diffusion control at long times. The above model was found to apply to oxidation in oxygen and water vapour-oxygen atmospheres at temperatures from 700°-1200°C. Both the linear rate and parabolic rate constants were proportional to the partial pressure of the oxidant. Similar observations were also made by Nakayama and Collins(82) and Burkardt and Gregor(83) when silicon was oxidized in argon-water vapour atmospheres at 900-1200°C.

During the oxidation of silicon, neither quartz nor tridymite has been identified after oxidation at temperatures from 500-1420°C. At temperatures below 1050°C, amorphous silica is generally detected whereas above this temperature, the oxide layer consists of cristobalite. Tridymite is the stable form between 867° to 1470°C but has not been found in oxide layers formed on silicon in this range.

3.3 Oxidation of Iron-Silicon Alloys

3.3 (a) General Features

The oxidation characteristics of iron-silicon alloys have been studied by a large number of investigators under various experimental conditions using techniques such as thermogravimetric measurements, X-ray and electron diffraction, optical and electron microscopy, chemical and spectrochemical analyses. There has been considerable disagreement about the structure and thicknesses of various oxide layers and their mechanism of growth. This disagreement, however, is due to the fact that the types of scales formed are dependent on the experimental conditions such as temperature, composition of reaction atmosphere, time of exposure and also on the composition of the alloy.

The oxides to be expected on iron-silicon alloys are the three oxides of iron; wustite, magnetite and hematite, silica and mixed oxides. The mixed oxides are fayalite and ferrosillite. On reviewing the literature, one finds that three types of oxide layers have been mainly observed. These three basic types are:

a) External scale of either amorphous or crystalline forms of protective oxide, silica(84, 85).

b) External scale consisting of the three oxides of iron, mixed oxide $2FeO.SiO_2$ and subscale or internal precipitate of silica in alloy matrix(88-97).

c) No external scale with pronounced internal oxidation with precipitation of silica in a fine dispersion(86, 87).

Seybolt et al(84) and Sugiyama et al(85) have studied the formation of thin silica films on Fe-Si alloys. Seybolt studied the oxidation of a 3.25% Si alloy using H_2O/H_2 as the oxidizing agent over the temperature range of 400-1000°C. The oxide films formed at an oxygen potential of 10^{-4} atm. were studied using electron diffraction and were found to consist of amorphous silica at short times. On standing or thickening these films transformed to high cristobalite. For longer exposure and at high temperature high cristobalite transformed to high tridymite, which on cooling to room temperature transformed to low tridymite. Sugiyama also found amorphous films of silica formed on alloys containing 3 - 6 % Si upon exposure in air at temperatures in the range 700-1000°C, which could be converted to high cristobalite by heating the films to 1200°C for 3 hours. Also, fayalite layers were formed inside the iron oxide scales at the surface of Fe-Si alloys (1-6% Si) oxidized at 1100-1200°C in air.

Bohenkamp et al(86) and Schenck et al(87) studied the exclusive internal oxidation of iron-silicon alloys containing 0.14-1.76% Si using hydrogen-water vapour atmospheres in the temperature range 820 - 1100°C. By suitable choice of oxidizing atmospheres, it was possible to completely eliminate external scale formation and only internal oxidation was observed with precipitation of silica in fine dispersion. Schenck et al observed that depth of internal oxidation increased with decreasing silicon content and increasing temperature. They used Rhines' et al(63) analysis for internal oxidation to explain their results. Bohemkamp's observations were similar but they used Wagner's internal oxidation model and were able to determine the product $N_o D_o$ for α and γ iron and found that it depended on silicon content. Also from combined gravimetric and thickness measurements, the authors were able to evaluate values for diffusivity of silicon under these conditions.

A number of investigators report formation of scales containing Fe_20_3, Fe_30_4, Fe0, Fe0 + Fe_2Si0_4 as various constituent layers on iron-silicon alloys containing less than 3.0% silicon when oxidized in air or oxygen at temperatures between 700 - 1150°C(88-97). Tuck(93, 94), Rahmel and Toboloski(95-97) report a similar type of scale formation in carbon monoxide-carbon dioxide atmospheres except that the highest oxide of iron Fe_20_3 is absent.

3.3 (b) Oxidation Mechanisms in Iron-Silicon Alloys

Most of the investigations on the iron-silicon system have been primarily kinetic studies of oxidation under different experimental conditions with alloys ranging in composition from 0.2 to 4% Si. A decrease in oxidation rate has been generally reported with increasing silicon content and decreasing temperature. Darken(98) has predicted theoretically that internal oxidation of an alloy should occur at low silicon contents, but that a barrier to oxidation in the form of a silica rich layer should occur at higher silicon content. The change in mechanism was predicted to occur between 2 to 3% silicon, which was confirmed experimentally by Ward(99). This explanation was based on the assumption that the diffusion of silicon would play a major role, when the volume of the precipitated oxide exceeded a critical volume fraction in the matrix.

Ipatayev and Orlova(88) found that in the oxidation of a 1.43 $^{w}/o$ silicon alloy in air, the alloy oxidized in two stages and followed a parabolic law in both periods. The initial period of fast reaction rate decreased with increasing temperature from 140 hrs. at 700°C to 10 hrs. at 1000°C. They attributed the change in reaction rate constant after the initial period of fast reaction rate, to a change in structure of the scale. On the basis of special experiments to check this hypothesis, it was found that the decrease of rate corresponded to a change in the relative thicknesses of the wustite and fayalite layers in the scale. Evans and Chatterjee(92) observed the opposite behaviour with 0.5 $^{w}/o$ silicon alloy oxidized at 850° - 1200°C, with the existence of an initial period of slow reaction rate which disappeared at temperatures greater than 1100°C. At 1170 - 1180°C, the oxidation was catastrophic since the melting point of fayalite is 1180°C. The slow initial period was associated with the precipitation of silica at the metal-oxide interface, but with the occurrence of a solid state reaction between wustite and silica the resulting fayalite was sufficiently conducting to give a fairly rapid scaling rate.

An extensive investigation was carried out by Schmahl(89-91) et al on the oxidation kinetics of a series of iron-silicon alloys ranging from 0.03 - 3.63 $^{w}/o$ silicon at 890°, 950° and 1050°C in 1 atmosphere of oxygen. They observed a sharp change in oxidation rate beyond 1.0% Si and attributed the change to the α - γ transition of the alloy which occurs in this temperature range. Silicon diffuses faster in

α-iron, hence silica formed at the start of reaction and slowed down the rate. In a later investigation,(90) the authors found that scale formation depended on the alloy composition and oxygen pressure. An alloy containing 1.6% silicon showed an increase in oxidation with increasing oxygen pressure from 3 to 695 mm Hg. The rate curves showed a parabolic relationship at all pressures. This finding was offered as evidence that the reaction rate was diffusion controlled. However, the oxide scales formed on alloys containing 2-3% Si were pressure dependent only in the initial stages of oxidation and the parabolic relationship was not obeyed. It was also found that 0.04%C in 3% Si alloy changed the oxidation characteristics of the alloy markedly. This behaviour was explained on the basis of reduction of SiO_2 by carbon, which left pores in the scales.

Tuck(93) reported a transition from a parabolic relationship at 800 - 950°C to nearly linear at 1000 - 1120°C in alloys containing 1.0% and 1.74% silicon oxidized in carbon dioxide. There also occurred a period of rapid linear rate in oxidation at 800 - 950°C before onset of parabolic behaviour. The scales formed at different temperatures only differed in the size of fayalite imbedded in the conglomerate, being larger at higher temperatures. The changes in oxidation rate were correlated to the scale structure and evidence was presented to show that the changes are related to the formation and growth of the fayalite layer. It was also observed that alternate layers of wustite and fayalite formed on 1.0% Si iron oxidized for 1/2 hr. at 1120°C and on 3.0% Si iron oxidized for 4 hrs. at 950°C. The mechanism proposed for this type of scale formation was:

a) formation of fayalite at the alloy surface causing impoverishment of silicon below the surface,

b) continued oxidation by outward diffusion of iron ions through the fayalite with concurrent formation of wustite below the layer.

Accordingly the scale-alloy interface advanced inward and silicon diffused outward towards this interface until,

c) the silicon concentration became again sufficiently high for the formation of another layer of fayalite with simultaneous removal of silicon from the alloy.

In a later investigation on a 1.74% Si alloy, Tuck(94) observed that protective oxidation or non-protective oxidation became possible by use of suitable atmospheres consisting of oxygen-carbon dioxide. Protective scaling was observed in oxygen and non-protective scaling in carbon dioxide at 1000°C. Apparently an atmosphere of carbon dioxide caused the protective layer of silica and hematite to breakdown, with subsequent formation of fayalite and lower oxides of iron. A mechanism for the breakdown of the silica - hematite layer was proposed based upon the instability of hematite in carbon dioxide. Hematite, upon being reduced to magnetite, would be accompanied by a reduction in oxide volume of about 2 percent. Cracking of oxide or porosity in the scale could then occur. The porosity may be such that carbon dioxide is admitted through the silica rich layer and there reacts with iron diffusing outwards through the cracks in the silica film, forming wustite. Once wustite is present fayalite formation follows rapidly.

Rahmel and Toboloski(95-97) made similar observations during the addition of both carbon dioxide and water vapour to oxygen used for oxidation of iron-silicon alloys containing 0.35 - 4.0% Si at temperatures of 750 - 1050°C. With the help of marker experiments, it was found that markers placed on the alloy surface were found after oxidation at the fayalite/wustite or the fayalite and wustite/wustite boundary. The fayalite layer formed under $CO_2 + 0_2$ or $H_20 + 0_2$ oxidizing atmospheres was markedly loosened and imbedded in the wustite matrix. The inner scale layer was very porous. These observations were interpreted by assuming the following model and mechanism for the oxidation process. There occurs, in the pores close to the alloy-oxide boundary, a H_2/H_20 or CO/CO_2 atmosphere which permits rapid transfer of oxygen inward through a gaseous phase along pores extending from the wustite to the alloy surface. This permits the formation of fresh oxide immediately on the alloy surface, which has the effect of reducing the plastic flow inhibitions of the scale at the alloy-oxide boundary and also causes the fayalite particles to become imbedded in the wustite matrix.

The work of the previous investigators may be summed up as follows: The mode of the oxidation of iron-silicon alloys is dependent on the composition of the reacting gas, composition of the alloy and the temperature of reaction. The scales formed on iron-silicon alloys are most commonly layers of the oxides of iron, namely, hematite, magnetite and wustite, one or more layers of fayalite and layers of a conglomerate of wustite and fayalite. The kinetics of oxidation are either parabolic or linear, depending mainly on the temperature of reaction and composition of the reacting gas.

CHAPTER IV

THEORETICAL CONSIDERATIONS

4.1 Introduction

In the introduction, it was emphasized that atmospheres containing carbon dioxide and carbon monoxide of suitable oxidizing potentials would be used in this study to reduce the number of oxide layers formed in the scale on the alloy to two, namely, wustite and fayalite. It is evident from the review on the oxidation properties of iron-silicon alloys that the occurrence of multilayered scales lead to complex oxidation behaviour. Under the experimental conditions used in this investigation, the reaction produced the growth of a simple duplex scale consisting of wustite and fayalite. Since wustite forms the external layer, the oxidation mechanism would appear to be similar to that of iron. Therefore, in this section an attempt will be made to expand some of the oxidation concepts outlined for iron, in order to derive a theoretical rate expression for iron-silicon alloys. This theoretical expression can then be tested by reacting an alloy containing an appropriate concentration of silicon in atmospheres containing different oxygen potentials at a relatively high temperature of 1000°C.

It has been established that oxidation in the early stages does not necessarily proceed uniformly on the entire specimen but nuclei of different oxides may form on different areas of the specimen in alloys, for example, nickel-aluminum(100), nickel-chromium(101, 102), iron-chromium(103, 104). Silicon behaves in a manner similar to aluminum and chromium in the above systems. A simple model will be advanced to explain the growth of nuclei on an alloy under these conditions. In order to apply these concepts for scale formation on iron-silicon alloys, it is necessary to have a broad understanding of the iron-silicon-oxygen phase equilibria.

4.2 Iron-Silicon-Oxygen Phase Diagram

A phase diagram for the temperature of 1000°C is shown in Fig. IV-1. It was constructed from the data of Darken(105), from the study on equilibration of iron-silicon alloys with oxides. The compositions of the alloy in the iron-rich corner in equilibrium with wustite-fayalite and fayalite-silica of 0.7 and 2.3 w/o silicon are only approximations obtained from the results of Kanz et al(107) and White(106). The solid solubility of oxygen in the alloy is not depicted in the diagram since it is very small - of the order of a few ppm of oxygen. As shown by the diagram, alloys of various silicon contents may be equilibrated with wustite, wustite-fayalite, fayalite, fayalite-silica and silica. One must regard the compositions within each phase field as only being of schematic significance since no detailed information on phase fields of iron-silicon-oxides is available in the literature. The oxygen pressures at 1000°C for equilibration of the phases are presented in the pseudo-binary diagram of Fig. IV-2. The appropriate standard free energies of formation for the binary iron oxides and silica for the calculation of the dissociation pressures were taken from Elliot and Gleiser(108) and in the case of the ternary iron silicate from Taylor and Schmahlzried(109).

4.3 Linear Oxidation Rates

The assumption is made that the kinetics governing formation of fayalite-wustite duplex scale may be interpreted by a model for the transport of iron via vacancies and positive holes in wustite to react with oxygen at the oxide-gas interface, the dissociation of carbon dioxide to chemisorbed oxygen and its incorporation into the wustite lattice being

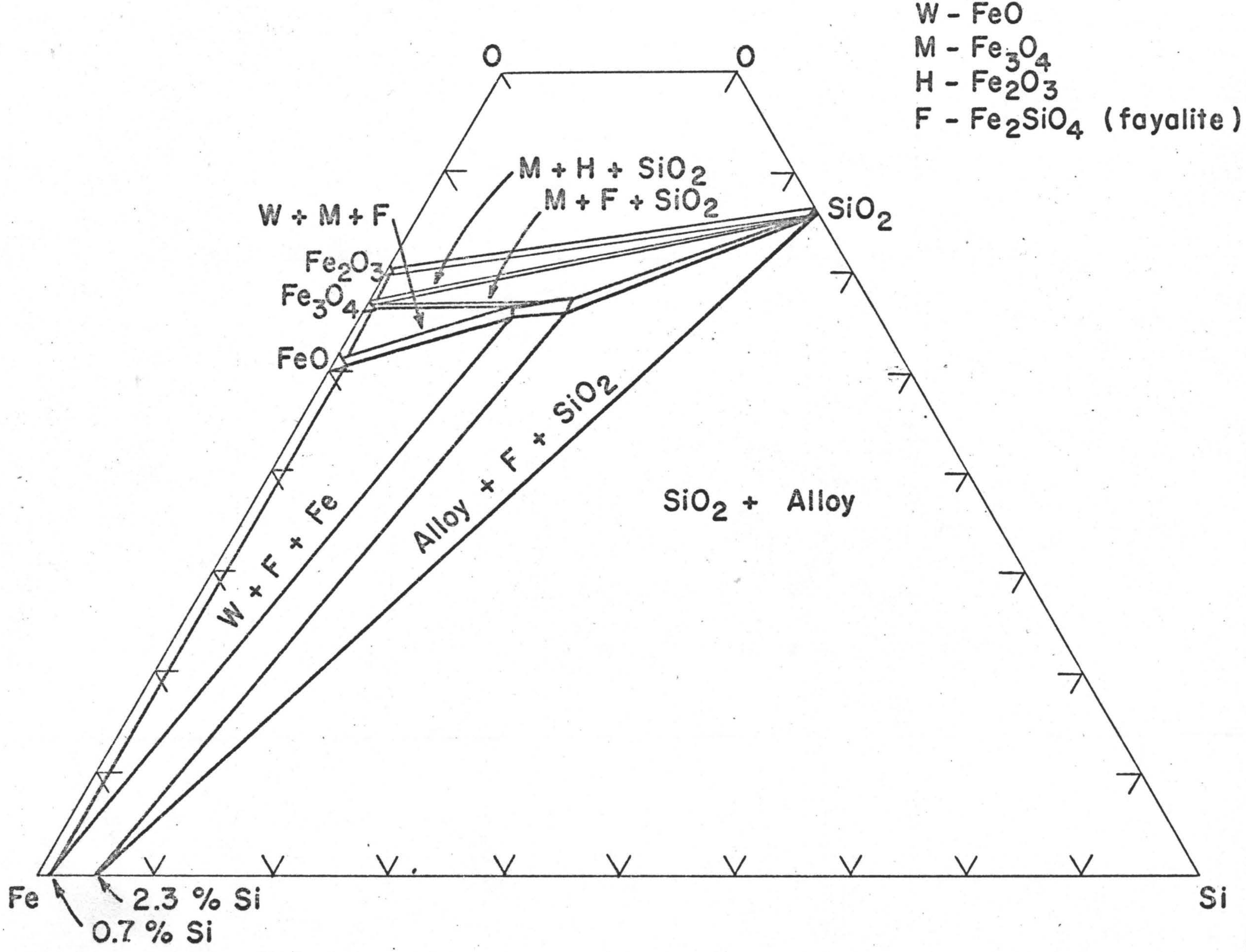

Fig. IV-1: Ternary Fe-Si-O Phase Diagram for 1000°C

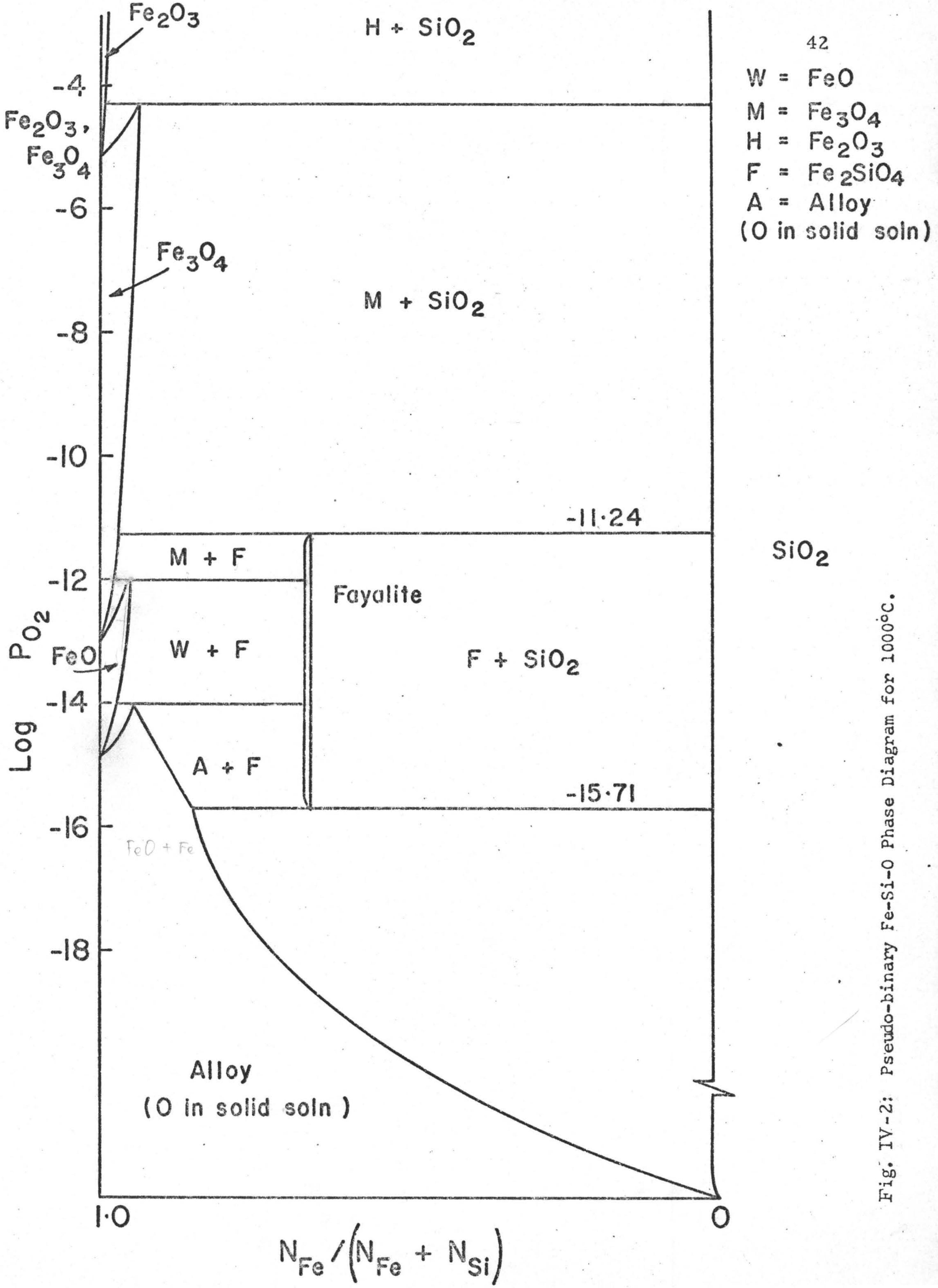

Fig. IV-2: Pseudo-binary Fe-Si-O Phase Diagram for 1000°C.

assumed to determine the reaction rate. To interpret the morphological development of the scale on an iron-silicon alloy, it is only necessary to invoke the additional condition that oxygen required for the growth of the wustite-fayalite conglomerate layer was supplied by a dissociative reaction of wustite at an internal interface.

Oxygen uptake for wustite scale growth may then be represented by the following reaction steps:

$$CO_{2(g)} = 0^{2-}_{(ads)} + CO_{(g)} + 2 \oplus \tag{4-1}$$

$$0^{2-}_{(ads)} = (FeSi)\ 0 + Fe\overset{''}{\square} \tag{4-2}$$

$$Fe\overset{''}{\square} + 2 \oplus + Fe\ (Alloy) = Nil \tag{4-3}$$

$$Si_{\{(FeSi)\,0\}} = Si_{(Fe_2Si0_4)} \tag{4-4}$$

where subscript (g) refers to the gas phase.

Equations 4-1 and 4-2 represent the rate controlling reaction steps involving dissociation of carbon dioxide and incorporation of chemisorbed oxygen into the wustite lattice. Nil refers to the annulment of lattice defects by solution of iron in wustite (FeSi)0 containing trace amounts of silicon dissolved in its matrix$^{(105)}$. Transport of iron through the wustite phase by means of iron vacancies and positive holes in the inner conglomerate of oxides and through the external wustite layer is regarded as sufficiently rapid by diffusion at the high temperatures of this investigation to maintain the concentration of lattice defects in wustite under the steady state oxidation condition at values near those for equilibrium between this oxide with the alloy.

A detailed balance of the elementary reaction steps 4-1 to 4-3 yields an expression to account for the occurrence of linear kinetics.

The forward and backward reaction rate constants for reactions 4-1 and 4-2 are denoted as k_1, k_2 and k_1', k_2', respectively, the primes distinguishing the backward rate steps. The steady state values approximating closely to equilibrium values of the compositional parameters are designated by asterisks. Since equation 4-2 accounts for the total uptake of oxygen, $\frac{\Delta M}{A}$, the linear rate constant is,

$$\frac{d(\Delta M/A)}{dt} = K_L = k_2\theta_o - k_2'\,\theta_v\,a_o^*\left[\square^*\right] \qquad 4\text{-}5$$

or

$$K_L = k_2\,\theta_v\left(\frac{\theta_o}{\theta_v} - \frac{k_2'}{k_2}\,a_o^*\left[\square^*\right]\right) \qquad 4\text{-}6$$

Here, θ_o and θ_v are fractions of surface sites covered and devoid of adsorbed oxygen, respectively, a_o^* is the oxygen activity and $\square^*$ is the vacancy concentration in the external wustite phase formed on the alloy.

If the oxygen surface coverage is regarded as constant during the steady state condition of oxidation,

$$\frac{\theta_o}{\theta_v} = k_1\,P_{CO_2} + k_2'\,a_o^*\left[\square^*\right]/(k_1'\,P_{CO}\left[\oplus^*\right]^2 + k_2) \qquad 4\text{-}7$$

where $\oplus^*$ is the positive hole concentration in wustite.,

Since the rate of oxide formation is zero when wustite and fayalite are equilibrated with the alloy,

$$\frac{\theta_o^*}{\theta_v^*} = \frac{k_2'}{k_2}\,a_o^*\left[\square^*\right] = \frac{k_1\,P_{CO_2}^*}{k_1'\,P_{CO}^*\left[\oplus^*\right]^2} \qquad 4\text{-}8$$

Substitution of 4-7 and 4-8 into 4-6 gives,

$$K_L = \frac{k_1\, k_2\, \theta_v}{k_2 + k_1' \left[\oplus^*\right]^2 P_{CO}} \left\{1 - \frac{a_o^*}{a_o^{(g)}}\right\} P_{CO_2} \qquad 4\text{-}9$$

upon relating the oxygen activities to the partial pressures of the reacting gas and the equilibrium constant for the reaction,

$$CO_2 = CO + O \qquad 4\text{-}10$$

by $a_o^* = K\,(P_{CO_2}/P_{CO}^*)$; $a_o^{(g)} = K\,(P_{CO_2}/P_{CO})$ 4-11

$$K_L = \frac{k_1\, k_2\, \theta_v\, (1+k)\, (P_{CO_2} - P_{CO_2}^*)}{k_2 + k_1' \left[\oplus^*\right]^2 P_{CO}} \qquad 4\text{-}12$$

Equation 4-12 can be rewritten as,

$$K_L = \frac{k_1\, k_2\, \theta_v\, (1+K)\; P'\, (N'_{CO_2} - N'^*_{CO_2})}{k_2 + k_1' \left[\oplus^*\right]^2 P_{CO}} \qquad 4\text{-}13$$

where $P' = P_{CO_2} + P_{CO}$ and $N'_{CO_2} = \dfrac{P_{CO_2}}{P_{CO_2} + P_{CO}} = \dfrac{P_{CO_2}}{P'}$ 4-14

If $k_1' \left[\oplus^*\right]^2 P_{CO} << k_2$, equation 4-14 reduces to,

$$K_L = k_1\, \theta_v\, (1+K)\; P'\, (N'_{CO_2} - N'^*_{CO_2}) \qquad 4\text{-}15$$

This particular form of the rate expression is valid when the rate of dissociation of carbon dioxide is the rate controlling surface reaction.

It is often useful to add an inert gas, for example, argon to the reaction atmosphere in order to study the effect of altering the partial pressure of the reacting gas upon the linear reaction rates. Equation

4-15 can then be rewritten as,

$$k_L = \frac{K_L}{P'} = k_1 \ \theta_v \ (1+K) \ (N'_{CO_2} - N'^{\,*}_{CO_2}) \qquad 4\text{-}16$$

It is apparent that, for the case of pure iron, this equation is equivalent to the expressions 3-8, 3-15 and 3-20 given in Chapter III and derived by Pettit and Wagner(42), Smeltzer(44, 50) and Turkdogan et al(77). It is also equivalent to the expression derived by Morris and Smeltzer(46) to account for the linear reaction kinetics for iron-nickel alloys. The validity of the above expressions for the kinetics of iron-silicon alloys oxidation will be established in this investigation.

On the other hand, if $k'_1 \left[\oplus^*\right]^2 \ P_{CO} \gg k_2$, equation 4-9 reduces to,

$$K_L = \frac{k_1 \, k_2 \, \theta_v}{k'_1 \left[\oplus^*\right]^2} \left\{ 1 - \frac{a_o^{\,*}}{a_o^{(g)}} \right\} \frac{P_{CO_2}}{P_{CO}} \qquad 4\text{-}17$$

Substitution of 4-11 into 4-17 gives,

$$K_L = \frac{k_1 \, k_2 \, \theta_v}{k'_1 \left[\oplus^*\right]^2 K} \left\{ \frac{P_{CO_2}}{P_{CO}} - \frac{P_{CO_2}^{\,*}}{P_{CO}^{\,*}} \right\} \qquad 4\text{-}18$$

This particular form of the rate expression is valid when both the dissociation of carbon dioxide and rate of incorporation of oxygen into the oxide play a role in determining the overall reaction rate.

4.4 Initial Oxidation Rates

It is proposed that these kinetics may be interpreted by a model for growth of oxide nodules. The wustite nodules are assumed to grow both laterally and vertically, whilst the rest of the alloy surface is covered with a amorphous silica film which grows vertically. As discussed in the literature review, Evans(14), Bartlett(31), Beck et al(34) and Fawcett et al(33) have derived expressions for nodule and nuclei growth on a metal under various experimental conditions. The general form of the expression describing the fractional surface coverage 'α' at time 't' may be expressed as,

$$\alpha = 1 - \exp(-\beta t^n) \qquad 4\text{-}19$$

where n is determined by the mode of nucleation. If nuclei appear simultaneously at the start of the reaction and the density of nuclei remains constant, n = 2. This case pertains to high supersaturations and when only certain preferred sites serve as nucleation centres. If the two-dimensional nucleation rate is constant then n=3. That is, nuclei appear sporadically in time and position on the uncovered position. On the other hand, if the growth rate of nuclei is limited by the supply of one of reactants through surface diffusion to nuclei edges then n=1.

Using the concepts outlined above, an expression can be derived for the reaction rate in the initial stages of the oxidation process.

The model depicting this type of nodular growth of oxide is illustrated in Fig. IV-3. The expression for the fractional coverage used in this derivation is chosen to be,

$$f_i = 1 - e^{-\beta(t + t_o)} = \frac{A_i}{A_o} \qquad 4\text{-}20$$

where A_i, A_o are the surface coverage of phase i and A_o is the surface area of the specimen. β is the lateral growth rate parameter and t_o is a time correction for t. This 't_o' is necessary to account for the fact that before the oxidation test is conducted in the carbon dioxide-carbon monoxide atmosphere, the specimen is annealed in argon and during

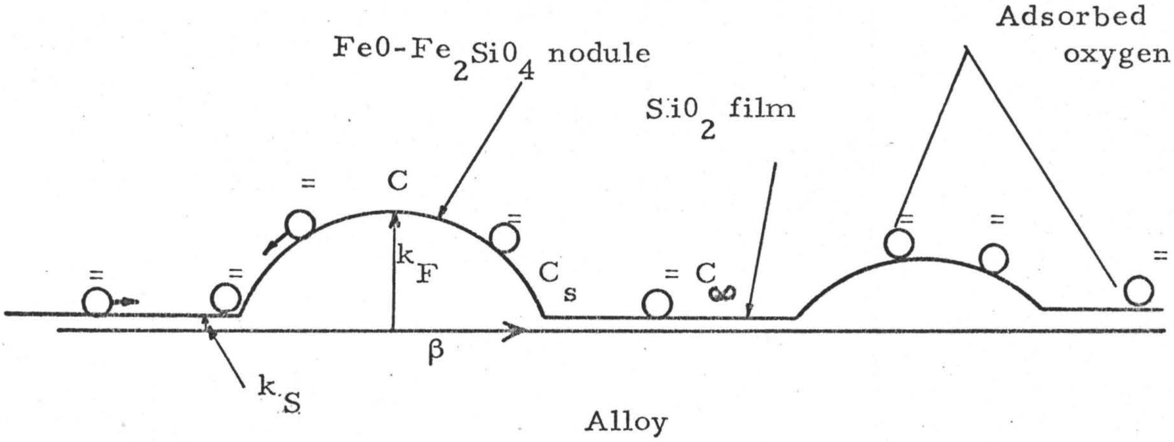

k_F, k_S are the vertical growth rates of FeO-Fe_2SiO_4 nodules and silica film respectively. β is the lateral growth rate of nodules.

Fig. IV-3: A schematic model for oxide nodule growth on alloy in initial stages.

this process a certain amount of oxidation takes place via residual oxygen impurity in the inert gas. The oxide phases are assumed to grow according to linear kinetics.

In order to derive expressions for the initial reaction rate, the following symbols are introduced where the suffixes 1 and 2 refer to the wustite and silica phases respectively:

ρ_i	density of the phase i.
k_i	vertical growth rate constant in expression of the form $x_i = k_i (t + t_o)$
A_i	surface coverage at time t
V_i	volume of phase i at time t
W_i	weight of phase i at time t
W	total weight gain in mgo/cm^2 at time t
x_i	thickness of the oxide at time t
γ_i	geometrical factor depending on shape of the oxide nodule.
α_o	fractional initial surface coverage by wustite phase
Ω_i	oxygen to cation ratio in oxide phase

Since the volume of phase $V_i = \gamma_i A_i x_i$, 4-21

$$\frac{dV_i}{dt} = \gamma_i \left[x_i \frac{dA_i}{dt} + A_i \frac{dx_i}{dt} \right] \qquad 4\text{-}22$$

It is assumed at zero time that the fractional surface coverage by phase 1 is α_o, whilst the rest of the specimen is covered by phase 2. These assumptions are based on the boundary conditions set up by the experimental oxidation test procedure. The expression for fractional surface coverage by phase 1 is,

$$\frac{A_1}{A_o} = 1 - (1 - \alpha_o)\, e^{-\beta t} = 1 - e^{-\beta(t + t_o)} \qquad 4\text{-}23$$

i.e.

$$1 - \alpha_o = e^{-\beta t_o} \tag{4-24}$$

and

$$\frac{A_2}{A_o} = (1 - \alpha_o)\ e^{-\beta t} \tag{4-25}$$

Substituting 4-25 and 4-23 into 4-22 gives,

$$\frac{dV_1}{dt} = k_1 \gamma_1\ A_o \left[1 + (\beta t + \beta t_o - 1)\,(1 - \alpha_o)\ e^{-\beta t}\right] \tag{4-26}$$

and

$$\frac{dV_2}{dt} = k_2\ \gamma_2\ A_o \left\{(1 - \alpha_o)(1 - \beta t - \beta t_o)\ e^{-\beta t}\right\} \tag{4-27}$$

Integrating equations 4-26 and 4-27 with respect to t from t = 0 to t = t.

$$V_1 = k_1 \gamma_1 A_o \left[t - (1 - \alpha_o)\,(t + t_o) e^{-\beta t} + t_o\,(1 - \alpha_o)\right] \tag{4-28}$$

$$V_2 = k_2 \gamma_2 A_o\ (1 - \alpha_o) \left[(t + t_o) e^{-\beta t} - t_o\right] \tag{4-29}$$

Now $W_i = \rho_i\ V_i$. Substitution of 4-28 and 4-29, respectively, into 4-30 yields, 4-30

$$W_1 = \rho_1\, k_1\, \gamma_1\, A_o \left[t - (1 - \alpha_o)\,(t + t_o) e^{-\beta t} + t_o\,(1 - \alpha_o)\right] \tag{4-31}$$

$$W_2 = \rho_2\, k_2\, \gamma_1\, A_o \left[(1 - \alpha_o)\,(t + t_o) e^{-\beta t} - (1 - \alpha_o)\, t_o\right] \tag{4-32}$$

The net weight gain of oxygen per unit area of specimen is,

$$W = \frac{1}{A_o} \sum_{i=1}^{2} \Omega_i\ W_i \tag{4-33}$$

Substitution of 4-31 and 4-32 into 4-33 gives,

$$W = \rho_1 k_1 \Omega_1 \gamma_1 \left[t = (t + t_o)(1 - \alpha_o) e^{-\beta t} + t_o (1 - \alpha_o)\right]$$

$$+ \rho_2 k_2 \Omega_2 \gamma_2 \left[(1 - \alpha_o)(t + t_o) e^{-\beta t} - t_o (1 - \alpha_o)\right] \qquad 4\text{-}34$$

Upon designating $k_F = \rho_1 k_1 \Omega_1 \gamma_1$ and $k_s = \rho_2 k_2 \Omega_2 \gamma_2$, equation 4-34 simplifies to,

$$W = k_F t + (k_s - k_F)(1 - \alpha_o)\left[(t + t_o) e^{-\beta t} - t_o\right] \qquad 4\text{-}35$$

Differentiating equation 4-35 with respect to t, the reaction rate S can be obtained,

$$S = \frac{dW}{dt} = k_F + (k_s - k_F)(1 - \alpha_o)(1 - \beta t - \beta t_o) e^{-\beta t}. \qquad 4\text{-}36$$

Let us consider the reaction rate at very short times,

$$S_{t \to o} = \underset{t \to o}{Lt} \left[k_F + (k_s - k_F)(1 - \alpha_o)(1 - \beta t - \beta t_o) e^{-\beta t}\right]$$

$$= k_F + (k_s - k_F)(1 - \alpha_o)(1 - \beta t_o)$$

$$\therefore \; k_I = S_{t \to o} = k_F + (k_s - k_F)(1 - \alpha_o)(1 - \beta t_o) \qquad 4\text{-}37$$

The rate expression used for k_F in equation 4-35 corresponds in form to that derived for the linear rate constant in the preceding section, equation 4-9. The above rate expression 4-35 is valid for the restrictions under which equation 4-9 was derived.

An expression can readily be derived for k_s, the linear rate constant for silica growth according to the above procedures for wustite growth. In the case of silica growth the reaction rate is determined by the dissociation of carbon dioxide and the incorporation of oxygen into the silica lattice. The mechanism for this latter step is by the annulment of oxygen vacancies and free electrons at the gas-oxide interface. The formalism for generating the expression for the reaction rate is as given in the previous section, where lattice defects would represent oxygen vacancies and free electrons rather than cation vacancies and positive holes as in wustite. That is, the reaction mechanism is,

$$2CO_2 + 4e = 2CO_{(g)} + 20^{=}_{ads} \tag{4-38}$$

$$20^{=}_{ads} + 20\overset{''}{\square} - 4e = \text{Nil} \tag{4-39}$$

$$20^{=}_{o} + \text{Si (Alloy)} = \text{Si}0_2 + 20\overset{''}{\square} \tag{4-40}$$

$$\text{Si}_{(\text{Si}0_2)} = \text{Si}_{(\text{Alloy})} \tag{4-41}$$

Thus,

$$k_s = \frac{k_1^s\, k_2^s\, \theta_v^s}{k_2^s + k_1'^s \left[e^*\right]^2 P_{CO}} \left(1 - \frac{a_o^*}{a_o^{(g)}}\right) P_{CO_2} \tag{4-42}$$

Using equation 4-11, equation 4-42 can be rewritten as,

$$k_s = \frac{k_1^s\, k_2^s\, \theta_v^s\, (1 + K^s)\, (P_{CO_2} - P_{CO_2}^{**})}{k_2^s + k_1'^s \left[e^*\right]^2 P_{CO}} \tag{4-43}$$

where superscript s refers to the silica phase.
Since $P_{CO_2}^{**}$, the equilibrium partial pressure of carbon dioxide for the Si/Si0$_2$ equilibria, is much smaller than P_{CO_2} under the experimental conditions, equation 4-43 reduces to,

$$k_s = \frac{k_1^s\, k_2^s\, \theta_v^s\, (1 + K^s)\, P_{CO_2}}{k_2^s + k_1'^s \left[e^*\right]^2 P_{CO}} \tag{4-44}$$

This expression may be simplified by the following substitutions,

$$k_3 = k_1^{\,s}\ \theta_v^{\,s}\ (1 + K^s)$$

and

$$\epsilon_s = \frac{k_2^{\,s}}{k_1^{\,s\prime} \cdot \left[e^*\right]^2}$$

Therefore

$$k_s = \frac{k_3\, \epsilon_s\, P_{CO_2}}{\epsilon_s + P_{CO}} \qquad 4\text{-}45$$

Similarly from equation 4-9,

$$k_F = \frac{k_4\, \epsilon_F\, (P_{CO_2} - P_{CO_2}{}^*)}{\epsilon_F + P_{CO}} \qquad 4\text{-}46$$

where $k_4 = k_1\ \theta_v\ (1 + K)$

and $\epsilon_F = \dfrac{k_2}{k_1' \left[\oplus^*\right]^2}$

Returning to the expression for the reaction rate, equation 4-36 in particular,

$$S = k_F + (k_s - k_F)\,(1 - \alpha_o)\,(1 - \beta t - \beta t_o)e^{-\beta t}$$

At long times, as $t \to \infty$, $S = k_F$.

That is, the reaction will achieve a final linear rate at long times.

Experimentally, linear reaction rates are observed at long times before onset of parabolic behaviour. Thus the measured linear rate is a good estimate of k_F.

Eliminating k_s between equations 4-36 to 4-37, since k_I and k_F are known rather than k_s, we obtain

$$S = k_F + \frac{(k_I - k_F)(1 - \beta t - \beta t_o)}{(1 - \beta t_o)} e^{-\beta t} \qquad 4\text{-}47$$

Differentiating S with respect to t we get,

$$\frac{dS}{dt} = \frac{(k_I - k_F)(\beta t + \beta t_o - 2)\beta e^{-\beta t}}{(1 - \beta t_o)} \qquad 4\text{-}48$$

For S to have an extrema,

$$\frac{dS}{dt} = 0 \qquad 4\text{-}49$$

Hence S has an extrema when

$$\beta t_e = 2 - \beta t_o \qquad 4\text{-}50$$

Differentiating 4-45 once more with respect to t,

$$\frac{d^2S}{dt^2} = \frac{(k_I - k_F)\beta^2}{(1-\beta t_o)} (3 - \beta t_o - \beta t)e^{-\beta t} \qquad 4\text{-}51$$

Evaluating of $\frac{d^2S}{dt^2}$ at the extrema, $\beta t_e = 2 - \beta t_o$,

$$\left(\frac{d^2S}{dt^2}\right)_{t=t_e} = \frac{(k_I - k_F)}{(1-\beta t_o)} \beta^2 e^{-2 + \beta t_o} \qquad 4\text{-}52$$

Therefore it is obvious that the total reaction rate S has a maxima when $k_I > k_F$ and a minima when $k_I > k_F$.

The experiments carried out in this investigation have been designed to test these theoretical considerations for the initial oxidation rates of an iron silicon alloy. The above equations will be shown to be valid for the oxidation of an iron-1.5 $^w/_o$ silicon alloy before onset of linear reaction kinetics in carbon dioxide - carbon monoxide atmospheres.

CHAPTER V

EXPERIMENTAL PROCEDURE

5.1 Introduction

The major portion of this chapter will deal with the preparation of specimens, the oxidation apparatus, electron microprobe analysis, electron microscopy and X-ray diffraction studies.

5.2 Specimens

The iron-1.5 $^{w}/o$ silicon alloy used in the major section of the program was obtained through the courtesy of Dr. G.R. Purdy. The chemical composition of the alloy is listed in Table V-1.

A series of iron-silicon alloys were prepared to serve as standards for electron-microprobe analyes. Electrolytic iron and silicon were used to prepare the alloys. Portions of each material were accurately weighed to yield alloys containing 0, 0.2, 0.6, 0.9, 1.2, 2.0, 2.5, 3.5 and 4.0, weight percent silicon. Approximately 120-150 grams of material were placed into the melting chamber of a non-consumable arc furnace. A tungsten electrode was used for the melting operation, carried out under 200 mm pressure of argon. Each charge was melted, inverted and remelted until a total of 4 melting operations were made so as to prevent any long range segregation. The product was a button approximately 50 mm in diameter and 5-10 mm thick. These buttons were then homogenized in vacuum at 1050°C for seven days and subsequently hot rolled at 800°C to a thickness of 1.5 mm. The surfaces of each sheet were cleaned by abrasion using 320 grit silicon carbide polishing paper.

The test specimens (1.5 $^{w}/o$ Si alloy) for oxidation tests were obtained in the following manner. A slab of the alloy, 6 mm thick, was

TABLE V-1

Chemical Analysis of Specimens

Chemical Composition of the Alloy Used in Kinetic Oxidation Tests

Si	Mn	C	S	P	Cu	Cr	Al	Fe
1.52	0.08	0.025	*tr	0.08	*tr	0.01	**nd	Rest.

Spectroscopic Analysis of Base Materials Used for Preparation of Alloys for Electron-Microprobe Analysis (in ppm)

	Al	Cd	Cr	Ca	Cu	Mg	Mn	Mo	Si	Ti	V
Fe -	tr	nd	tr	nd	10	30	tr	tr	30	tr	tr
Si -	tr	10	tr	100	nd	50	nd	nd	Rest	80	41

Chemical Analysis of Alloys

***Nominal Composition (wt. % Si)	0.2	0.6	0.9	1.2	2.0	2.5	3.5	4.0
Actual Composition (wt. % Si)	0.185	0.58	0.93	1.17	2.05	2.65	3.50	4.18

* trace
** not detected
*** nominal composition used in text

cut from the bar stock obtained and cold rolled down to 1.5 mm. The resulting strip was homogenized in vacuum at 1050°C for seven days. Test specimens were obtained by cutting the sheets into platelets 1 cm x 1.5 cm on a precision shear. A suspension hole was drilled in each plate, the hole diameter being selected so that the area removed equalled the area introduced. The plates were then batch annealed in vacuum at 1050°C for 3 days. The annealing operation eliminated any short range segregation and allowed the specimens to achieve an equilibrium grain size.

Prior to oxidation, the specimens were metallographically polished following the procedure outlined by Samuels[110]. The plates were mounted flat in bakelite and polished through 240, 320, 400, 600 grit silicon carbide using water as lubricant followed by final polishing on selvyt cloths impregnated with 6 micron and 1 micron diamond abrasive using kerosene as lubricant. The kerosene was removed by washing with petroleum ether, and the specimens were stored under acetone. Immediately before an experimental test, a specimen was dried, weighed to ± 2 micrograms, and its surface area was computed by measuring the specimen dimension with a micrometer.

The chemical composition of all the alloys used in this investigation are given in Table V-1.

5.3 Oxidation Apparatus

The apparatus used for the oxidation tests is shown pictorially in Fig. V-1. A schematic illustration of the balance assembly is shown in Fig. V-2.

The vacuum system consisted of a mechanical pump, a two stage water-cooled diffusion pump with a chevron water-cooled baffle. Liquid air traps were suitably placed to prevent back diffusion of diffusion pump oil and to collect mercury from the McLeod gauge and

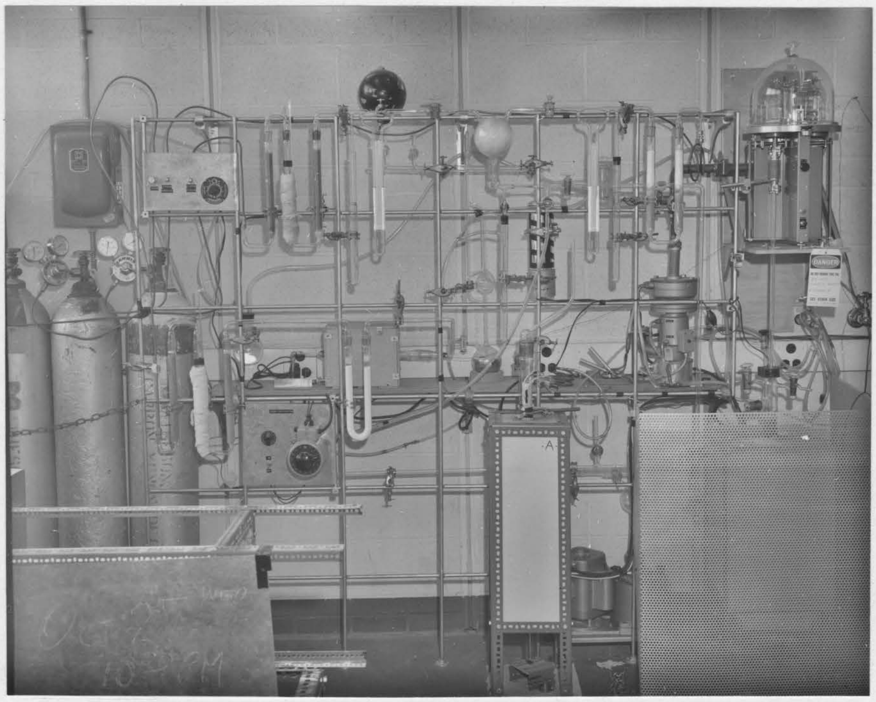

Fig. V-1: Photograph of the Apparatus

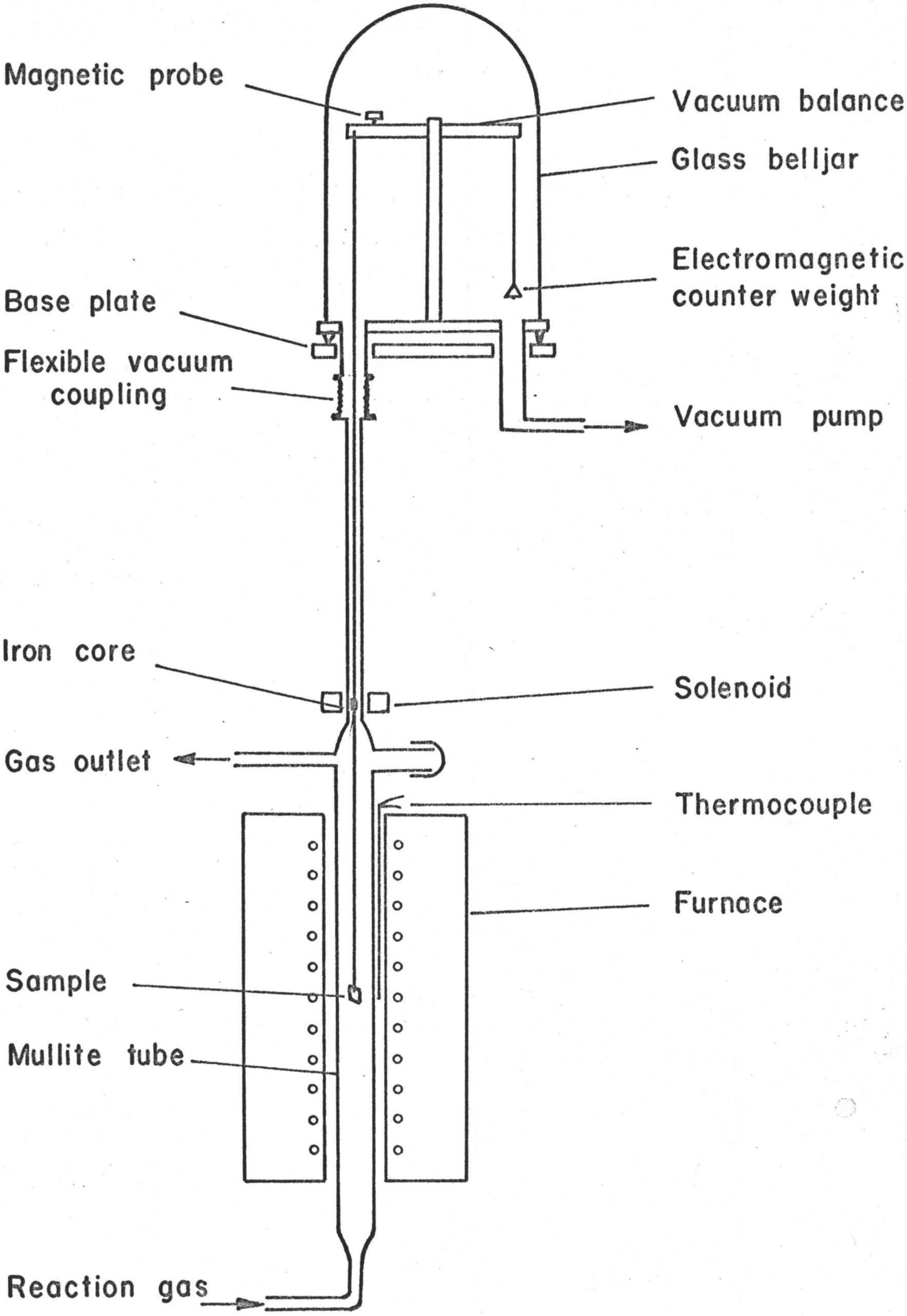

Fig. V-2: Schematic Representation of Balance Assembly manometer.

The oxidation tests were carried out in flowing carbon dioxide-carbon monoxide atmospheres. The ratios of the gases were accurately controlled by metering the components with simple capillary flowmeters similar to those described by Darken and Gurry(111). These authors have also demonstrated that linear flow rates should exceed approximately 0.6 cm/sec in order to eliminate the undesirable effects of thermal segregation. With this in mind, the capillary dimensions for a suitable flow range were estimated from the relation(112, 113),

$$-\frac{\Delta p}{l} = \frac{32\mu V}{g_c D^2} \qquad 5\text{-}1$$

where Δp is pressure drop across capillary in gm/cm^2, l is the capillary length in cm., g_c is 980 gm/sec^2, μ the gas viscosity in gm/cm-sec, D the capillary diameter in cm., and V the velocity of the gas in cm/sec.

The flowmeters were calibrated by measuring the rate of displacement of a soap film up a calibrated gas burette. The meters were calibrated with the respective gases, that is, carbon monoxide, carbon dioxide and argon. The calibration curves are shown in Figs. V-3.

The carbon dioxide, carbon monoxide and argon used in the tests were supplied by the Matheson Co. and typical analyses are given in Table V-2. The gas cylinders were connected to the pyrex glass assembly through suitable pressure gauges and needle valves via 1/4 inch copper tubing. The carbon dioxide passed through columns containing silica gel, reduced copper oxide at 400°C and activated alumina, the carbon monoxide through columns containing magnesium

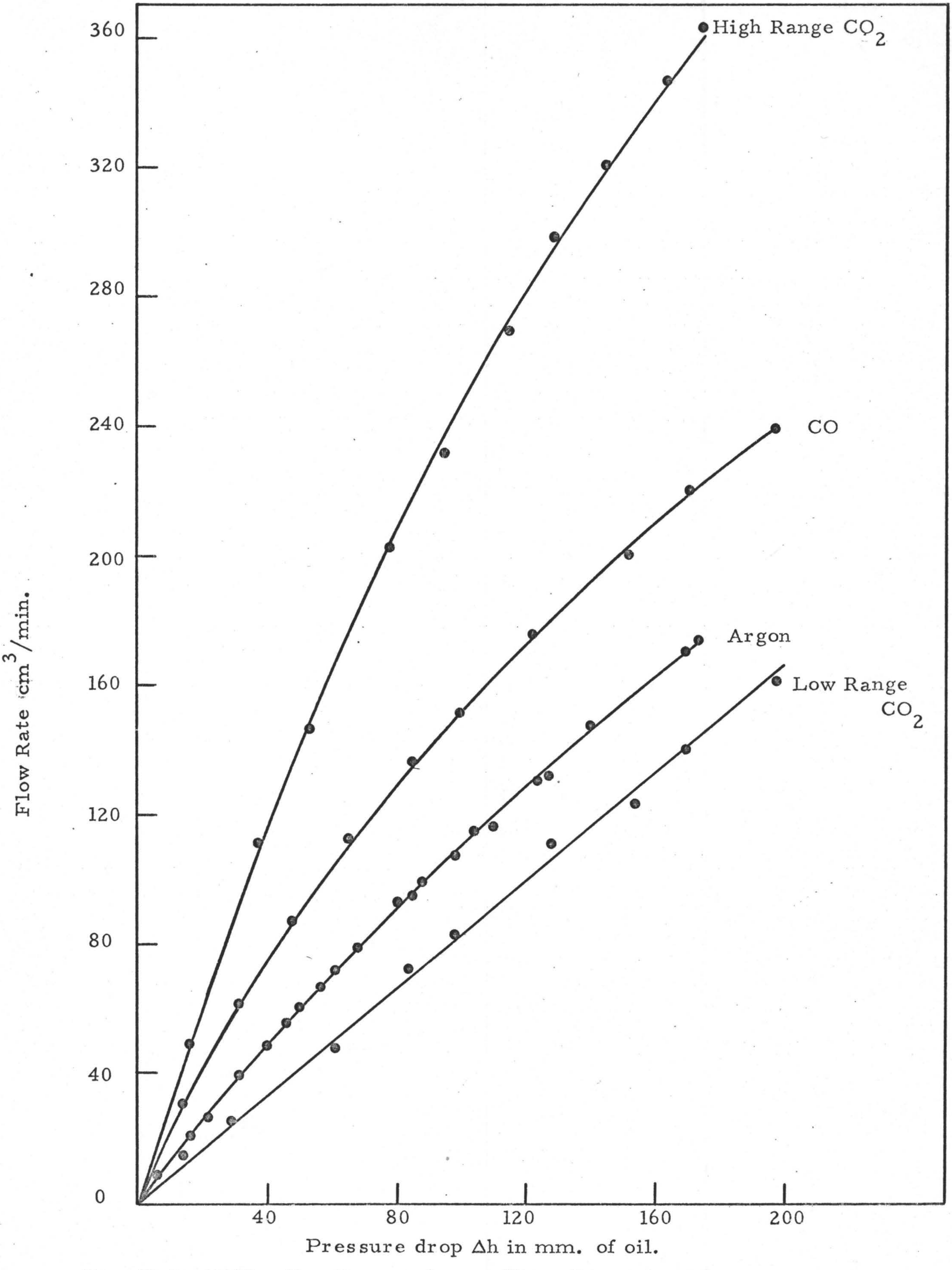

Fig. V-3: Calibration Curves for capillary flowmeters.

TABLE V-2

Typical Analyses of Carbon Dioxide, Carbon Monoxide and Argon Supplied by Matheson Co.

Carbon Monoxide: C. P. Grade, 99.5% (min.)

CO_2: 200 ppm
O_2: 20 ppm
N_2: 75 ppm

Dew point: - 60°F

Carbon Dioxide: Bone Dry Grade, 99.95% (min.)

$N_2 + O_2$: 500 ppm

Dew point: - 30°F

Oil content < 5 ppm

Argon: High Purity Grade, 99.995% (min.)

O_2: 30 ppm

Dew point: - 50°F

perchlorate and ascarite, and argon through columns containing silica gel, activated B. T. S. catalyst at 150°C, ammoniacal chromous sulphate, magnesium perchlorate, ascarite and zirconium chips at 600°C. Carbon dioxide and carbon monoxide were mixed in a 1 litre bulb packed with glass wool and subsequently mixed with argon in another 1 litre glass bulb when necessary. The mixture of gases was directed to an inlet at the bottom of the mullite reaction tube through glass tubulation. A capillary constriction and an air damping pot were placed between the furnace and the flowmeters to reduce oscillations in the levels of the flowmeters due to pressure fluctuations in the lines.

The furnace assembly consisted of a 20" Kanthal element imbedded in insulation which surrounded a 1 5/8" diameter mullite reaction tube. The mullite reaction tube was directly sealed to the pyrex glass tubing. The top of the furnace was water cooled to minimize heat conduction to the balance assembly. Power was supplied to the element by means of a 2500 V. A. transformer. The temperature was controlled to ± 2°C by a Phillips controller-recorder and a Pt - Pt-10% thermocouple, which activated a mercury relay in the circuit. The control thermocouple was located between the windings and mullite reaction tube and the measuring thermocuple was placed in the same position at the sample level. It was found that there existed a 3°C temperature difference between the measuring thermocouple and the temperature inside the reaction tube at the sample level, and this was accounted for in the temperature setting. The temperature variation in the hot zone was 1°C over a distance of 4 inches. The variation of temperature in the centre of the hot zone was less than ± 0.5°C.

A schematic diagram of the oxidation assembly is given in Fig. V-2. The oxidation cell consisted of a mullite tube, 1 5/8" O. D.

and 30" long to which were fastened pyrex glass connections. An Ainsworth vacuum automatic recording balance with a capacity of 100 grams and a sensitivity of 30 μg. was situated above the oxidation cell. The balance was connected to the glass connections by a flexible vacuum coupling. A vacuum tight movable joint was maintained between the flexible coupling and the glass tubing. The suspension system for the specimen consisted of a pyrex glass tube hung from the balance pan by a nylon thread. An Armco iron core was placed inside the glass tube, and this core could be raised or lowered by means of a magnet from the outside. The specimen was suspended from the Armco iron core with a 0.005" platinum wire.

In a typical experiment, the specimen was maintained at the level of the loading inlet while the assembly was evacuated to 10^{-4} torr and the furnace heated to the reaction temperature. The assembly was then flushed with purified argon. The specimen was then lowered into position in the furnace and annealed for 2 hours to eliminate any surface stresses developed during the polishing operations. Reaction was initiated by admitting the desired atmosphere, the initial oxidation point being taken 10 minutes after gas admission, in order that steady state might be attained. After the test, the specimen was quickly raised into the cooler positions of the tube in approximately 5 seconds, and allowed to cool to room temperature in the flowing gas. The oxide surface was examined under the microscope, and then the specimen was mounted edgewise in epoxy resin. The mount was then polished in a manner similar to that used for surface preparation, and stored in a dessicator until required.

5.4 Electron Probe Microanalysis

The theory associated with electron probe microanalysis will not be described here and a complete description may be obtained by referring to standard texts$^{(114-117)}$. A Cameca electron microprobe was used during this investigation.

In order to use the microprobe for quantitative analyses it is necessary that it be calibrated for the elements of interest. If standards containing known amounts of the elements in a homogeneous distribution can be obtained, the calibration is a relatively simple process. Such is the case for the iron-silicon system. The X-ray intensity from a given element, minus the background intensity is proportional to the amount of the element present. The background intensity is determined by counting with the spectrometer set at a few degrees off peak or, as in the case of iron-silicon, by setting the spectrometer for silicon and counting on pure iron. Since the observed corrected absolute intensity varies from day to day, only relative intensity calibration curves can be usefully plotted. A convenient ratio is the ratio of the corrected intensity of an alloy to the corrected intensity from the pure element of interest.

The microprobe was calibrated for iron-silicon alloys in the above manner. Small alloy plates, 2mm in thickness of known composition, were mounted in bakelite along with standards of pure iron and silicon. Intensity ratios were computed from an average of 3 determinations for a series of alloys containing 0.2 to 4.2 wt.% silicon. The calibration curve is shown in Fig. V-4.

The composition of an unknown specimen may then be determined by comparing the measured intensity ratio with the curves. Attempts were made to measure the concentration profile of silicon in the alloy phase at the alloy-oxide interface and the concentration gradients in the external wustite and the conglomerate of wustite and fayalite. The latter proved to be quite difficult because the conglomerate consisted

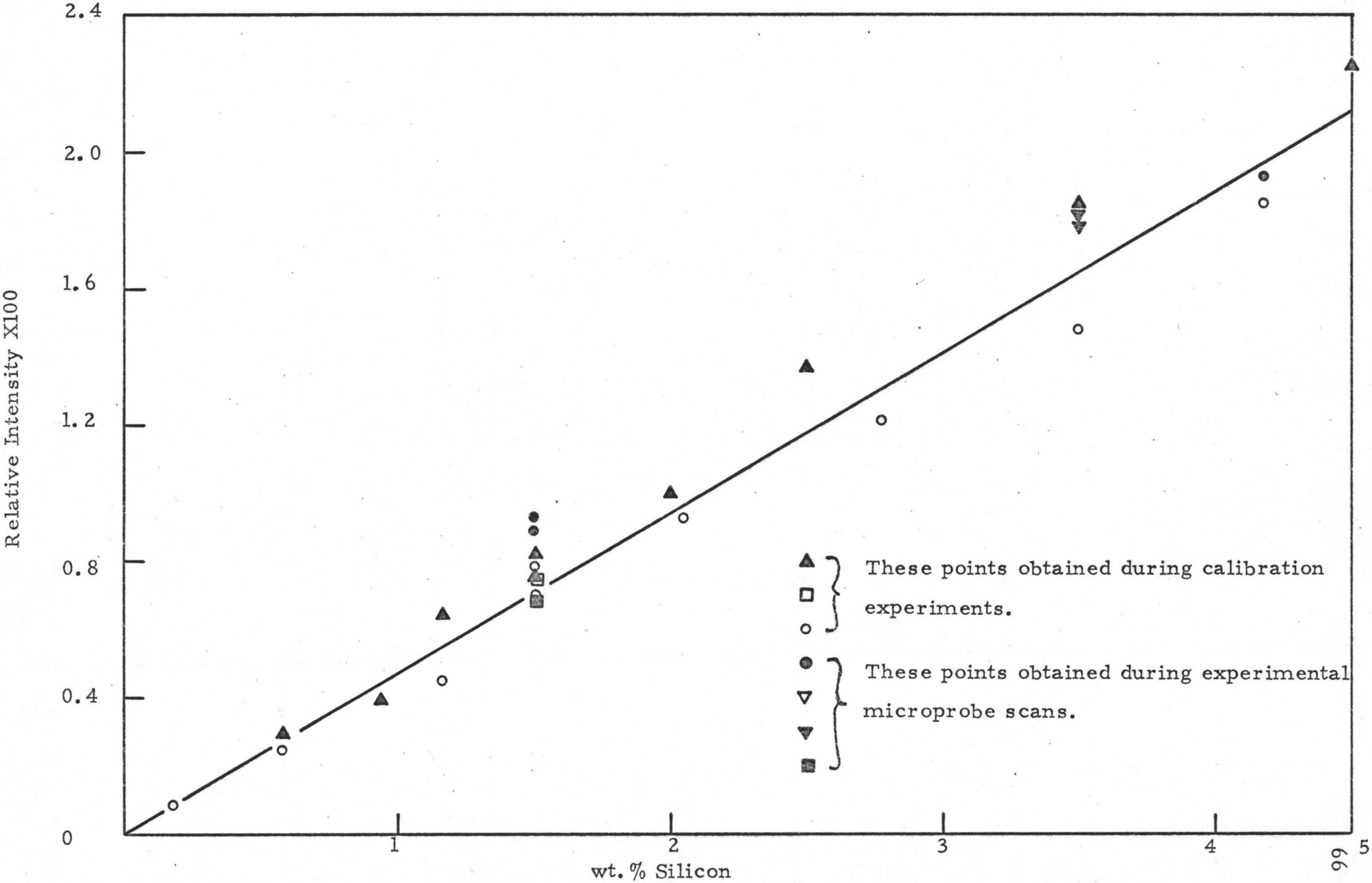

Fig. V-4: Relative Intensity versus concentration of silicon in a Fe-Si alloy at 15 kV.

of bands of fayalite interspersed in a matrix which itself was a fine mixture of wustite and fayalite on the microscopic scale. Since it was only possible to measure the relative intensitites of iron and silicon it was quite difficult to determine the concentrations of iron and silicon in the conglomerate phase. To obtain the concentration gradients in the oxide phases, calibration curves of relative intensity versus composition were necessary. These curves could be obtained by two methods : by the use of standards or theoretical calculations using all the available knowledge of the various corrections necessary. All efforts to make mixed wustite-fayalite standards and a fayalite standard proved unsatisfactory. The main drawback was the poor homogenity of specimens obtained. Therefore, the calibration curves were obtained by theoretical calculations and are shown in Figs. V-5 and V-6. A detailed description of the various corrections made and the assumptions made for the calculation of the calibration curves is given in Appendix I.

The operating conditions to obtain the best results for the iron-silicon system were found to be 15 kV and a specimen current between 50-80 nanoamps. The iron-silicon system is difficult to analyse, especially for the dilute silicon alloys of interest in this study, because of the interplay of the following phenomena:

(i) There is a large atomic number difference between the two components, iron and silicon, which are 26 and 14, respectively.

(ii) Silicon X-rays are heavily absorbed both in iron and silicon and this absorption increases with the operating voltage.

(iii) An operating voltage of 22 kV ($\gtrsim$3 times the excitation voltage of iron) is recommended to obtain efficient X-ray production and good counting statistics for iron.

Therefore, the operating conditions are a severe compromise in this particular situation. The same operating

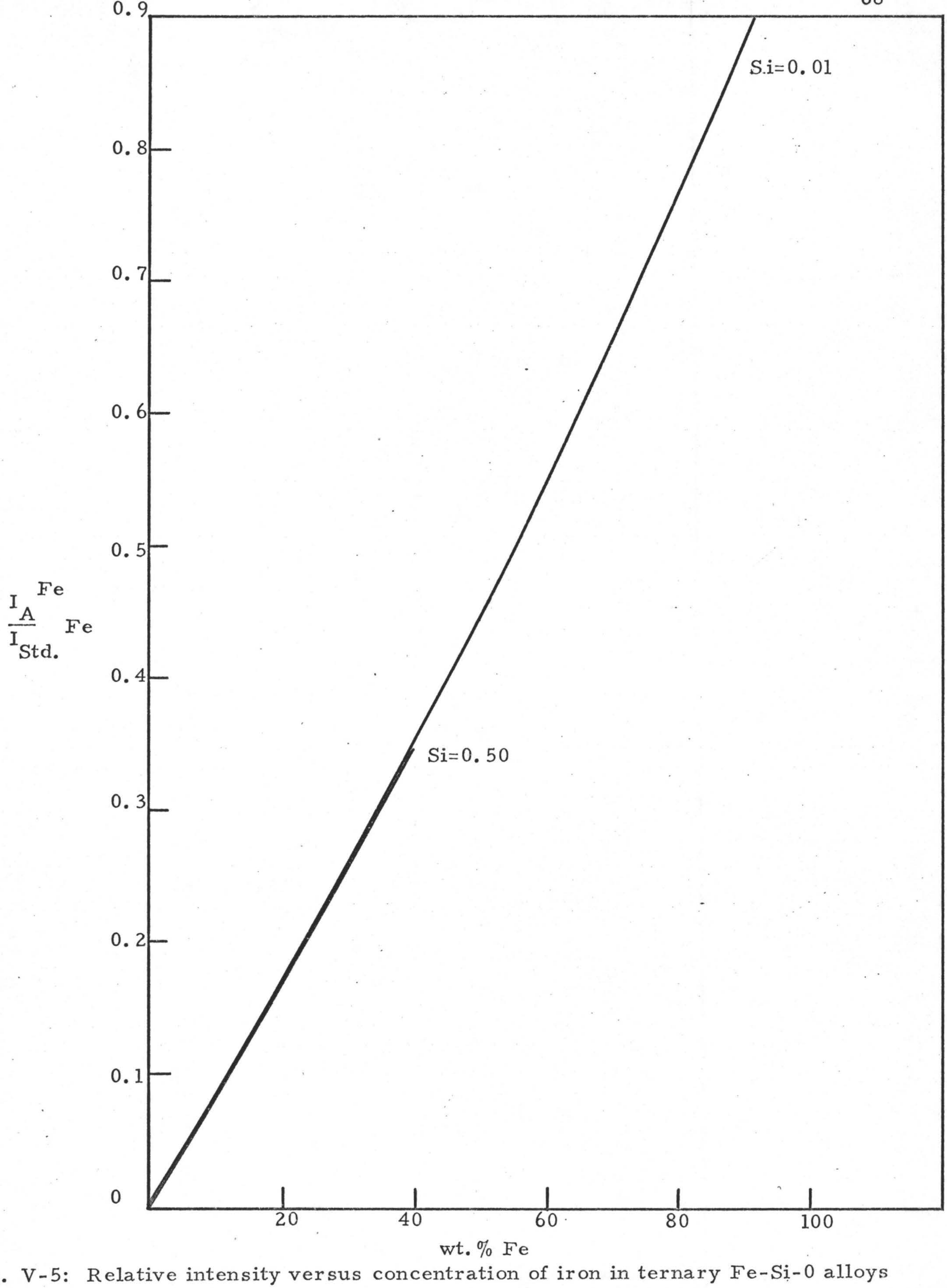

Fig. V-5: Relative intensity versus concentration of iron in ternary Fe-Si-0 alloys at 15 kV.

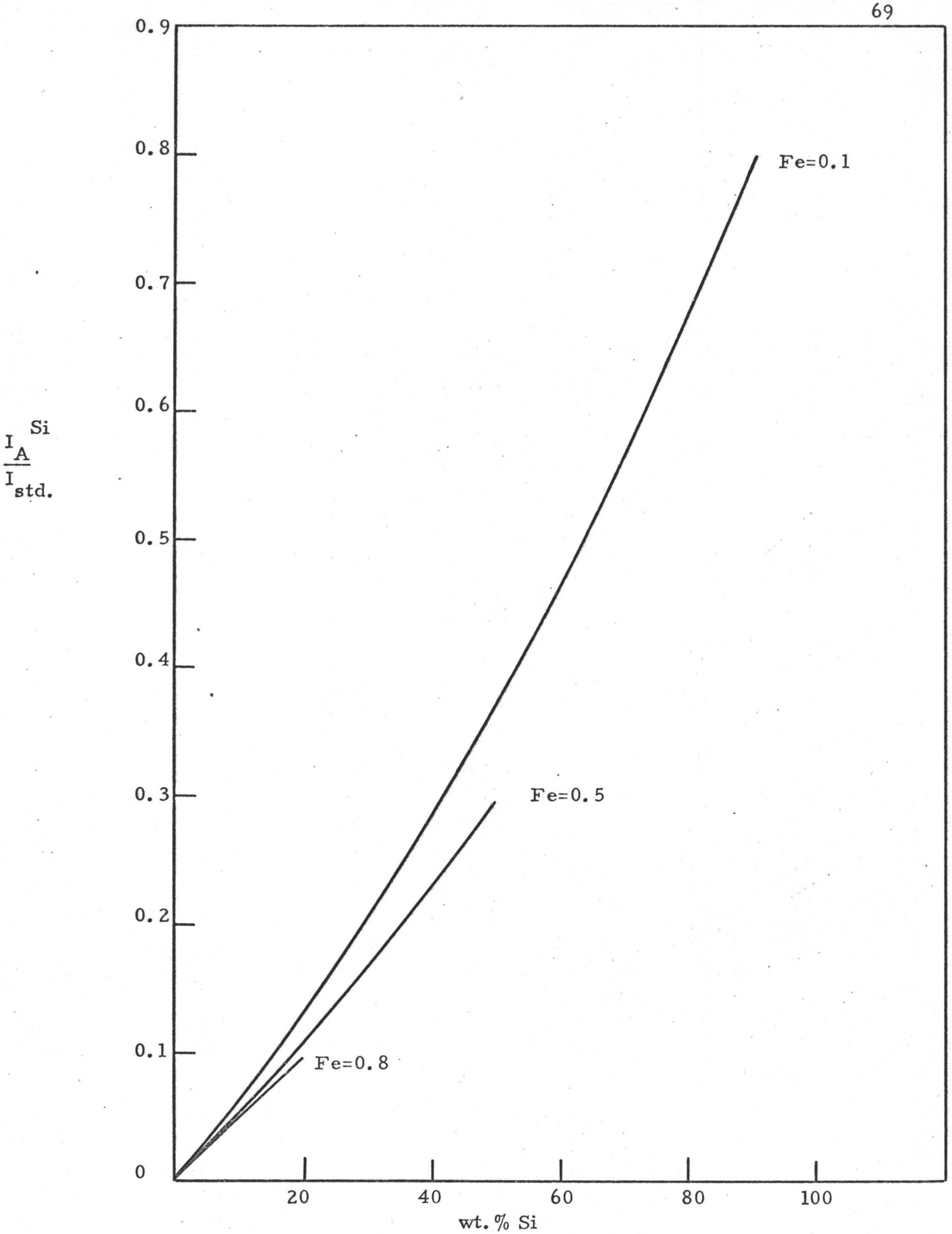

Fig. V-6: Relative intensity versus concentration of silicon in ternary Fe-Si-0 alloys at 15 kV.

conditions were also used in the case of the analysis of the oxide phases, because they were found both suitable and convenient.

5.5 X-Ray Diffraction

X-ray powder diffraction techniques were used for the purpose of phase identification on a number of specimens.

The X-ray powder diffraction patterns were obtained using Debye-Scherrer cameras along with a Phillips X-ray generator. Iron filtered cobalt radiation was used. The oxides were mechanically removed from the specimens and ground in an agate pestle and mortar. A base coat of nailpolish was added to the powder and just prior to setting, a quartz rod was inserted into the viscous mixture and slowly withdrawn. This produced an approximately 0.2-0.5 mm diameter filament of oxide powder on the tip of the rod. The filaments were dried and mounted in the X-ray cameras.

X-ray diffractometer traces were also obtained for a few samples. The samples consisted of mechanically stripped oxide samples from the oxidized samples. Manganese filtered iron radiation was used in a Norelco diffractometer.

5.6 Electron Microscopy

The theory involved in electron microscopy may be obtained by referring to standard texts(118, 119). Both transmission and reflection microscopy along with selected area diffraction were utilized to obtain information about the initial stages of oxidation. The electron microscope used was a Siemens model.

The specimens used for transmission electron microscopy consisted of oxide films removed from an oxidized sample by dissolution in a solution of 10% bromine in methanol. The samples were oxidized for periods up to 1 hr. and argon-preannealed specimens were also studied. The estimated oxide thicknesses of the samples studied was in the range 1000 - 7000Å. Selected area electron diffraction was also done in conjunction with most of the transmission microscopy.

The samples used in reflection electron microscopy consisted of oxide stripped from the specimens on which the kinetic oxidation tests were conducted. The oxide thicknesses were of the order of 20 - 100 microns and specimens used were 2 mm x 5 mm in size.

5.7 Optical Metallography

The specimens were examined and photographed using standard metallographic techniques. In several cases, the rates of growth of the external wustite scale and the conglomerate phase were determined. These results were obtained by measuring the thickness of the scales using a calibrated filar eyepiece with a Reichert metallograph at a suitable magnification. The scale-gas and alloy-scale interfaces were quite rugged, therefore the results to be reported are the average values of a sufficiently large number of observations to obtain a realistic average of the thicknesses.

CHAPTER VI

EXPERIMENTAL RESULTS

6.1 Introduction

The results obtained from the various experimental tests will be presented in this section in the usual manner, that is, in the form of graphs, tables and photomicrographs. The experimental oxidation tests were conducted at two temperatures, 890°C and 1000°C.

6.2 Oxidation Kinetics

The results from the investigation on the oxidation kinetics, obtained by recording the increase in specimen weight as a function of time are illustrated in Figs. VI-1 to 5 for the alloys investigated. The results are presented as smooth curves since a continuous recording balance was used. In all cases, the weight gains are expressed in mg/cm^2 and times in hours. A weight gain of 1 mg/cm^2 corresponds approximately to 7.6μ of wustite. The experimental conditions are indicated on the graphs. The total reacting gas pressures in tests at 1000°C were 1.0, 0.7 and 0.5 atmosphere, whilst the tests at 890°C were conducted at a total pressure of 1 atmosphere. The volume percentages of carbon dioxide in the atmosphere varied generally from 0.4 to 1.0. Tests were only required at one pressure for this latter temperature, since the results were to be utilized primarily to test the effect of a phase change in the alloy substrate on the reaction behaviour.

The weight gain curves for all gas compositions can be best described as composed of three intervals:

(i) An initial period during which the reaction rate increased or decreased continuously.

(ii) An intermediate period during which the continuous curves

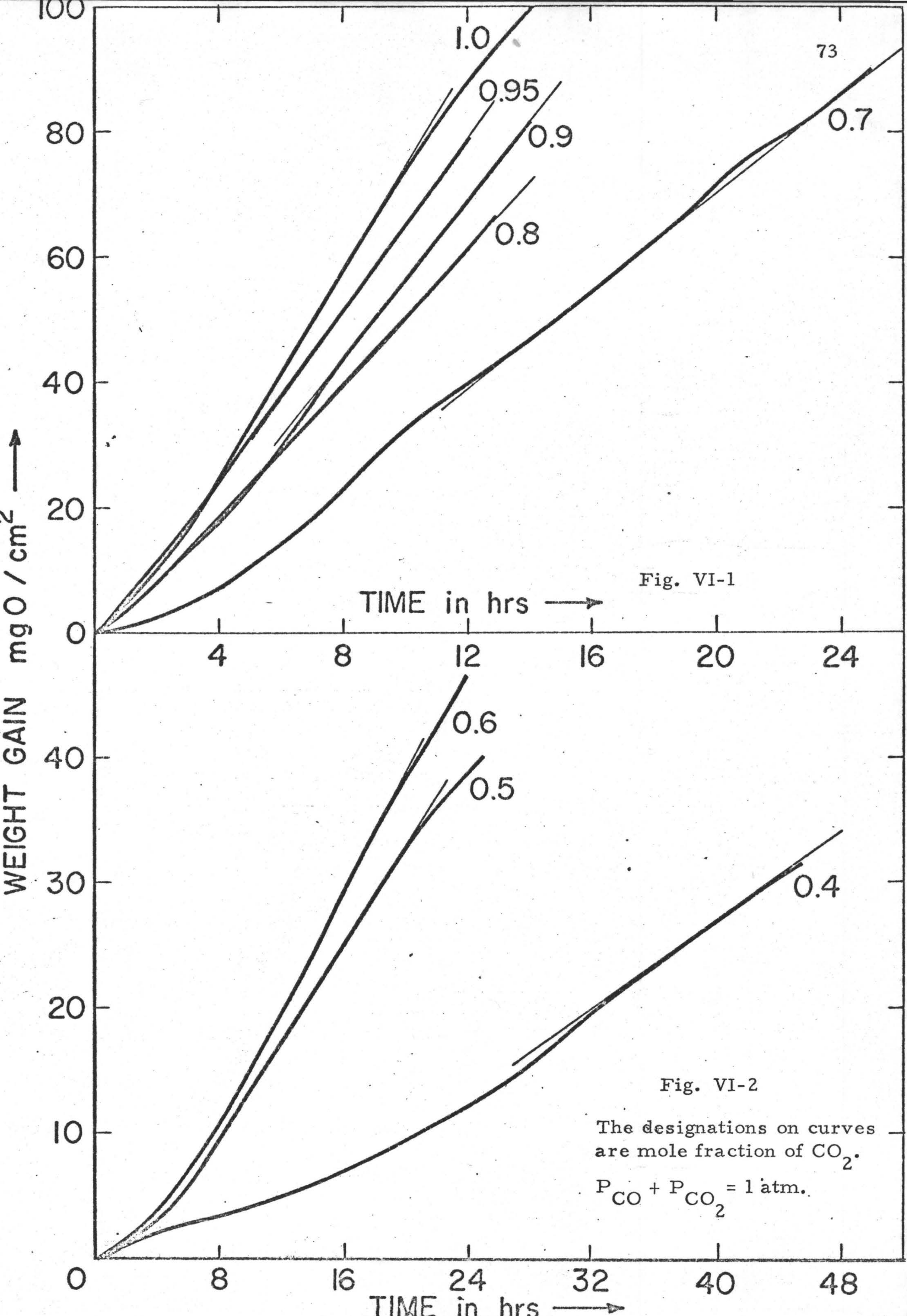

Fig. VI-1

Fig. VI-2

The designations on curves are mole fraction of CO_2.

$P_{CO} + P_{CO_2} = 1$ atm.

Fig. VI-1 and 2: Oxidation kinetics at 1000° C in CO_2-CO atmospheres.

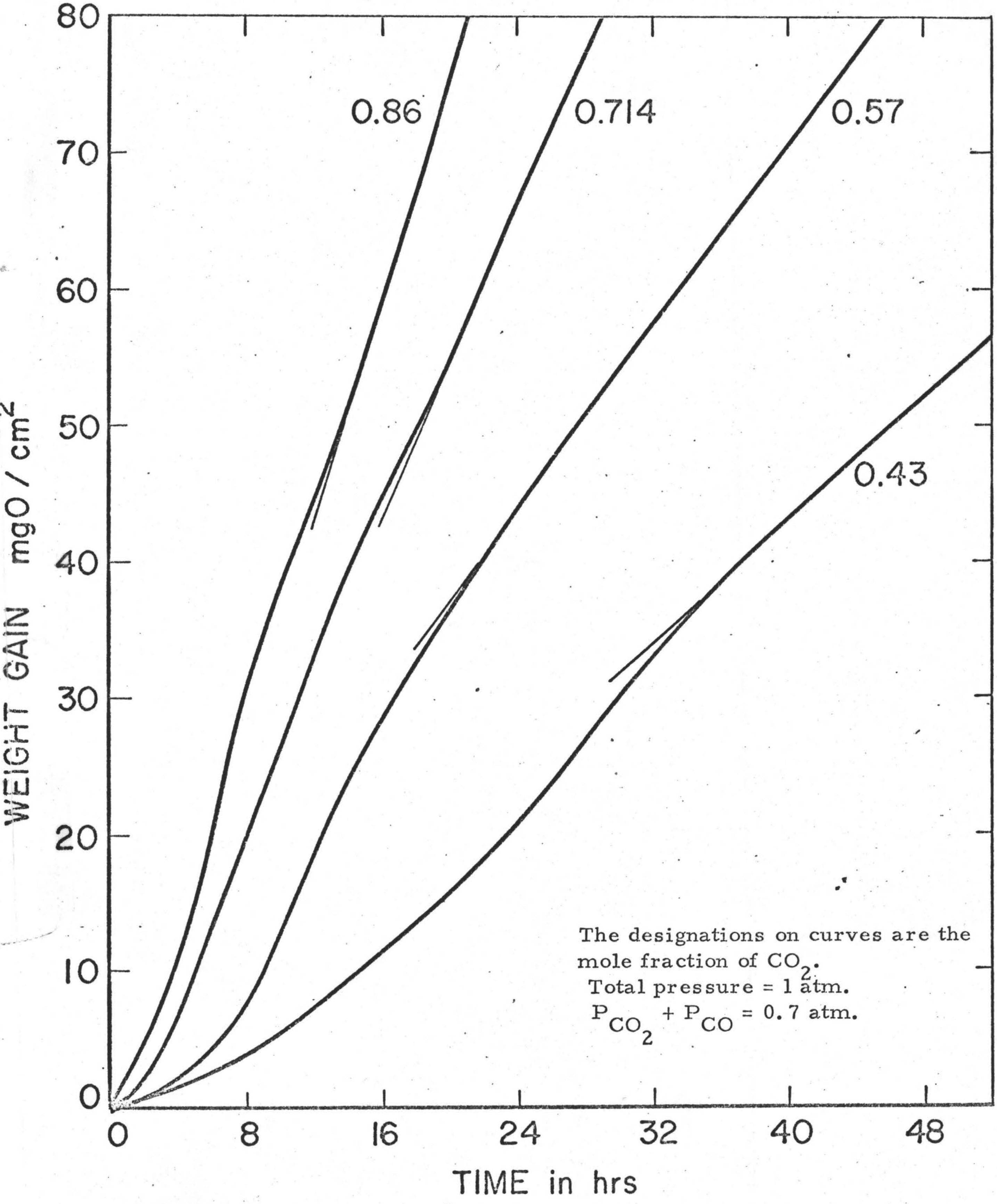

The designations on curves are the mole fraction of CO_2.
Total pressure = 1 atm.
$P_{CO_2} + P_{CO} = 0.7$ atm.

Fig. VI-3: Oxidation kinetics at 1000°C in carbon dioxide-carbon monoxide atmospheres containing argon.

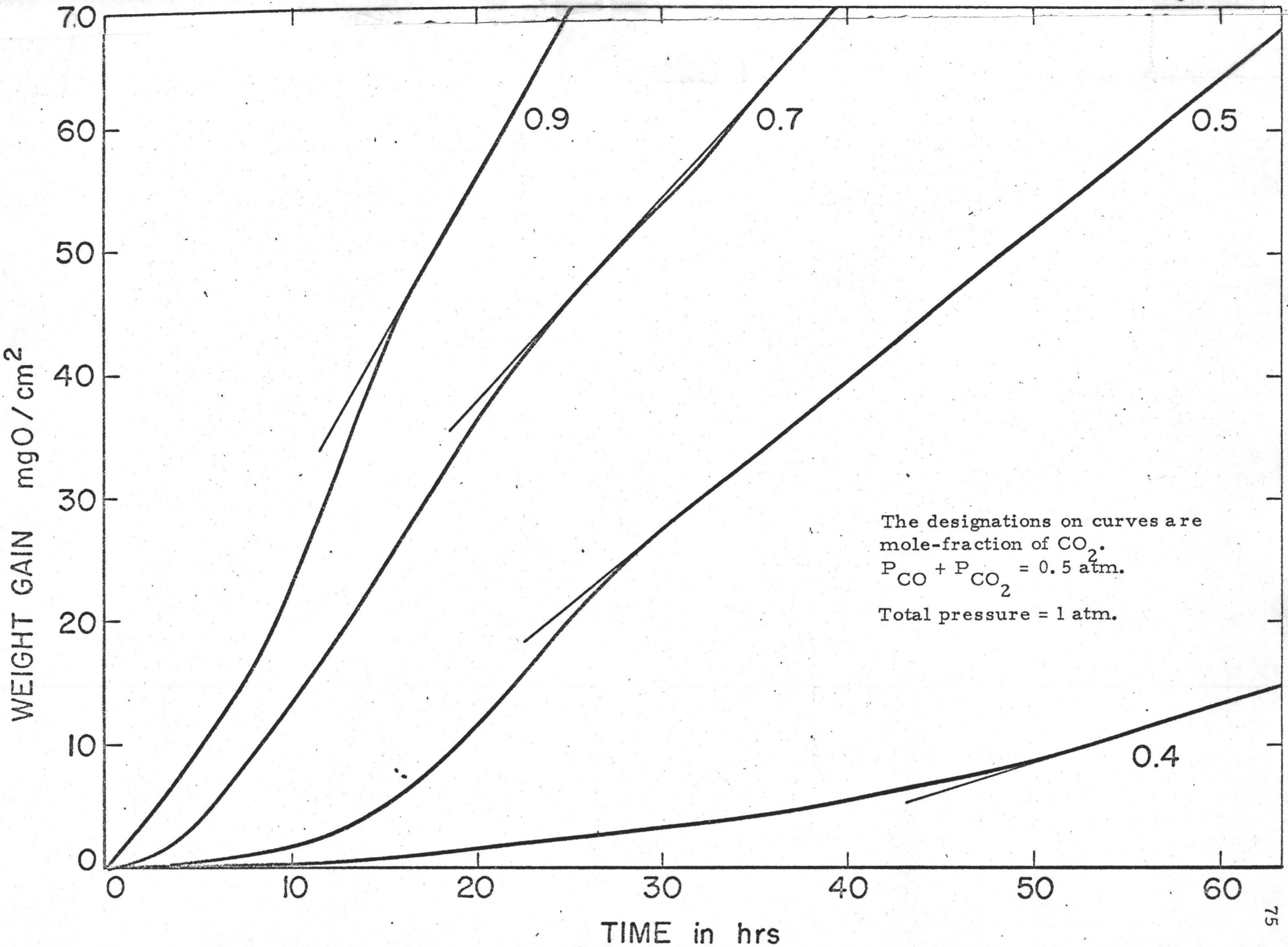

The designations on curves are mole-fraction of CO_2.
$P_{CO} + P_{CO_2} = 0.5$ atm.
Total pressure = 1 atm.

Fig. VI-4: Oxidation kinetics at 1000°C in CO_2 - CO atmospheres containing argon.

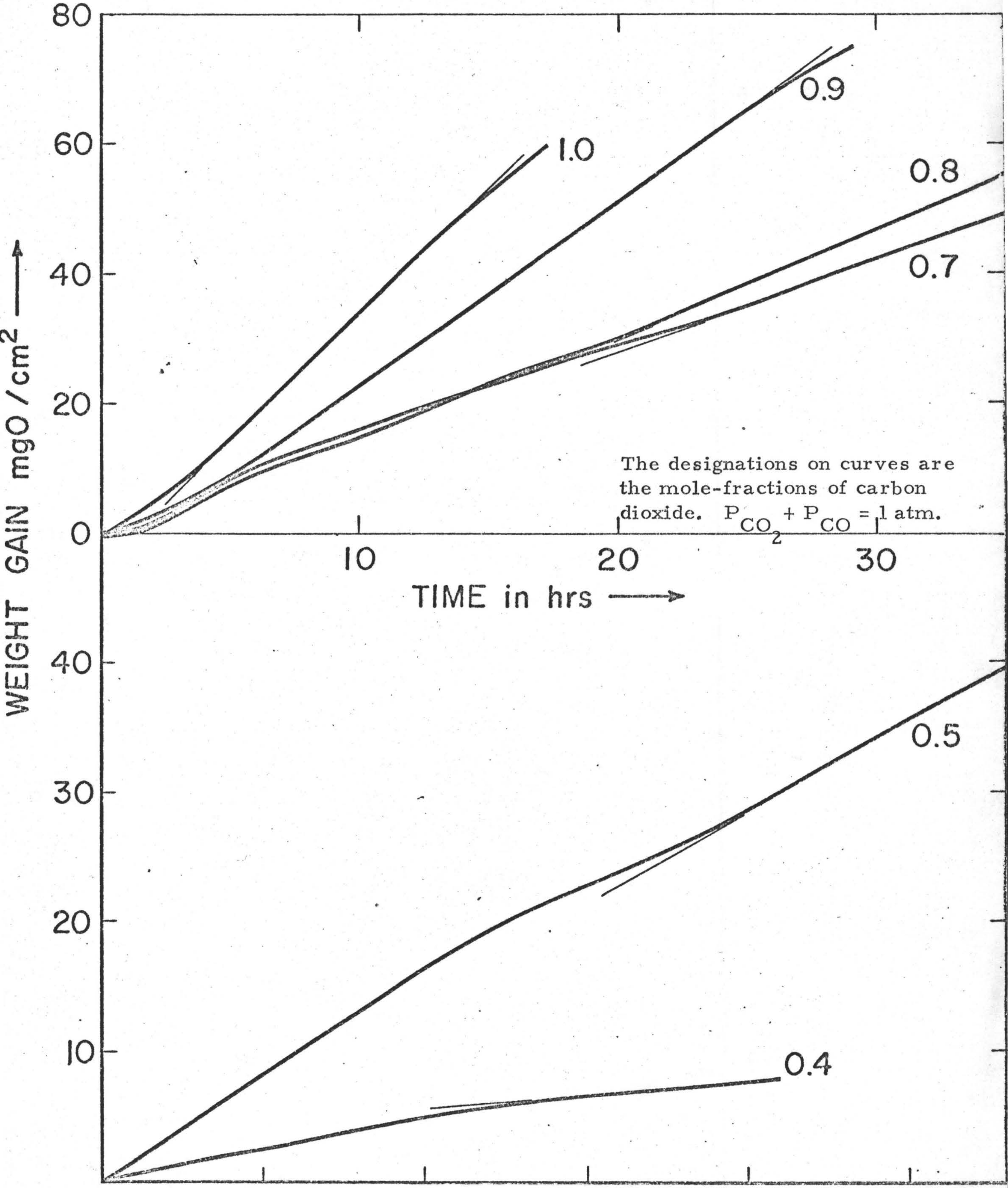

The designations on curves are the mole-fractions of carbon dioxide. $P_{CO_2} + P_{CO} = 1$ atm.

ig. VI-5: Oxidation kinetics at 890°C in CO_2-CO atmospheres.

exhibited a number of maxima due to a variable reaction rate.

(iii) A final period during which the results can be best described by a straight line, corresponding to a constant reaction rate.

The linear regions of constant reaction rate are indicated on the graphs by tangents. This above classification into three periods becomes more apparent, when the reaction rate curves are constructed.

A reaction rate curve was obtained from the weight gain data by numerical differentiation, by the method of differences. The theoretical basis and other details for this method are given in Appendix II. The reaction rate curves are shown in Fig. VI-6 to VI-10 for the alloy investigated. In all cases, the reaction rates are expressed in mg/cm^2-hr. and the time in hrs. with the experimental conditions indicated on the graphs. The mean linear reaction rate constants determined from the reaction rate data are the arithmetic means of the reaction rates, over the linear period of reaction behaviour as shown on the graphs.

Initial reaction rate constants were obtained by drawing tangents to the weight gain curve at zero time. The initial reaction rate and mean linear reaction rate constants are reported in Table VI-1. Several tests were repeated in order to determine the reproducibility of the data. The results for such a set of tests are shown in Fig. VI-11. The reproducibility, as determined by the deviation from the arithmetical mean of two runs, was $\pm$ 10%.

As previously described the reaction proceeds in a distinct manner in each of three periods. Accordingly, the relevant oxide structures, morphologies and concentration gradients in the oxides and the alloys will be described separately for each of the time periods in the following sections.

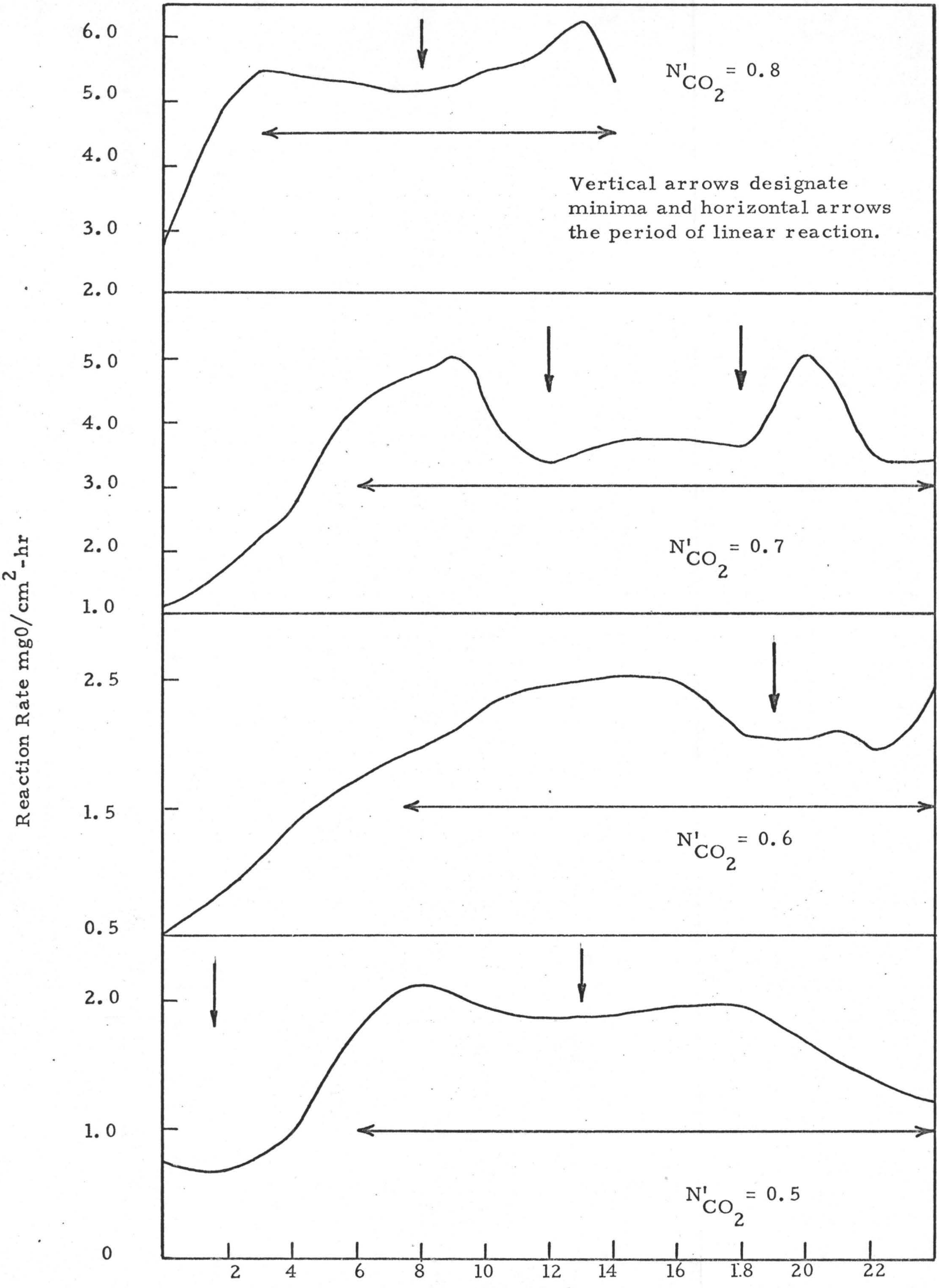

Vertical arrows designate minima and horizontal arrows the period of linear reaction.

Fig. VI-6: Reaction rate at 1000°C in CO_2-CO atmospheres, $P_{CO_2} + P_{CO} = 1$ atm

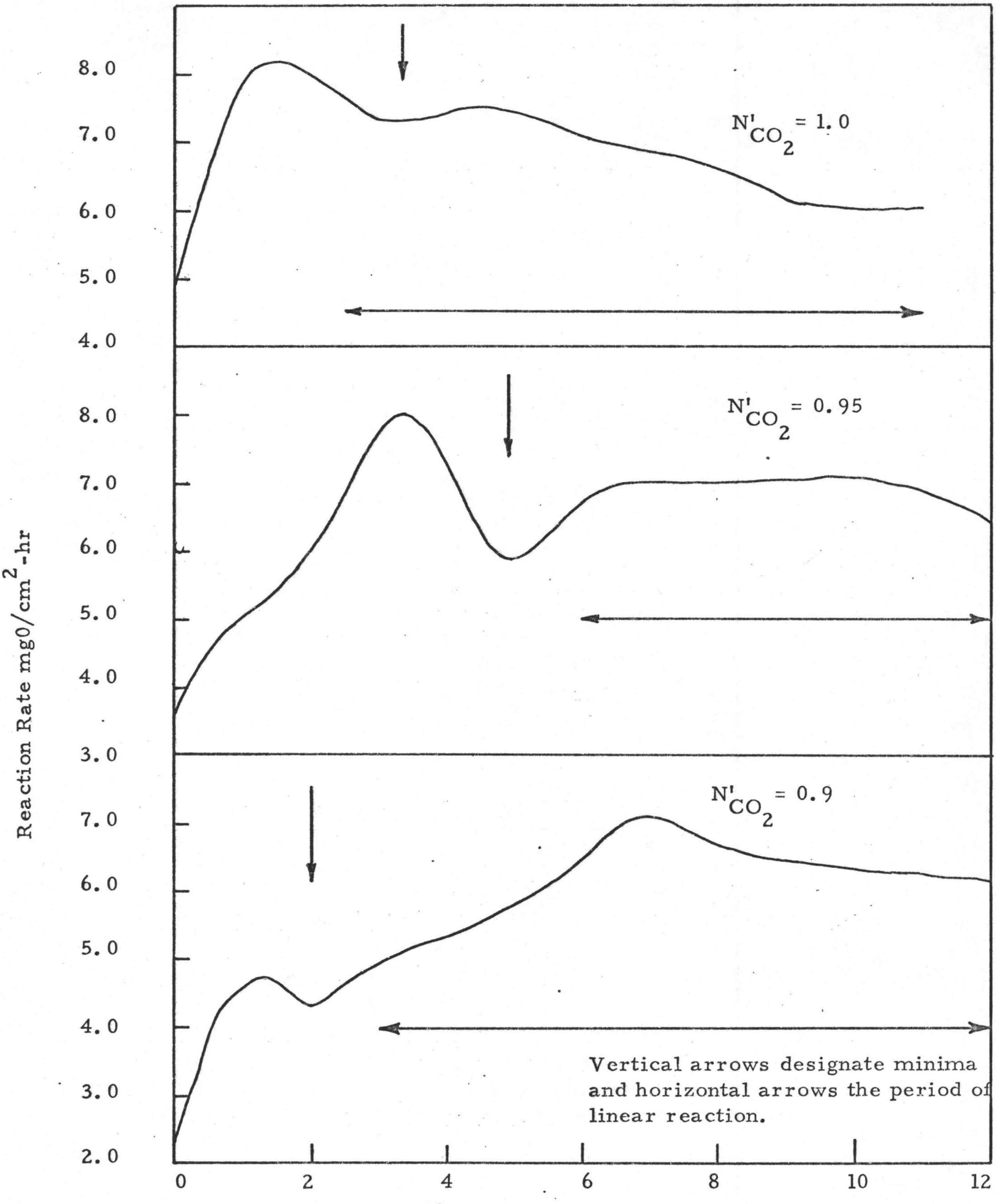

Fig. VI-7: Reaction rates at 1000°C in CO_2-CO atmospheres, $P_{CO_2} + P_{CO} = 1$ atm.

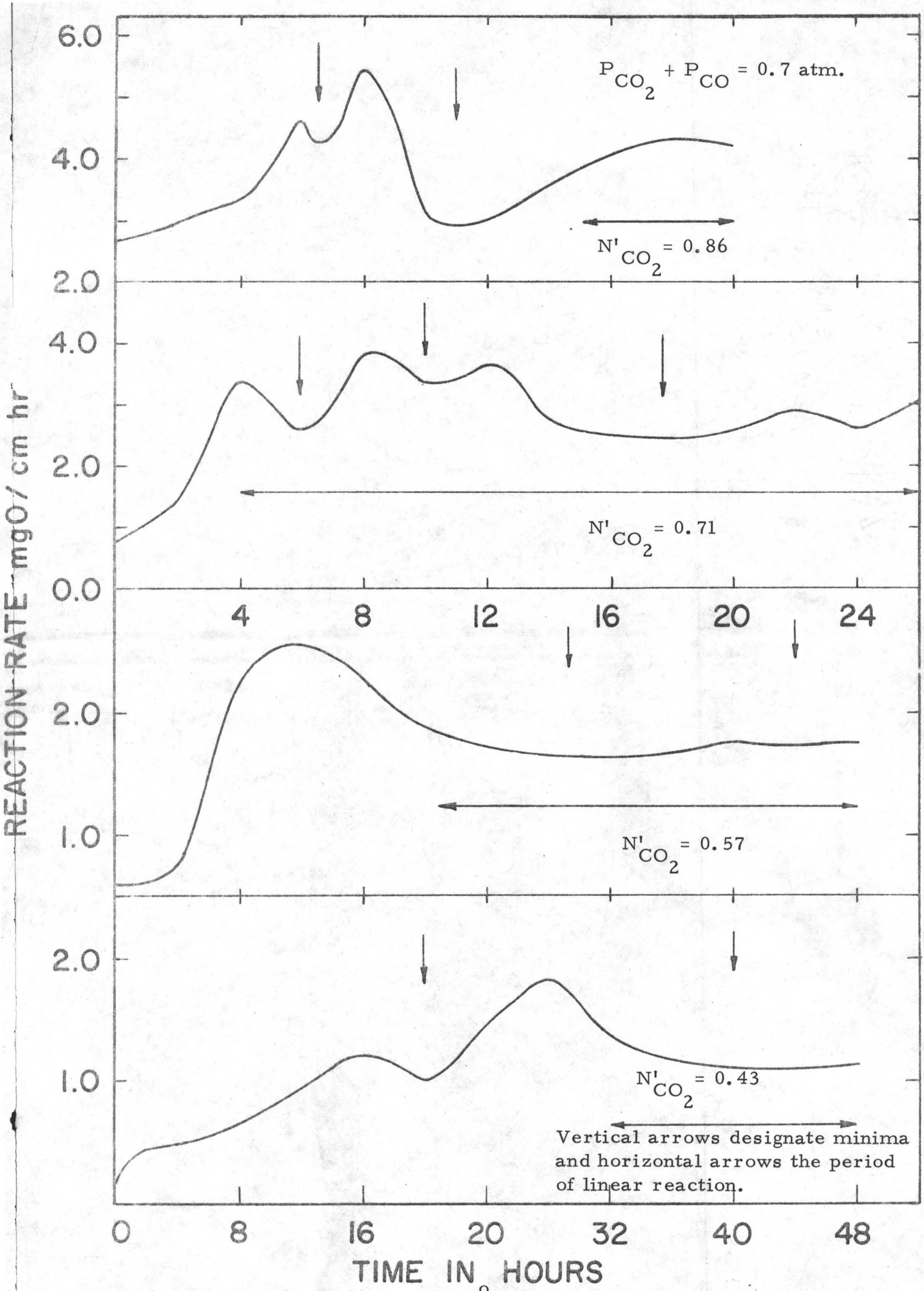

Fig. VI-8: Reaction rates at 1000°C in CO_2-CO atmospheres containing argon.

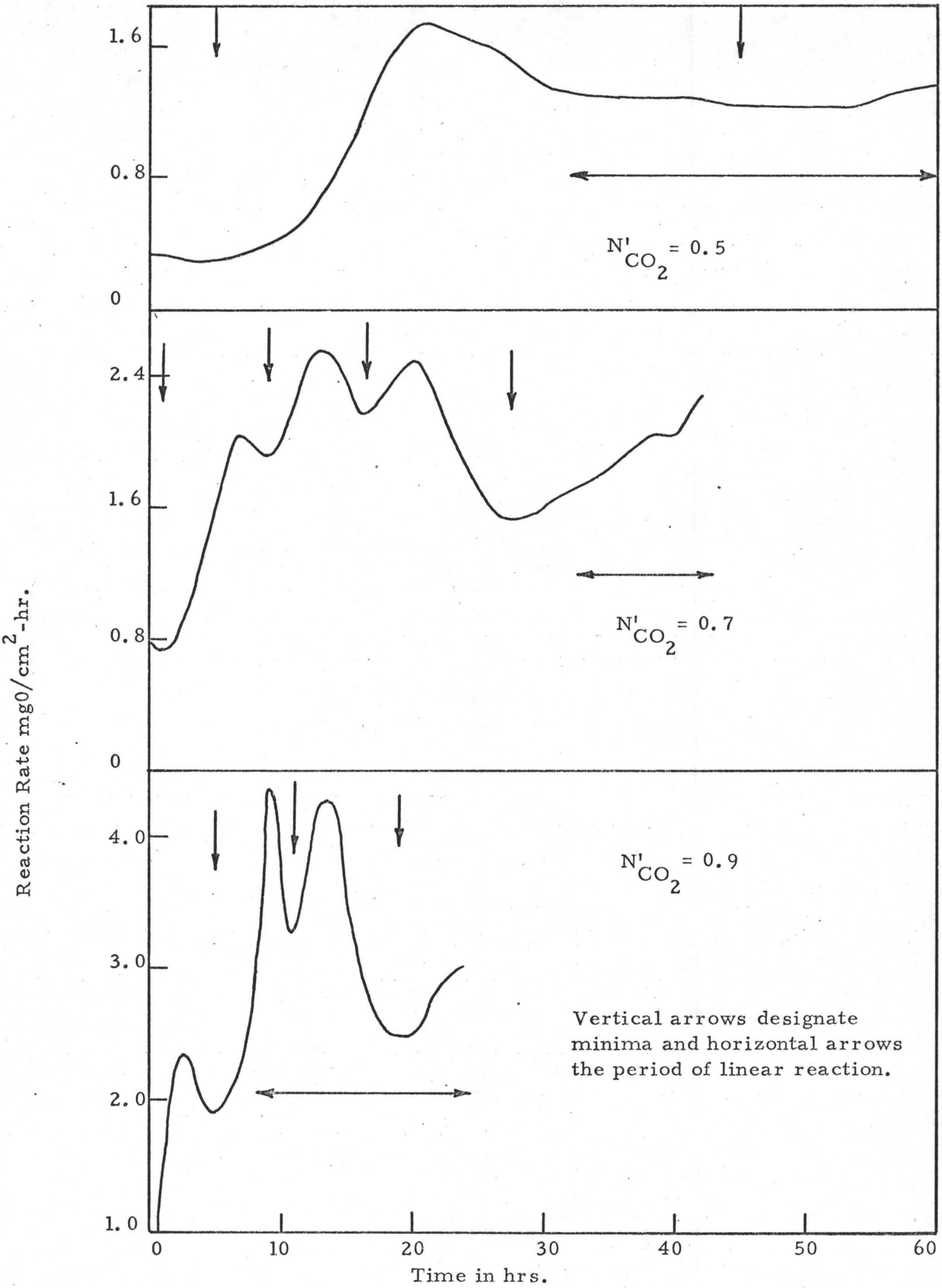

Vertical arrows designate minima and horizontal arrows the period of linear reaction.

Fig. VI-9: Reaction rates at 1000°C in CO_2 - CO atmospheres containing argon, $P_{CO_2} + P_{CO} = 0.5$ atm.

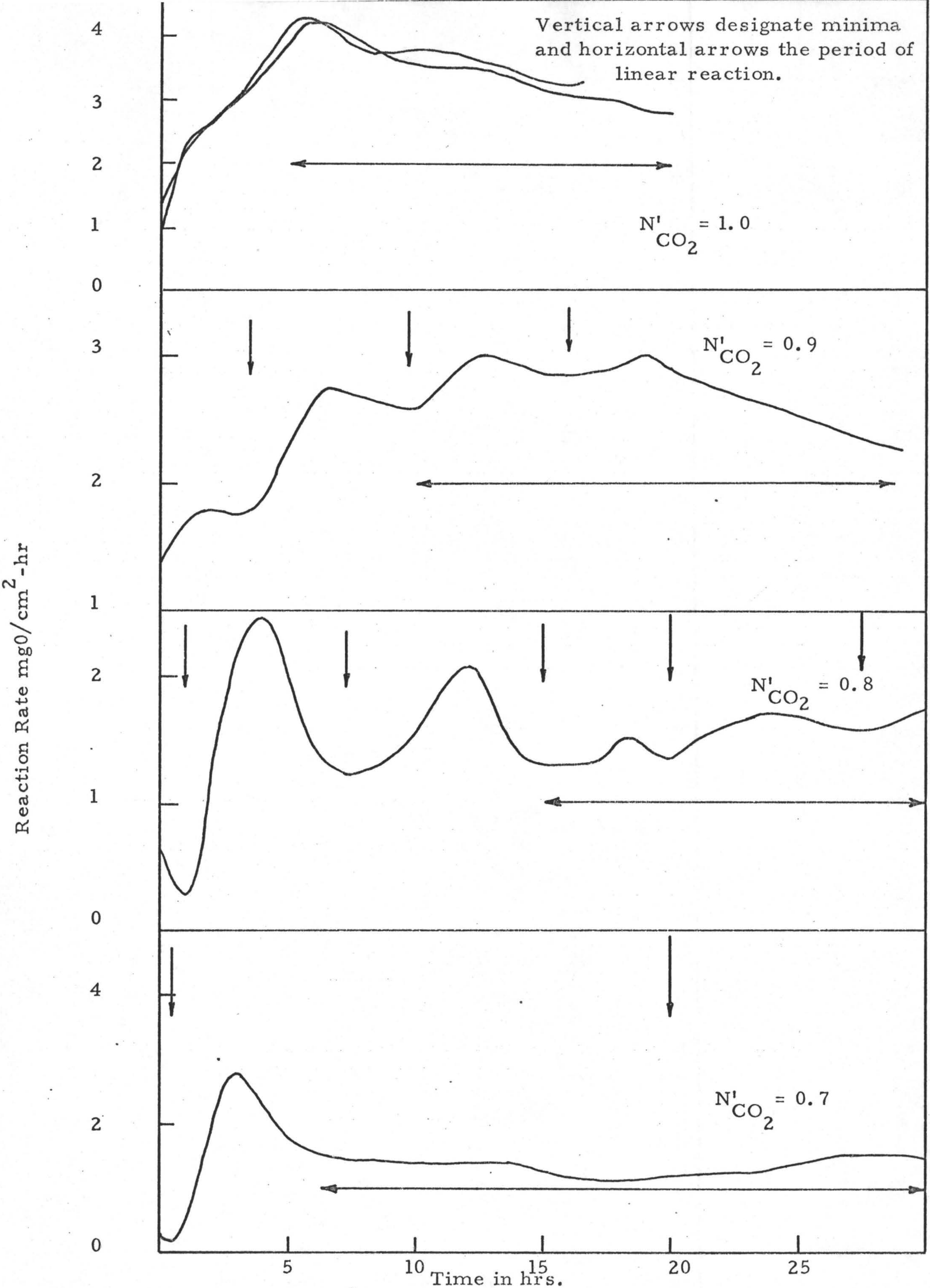

Fig. VI-10: Reaction rates at 890°C in CO_2-CO atmospheres, $P_{CO_2} + P_{CO} = 1$ atm.

TABLE VI-1

Reaction Rate Constants at 890°C and 1000°C

Reaction Temperature 1000°C

Gas Composition P' in atm.	N'_{CO_2}	Mean Linear Reaction Rate in $mg/cm^2 hr$	Initial Reaction Rate in $mg/cm^2 hr$	Maximum Reaction Rate in mg/cm^2 hr
1.0	0.40	0.92 ± 0.15	0.53	1.12
"	0.50	1.79 ± 0.27	0.71	2.14
"	0.60	2.24 ± 0.24	0.48	2.53
"	0.70	3.97 ± 0.57	1.17	5.05
"	0.80	5.46 ± 0.33	2.76	6.27
"	0.90	6.11 ± 0.62	3.10	7.14
"	0.95	6.80 ± 0.34	2.44	8.23
"	1.00	7.04 ± 0.60	-	8.00
"	1.00	7.22 ± 0.83	3.96	8.28
0.70	0.428	1.14 ± 0.07	0.46	1.88
"	0.571	1.70 ± 0.08	0.40	2.96
"	0.714	2.96 ± 0.40	0.65	3.85
"	0.857	4.14 ± 0.14	2.00	5.50
0.50	0.40	0.88 ± 0.03	0.20	0.92
"	0.50	1.28 ± 0.06	0.39	1.74
"	0.70	1.84 ± 0.17	0.74	2.67
"	0.80	2.68 ± 1.21	0.99	3.63
"	0.90	3.21 ± 0.65	1.85	4.38

Reaction Temperature 890°C

Gas Composition P' in atm.	N'_{CO_2}	Mean Linear Reaction Rate in $mg/cm^2 hr$	Initial Reaction Rate in $mg/cm^2 hr$	Maximum Reaction Rate in mg/cm^2 hr
1.0	0.40	0.11 ± 0.28	0.10	0.16
"	0.50	0.33 ± 0.03	0.41	0.41
"	0.70	1.45 ± 0.07	0.67	0.67
"	0.80	1.65 ± 0.11	0.50	0.50
"	0.90	2.89 ± 0.12	1.67	1.67
"	1.00	3.66 ± 0.33	1.97	1.97
"	1.00	3.70 ± 0.15	2.29	2.29

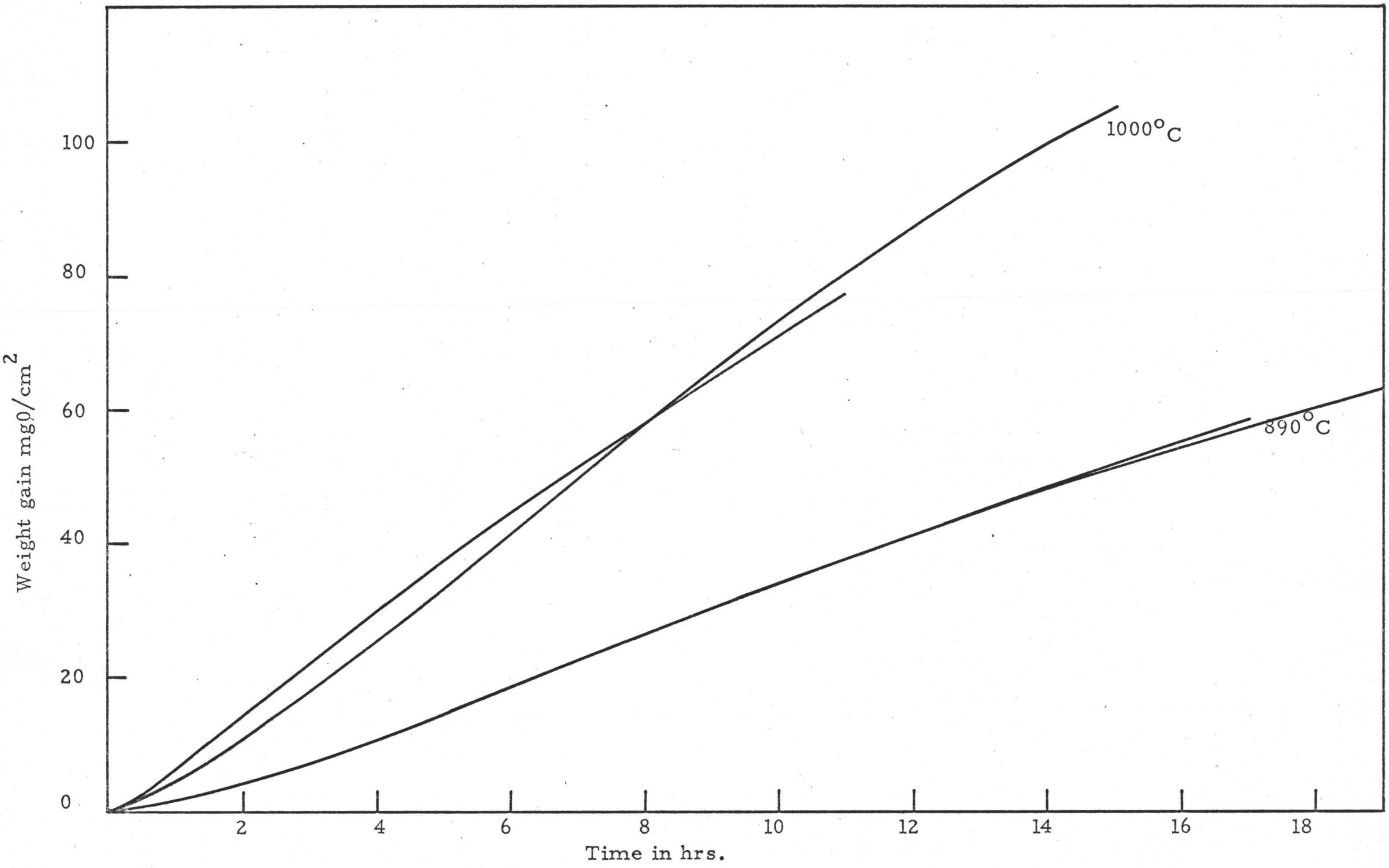

Fig. VI-11: Reproducibility Tests of oxidation of 1.5 w/o Si-alloy in CO_2.

6.3 Initial Stage Studies

6.3 (a) Optical Microscopy

An attempt was made to study the exterior surface morphology during development of wustite on the alloy at early times under fixed conditions of temperature and gas composition. The chosen conditions were a gas composition of $N_{CO_2} = 0.5$, total pressure of 1 atmosphere and reaction temperature of 1000°C. Samples were reacted for different periods of time up to 8 hrs. and the samples were subsequently examined with an optical microscope. The results are illustrated in Fig. VI-12 to VI-13. Wustite developed as isolated growths which may be classified as nodules in this stage. They tended to grow laterally quite rapidly and achieve a hemispherical shape as suggested by Fig. VI-12a. There is a marked tendency also for the coalescence of adjoining nodules to form a chain which spreads lineally. It was also observed that the initial nucleation of nodules takes place, not only at three-fold grain boundary intersections and grain boundaries but also inside the grains themselves, as can be seen in Fig. VI-12a. However, it can be readily seen from the micrograph of this sample oxidized for 30 minutes that only nuclei formed at grain boundaries grow rapidly, whilst the nuclei in the centre of the grains do not grow at an appreciable rate and may virtually cease growing after reaching a dimension of only 40 microns. Some confirmation for this latter consideration is shown by the micrograph in Fig. VI-12b for a specimen exposed to the oxidizing atmosphere for 1 hr. It is also observed that the areal coverage rate of the surface by wustite nodules slows down after an initial period of rapid growth of 2 hrs. and nearly total coverage was achieved after a period of 8 hrs. as seen in Fig. VI-13c. An estimate of the surface coverage was made for each period of oxidation and the values are listed under each micrograph.

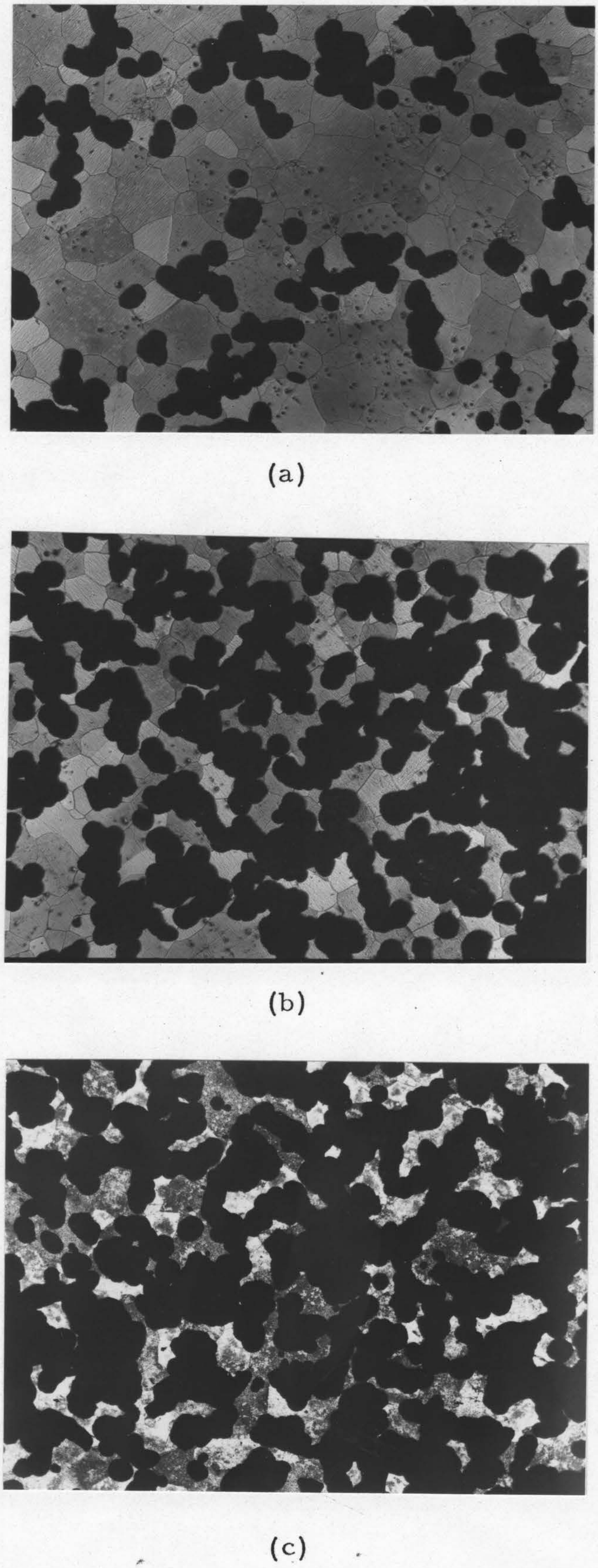

Fig. VI-12: Growth of oxide nodules at 1000°C in initial stages of oxidation, X20.

(a) Time = 30 min., Areal coverage = 0.30
(b) Time = 1 hr., Areal coverage = 0.60
(c) Time = 2 hr., Areal coverage = 0.80

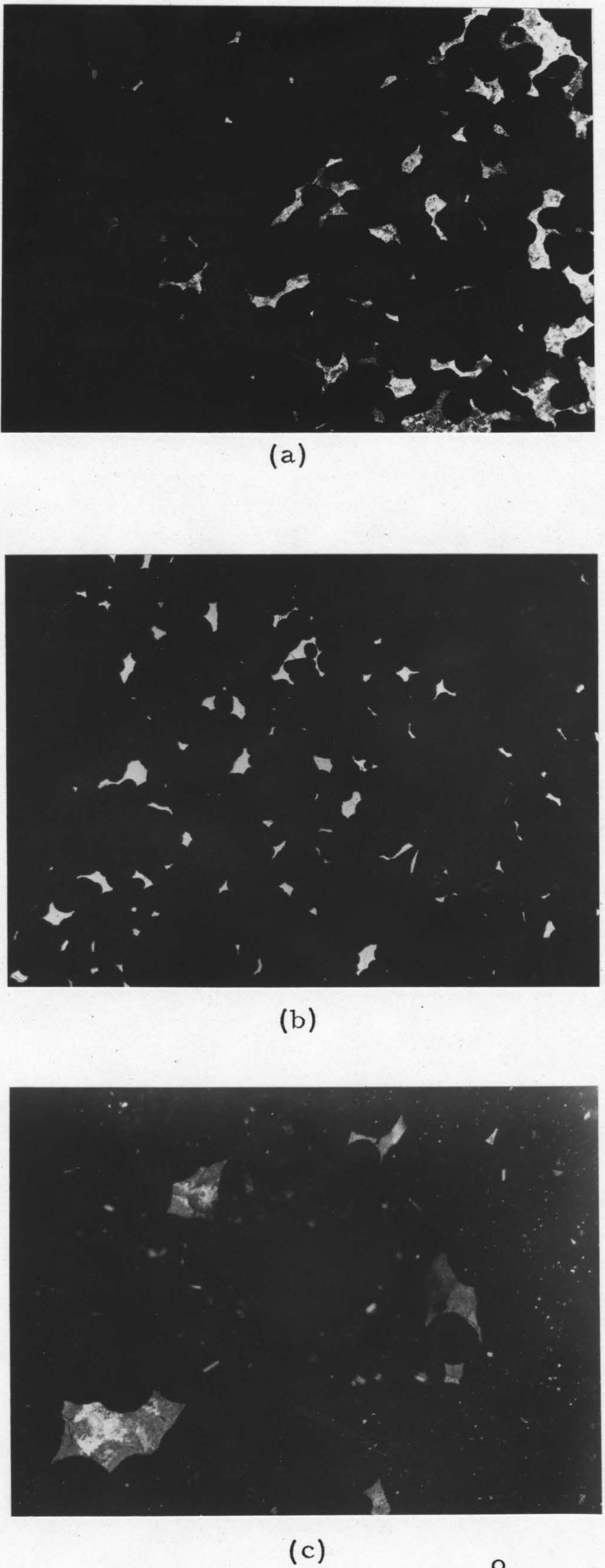

Fig. VI-13: Growth of oxide nodules at 1000°C in the initial stages of oxidation, X20.

(a) Time = 4 hr., Areal coverage = 0.95
(b) Time = 8 hr., Areal coverage = 0.99
(c) Time = 8 hr., Areal coverage = 0.99

The oxide nodules formed were identified as wustite by analyses of oxide scraped off from the surface of specimens, by use of the standard X-ray Debye-Scherrer powder method. The X-ray results showed in addition the presence of fayalite in minute quantities. To further elucidate the formation of nodules, the study of thin films of oxide formed on the specimens was initiated using the techniques of electron microscopy.

The nodules consisted of a large number of crystallites of oxide during the initial stages of oxidation. The oxide consisted of grains of irregular shape with some regions of well faceted, thick oxide grains at short times. At longer times, the faceted oxide grains completely covered the specimen by lateral growth of the oxide grains. These features of the oxide growth in the initial stages were initially detected by light microscopy as illustrated in Figs. VI-14.

6.3 (b) Electron Microscopy

The transmission electron micrographs of oxide films in Fig. VI - 15 illustrate the general features of oxide films formed after oxidation for 1/2 and 1 hr. at 1000°C. These micrographs were obtained at magnifications in the range 14,000-20,000X. The films consist of large spherical crystallites which increased in size with continued oxidation and a matrix of smaller irregular shaped crystallites. Although, it was possible to obtain electron transmission through certain sections of these films of average thickness greater than 20,000Å as determined by the weight gain measurements, it was not possible to obtain any identifiable diffraction patterns. The patterns appeared to be composed of reflections from a large number of crystallites of slightly different orientations. An example of this type of pattern is shown in Fig. VI - 16.

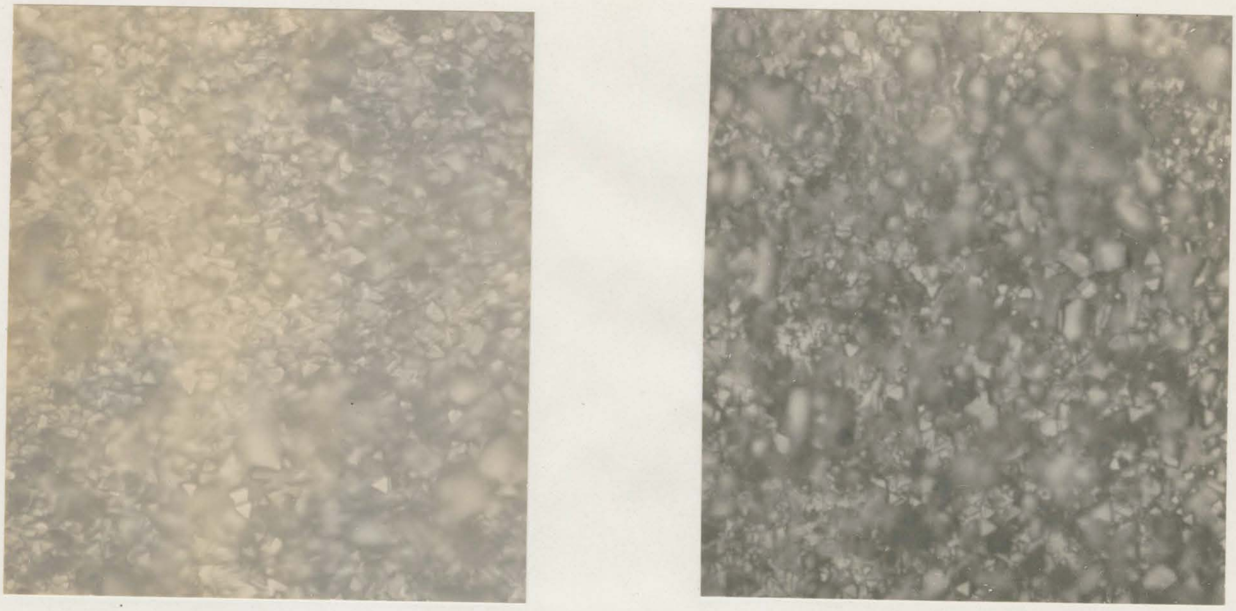

(a) Oxidized for 1 hr.

(b) Oxidized for 2 hrs.

(c) Oxidized for 4 hrs.

(d) Oxidized for 8 hrs.

Fig. VI-14: Surface topology of oxide during the initial stages of growth in an atmosphere with $CO_2/CO = 1$ at $1000^\circ C$.

X500

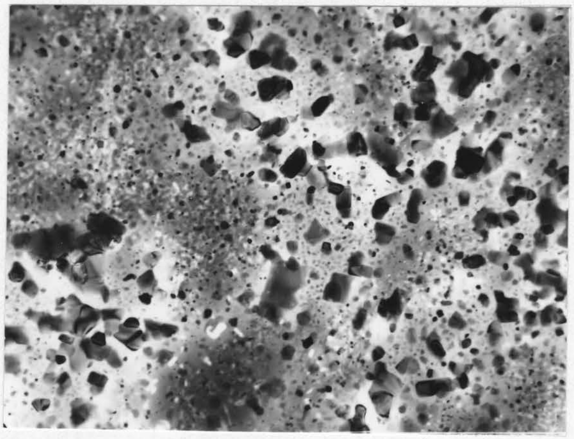

(a) Oxidation time = 1/2 hr.
X14000

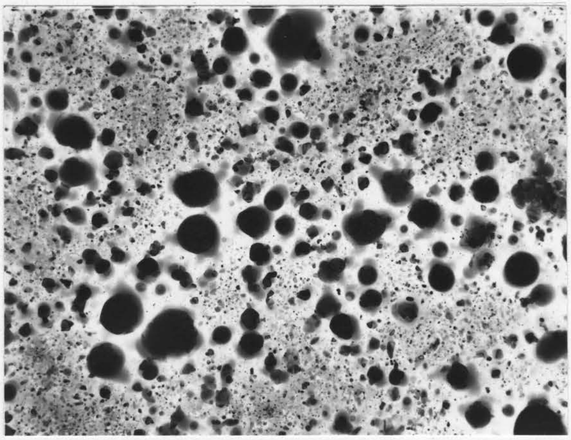

(b) Oxidation time = 1 hr.
X14000

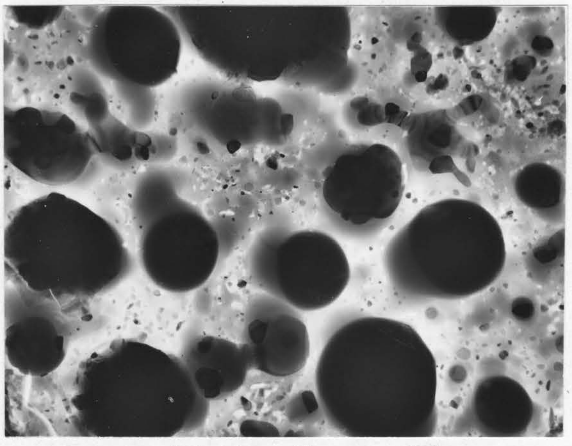

(c) Oxidation time = 1 hr.
X20000

Fig. VI-15: Oxide films formed at 1000 °C in a CO_2-CO atmosphere containing 50 $^{v}/_{o}$ CO_2.

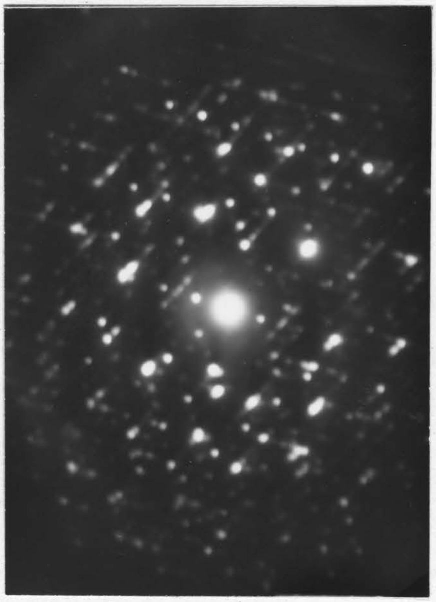

Fig. VI-16: Diffraction Pattern from initial oxide film formed at 1000°C after 30 min. of oxidation in a CO_2-CO atmosphere containing 50 $^v/o$ CO_2.

Replicas of outer surfaces of similar oxide films were also examined and are shown in Fig. VI - 17. The replicas show the surfaces of samples as polished, after an argon anneal of 2 hrs. and oxidation for 1/2 hr. and 1 hr., respectively. Small spherical crystallites are present in the film after annealing in argon, indicating a small amount of oxidation does take place during this period because the argon contained small amounts of oxygen (less than 10 ppm). This is in agreement with the small weight gain of 40 ug/cm^2 observed. These replicas provide further evidence that the crystallites increased in size with continued oxidation as shown in Fig. VI - 17c and VI - 17d. It is also observed in Fig. VI - 17d that the rate of growth is not uniform over the entire surface of the specimen.

Further studies were carried out on specimens annealed in argon for 2 hrs. and on specimens oxidized for 1/4 hr. in carbon dioxide - carbon monoxide after the argon anneal, since these specimens were found to be suitable for transmission electron microscopy and selected area diffraction. The transmission electron micrographs and inset electron diffraction patterns in Fig. VI - 18 to 21, illustrate the general features of thin oxide films formed at 1000°C. These films are composed of numerous small irregular shaped oxide crystallites in a matrix of amorphous oxide. The electron diffraction patterns obtained are single crystal spot patterns or amorphous ring patterns. The patterns in Figs. VI-18 and 19 are from specimens oxidized in CO/CO_2 after argon anneal and are identified as due to the intramolecular double-oxide fayalite, $2FeO.SiO_2$. As previously stated in the optical microscopy section, the nuclei nucleated at grain boundaries appeared to grow to a larger size than nuclei nucleated at the centres of grains. The nuclei not growing seem to stop at a size about 0.2μ and the subgrain size is about 1.5μ. These features can be seen in Fig. VI-18. The nuclei are quite irregular

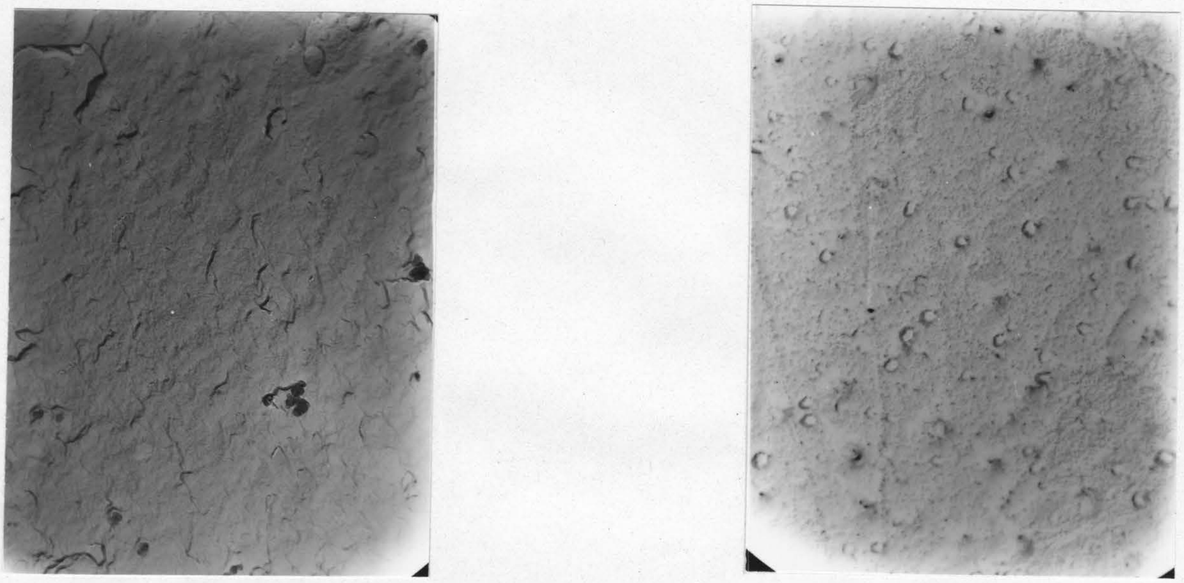

(a) As polished

(b) Annealed in argon for 2 hrs.

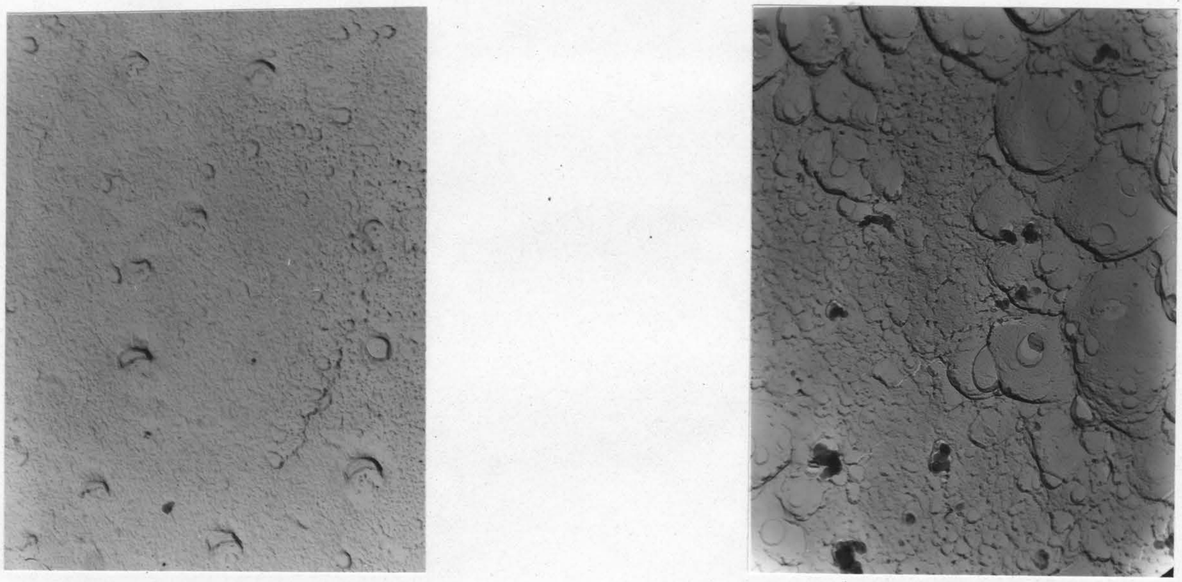

(c) Oxidized for 30 mins.

(d) Oxidized for 60 mins.

Fig. VI-17: Replicas of the surface of specimens before and after oxidation at 1000°C.

X20000

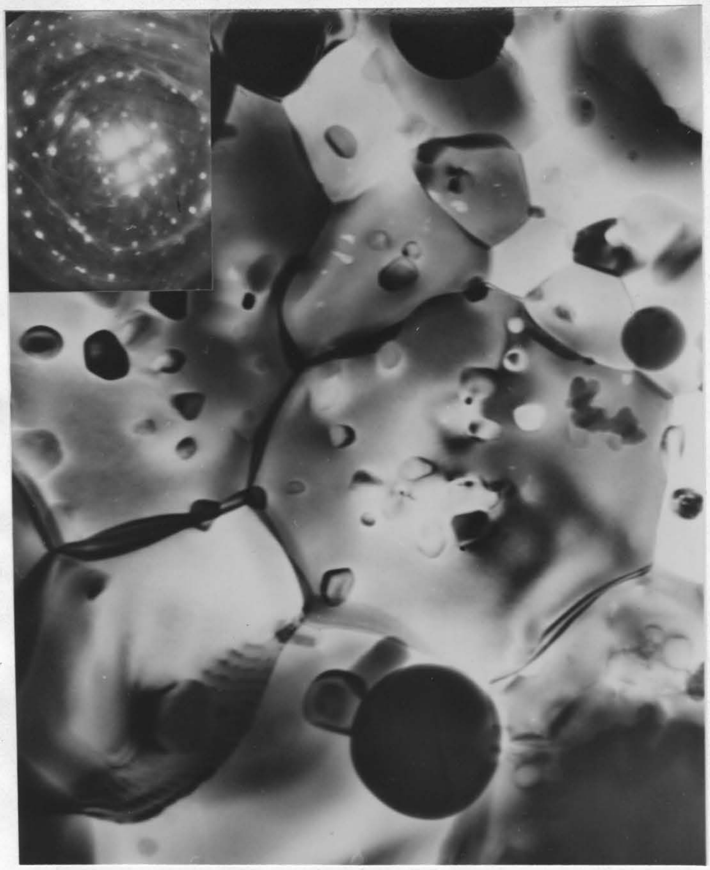

Fig. VI-18: Oxide film formed at 1000°C after oxidation for 15 mins., X4 0000

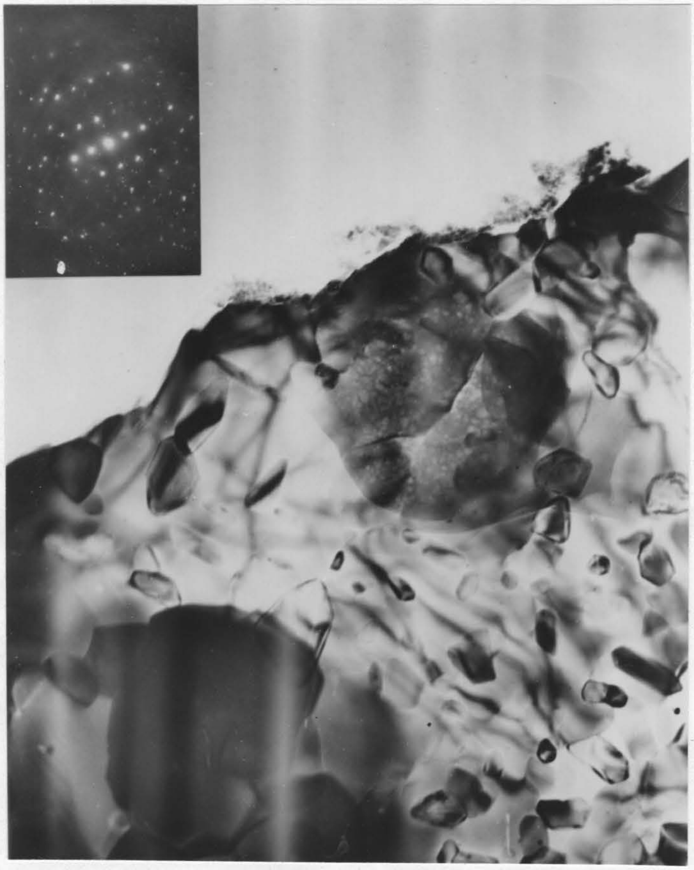

Fig. VI-19: Oxide film formed at 1000°C after oxidation for 15 mins., X4 0000

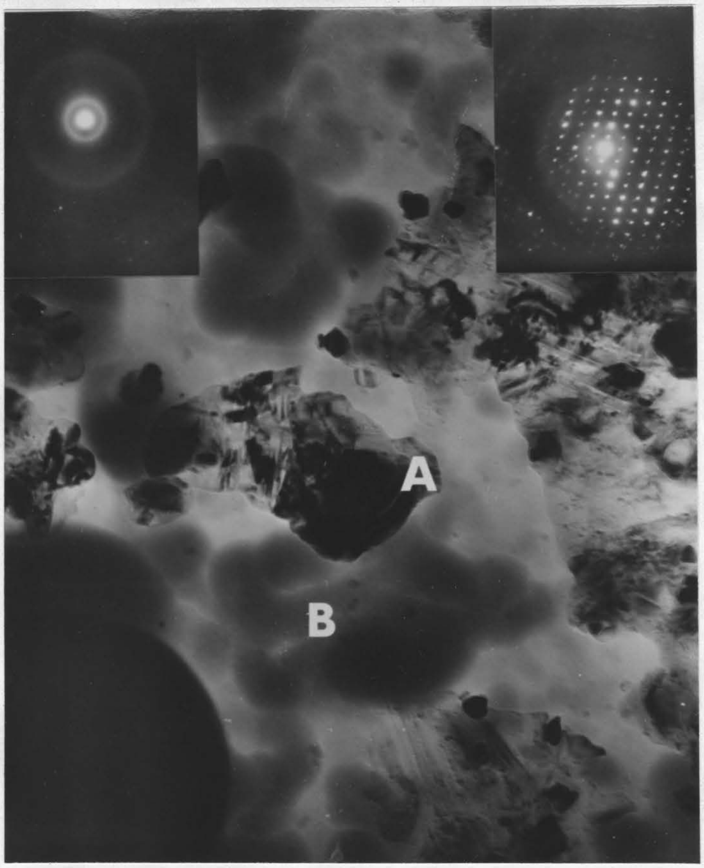

Fig. VI-20: Oxide film formed at 1000°C after annealing in argon for 2 hrs. X40000

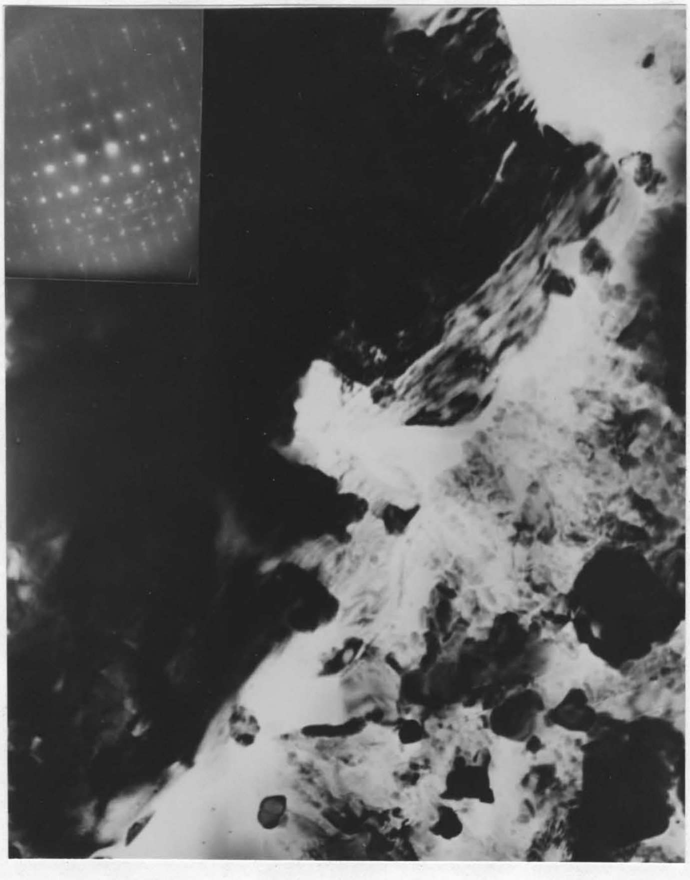

Fig. VI-21: Oxide film formed at 1000°C after annealing in argon for 2 hrs. X40000 in their shape at this stage compared to the spherical shapes found at later times as seen in Fig. VI-15.

The micrographs shown in Fig. VI - 20 and 21 were obtained from specimens annealed in argon. The two diffraction patterns A and B illustrated in Fig. VI - 20 are from areas labelled A and B on the electron micrograph. The pattern A is a single crystal pattern which is obtained from the fayalite phase, the diffuse ring pattern B can be identified as amorphous silica(120). The fayalite phase is the dull grey phase in the region marked A of the micrograph, surrounding the dark nodule. The area surrounding the fayalite phase is the amorphous silica phase, marked B in micrograph. The dark nodules seen in the micrograph can hence be predicted to be composed of iron oxide. This was confirmed by analysis of oxides from the specimens by the X-ray powder method. The main component was identified as wustite, FeO. The diffraction pattern shown in Fig. VI - 21 was indexed as β-cristobalite, a crystalline form of silica. An example of the method for indexing the single crystal spot patterns due to fayalite is given in Appendix III. The phases identified on the electron micrographs and the electron diffraction patterns indexed are listed in Table VI - 2.

The fact that nodules grow at different rates and habits on different areas of the specimen is illustrated by the micrograph in Fig. VI - 22. In the upper left corner of the micrograph, the average size of the nodules is about 600Å, whilst the nodule size in the rest of the micrograph is about 1400Å. There is also more fayalite phase present around the larger nodules compared with the smaller nodules. The dull grey areas around the nodule consist of the fayalite phase.

Replicas of the outer surfaces of oxide films in this range were examined and the results are shown in Fig. VI - 23 to 25. The specimen in the first micrograph was annealed in argon for 2 hrs. and

TABLE VI-2

A Summary of Electron Diffraction Data of Initial Stage Oxides

Specimen Treatment	Plate No.	R in mm.	d in Å	hkl	Θ_m	Θ_c	$d_{calc.}$ Å	Oxide Phase and Zone
Annealed in Argon	2254	3.33	5.58	011	32	32.6	5.27	Fe_2SiO_4 100
		6.25	2.98	$0\bar{1}2$	44	46.9	2.92	
		4.94	3.76	$0\bar{2}1$			3.97	
"	2277	4.4	4.23	$1\bar{1}1$	58.5	58.5	4.14	SiO_2 β-cristobalite $1\bar{1}\bar{2}$
		8.5	2.19	311	31.5	31.5	2.15	
		7.5	2.48	220			2.53	
Annealed in Argon and Oxidized in CO/CO_2 for 1/4 hr.	2021	5.5	3.38	120	45.5	44.1	3.54	Fe_2SiO_4 $4\bar{2}1$
		9.5	1.96	132	36.0	35.0	2.07	
		7.0	2.66	012			2.93	
"	2257	4.66	4.00	021	44.0	47.5	3.97	Fe_2SiO_4 $\bar{1}1\bar{2}$
		11.10	1.68	241	25.0	24.0	1.70	
		8.54	2.18	220			2.19	
"	2081	6.18	3.01	$1\bar{2}1$	49.0	50.4	3.06	Fe_2SiO_4 $\bar{3}15$
		8.50	2.19	211	46.0	45.3	2.19	
		6.31	2.95	130			2.83	
"	2270	5.25	3.54	$1\bar{2}0$	52	55.5	3.55	Fe_2SiO_4 001
		8.12	2.29	210	42	41.1	2.35	
		6.68	2.78	130			2.83	
"	2273	7.45	2.51	$\bar{1}12$	61	61.5	2.50	Fe_2SiO_4 $\bar{1}1\bar{1}$
		9.14	2.04	132	48	50.3	2.07	
		8.53	2.18	220			2.19	

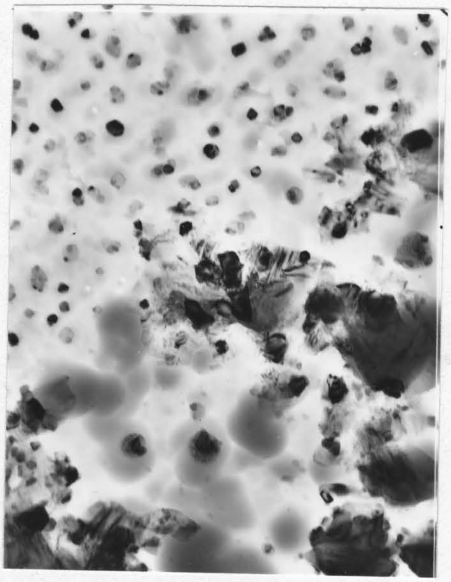

Fig. VI-22: Initial oxide film formed at 1000°C in CO_2/CO atmosphere containing 50 $^v/o$ CO_2. X20000

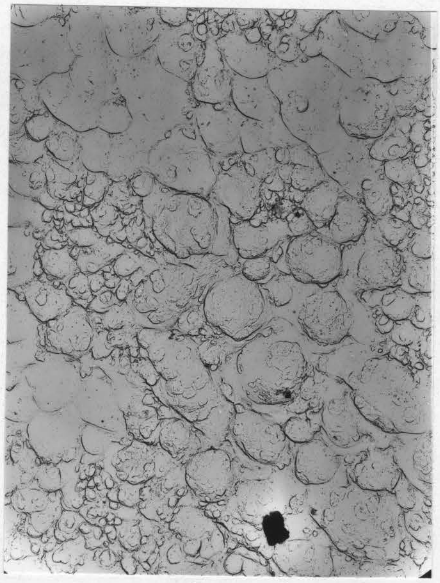

Fig. VI-23: Replica of outer oxide surface after oxidation for 15 mins. at 1000°C X2000

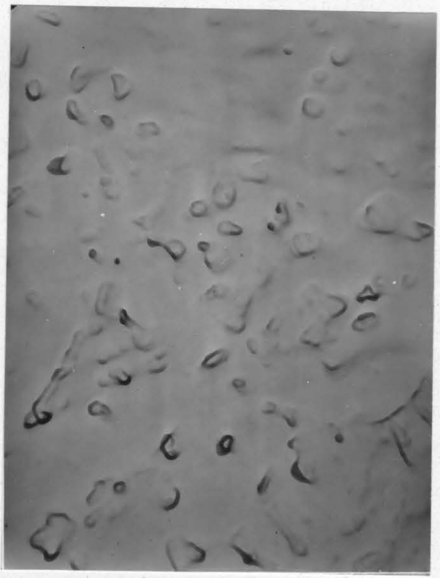

Fig. VI-24: Replica of outer oxide surface after argon anneal for 2 hrs. at 1000°C. X40000

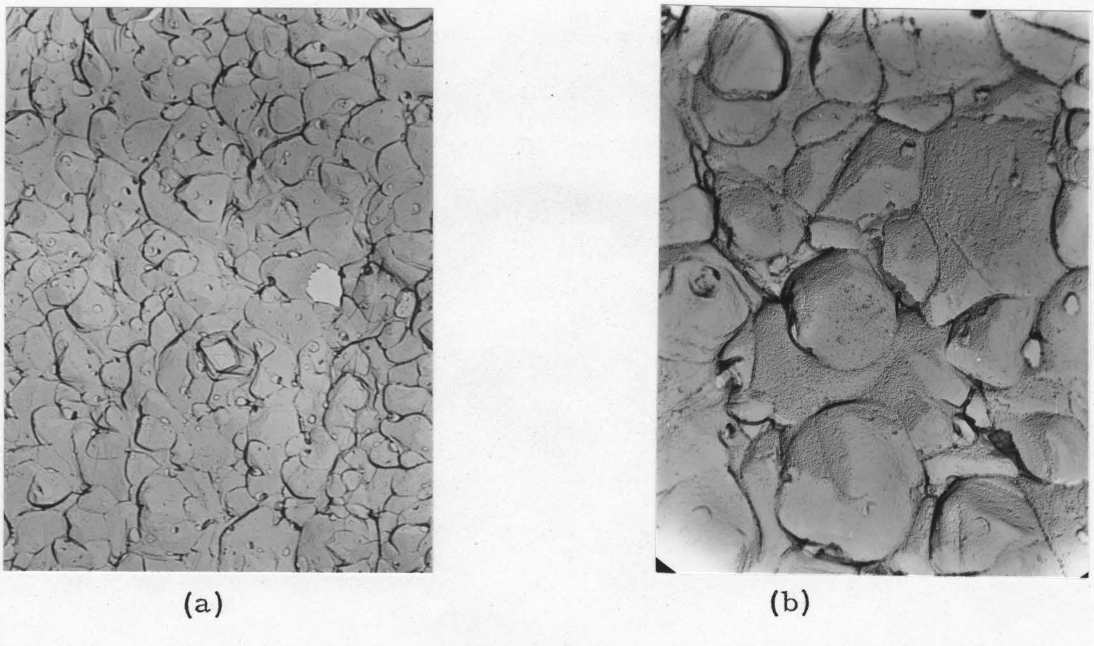

(a) (b)

Fig. VI-25: Replicas of outer oxide surface after oxidation for 15 mins. at 1000°C on two areas of the same specimen. X20000 oxidized in carbon dioxide - carbon monoxide for 1/4 hr. The variation in size of the nodules is seen quite clearly in this micrograph, where the spread of sizes is from 5000Å to 40,000Å. It is also seen that the smaller nodules are clustered into groups in the regions between the larger nodules. The replicas in Fig. VI - 25a and b were from a sample similarly treated as above and the variation in size of nodules is quite apparent over the different areas of the sample. The nodule size in Fig. VI - 25a is about 2000Å and 8000Å in Fig. VI - 25b. Nodules were angular at smaller sizes and become hemispherical as they enlarged in size. The replica illustrated in Fig. VI - 24 is from a sample annealed in argon for 2 hrs. The size of the nodules is about 500Å at this stage and the shape is quite irregular.

6.3 (c) Growth Rate of External and Internal Oxides

Thicknesses of the external oxide and of the internal oxide zone were measured microscopically using a calibrated eyepiece on specimens which were previously used for the observations on the external oxide morphology. The results are shown in Fig. VI - 26a. The external oxide grows at a linear rate whilst the internal oxide zone would appear to grow by a decreasing rate defined by a parabolic relationship up to a period of 4 hrs. The internal oxide zone growth rate then decreased from this above relationship. This rate decrease appeared to be associated with the formation of the wustite-fayalite conglomerate layer in the external oxide at the alloy surface. As illustrated in Fig. VI - 26b, this conglomerate layer completely covered the alloy surface after a specimen has been oxidized for 8 hrs. The measurements above were made on specimens oxidized in the initial stage of oxidation.

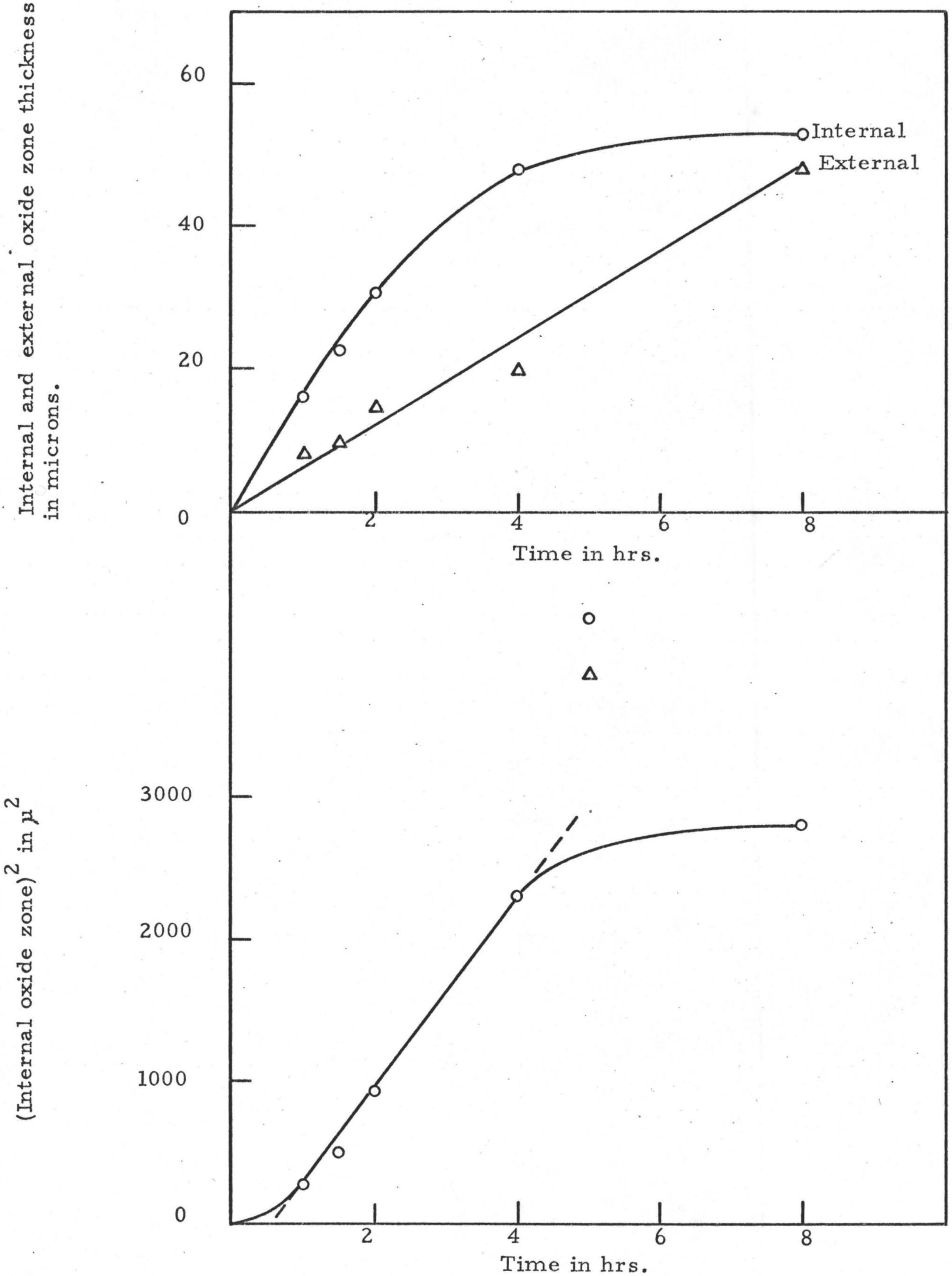

Fig. VI-26a Kinetics of external and internal oxidation at 1000°C in the initial stages.

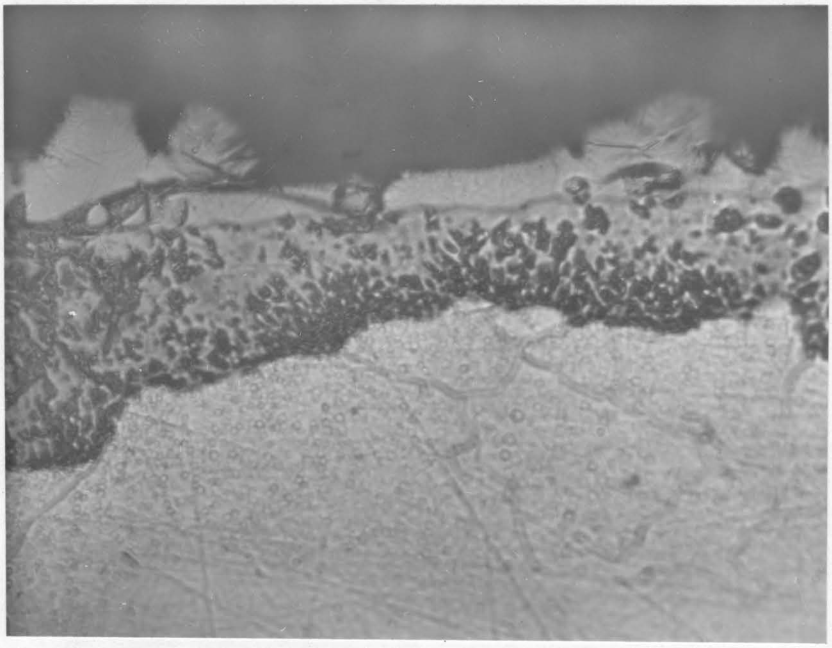

Fig. VI-26b: Photomicrograph of scale cross-section after oxidation for 8 hrs. in CO_2-CO atmosphere containing 50 $^v/o$ CO_2. X480

6.4 Oscillatory Reaction Rate Region Studies

6.4(a) Reaction Rate

The reaction rate curves for the alloy investigated in gases of varying compositions were illustrated in Fig. VI-6 to 10. A typical rate curve in the region of interest shows a number of maxima. The difference in the reaction rate between the maxima and the following minima may be as large as 20%. The number of maxima observed increases up to a total of four in some cases. Maximum and mean reaction rates over this region are listed in Table VI-1 for the specimens reacted at 890°C and 1000°C in atmospheres of various oxidizing potentials.

6.4(b) Structure in the Conglomerate Zone

In specimens observed in cross-section after the end of the oxidation test, several bands of precipitation were observed in the wustite-fayalite conglomerate phase. An example of these precipitation bands is shown in Fig. VI-27 and the corresponding reaction rate curve is illustrated in Fig. VI-28. In this particular case it was observed that there was a one to one correspondence in the number of minima in a reaction rate curve and the number of bands observed in the conglomerate zone. In the light of this singular observation, the number of minima obtained were then compared with the number of fayalite bands observed for all cases and the results are shown in Table VI-3. The width of the precipitate bands and the distance from the alloy-conglomerate interface are also listed in this table. It is clear that there is a significant correspondence between the number of minima in a reaction curve and the number of precipitation bands observed. We note also that the distances between consecutive bands decreases as their distances from the alloy interface increases.

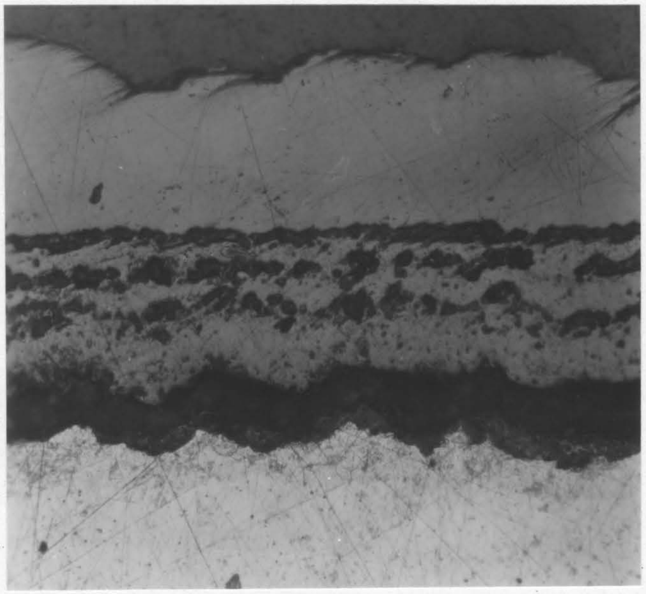

Fig. VI-27: Oxide scale cross-section formed at 1000°C. Light outer oxide is wustite and dark oxide in bands is massive fayalite precipitation. X200

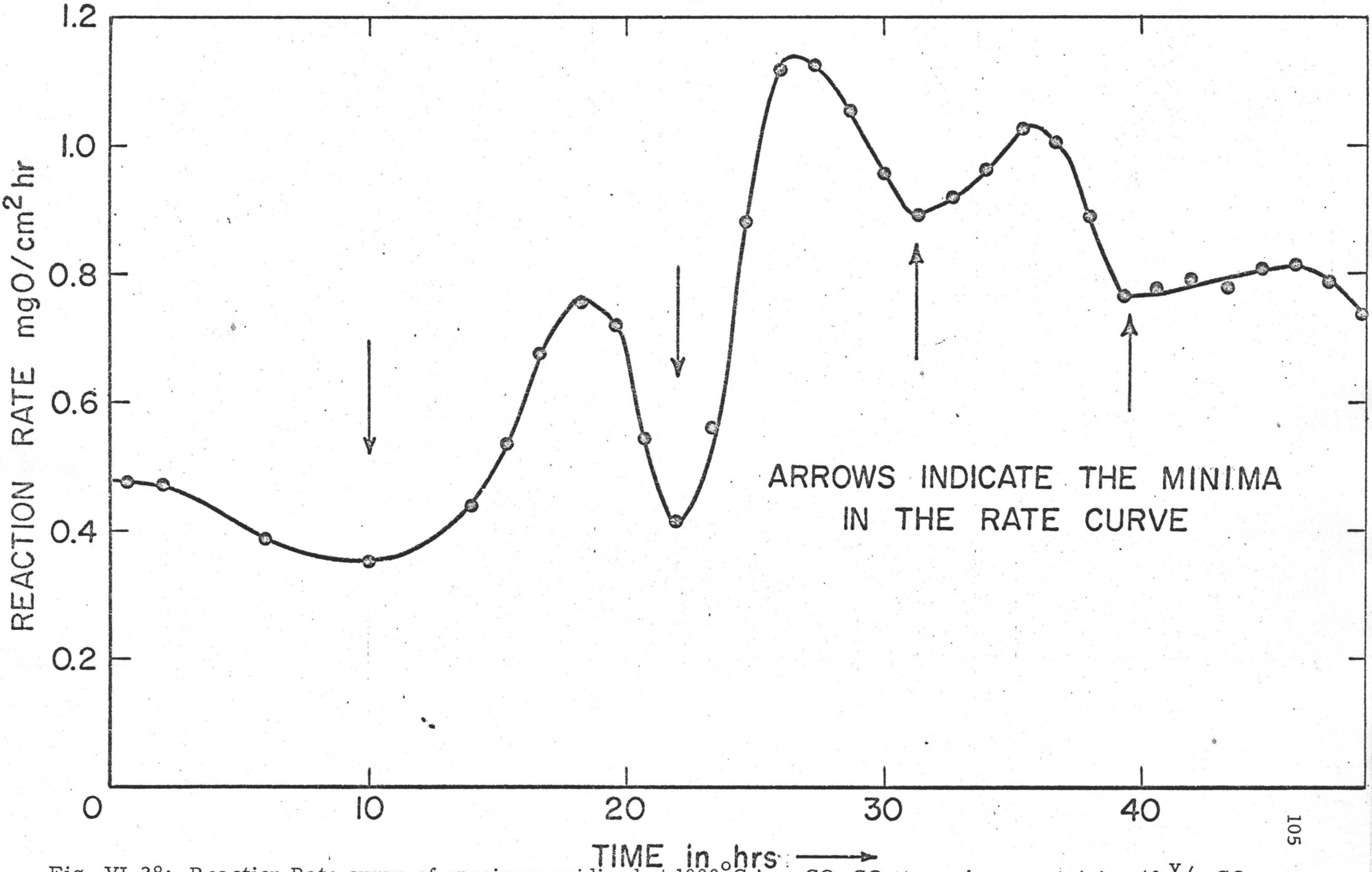

Fig. VI-28: Reaction Rate curve of specimen oxidized at 1000°C in a CO_2-CO atmosphere containing 40 $^v/o$ CO_2. The scale for this exposure is illustrated in Fig. VI-27.

TABLE VI-3

Correlation Between the Precipitation Bands and Number of Minima in the Reaction Rate Curve

Run No.	No. of Minima in Rate Curve	No. of precipitation bands	Width of bands in μ				Distance of band from alloy-oxide interface			
			w_1	w_2	w_3	w_4	d_1	d_2	d_3	d_4
K17	4	4	32	15	14	14	7	40	74	260
K16	3	2	22	21			27	260		
K15	2	2	16	16			53	160		
K14	2	2	80	64			144	224		
K21	2	2	34	34						
K20	1	1	120				256			
K19	1	-								
K2	1	1								
KA14	3	2	48				50			
KA12	3	3	40	40	40		25	94	228	
KA11	4	3	70	70	70		72	184	320	
KA10	3	3	42	44	34		36	88	160	
KA9	1	2	46	46			96	304		
KA6	2	2	61	61	30		0	192	464	
KA5	4	3	56	56	56		28	132	232	
KA1	1	1	30	26			31	207		
K8910	3	3	36	54	50		30	217	311	
K896	4	3	68	57			32	203		
K895	3	3	44	40	40		91	160	234	
K899	5	4	33	40	57	13	38	137	241	352
K894	3	4	96	90	78	75	51	188	279	387
K893	1	3	48	49	48		24	180	249	
K892	1	2	52	52			26	160		

6.5 Region of Linear Reaction Behaviour

6.5 (a) Surface Topology of Oxide Scales

Examination of scale surfaces showed that the oxide crystals, which grew by both lateral and vertical growth of platelets caused the development of a very uneven topology, as shown in Fig. VI - 29. The size of the oxide crystals was dependent on the oxidizing potential and time of oxidation. This is illustrated in Figs. VI - 30 to 33, which show the effect of gas composition on the crystallite size and shape in the surface oxide scale. At low concentrations of carbon dioxide ($N'_{CO_2} = 0.3$) there is a high density of faceted grains. The faceted oxide grains had corners at angles of 60°, as seen in Fig. VI - 30. Since wustite is a cubic crystal, the facets may be identified as having $\{111\}$ planes parallel to the substrate. At higher carbon dioxide concentrations in the atmosphere, the faceted oxide is observed but ledge formation on the crystallite is observed and the $\{111\}$ planes are not visible. At $N'_{CO_2} = 0.7$, the structure of the surface oxide becomes quite complicated with various surface morphologies present, two examples of which are shown in Figs. VI - 33. The oxide scale was identified as wustite by the X-ray Debye Scherrer powder method in all cases.

6.5 (b) Oxide Structure

An oxide scale examined at the end of an oxidation test in cross-section, was composed of an external compact layer of wustite and fayalite interspersed with bands consisting largely of fayalite as shown in Fig. VI - 34. The oxides in the different regions of a scale were identified by powder X-ray analyses of selected samples. A list of the structures of oxides formed on the iron silicon alloy are given in Table VI - 4 under different oxidizing conditions.

Fig. VI-29: Topology of wustite scale formed at 1000°C X500

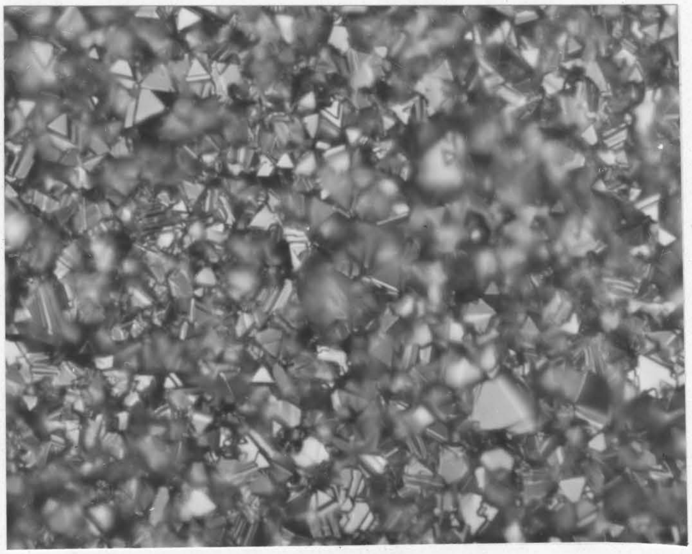

Fig. VI-30: Topology of external FeO scale formed in atmosphere containing 30 $^v/o$ CO_2. X1000

Fig. VI-31: Topology of external FeO scale formed in atmosphere containing 40 $^{v}/o$ CO_2 X150

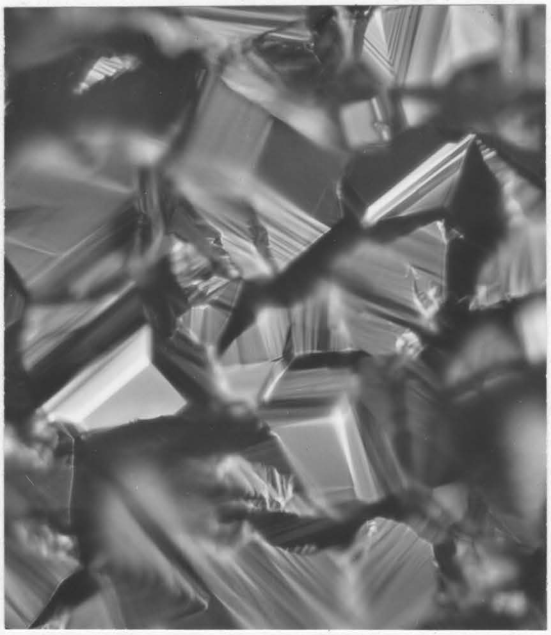

Fig. VI-32: Topology of external FeO scale formed in atmosphere containing 50 $^{v}/o$ CO_2 X500

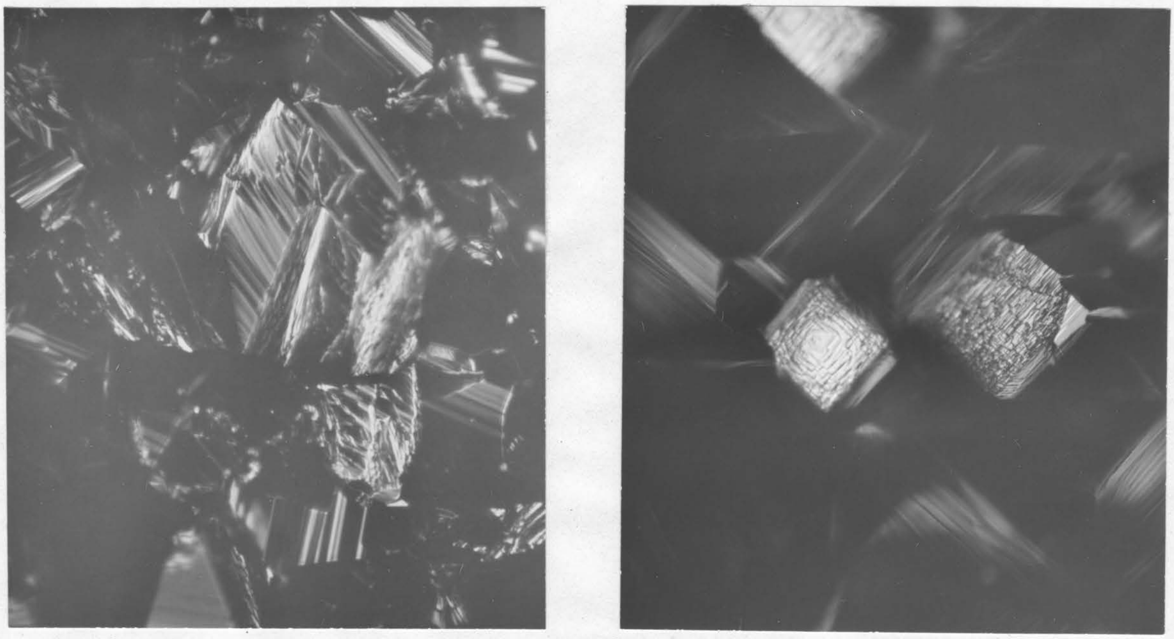

(a) (b)

Fig. VI-33: Topology of external FeO scale formed in atmosphere containing 70 $^{v}/o$ CO_2.

(a) Oxidation time 5 hrs. X150
(b) Oxidation time 12 hrs. X100

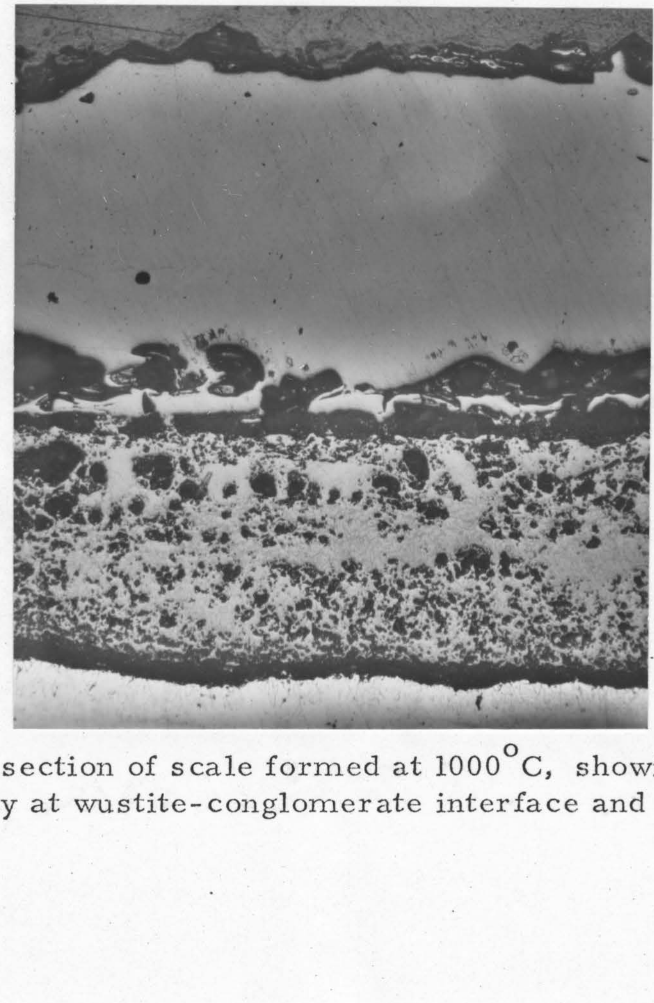

Fig. VI-34: Cross-section of scale formed at 1000°C, showing marked porosity at wustite-conglomerate interface and in conglomerate layer. X100

TABLE VI-4

Summary of Constitution of Scales Formed on the Alloy at 890° and 1000°C

Temperature °C	Gas Composition CO_2/CO	Outer Scale	Inner Scale
1000°	95/5	$Fe0 + Fe_3 0_4$	$Fe0 + Fe_2 Si0_4$
	80/20	$Fe0 + Fe_2 Si0_4$*	$Fe0 + Fe_2 Si0_4$
	40/60	$Fe0$	$Fe0 + Fe_2 Si0_4$
890°	40/60	$Fe0 + Fe_3 0_4$	$Fe0 + Fe_2 Si0_4$

* Fayalite contamination from inner scale during sampling of the scale.

While the wustite phase in the external and conglomerate layers appeared to be compact, it is not possible to formulate an unequivocal conclusion on the degree of porosity in the conglomerate layer. A few examples of the wustite-fayalite conglomerate in specimens oxidized in different oxidizing conditions are shown in Fig. VI - 35. The porosity in this portion of the scale was mostly associated with the fayalite rich areas, whilst the two phase structure was essentially free of porosity. The micrographs in Figs. VI - 36 and 37 are of a specimen oxidized in pure carbon dioxide for 2 hrs. at 1000°C. Fig. VI - 36 shows a layer of fayalite at the wustite-conglomerate interface along with an external wustite layer. A considerable amount of grain boundary precipitation is seen in the alloy phase, and this is shown in greater detail in Fig. VI - 37. Although a small amount of oxide precipitates in the alloy matrix, the largest amount occurred as precipitate at the grain boundaries. Internal oxidation takes place by lattice and grain boundary diffusion, with the grain boundaries serving as preferential nucleation sites.

6.5 (c) Growth Rates of Wustite and Conglomerate Layers

The growth rates of the wustite and conglomerate layers were determined for a particular gas composition, which was 50% carbon dioxide in an atmosphere of CO - CO_2 at a total pressure of 1 atmosphere at 1000°C. The thicknesses of these layers are shown as a function of time in Fig. VI-38. The wustite grew at an increasing rate for short times and finally achieved a constant rate. The conglomerate layer did not start growing from the start of the reaction, but commenced growing at a parabolic rate after a period of 8 hrs. This is demonstrated in Fig. VI - 39, where the thickness of the conglomerate layer is plotted versus time on a

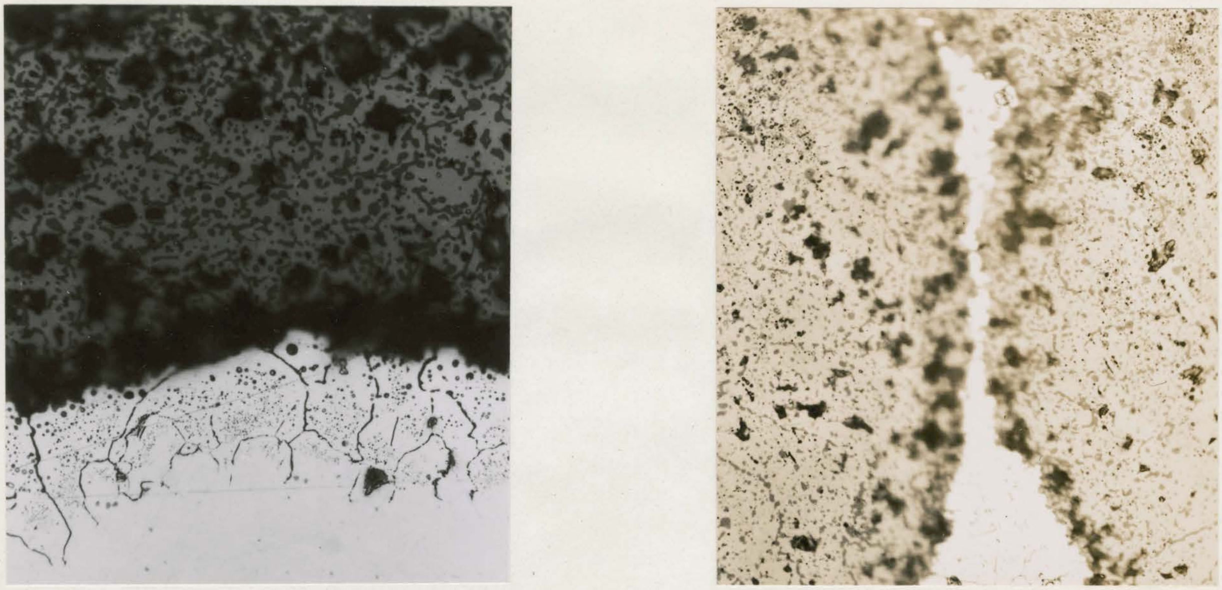

(a) $N'_{CO_2} = 0.5$, $P' = 0.7$ atm.
Temperature = 1000°C, X500

(b) $N'_{CO_2} = 0.5$, $P' = 1$ atm.
Temperature = 1000°C, X500

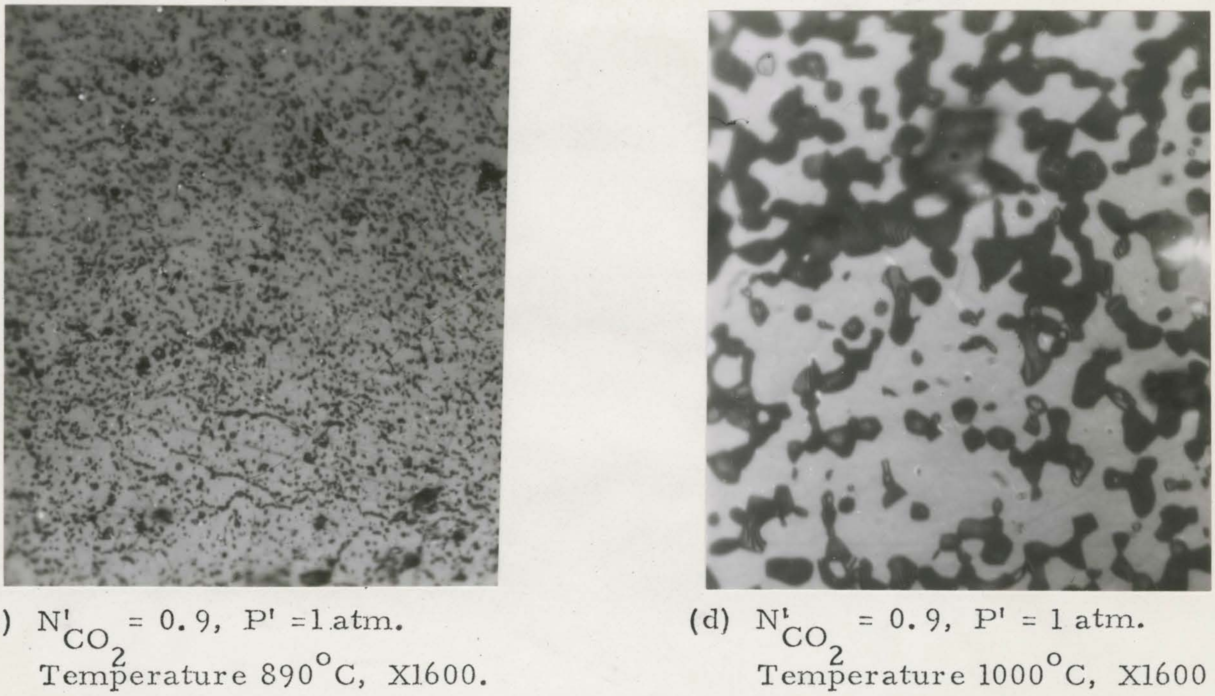

(c) $N'_{CO_2} = 0.9$, $P' = 1$ atm.
Temperature 890°C, X1600.

(d) $N'_{CO_2} = 0.9$, $P' = 1$ atm.
Temperature 1000°C, X1600

Fig. VI-35: Micrographs showing the conglomerate ($FeO-Fe_2SiO_4$) scale under various experimental conditions.

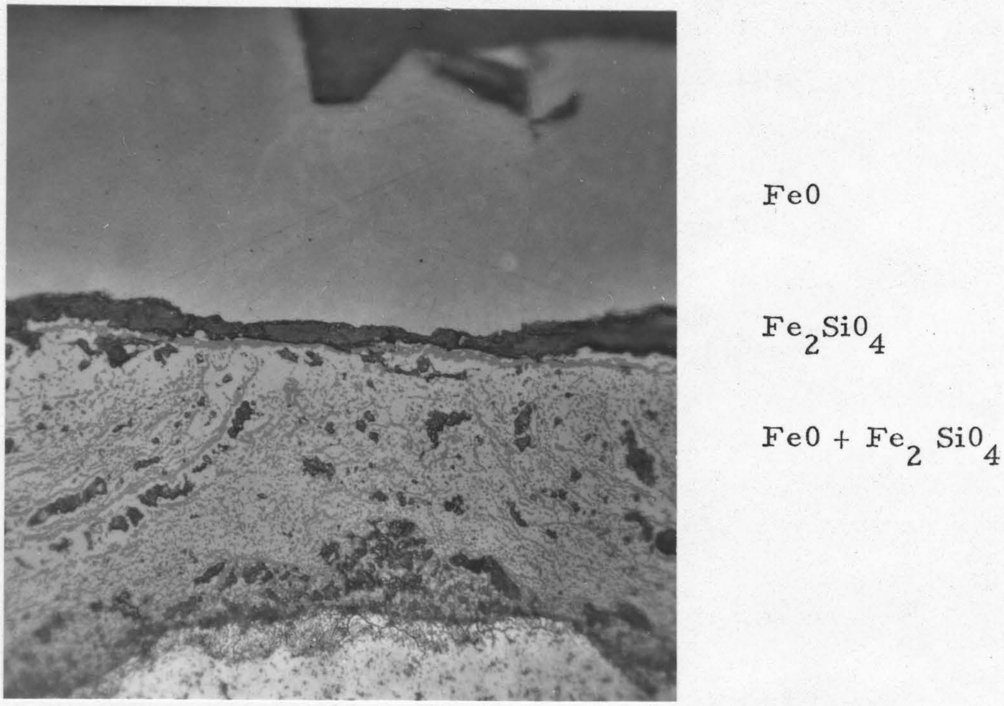

Fig. VI-36: Specimen oxidized at 1000°C for 2 hours
Etched in 2% Nital X750

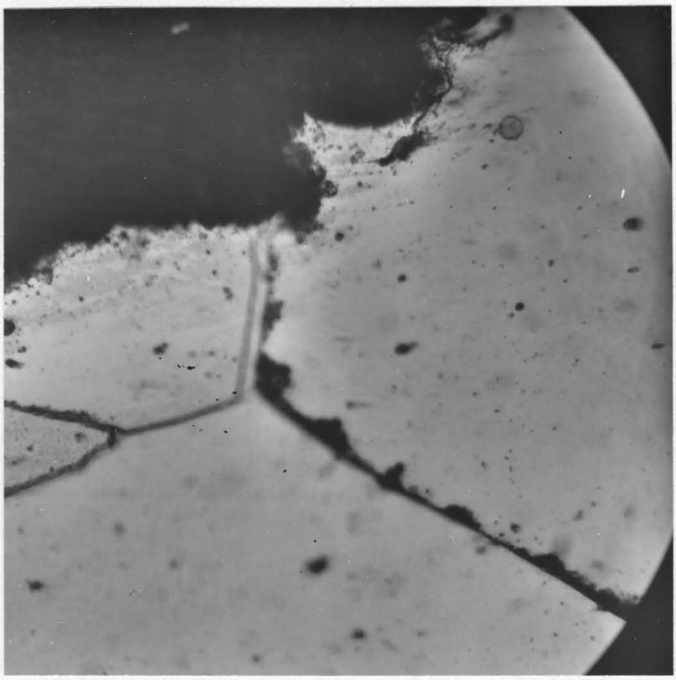

Fig. VI-37: Showing detail of grain boundary precipitation in
specimen above. X1500

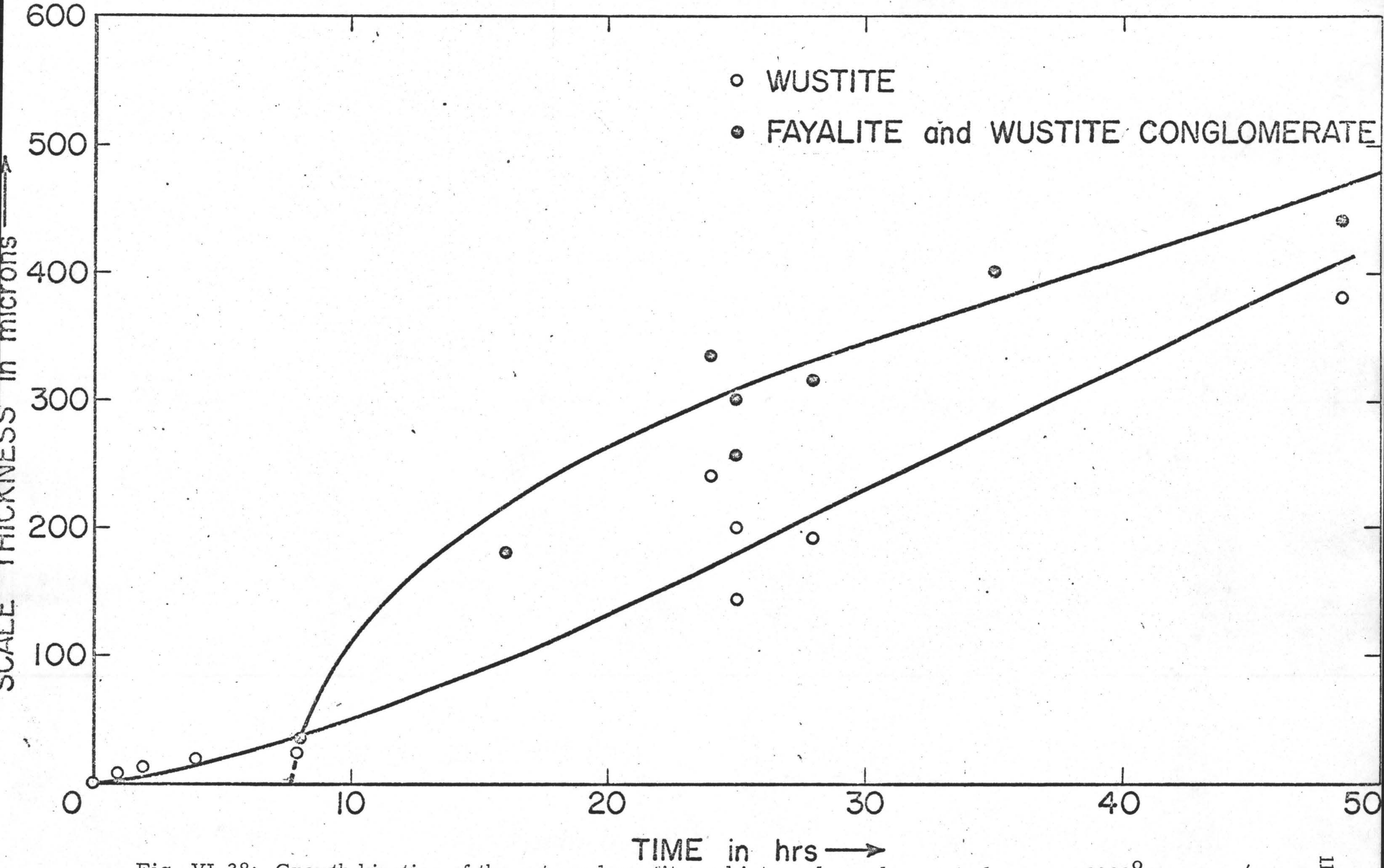

Fig. VI-38: Growth kinetics of the external wustite and internal conglomerate layers at 1000°C in CO_2/CO atmosphere containing 50 $^v/o$ CO_2.

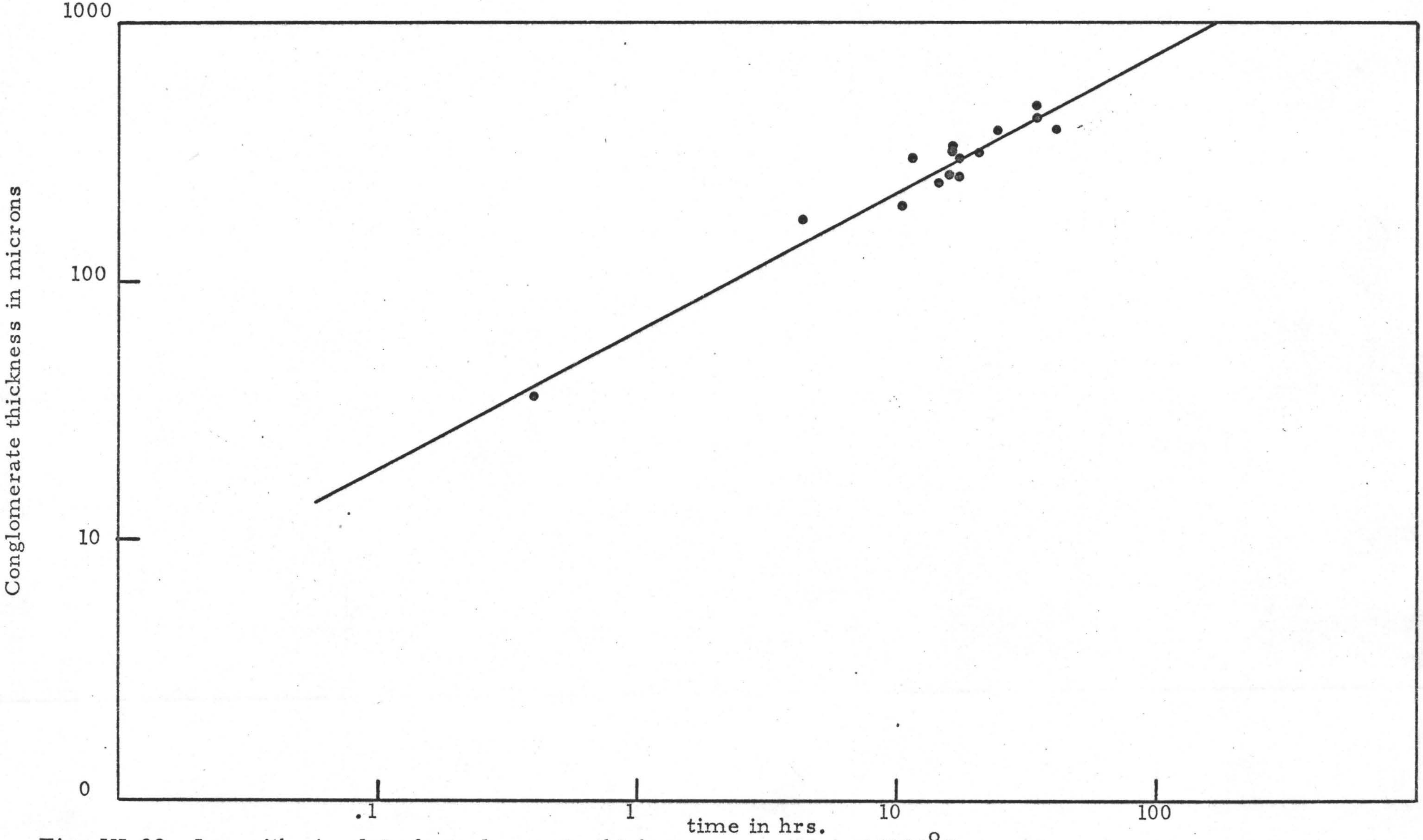

Fig. VI-39: Logarithmic plot of conglomerate thickness versus time at 1000°C.

logarithmic plot. The slope of the line was found to be 0.54 ± 0.07, which should have been 0.5 for a perfect parabolic plot. The linear wustite growth rate was 9.86 μ/hr. and the conglomerate growth rate was 66 $\mu/\text{hr.}^{1/2}$.

6.5 (d) Electron Microprobe Analysis

Specimens which had been oxidized in the kinetic oxidation tests were examined to determine the concentration profile of silicon and iron in the various phases present. The silicon concentration profile in the alloy phase in a typical case is shown in Fig. VI - 40. The concentration of silicon is plotted as weight percent versus the distance from the alloy-conglomerate interface. Since the unoxidized inner region of the alloy was found to be a better internal standard than pure silicon, it was used in evaluation of the concentration in the alloy phase. The concentration of silicon in the internal oxidation zone was irregular and the average composition is plotted as determined by the smooth curve drawn through the electron microprobe scan. This was probably caused by the silica precipitated in this zone in a matrix of alloy with very small amount of silicon present. The concentration of silicon at the alloy-internal oxidation interface was determined as a function of time in one particular case. The alloy was oxidized in a 50 $^{v}/o$ CO_2 atmosphere of CO-CO_2 at 1 atmosphere at 1000°C. The results of these experiments are illustrated in Fig. VI - 41. It is seen that concentration of silicon is not constant but decreases with time and possibly is approaching a constant value at long time, that is, after about 40 hrs. There is also a sharp drop in concentration at short times, during the period of incubation where oxidation proceeded slowly. The interface concentrations of alloys oxidized under

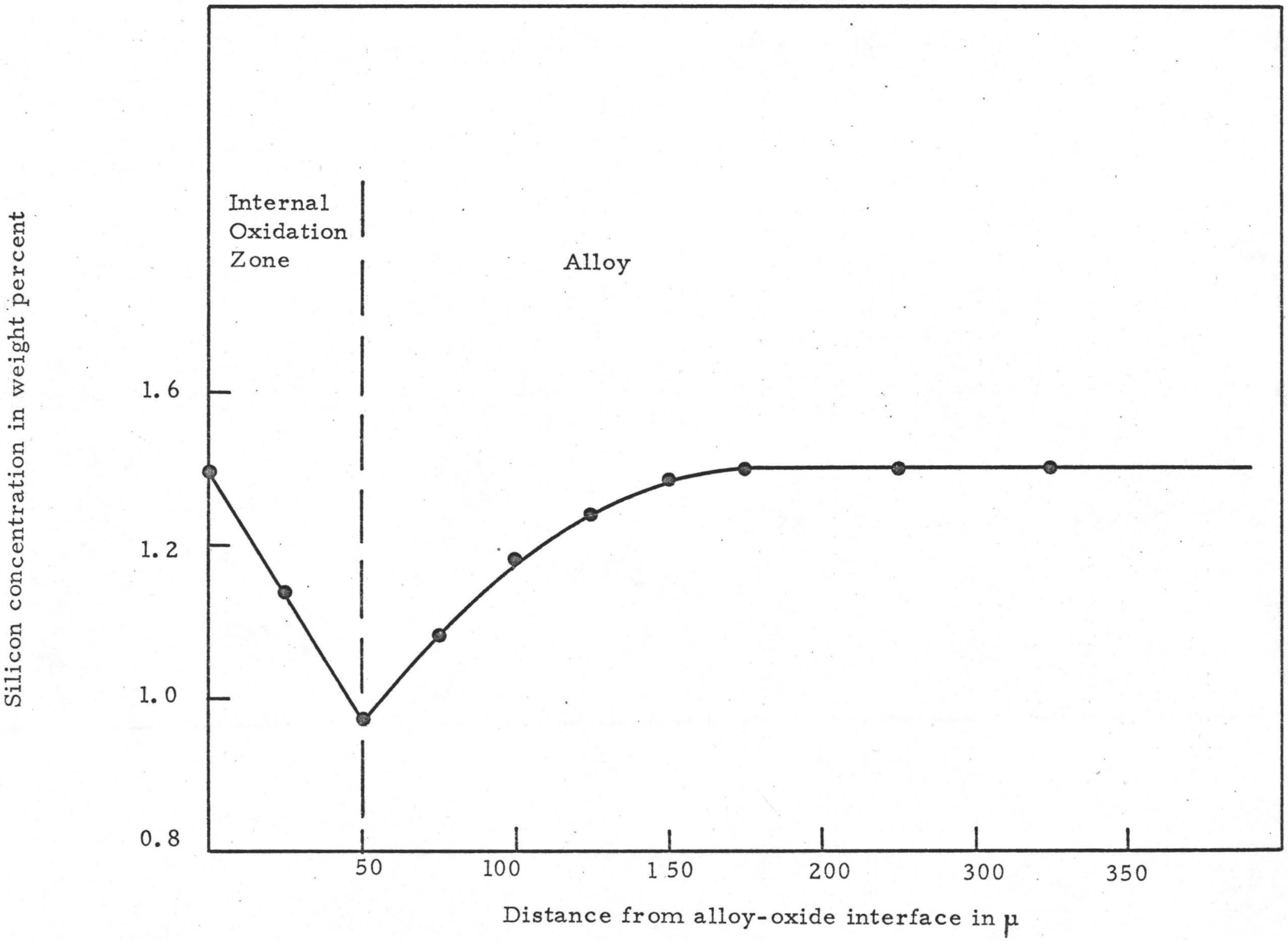

Fig. VI-40: Silicon concentration profile across the alloy and internal oxidation zone at 1000°C.

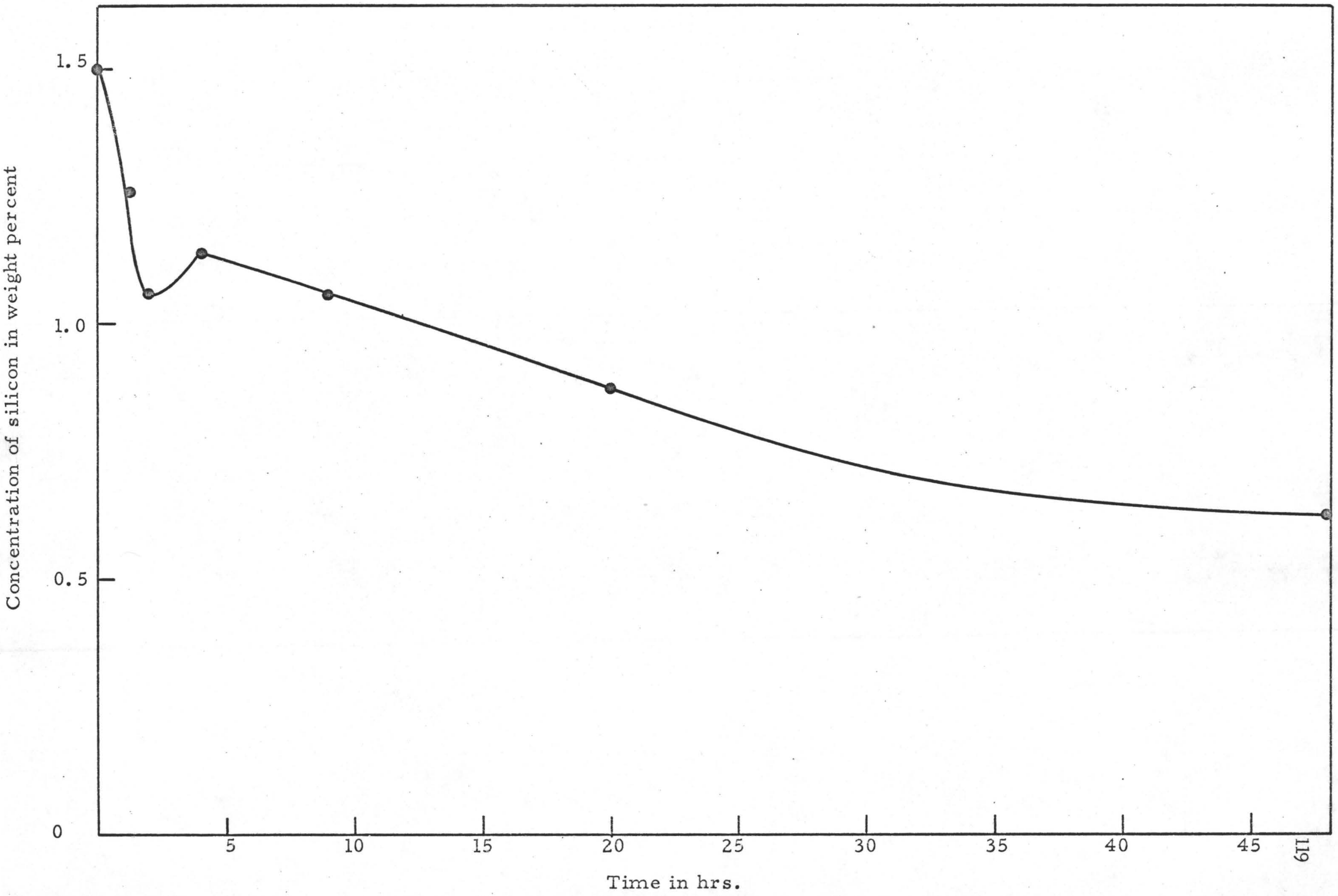

Fig. VI-41: Silicon concentration at alloy-internal oxidation zone interface versus time.

different oxidizing potentials were also obtained and a list of all the results are given in Table VI - 5. Irrespective of the oxidizing potential in these atmospheres the silicon content in the alloy tends to approach a value in the range 0.6-0.7% after long oxidation times.

The concentration profiles across oxide scales and adjoining alloy are illustrated in the electron microprobe scans in Figs. VI - 42 to 47. An optical micrograph of the corresponding sample is also shown as an inset in the figure. The concentration profiles consist of three regions, (i) the alloy and internal oxidation zone discussed in detail in the preceding paragraph, (ii) the wustite-fayalite conglomerate layer where the silicon and iron concentration are not constant across the layer, (iii) the external wustite layer which has a very low silicon concentration and an essentially constant iron concentration.

The wustite-fayalite conglomerate layer has certain features of interest. The maxima in iron concentration in this layer are the same in most cases as the iron concentration in the external wustite layer. This suggests that wustite was the major constituent of the conglomerate layer. The minima in the iron concentration correspond to a phase consisting of about 70 wt.% wustite. This is the theoretical wustite content of the fayalite phase. Silicon concentration in the regions of minimas of iron concentration confirm the fact that these regions are of high fayalite content. The observed silicon concentration in these regions are lower than the silicon concentration of 13.8 wt.% in pure fayalite in most cases. The external wustite layer suggests a small amount of dissolved silicon in the range of 0.01 - 0.02 wt.% at the wustite-conglomerate interface and decreases across the wustite layer.

The electron microprobe scans across specimens oxidized at 890°C are different from specimens at 1000°C described above

TABLE VI-5

Concentrations of Silicon at the Alloy-Internal Oxidation Zone Interface in the Various Oxidizing Conditions at 1000°C

Gas Composition	Time of Oxidation in hrs.	Silicon Concentration in wt. %
50/50 CO_2-CO	1	1.26
"	2	1.06
"	4	1.14
"	8	1.06
"	25	0.87
"	48	0.63
50% argon, 80/20 CO_2-CO	9	0.75
30% argon, 43/57 CO_2-CO	50	0.70
30% argon, 71/29 CO_2-CO	27.3	1.14
90/10 CO_2-CO	18.5	0.81
70/30 CO_2-CO	25.3	0.64
60/40 CO_2-CO	24.0	1.30

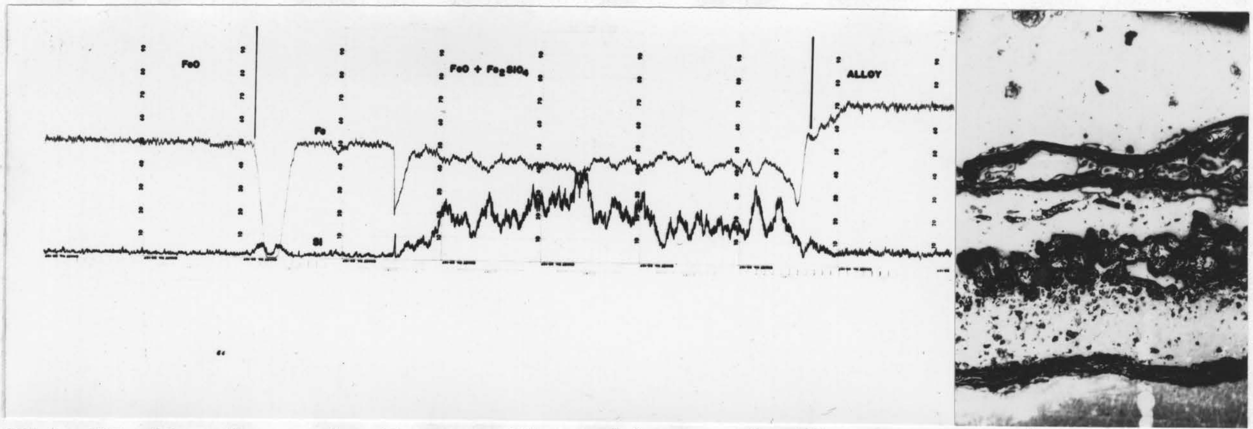

Fig. VI-42: Concentration profiles of iron and silicon across the scale and alloy after oxidation at 1000 °C for 8 hrs. in CO_2-CO atmosphere containing 80 $^v/o$ CO_2, $P_{CO_2} + P_{CO} = 0.5$ atm.

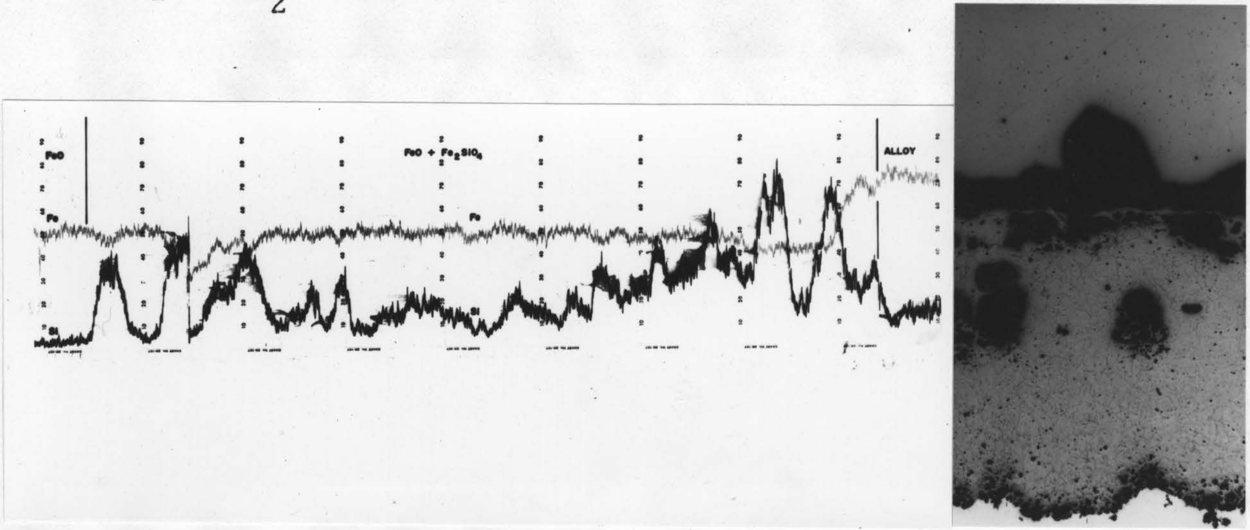

Fig. VI-43: Concentration profiles of iron and silicon across the scale and alloy after oxidation at 1000 °C for 48 hrs. in CO_2 - CO atmosphere containing 50 $^v/o$ CO_2, and $P_{CO2} + P_{CO} = 1$ atm.

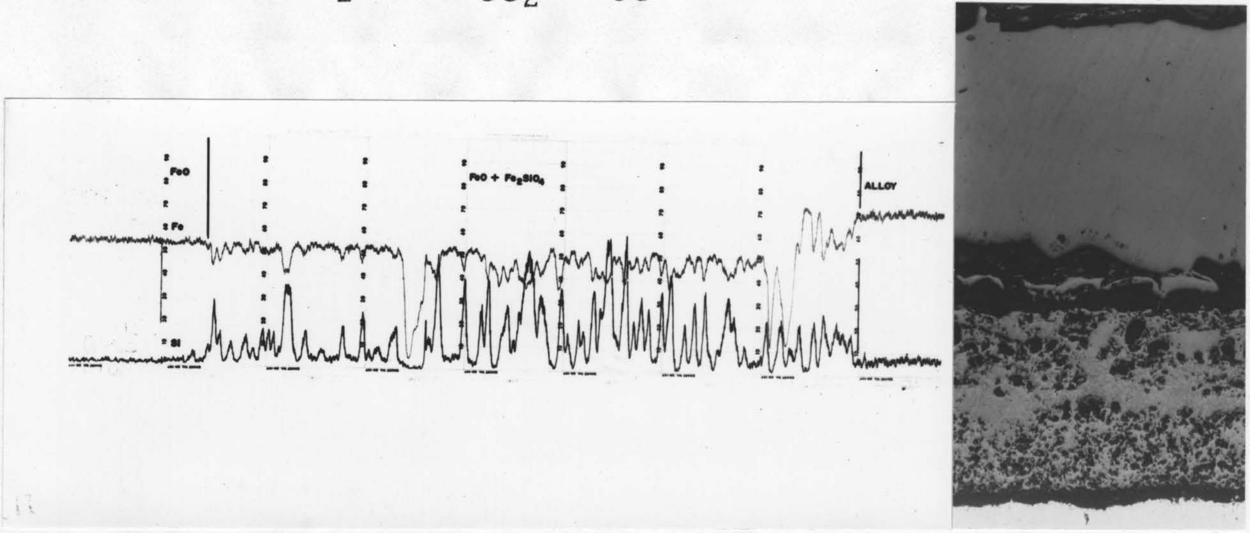

Fig. VI-44: Concentration profiles of iron and silicon across the scale and alloy after oxidation at 1000°C for 27 hrs. in CO_2-CO atmosphere containing 71 $^v/o$ CO_2 and $P_{CO_2} + P_{CO} = 0.7$ atm.

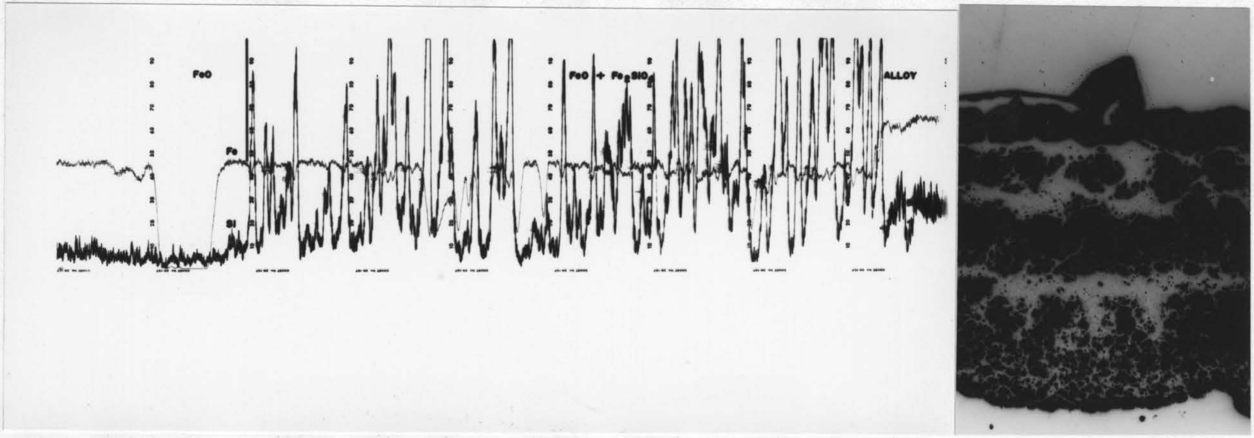

Fig. VI-45: Concentration profiles of iron and silicon across the scale and alloy after oxidation at 1000°C for 49 hrs. in CO_2-CO atmosphere containing 57 $^v/_o$ CO_2 and $P_{CO_2} + P_{CO} = 0.7$ atm.

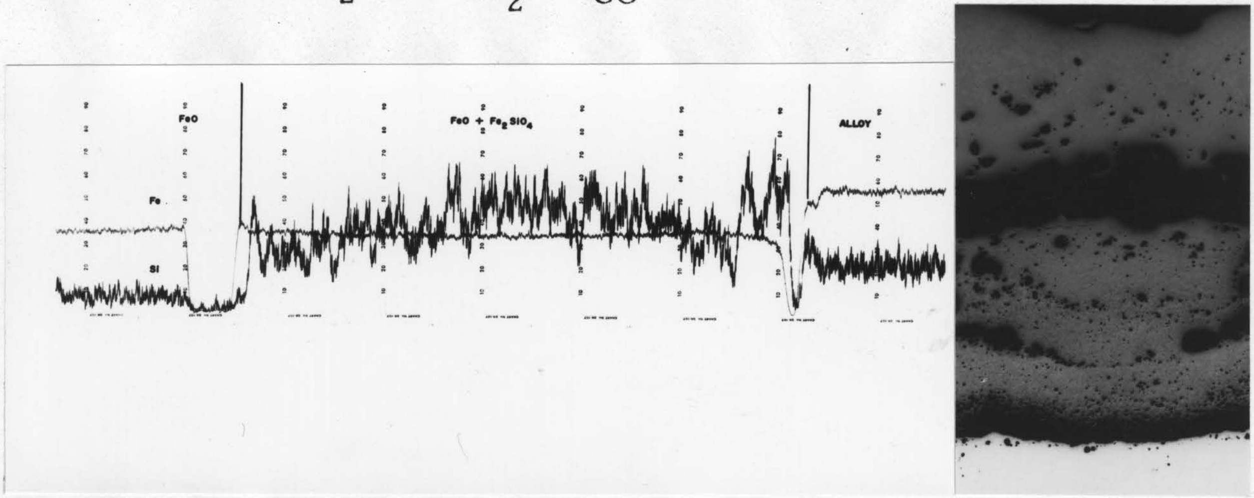

Fig. VI-46: Concentration profiles of iron and silicon across the scale and alloy after oxidation at 890°C for 21 hr. in CO_2 atmosphere.

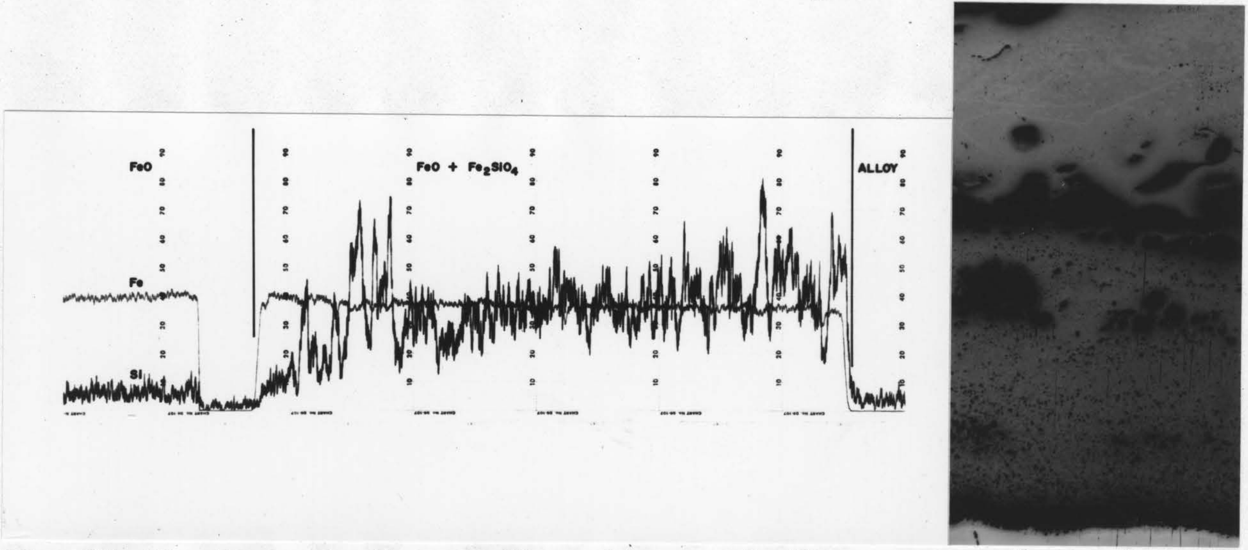

Fig. VI-47: Concentration profiles of iron and silicon across the scale and alloy after oxidation at 890°C for 40 hrs. in CO_2-CO atmosphere containing 70 $^v/_o$ CO_2.

in two features. The fluctuations of the iron concentration in the conglomerate phase are over smaller distances. The silicon concentration behaves in the same manner as at 1000°C. These features are illustrated in Fig. VI - 46 and 47. The silicon concentration in the alloy phase does not show the magnitude of decrease in silicon concentration observed at 1000°C at the alloy-internal oxide zone interface.

The results above will be discussed in greater detail with respect to the various phases present and their effect on reaction behaviour in the next chapter.

CHAPTER VII

DISCUSSION

7.1 Introduction

The use of carbon dioxide-carbon monoxide atmospheres facilitated the adjustment of oxygen potentials to values below the dissociation pressures of magnetite and hematite. This led to the formation of a superficial scale composed of inner and outer layers of a wustite-fayalite conglomerate and wustite upon exposure to the reaction atmosphere at 890° and 1000°C. As mentioned in Chapter VI, the reaction may be said to occur in three stages, namely, an initial stage of continuously increasing or decreasing reaction rate followed by a second stage of oscillating reaction rate and a final stage where the reaction rate is constant. That is, linear kinetics were observed at long exposures.

The oxidation mechanism of iron-silicon alloys in carbon dioxide-carbon monoxide atmospheres is complicated by a number of processes which occur at the reaction temperature. During the initial stage of the reaction, both silicon and iron oxidize simultaneously resulting in formation of an amorphous silica film and isolated growths containing wustite classified as nodules. The wustite nodules grow laterally and vertically, whilst the silica film thickens with time. Fayalite formed rapidly at the edges of the wustite nodules. The alloy also oxidized internally. Since the diffusivity of oxygen in wustite is negligible, the oxygen supply originated from the dissociation of wustite at the alloy-oxide interface. During the linear stage of the reaction, a superficial scale composed of two layers, the inner conglomerate and the outer wustite existed on the alloy. A steady state in the reaction was then reached and the wustite scale thickened by the diffusion of iron ions through the layers to the oxide-gas interface where reaction with the adsorbed oxygen took place. Since the total uptake of oxygen during this stage is directly proportional to time, a chemisorption reaction is rate controlling. Justification will be presented for this viewpoint.

Furthermore, bands of fayalite are observed in the wustite-fayalite conglomerate zone. They seem to have formed during the period of oscillating reaction rate. Consequently the linear reaction rates, the initial reaction rates and oscillatory reaction rate phenomena will be discussed in separate sections in terms of the theory previously presented and other relevant data.

7.2 Linear Oxidation Kinetics

7.2.1 General Discussion

It is apparent from the kinetic results that linear reaction behaviour does not occur from commencement of the reaction. This fact is more readily apparent when the reaction rate curves are used as the criterion for deciding the region of linear behaviour. In most cases, linear behaviour occurred after a weight gain of approximately 20-40 mg/cm^2. These characteristics have been observed previously for the oxidation kinetics of iron, iron-nickel and iron-titanium alloys in carbon dioxide (46, 50, 127).

When deviations occur following linear kinetics, the reaction proceeds at a decreasing rate, Fig. VI-1. Relatively thick scales are observed at high partial pressures of carbon dioxide in these atmospheres. For these cases, the diffusion of iron ions through wustite scales may become the rate controlling step. Smeltzer (44, 50) and Pettit and Wagner (43) have demonstrated that a transition from linear to parabolic kinetics for iron is associated with the transition from a chemisorption reaction control to diffusion reaction control. Two additional factors may account for the transition from linear to parabolic oxidation kinetics for the Fe-Si alloy. Firstly, the diffusion of iron through the conglomerate zone and fayalite layers may become a rate controlling reaction step. Secondly, the inward diffusion of oxygen in the conglomerate may play a rate determining role because the marker measurements, Fig. VII-9, have shown that oxygen migration in the scale may occur. Since the diffusion of oxygen in wustite and fayalite is very small, the oxygen diffusion has to occur along grain boundaries of the two phases or microscopic pores in the conglomerate zone.

It should be mentioned that linear kinetics would be observed if steady state diffusion were to take place through a resistance layer of constant thickness, either in the solid or gas phase, when this reaction step becomes sufficiently slow to be rate controlling. A solid phase layer of constant thickness is not observed in either the external scale or the conglomerate zone, Fig. VI-38. Hence the diffusion of the oxidizing gas through a boundary layer film adjacent to the oxide surface is another possibility for rate control. Assuming the rate of transport of carbon dioxide across a boundary layer film was rate controlling, the calculated rate of oxidation of the alloy in carbon dioxide would be approximately 28 times greater than the observed rate at 1000°C. Details of the calculation are given in Appendix IV.

The possibility of gaseous diffusion determining the reaction rate may also be checked by determining the activation energy for oxidation. Since the oxidation tests were only made at two temperatures 1000°C and 890°C, only an approximate value for the activation energy could be calculated. An activation energy of approximately 25-40 kcal/mole for the overall oxidation process was determined, compared to an activation energy of 1-5 kcal/mole as would be expected for a gaseous diffusion process$^{(121)}$. Gaseous diffusion, therefore, does not act as a rate determining step in the oxidation mechanism.

7.2.2 Oxidation Rate as a Function of Gas Composition

The linear rates may now be discussed in terms of the model presented in Chapter IV. Equation 4-13 was derived on the basis that a chemisorption reaction determined the reaction rate, the surface processes being the dissociation of carbon dioxide and the incorporation of adsorbed oxygen into the wustite lattice. Two limiting approximations to equation 4-13 were also obtained; these are equations 4-15 and 4-18. Equation 4-15 would be expected to be valid at high partial pressures of carbon dioxide where its dissociation rate would determine the reaction rate, whilst 4-18 is valid at low pressures of carbon dioxide where the reaction rate is determined in a complex manner by dissociation of carbon dioxide, incorporation of oxygen into wustite and desorption of adsorbed oxygen. Accordingly, the regions in which equations 4-18 and 4-15 are most applicable as limiting approximations shall be designated region I and region II respectively. Therefore the proposed mechanism can be verified, if plots of K_L versus $\frac{P_{CO_2}}{P_{CO}}$ satisfy equation 4-18 in region I and plots of K_L versus N'_{CO_2} satisfy equation 4-15 in region II. The reaction rates plotted as above are shown in Figs. VII-1 to 4 for the two reaction temperatures, 890°C and 1000°C. It was found that the linear reaction rate constants agreed with the predicted relationships.

The plots of K_L versus P_{CO_2}/P_{CO} in Figs. VII-1 and 2 for the results at 890° and 1000°C illustrate that region I based upon

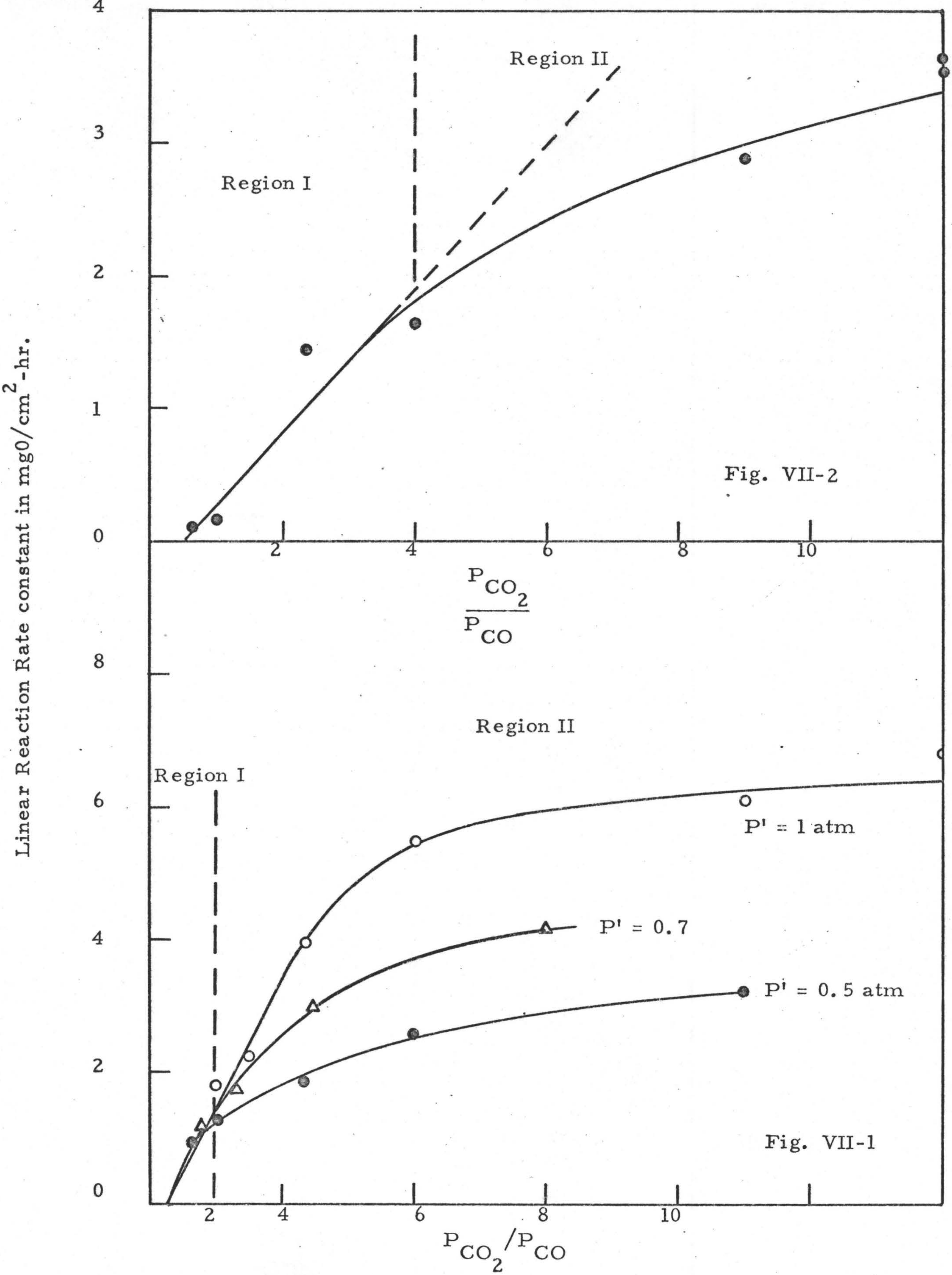

Fig. VII-1 and 2: The dependence of the linear oxidation rate constants at 1000°C and 890°C on the $\frac{P_{CO_2}}{P_{CO}}$ of the CO_2-CO atmospheres.

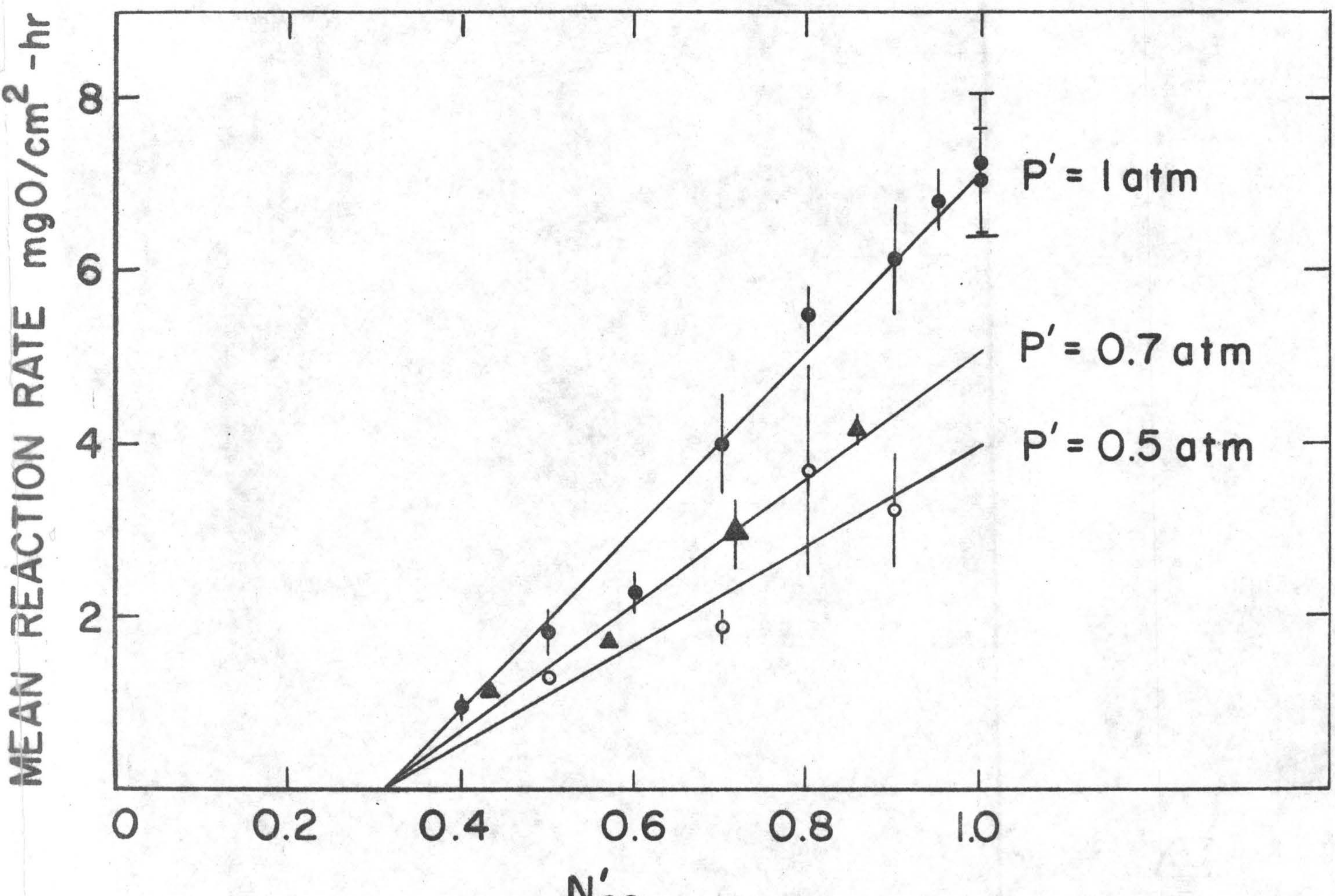

Fig. VII-3: The dependence of the linear oxidation rate constants determined at 1000°C on the mole-fractions of CO_2 in CO_2-CO atmospheres and those atmospheres containing argon at a total pressure of 1 atm. $P_{CO_2} + P_{CO} = P'$; $N'_{CO_2} = P_{CO_2}/P_{CO_2} + P_{CO}$.

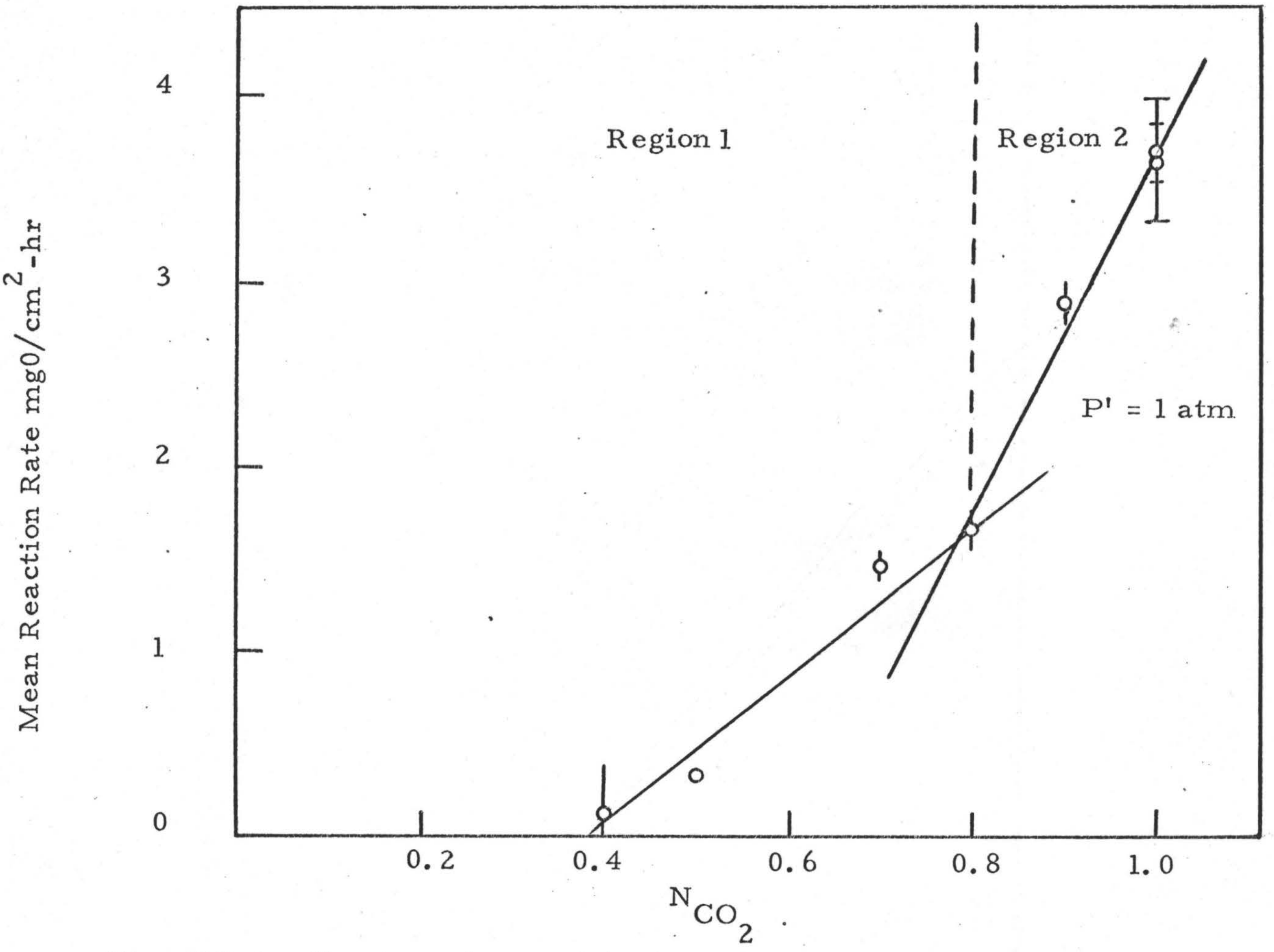

Fig. VII-4: The dependence of the linear oxidation rate constants determined at 890°C on the mole fractions of CO_2 in CO_2-CO atmospheres.

mixed reaction control is only applicable over a small range at low partial pressure of carbon dioxide. At 1000°C, region I was found to exist only over the small range, $N'_{CO_2} = 0.28$ to 0.50. It was also observed that in region I, the rate constants obeyed equation 4-18 and were independent of P' as expected. On the other hand, region I is more clearly defined at 890°C, (Fig. VII-2), and extended to a pressure ratio $P_{CO_2}/P_{CO} = 4$ or an equivalent carbon dioxide mole fraction range $N'_{CO_2} = 0.35$ to 0.70.

On the basis of equation 4-15, the additions of argon should have a strong effect in region II. This is apparent on checking the plots, (Figs. VII-3) for oxidation results at 1000°C. The data may also be plotted according to equation 4-16, where $k_L = \frac{K_L}{P'}$ is plotted versus N'_{CO_2}. A direct proportionality should be obtained for results in region II. A plot of the results at 1000°C in this form are shown in Fig. VII-5 and good agreement is obtained with the predictions. Accordingly argon acted only as a diluent in the reaction gas in region II and did not interfere in the surface reaction mechanism.

It is therefore apparent that the linear rate constants should be analysed using the complete equation 4-13, since the demarcation between regions I and II is not clearly defined. The data could not be graphically plotted to obtain all of the unknown kinetic and thermodynamic parameters, k_1, k_2, k'_1, $N'_{CO_2}{}^*$, $\oplus^{*2}$, θ_v, K. Accordingly equation 4-13 was transformed to 7-1, a form amenable to evaluation of certain combinations of the parameters, viz.,

$$K_L = \frac{k\, k_2 P' (N'_{CO_2} - N'_{CO_2}{}^*)}{k_2 + \epsilon P'(1 - N'_{CO_2})} \qquad 7\text{-}1$$

where $k = k_1\, \theta_v\, (1+K)$, $\epsilon = k'_1\, \oplus^{*2}$

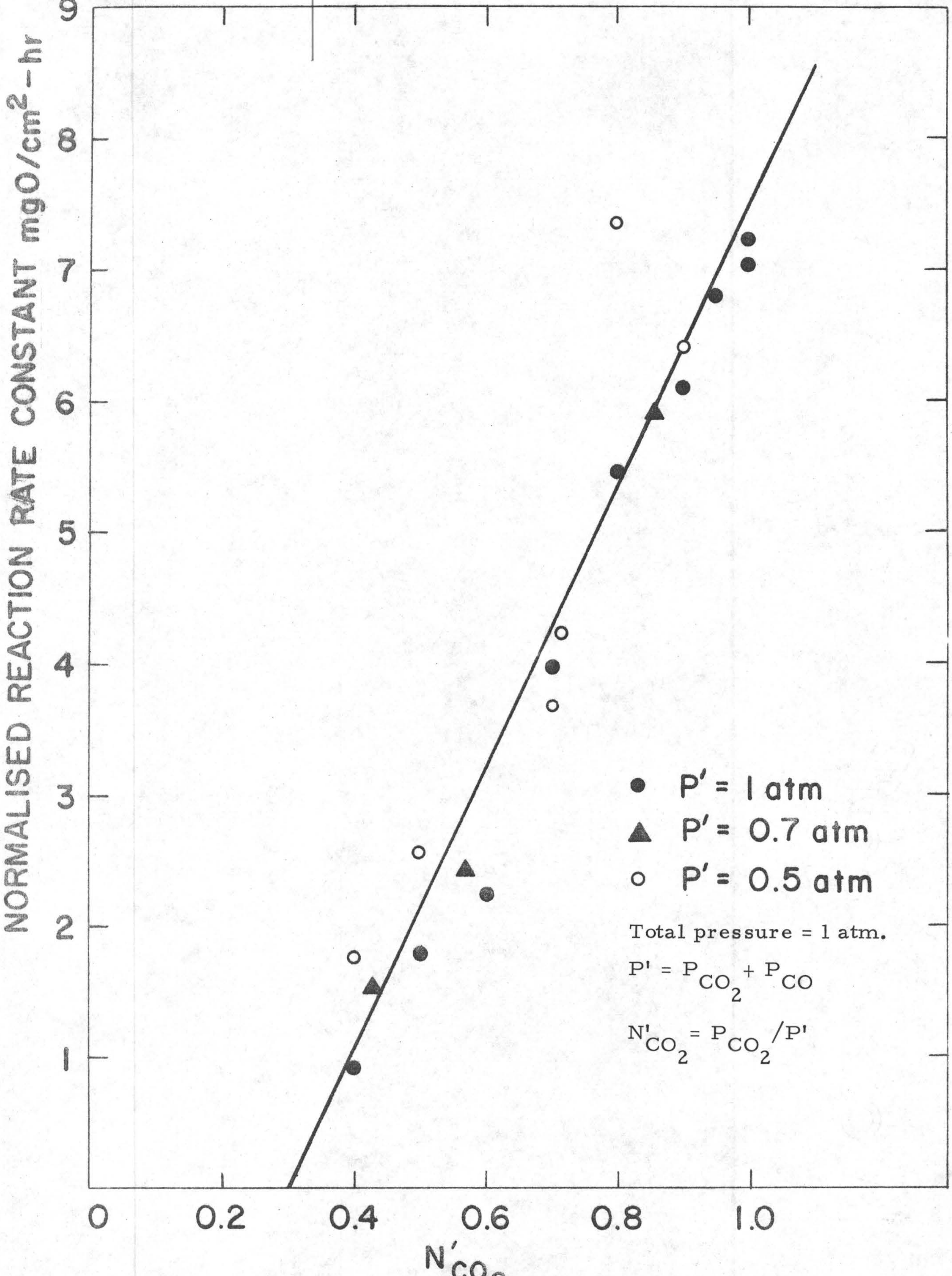

Fig. VII-5: The dependence of the normalized linear oxidation rate constant, k_L, determined at 1000°C on the mole fractions of CO_2 in CO_2-CO atmospheres and these atmospheres containing argon.

The data were fitted to equation 7-1 by a computer using a non-linear least squares program. The values of the parameters k_2, k, ϵ, $N'_{CO_2}*$ which minimized σ (the root mean square deviation of the experimental points from the calculated curve) and the value of σ itself were determined. The results of such a fit are shown in Figs. VII-6 and 7 for the two reaction temperatures. The solid line represents the calculated curve and the points are the experimental data. The values of the kinetic parameters are listed in Table VII-1.

The value of $N'_{CO_2}*$, the mole fraction of carbon dioxide in the gas atmosphere for equilibrium of the gas phase with wustite, appears in equation 4-13 and 4-15. For wustite scales formed on iron, the equilibrium value is given by the dissociation pressure of wustite in equilibrium with iron. Since it has been argued that there is only a small iron gradient across wustite, when oxidation is determined by the slow chemisorption step, the electron microprobe scans across the wustite phase on the alloy would be expected to be too insensitive to show any small iron gradient. Silicon solubility in wustite is also very small and probably would not be detected by this technique. These conclusions are shown to be valid by the microprobe scans shown in Figs. VI-42 to 47. No iron gradient was detectable across the wustite layer and the solubility of silicon in wustite observed was indeed small and below the detectable limit of silicon in wustite (0.02% Si). The observed values of $N'_{CO_2}*$ are 0.289 and 0.380 at 1000° and 890°C, respectively, which are to be compared to the values for iron/wustite equilibria at both temperatures of 0.286 and 0.350.(50) These correlations further corroborate the above conclusions. This is to be expected since the defect concentration of undoped wustite is quite large about 4 to 11% at these temperatures(111)

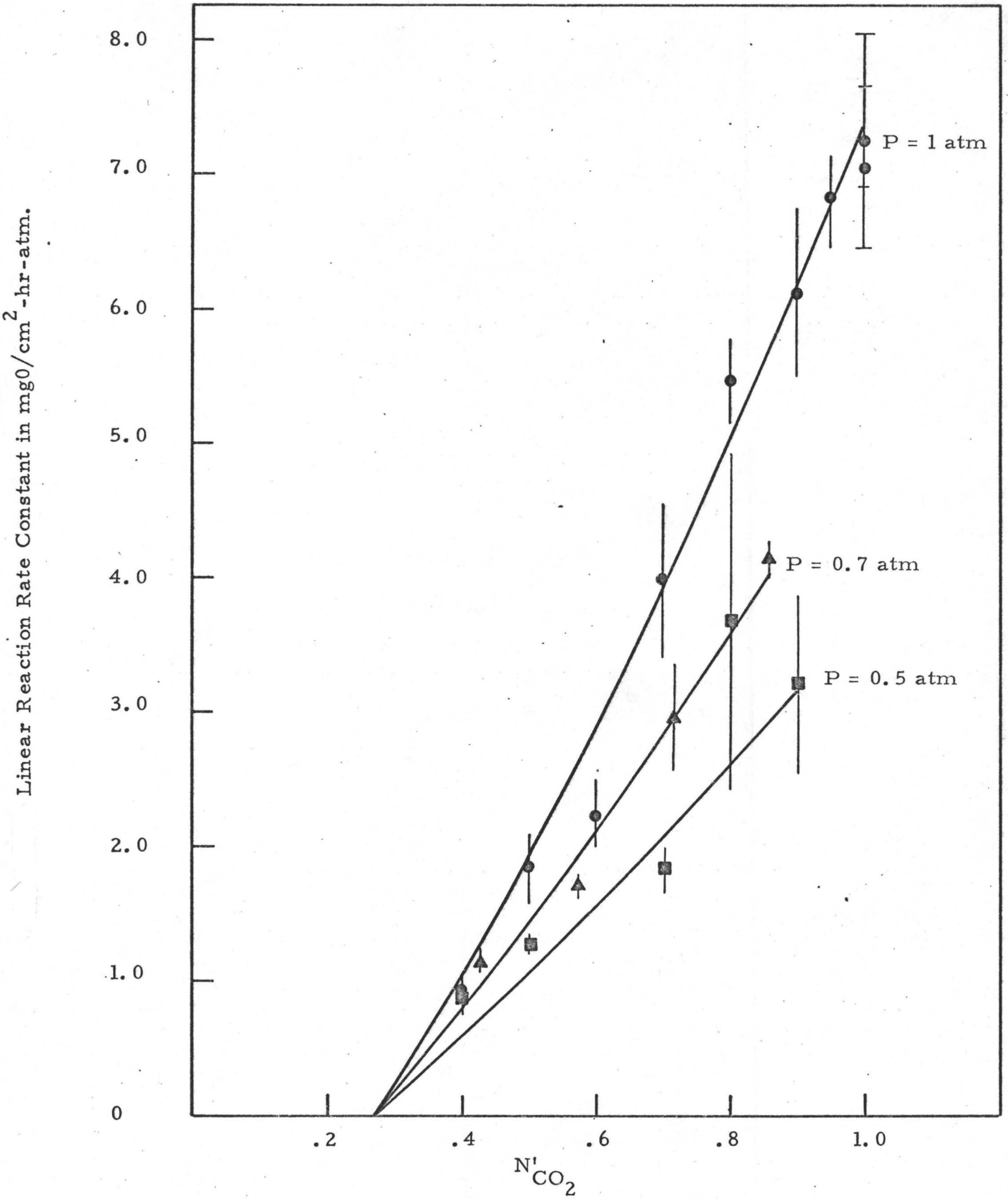

Fig. VII-6: Linear reaction rates at 1000°C versus the mole fraction of CO_2 in CO_2-CO atmospheres and these atmospheres containing argon.

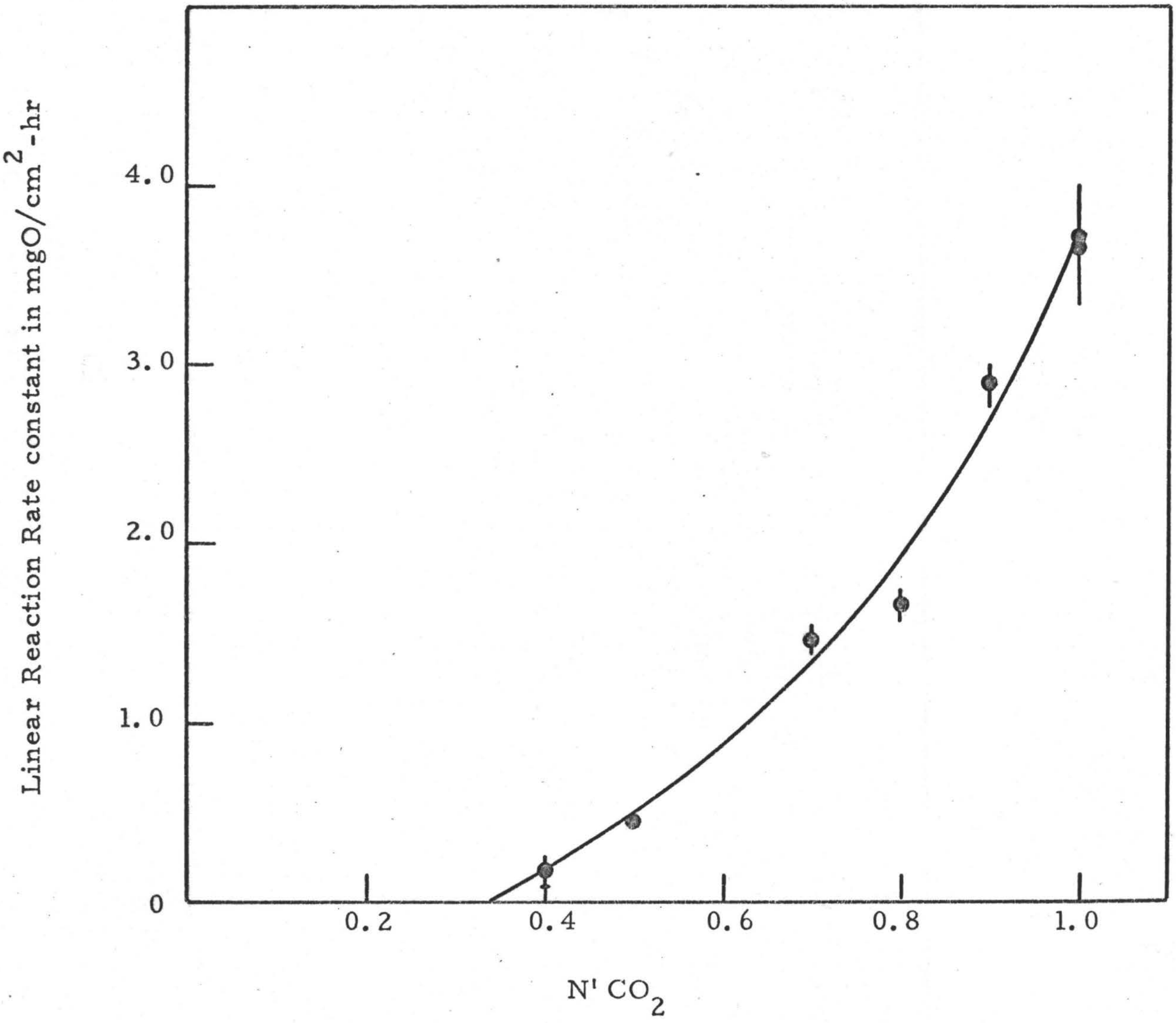

Fig. VII-7: Linear Reaction Rates at 890°C versus mole fraction of CO_2 in CO_2-CO atmospheres at a total pressure of 1 atm.

TABLE VII-1

Kinetic Parameters Obtained by Computer Fit of Data to eqn. 7-1

Temperature °C	k	k_2	$k_1' \oplus^{*2}$	$N'^{*}_{CO_2}$	σ
1000°	10.75	0.323	0.144	0.289	0.23
890	5.89	0.092	0.108	0.380	0.14

TABLE VII-2 (see reference on p. 157)

Initial Rate Kinetic Parameters Obtained by Computer Fit of Data at 1000°C to eqn. 4-43

Oxide Phase	k	k_2	$k_1' \oplus^{*2}$	$N'^{*}_{CO_2}$	σ
Wustite	11.48	0.723	1.71	0.380	0.81
Silica	7.15	0.954	1.87	0.353	0.47

Although the oxidation properties of the alloy were only investigated at two reaction temperatures, we can nonetheless show that parameters evaluated and listed in Table VII-1, are consistent with thermally activated processes by obtaining estimates of the activation energies of the various processes from the parameters using an Arrhenius analysis. The activation energy for the incorporation step was evaluated as 34 kcal/mole, which is in good agreement with previous results for iron oxidation(50). From the values of $N'_{CO_2}{}^*$, the activation energy for the formation of wustite from alloy was estimated to be 7 kcal/mole which is in order of magnitude agreement with the value of 4.4 kcal/mole for pure iron. Similarly from the value of $k_1' \oplus^{*2}$, the activation energy $\Delta H_v - \Delta H_{des} - \Delta H_{0_2}$, for the various combined intermediate steps of vacancy formation in wustite, desorption of oxygen by combination with carbon monoxide and enthalpy of oxygen in wustite can be evaluated. The combined activation energy of $\Delta H_v - \Delta H_{des} - \Delta H_{0_2} =$ 14 kcal/mole was obtained. Also $\Delta H_v = 34$ kcal/mole, since the vacancy formation at the wustite surface is the opposite of the incorporation step. Therefore $\Delta H_{des} + \Delta H_{0_2} = 48$ kcal/mole. Also ΔH_{0_2} is usually small and of the order of a few kcal/mole, hence $\Delta H_{des} = 40\text{-}45$ kcal per mole. This latter value is consistent with a value of 35-70 kcal/mole for the enthalpy of desorption of carbon monoxide from oxide substrates like Ni0, Co0 and $Cu_2 0$.(138)

The oxidation tests in which argon was added to the reaction gas confirmed the metallographic observation that the external wustite layer was compact, Fig. VII-8. Argon only acted as a diluent in the reaction gas and no effect that could be attributed to gas diffusion in pores was observed. Marker measurements carried out to determine the relative roles of iron and oxygen migration in the scale, Fig. VII-9, showed that wustite grew with the outward migration of iron whereas the growth of the conglomerate layer was

Fig. VII-8: Cross-section of scale formed at 1000°C in CO_2-CO atmosphere containing 70 $^v/o$ CO_2 in 25 hrs. X80

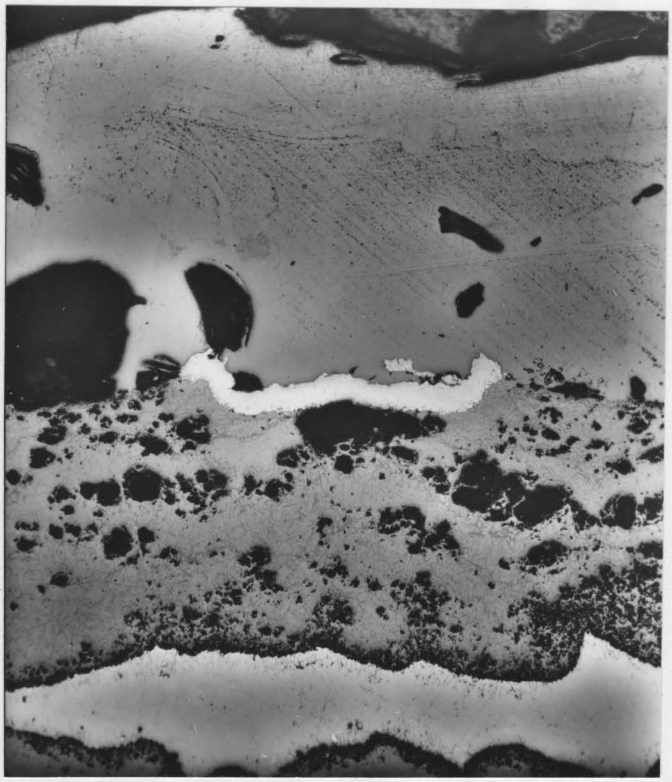

Fig. VII-9: Platinum markers in scale on alloy exposed for 41 hrs. at 1000°C to a CO_2-CO atmosphere; total pressure of 1 atm., N'_{CO_2} = 0.5. X100 associated with inward migration of oxygen. Since oxygen does not diffuse through wustite, the only source of oxygen supply is the decomposition of wustite at the wustite-conglomerate interface. While the oxygen is consumed by the internal reaction, the simultaneously formed iron ion diffuses outward through the wustite layer. For each oxygen atom consumed through internal oxidation, one iron atom is simultaneously removed from the wustite layer at the wustite-conglomerate interface. This may result in cavity formation at the inner boundary of wustite as seen in Fig. VI-9. This cavity formation is counteracted by the volume increase of the metal due to internal oxidation, formation of wustite in the conglomerate zone and possible plastic deformation of the wustite layer.

If physical contact is maintained between wustite and the metal, iron will diffuse outward by a solid state mechanism through the scale. However, the diffusion path is obstructed by porosity and the presence of $Si0_2$ particles in the internally oxidized zone of the alloy. These particles also serve as sites or areas for iron vacancy condensation. As a result cavities or porosity accumulate at the outer surface of $Si0_2$ particles. This porosity is subsequently found around the fayalite particles in the conglomerate layer, particularly the surface facing outwards, (Fig. VI-34). This porosity also reduces the available area for solid state diffusion of iron, but it probably does not severely limit the oxidation rate, as discussed in the literature(56-58, 96, 121, 122). Wustite on the cavity facing the outer surface decomposes, the iron diffuses outward and the oxygen is rapidly transferred across the cavity to the inner surface, where it in turn reacts with iron to form wustite. In this manner, wustite is formed beneath the original wustite layer and original alloy surface.

Concurrently, silica particles become partially surrounded by wustite and partially by pores. The silica and wustite gradually react to form fayalite. In all the samples examined in this study, fayalite rather than silica was present, we assume that this is also the case for the internal oxide in the alloy phase. The conglomerate layer is formed by the combination of internal oxidation and transport of gaseous oxygen across cavities in the inner layer. The outer wustite layer is formed through the outward diffusion of iron in areas where the wustite is in contact with the wustite matrix of the inner conglomerate layer.

It is difficult to estimate the porosity that is formed in the scale at the reaction temperature. Part of the porosity stems from the vacancy condensation described above. Some of the porosity is also related to the alloy composition. Thus, the flux of iron ions that react with oxygen at the outer surface is larger than the iron flux reacting with oxygen at the scale-metal interface. Since the alloy contains a bulk concentration corresponding to 2.95 $^{a}/o$ silicon, 5.9 $^{a}/o$ of the oxygen at this interface is consumed by the silicon to form silica precipitate in the alloy. This implies that about 6 $^{a}/o$ porosity would occur in the oxide conglomerate layer beneath the outermost compact layer of wustite. Other factors affecting porosity such as sintering and plastic deformation, both of which will tend to reduce porosity. This estimate of the porosity is qualitatively in agreement with the observation.

Since migration of oxygen resulted in the formation of the conglomerate layer, an oxygen gradient existed across the conglomerate. To confirm that this gradient was indeed small, the effect was determined at 1000°C of the oxidizing potential in the reaction atmosphere on the rates of the growth of the individual oxide layers. The rates of growth of the external wustite layer and conglomerate layer were found to be linear and parabolic, Fig. VI-38 and 39. Additional indications of parabolic growth of the conglomerate layer is given by the plots in Fig. VII-10, where the distances from the wustite-conglomerate interface to the individual fayalite bands are plotted in parabolic form as a function of time. The effect of the oxidizing potential on the rates of growth are shown in Fig. VII-11. The growth of the external wustite layer was directly dependent on the oxidizing potential. On the other hand, the parabolic conglomerate layer growth rate appeared to be independent of the oxidizing potential.

There are stringent limitations to the steady state approximation for linear reaction kinetics, in assuming that substantial equilibrium exists between wustite, fayalite and alloy. This condition can only exist for a unique alloy composition, which has been reported to be approximately 0.7 $^{w}/_{o}$ Si(106, 107). In the range of 1.5 $^{w}/_{o}$ silicon, an alloy can only exist in equilibrium with fayalite, (Fig. IV-1). Accordingly, the alloy during oxidation must have been depleted of silicon in the vicinity of the metal/oxide interface by formation of fayalite (and perhaps silica) as an internal oxide precipitate. Consequently, a situation arose where the silicon content in the alloy would approximate to an equilibrium concentration as assumed in the formulation of the reaction mechanism. The silicon concentrations at the interface did indeed approach this silicon concentration as is apparent from the measurements listed in Table VI-5. An approximate steady state was only obtained in a few cases at high oxidizing potentials as shown in Fig. VI-6 to 10. However, in the other cases there were regions obeying linear kinetics approximately. The deviations from linearity, were associated with the precipitation of fayalite and possible mechanical

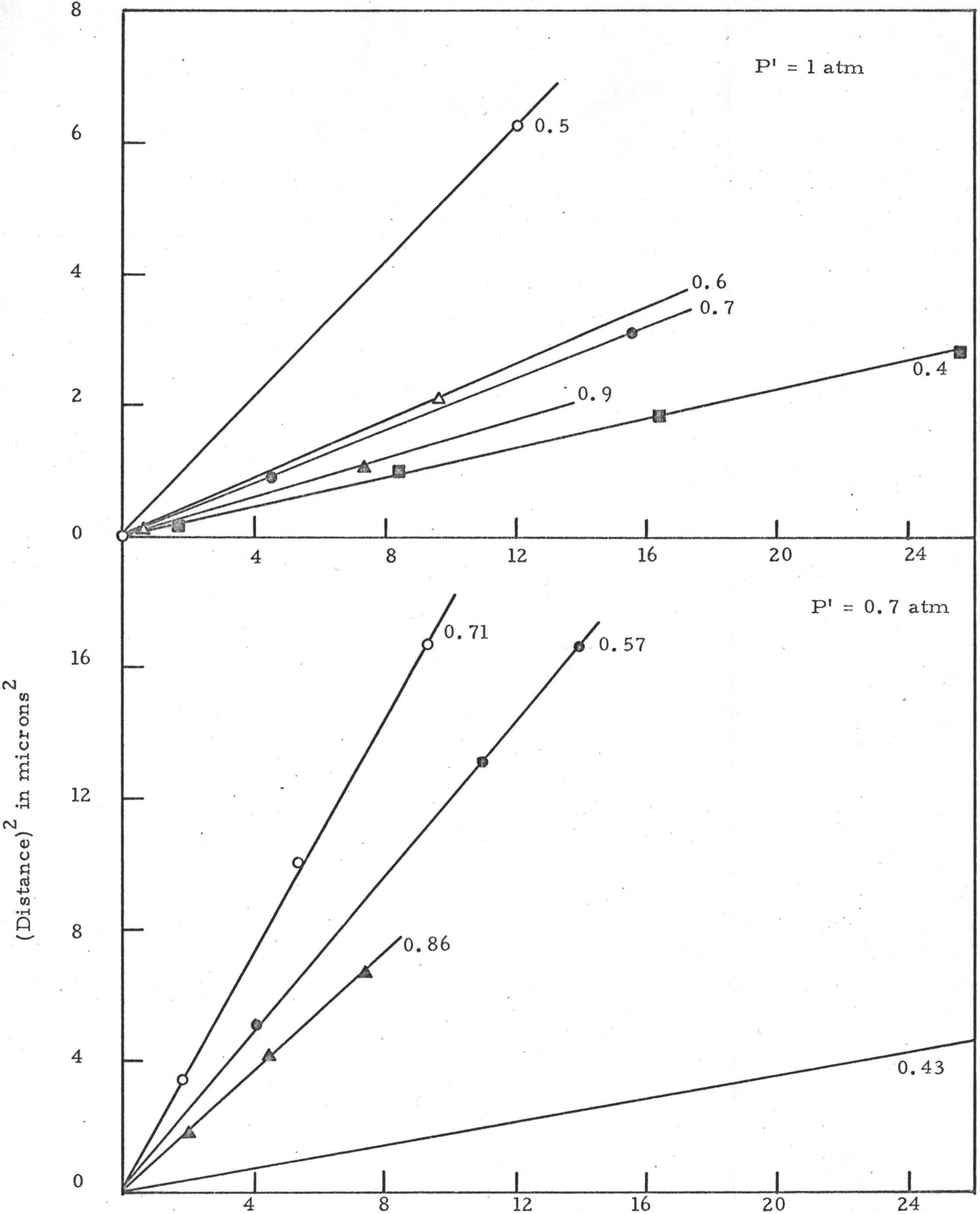

Fig. VII-10(a): Distance versus time plots of the precipitation of massive fayalite bands at 1000°C in CO_2-CO atmospheres.

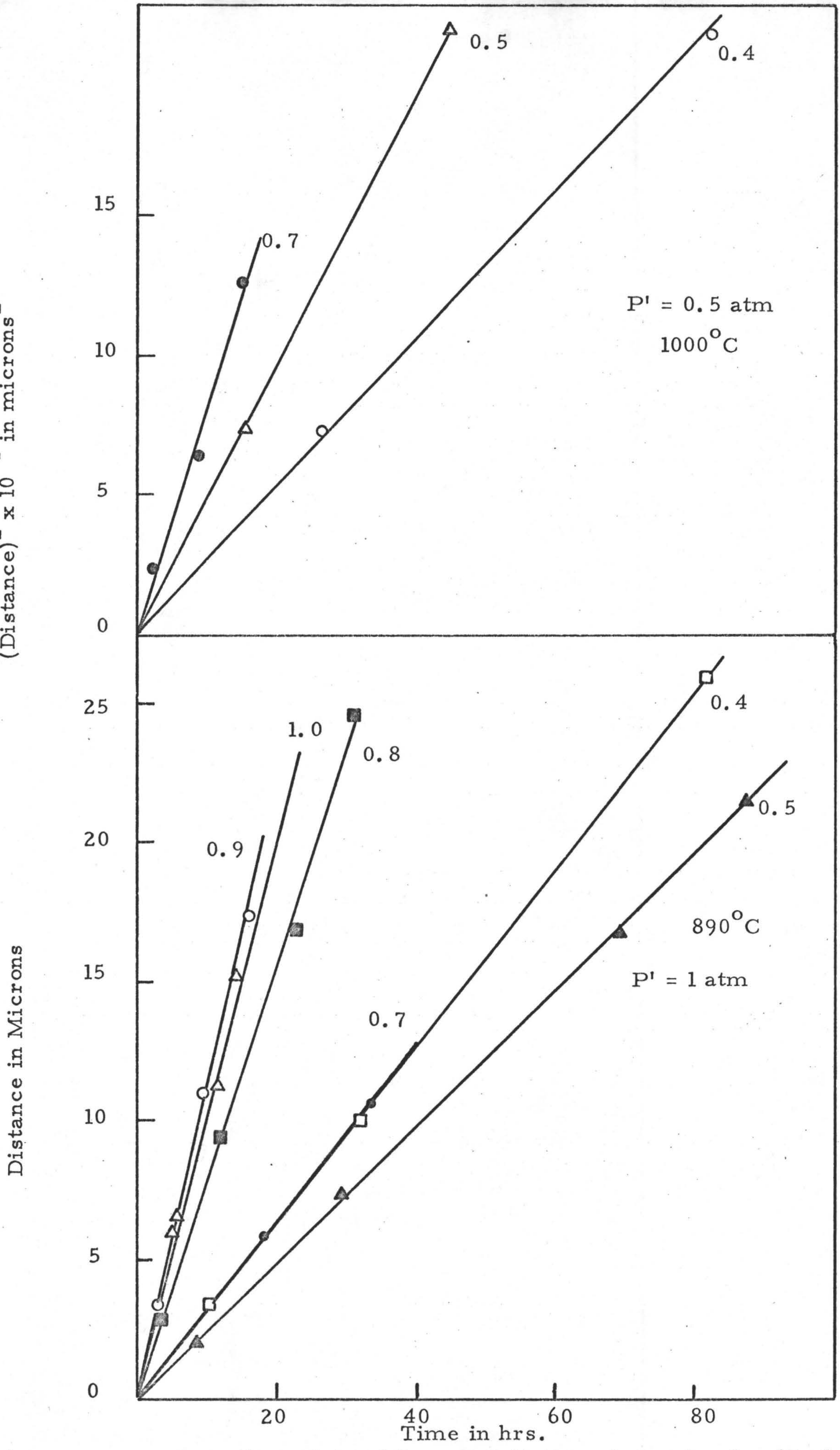

Fig. VII-10(b): Distance versus time plots of the precipitation of massive fayalite bands at 1000 and 890°C in CO_2-CO atmospheres.

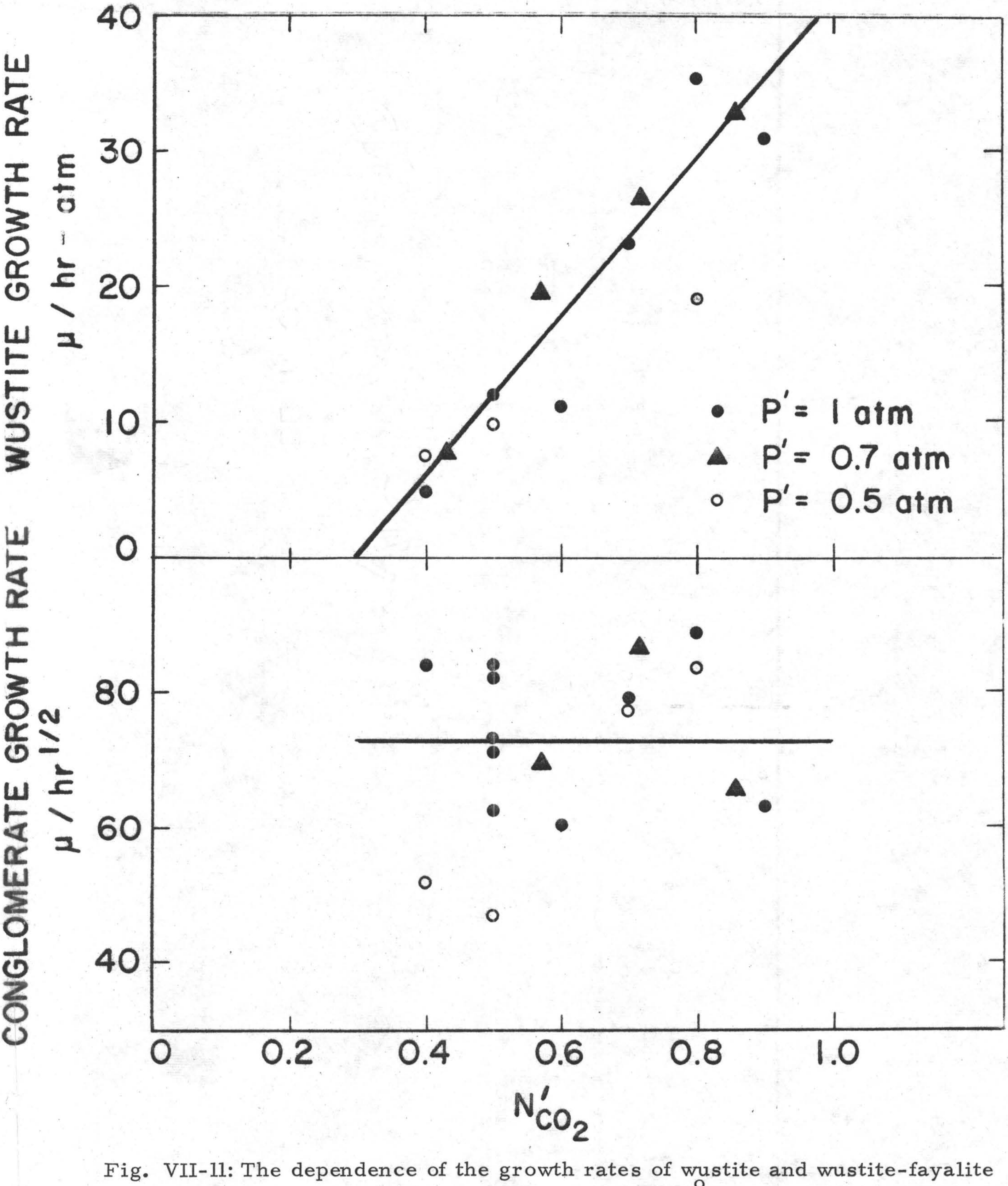

Fig. VII-11: The dependence of the growth rates of wustite and wustite-fayalite conglomerate layers determined at 1000°C on the mole fractions of carbon dioxide, N'_{CO_2}, in carbon dioxide - carbon monoxide atmospheres and these atmospheres containing argon.

breakdown at the conglomerate alloy interface. The fluctuations in reaction rate will be dealt with in more detail in a later section.

7.3 Initial Oxidation Kinetics

7.3.1 General Discussion

The reaction rates are continuously changing during the initial stages of the reaction. They either increased to a maximum rate or decreased to a minimum rate, as illustrated in Fig. VI-6 to 10. The oxide morphology during this stage of the reaction consisted of wustite nodules which grew both laterally and vertically at isolated points on the specimen, whilst the rest of the specimen surface was covered with an amorphous silica film which grew vertically. The amorphous silica film and some oxide nuclei were formed during the argon anneal and room temperature oxidation before the test. This is illustrated by comparing the replicas in Fig. VI-17a and 17b. Also electron micrographs of oxide films formed after the argon anneal revealed the presence of amorphous silica, β-cristobalite and fayalite, (Fig. VI-20 and 21). Since similar ring diffraction patterns as shown in Fig. VI-20 were obtained from oxide films examined after oxidation for longer times, that is, after oxidation in the reaction gas atmosphere, it is probable that amorphous silica continued to grow in the reaction gas. The presence of β-cristobalite in the oxide film, confirms the fact that a silica film did form during the argon anneal process. However, β-cristobalite is normally stable at temperatures greater than 1470°C, whilst the silica phase stable at 1000°C is tridymite. Kingery(123) has observed that in the silica system, at 1100°C, a silica glass could transform into either quartz, tridymite or cristobalite. The actual polymorph formed is dependent on the kinetics of transformation. It was found that the glass when heated for long periods of time at 1100°C transformed to form cristobalite. The explanation for the formation of cristobalite lies in the close similarity between the cristobalite and the amorphous silica structures. On cooling, β-cristobalite usually transforms to α-cristobalite. However, the presence of foreign impurity atoms like Fe, Mg, Al, were found to stabilize the high temperature polymorphs in the silica system, namely, cristobalite and tridymite(120).

That the size of the wustite nodules increases with time is shown quite clearly in electron micrographs and replicas of oxide films in the initial stages, (Fig VI-15 and 17). The wustite nodules are initially angular but tend to hemispherical shape at longer times. The size distribution of the nodules consists essentially of very large nodules which form at grain boundaries and three-fold grain boundary intersections and smaller nodules within the grain. The size of the nodules increases from about 500Å - 2000Å after the argon anneal to a size of 12,000-48,000Å after oxidation in 50/50 carbon dioxide-carbon monoxide atmospheres for 1 hr. Optical microscopy on specimens oxidized for 1/2 to 8 hrs. in the same atmosphere, showed that the wustite nodules grew to a maximum size of 200μ before coalescence between nodules occurred. The smallest nodules observed optically on a specimen oxidized for 1/2 hr. were of the order of the largest nodules observed by electron microscopy on the same specimen. This suggested that the stripped oxides were from areas between the larger nodules, where smaller oxide nuclei are observable, (Fig. VI-12a). Only oxide from these areas was penetrable by electrons during the transmission electron microscopy studies. This limiting thickness would be of the order of 3000Å for wustite and fayalite and possibly 7000Å for silica. The further growth of wustite nodules took place by continuous coalescence of the nodules in both a chain-like mode and an aggregate mode which increased their size as well as increased the length of the chain. The areal coverage of the wustite on the specimen surface was estimated from observations on these specimens and micrographs, (Fig. VI-12 and 13). The results are plotted versus time and illustrated in Fig. VII-12. The observed areal coverage is basically of the type defined by equation 4-20.

The vertical growth rate of wustite was found to be linear during the initial stages. The thickness of the wustite scale as a function of time is plotted in Fig. VI-26a. This linear rate is, however, lower than the corresponding wustite growth rate during the period of linear reaction behaviour at long times.

Reaction between the wustite nodules and the silica film occursat the edges of the nodules and leads to the formation of fayalite as illustrated in Fig. VI-20. The area A is typical of the place where fayalite is formed. Single crystal patterns were only obtained from such areas, since the silica film is usually amorphous and gives ring patterns as shown in the same micrograph. The wustite nodules are usually much thicker than the penetration distance of electrons and hence no electron diffraction identifications of wustite can be obtained. However, X-ray powder diffraction techniques revealed that the nodules were composed of wustite with small amounts of fayalite. During the initial stages, this type of reaction behaviour occurred in most cases and usually from the start of the reaction.

In a few cases, the sigmoidal type oxidation curve was not observed at short times. Instead linear or parabolic kinetics were observed. For example, at a mole fraction of carbon dioxide of 0.4, the kinetics were found to be linear at 1000°C and parabolic at 890°C for periods extending up to 10 hrs. For these cases, it is believed that the kinetics observed were due to the growth of the amorphous silica alone. Apparently the low oxidizing potential of the reaction

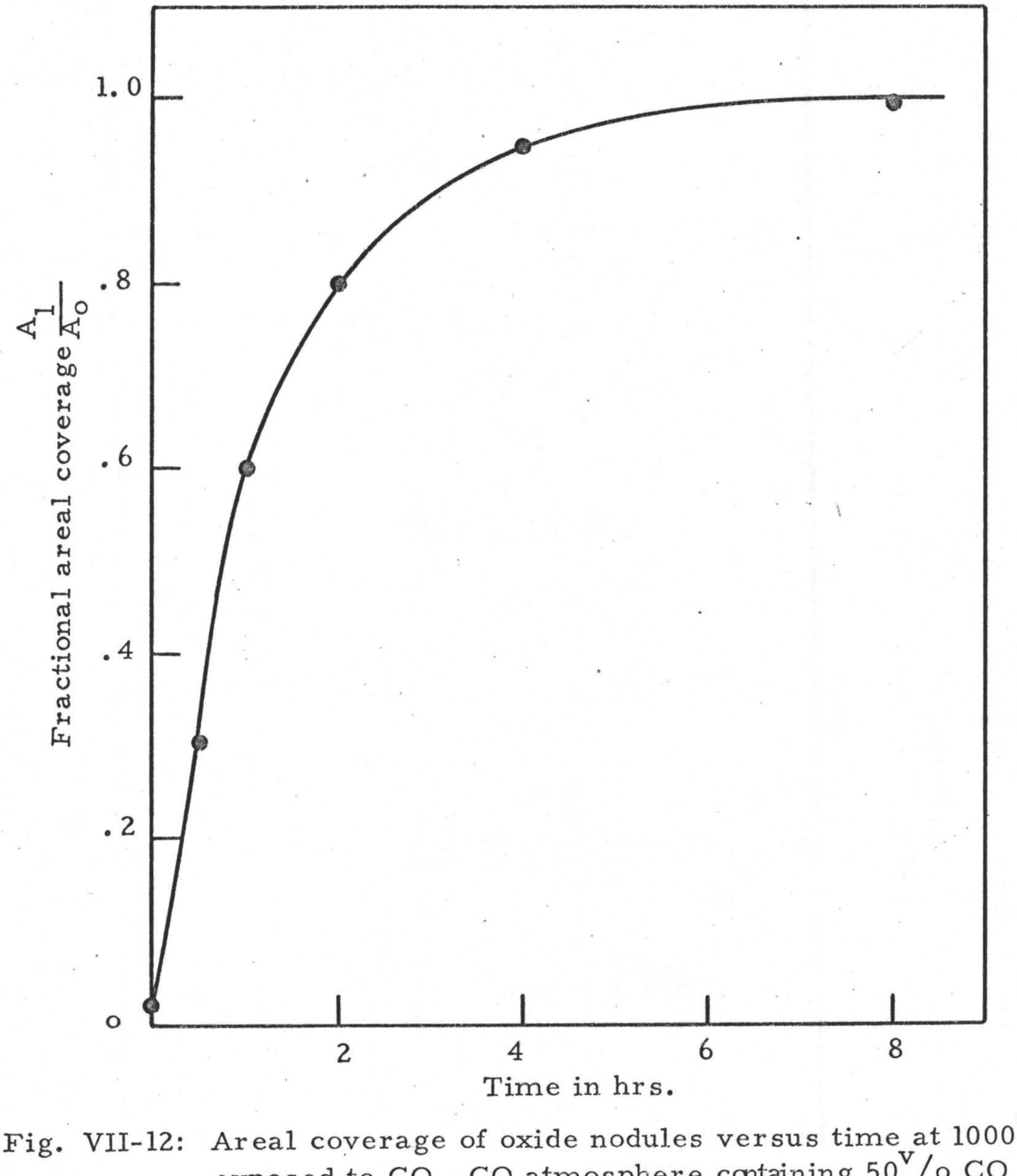

Fig. VII-12: Areal coverage of oxide nodules versus time at 1000°C, exposed to CO_2-CO atmosphere containing $50^v/o$ CO_2.

atmosphere was insufficient for nucleation and growth of wustite during this stage of the reaction.

7.3.2 Oxidation Rates as a Function of Gas Composition

The initial rates may now be discussed in terms of the model presented in Chapter IV. Equation 4-36 was derived on the basis that a chemisorption reaction determined the growth of the wustite nodules and the amorphous silica film. The wustite nodular coverage was represented by equation 4-20. This equation has been previously derived by Evans(3), Avrami(124) and in a slightly different form by Rhead(30). This equation was derived for the cases where the growth of the oxide nuclei or nuclei in solid solution was determined by the rate of supply of one of the reactants used in the growth process. In Rhead's derivation, he assumed that the supply of the metal, oxygen or metal-oxygen complex to the nuclei edge was determined by surface migration of the species. Under these conditions, the areal coverage of the oxide nuclei will increase uniformly with time. It was also shown in Chapter IV that a maximum or minimum rate would be observed in the initial stages of oxidation depending upon whether wustite or silica was the faster growing phase. Equation 4-50 gives the condition for the extrema described above.

Considering equation 4-50,

$$\beta t_e = 2 - \alpha_o \qquad 7\text{-}3$$

where β is the lateral growth parameter of wustite, t_e is the time at which the extrema occur and α_o is the wustite areal coverage after the argon anneal. Experimentally, from replicas of the surface of the specimen after argon anneal, $\alpha_o = 0.013$ at 1000°C.

Therefore $\beta t_e = 1.987$ 7-4

or $$\frac{1}{t_e} = \frac{\beta}{1.987} \qquad 7\text{-}5$$

For the oxidation tests conducted at 1000°C, one finds that there indeed are minima or maxima during the initial stages of the oxidation, Fig. VI-6 to 10. The only maximum or minimum considered is the first one observed in the oxidation test. The later fluctuations in the reaction rate are associated with other phenomena which will be discussed later.

Based on equation 7-5, the values of the lateral growth parameter, β, can be evaluated knowing the times at which extrema occur. The oxidation tests can be subdivided into two categories based on whether a maximum or minimum rate is observed during this period of oxidation. The lateral growth parameters of these two modes are quite different as shown in Figs. VII-13 and 14. Plots of β versus N'_{CO_2} in both cases show a close linearity between β and N'_{CO_2}.

The expression 4-36 derived for the reaction rate during this period of reaction may now be utilized in a modified form, to evaluate the vertical growth rate constant k_F and k_S of the wustite nodules and silica film respectively. Equation 4-36 may be re-written as,

$$S = k_F + (k_S - k_F)\,\emptyset \qquad 7\text{-}6$$

where $\emptyset = (1-\alpha_o)\,(1-\beta t-\beta t_o)\,e^{-\beta t}$ 7-7

i.e. $\frac{S}{\emptyset} = k_S + k_F\,\left(\frac{1-\emptyset}{\emptyset}\right)$ 7-8

or $S' = k_S + m\,k_F$ 7-9

where $m = \frac{1-\emptyset}{\emptyset}$ and $S' = \frac{S}{\emptyset}$ 7-10

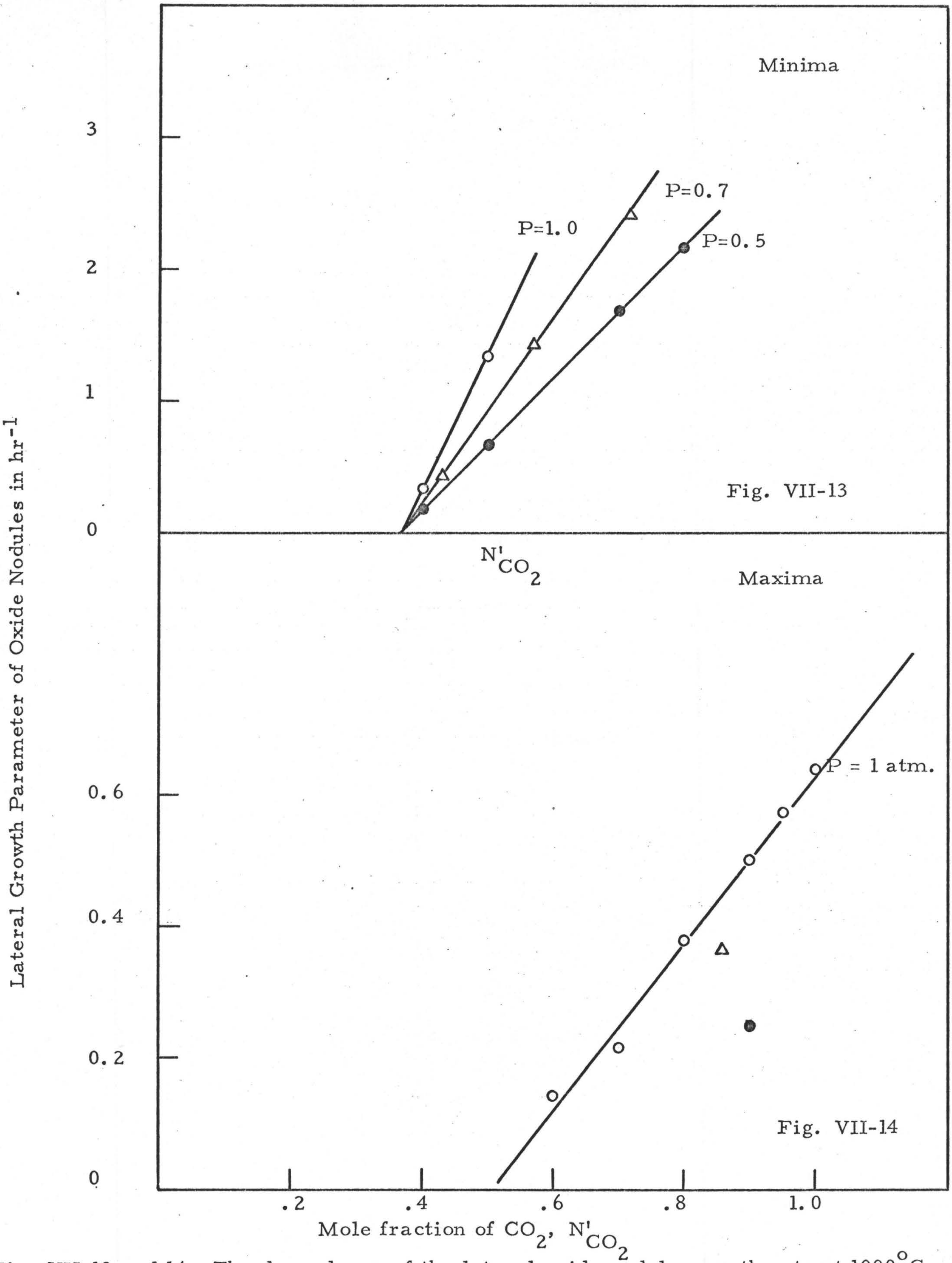

Fig. VII-13 and 14: The dependence of the lateral oxide nodule growth rate at 1000°C on the mole fraction of CO_2 in CO_2-CO atmospheres and these atmospheres containing argon.

It is to be noted that ϕ is a function of β, α_o, t, which are all known parameters, and S has also been calculated as a function of time. Accordingly the values of k_F and k_S for each oxidation run may be evaluated by a least squares fit of the experimental S' values to equation 7-9. A list of the calculated values of k_F and k_S are given in Table VII-3. The values of the lateral growth parameter, β, are also listed in the above table.

The rate constants k_F and k_S may now be discussed in terms of the oxide film model. It was shown in Chapter IV that these rate parameters may be treated in a manner similar to the linear reaction rate results, since the equations to describe k_F, k_S and K_L are similar in form. Plots of k_F versus $\frac{P_{CO_2}}{P_{CO}}$ and N'_{CO_2} are shown in Figs. VII-15 and 16. It is observed that there are two regions of behaviour as also found in the case of scale growth by linear reaction rates. A region of direct proportionality between k_F and $\frac{P_{CO_2}}{P_{CO}}$ is observed over most of the range of oxidizing potential. This means that the reaction proceeds under mixed reaction control rather than by pure dissociation of carbon dioxide. The values of the various kinetic parameters listed in Table VII-3 were evaluated by the use of the non-linear least squares program and equation 4-46. The fit of this equation to the data are shown in Fig. VII-16, the solid line representing the calculated curve.

The reaction rate constants of the silica growth, k_S, were plotted versus $\frac{P_{CO_2}}{P_{CO}}$ and N'_{CO_2}, and are shown in Fig. VII-17 and 18.

The rate constants increased with increasing concentration of carbon dioxide. These results can be analysed utilizing equation 4-43 and the values of the kinetic parameters evaluated. The results of such a fit are shown in Fig. VII-18. The values of the kinetic parameters

TABLE VII-3

Oxide Nodule and Silica Film Growth Rates Calculated for the Initial Stages of the Reaction at 1000°C

Run No.	Lateral Nodule Growth Rate, β	Silica Film Growth Rate, k_S	Vertical Nodule Growth Rate, k_F	Correlation Coefficient r
K17	0.33	0.55	0.48	0.9958
K16	1.34	0.77	0.76	0.9987
K15	0.14	0.47	1.27	0.9998
K14	0.22	0.70	1.80	0.9942
K21	0.38	3.32	5.08	0.9997
K20	0.50	3.70	4.50	0.9892
K19	0.58	3.53	5.45	0.9987
K1	0.64	4.89	8.54	1.000
K2	0.64	3.91	5.84	1.000
KA14	0.43	0.05	0.53	0.9793
KA12	1.44	0.61	0.44	0.9983
KA11	2.40	0.73	0.68	0.9832
KA10	0.37	2.26	3.05	0.9912
KA9	0.17	0.190	0.191	0.9990
KA6	0.67	0.52	0.34	0.9982
KA5	1.68	0.82	0.76	0.9998
KA1	2.18	1.87	1.01	0.9914
KA8	0.26	0.70	2.67	0.9973

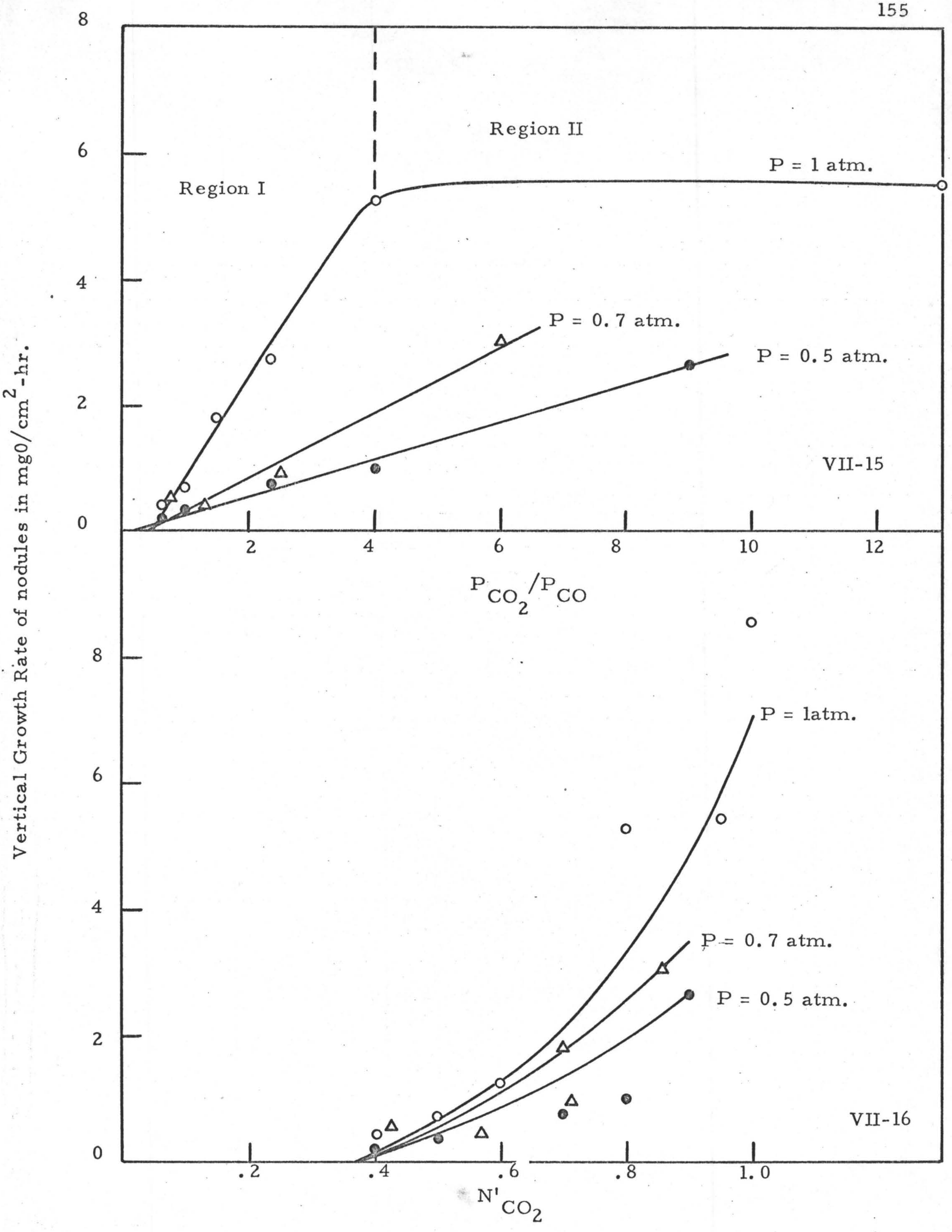

Fig. VII-15 and 16: Vertical growth Rates of wustite-fayalite nodules at 1000°C

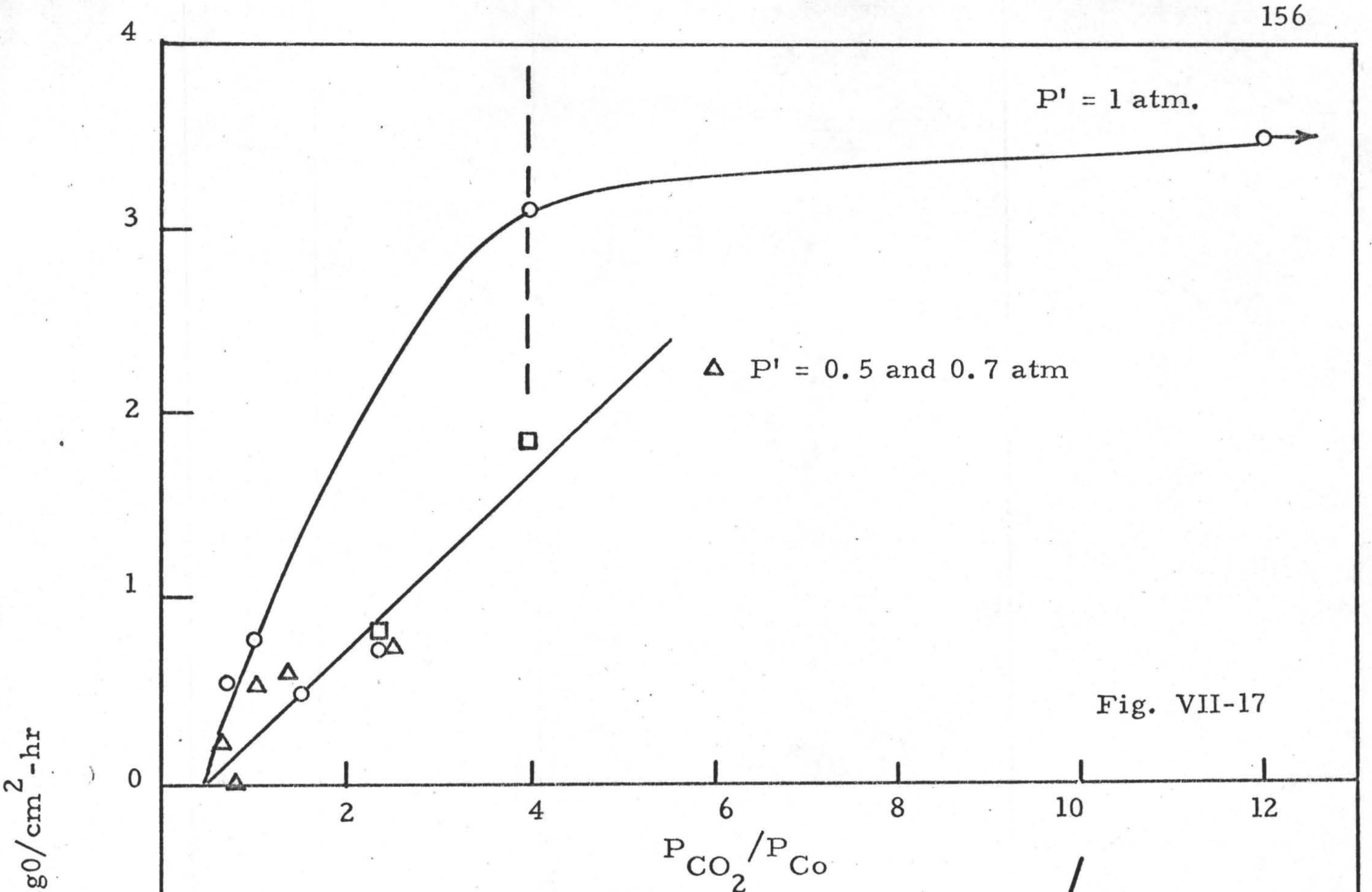

Fig. VII-17

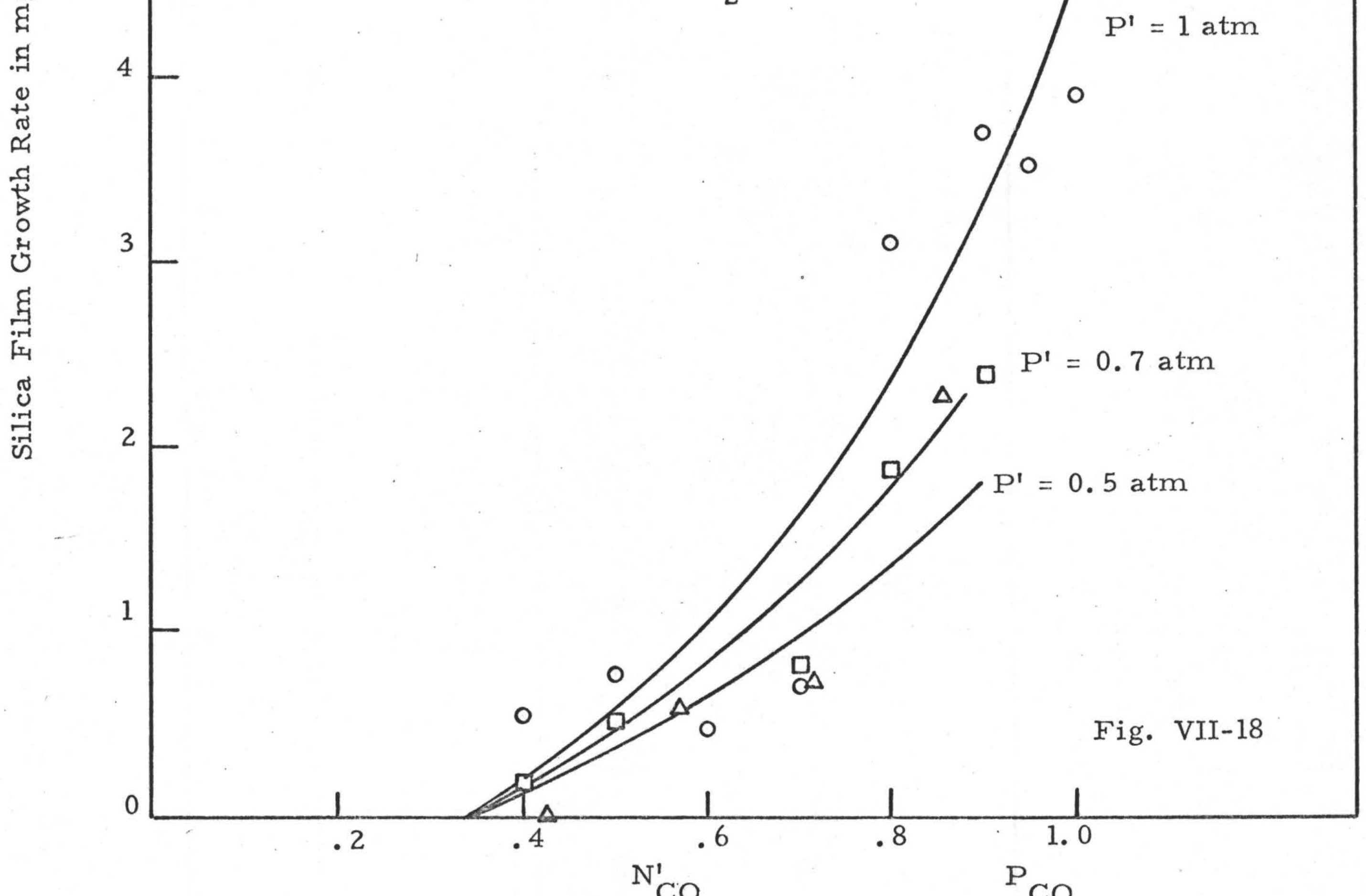

Fig. VII-18

VII-17: Vertical growth rates of silica film at 1000°C versus $\frac{P_{CO_2}}{P_{CO}}$ of CO_2-CO atmos.

VII-18: Vertical growth rates of silica film at 1000°C versus the mole fraction of CO_2 in CO_2-CO atmospheres.

are listed in Table VII-2. (p. 137)

The lateral growth parameter, β, may be defined as,

$$\beta = \Omega D_s n c \qquad 7\text{-}11$$

where D_s is the surface diffusion coefficient of the rate determining species, Ω is a geometrical factor dependent on the shape of particle, n is the nuclei density per cm^2, and c is the concentration or composition factor assuming circular geometry for the particle shape. As a good approximation during the early stages,

$$\Omega = 4\pi \quad \text{and} \quad c = \frac{C_\infty - C_s}{C - C_s} \qquad 7\text{-}12$$

According to the terminology of Rhead(30), C, C_s, C_∞ defined as the surface concentration of the adsorbed oxygen-complex or oxygen on the nodule, at the nodule edge and at a large distance on the silica surface from the nodule. In one particular case, the nodule density, n, has been estimated from replicas and micrographs by point counting of Figs. VI-15, 17, 23-25. It was found that the nodule density was between 3×10^8 to 1×10^9 nodules/cm^2, and that it was not a function of time. An average value of 5×10^8 nodule per cm^2 seems to be a reasonable estimate of the nodule density. Substituting this value of n into equation 7-11, we obtain,

$$c\, D_s = \frac{\beta}{12.5 \times 5 \times 10^8} = \frac{1.34}{6.25 \times 10^9} = 2 \times 10^{-10} \qquad 7\text{-}13$$

An evaluation of the factors in equation 7-13 may be made in order to obtain additional confirmation for the oxide film model involving growth of nodules during the early stages of the reaction. A rough estimate of c can be made from the observed height of the oxide nodules, which corresponds to about 10^5 atomic layers. If one assumes C_s to be very small, then

$$c = \frac{C_\infty - C_s}{C - C_s} \approx \frac{C_\infty}{C} \qquad 7\text{-}14$$

If monolayer coverage of oxygen on silica exists to within one atomic diameter of the nodule edge and the coverage of oxygen on the nodule surface is proportional to the height of the nodule, then

$$c = \frac{C_\infty}{C} = 10^{-5} \qquad 7\text{-}15$$

D_s is then found to be approximately 6×10^{-9} cm^2/sec from equation 7-13. This diffusion rate might be compared to that for diffusion of iron in wustite which is approximately 5×10^{-6} cm^2/sec at 1000°C which suggests that the reaction rate is determined by relatively slow surface processes involving the surface diffusion of either oxygen or an iron-silicon-oxygen complex on the wustite and silica surfaces.

7.4 Oscillatory Reaction Rate Oxidation Kinetics

7.4.1 General Discussion

This mode of reaction behaviour as defined in section 6.2 is prevalent at intermediate times in an oxidation test, generally occurring before the onset of linear kinetics and after the initial stage of nodular growth of the oxide to form a uniform scale. The reaction rate in this mode exhibits a number of maxima and minima, as illustrated in Fig. VI-6 to 10. As discussed in section 7.3.1, the first maximum or minimum is associated with the lateral growth of nodules, whilst the subsequent extrema are related to some other process or processes. The structure of the scale formed on the alloy in this mode consisted of an external wustite layer, an inner wustite-fayalite conglomerate layer interspersed with bands of fayalite and a narrow internal oxidation zone within the alloy, as shown in Fig. VII-19. As already stated in section 6.4b, there was a

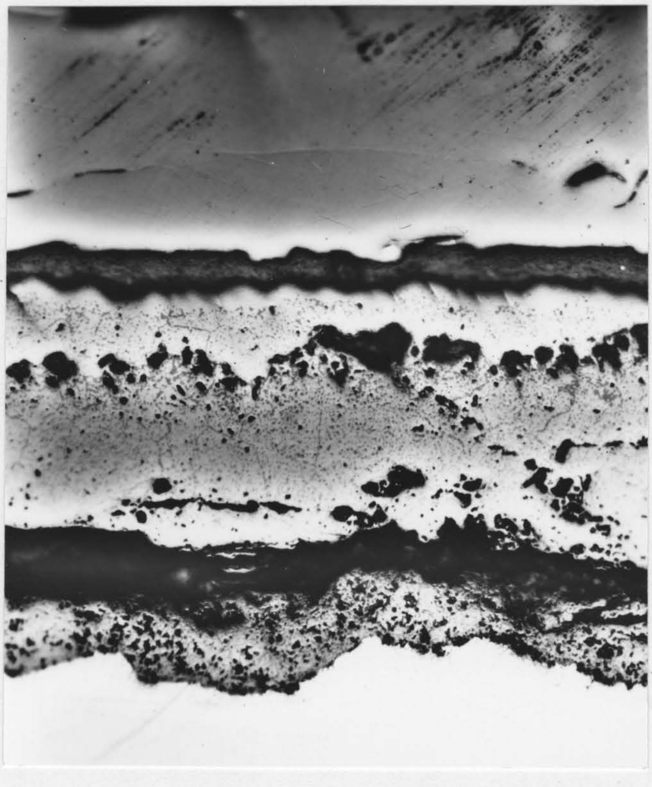

Fig. VII-19: Scale formed on alloy at 1000 °C in a CO_2-CO atmosphere containing 60 $^v/o$ CO_2 at a total pressure of 1 atm. X200 one to one correspondence in the number of precipitation bands and the number of minima in the rate curve. Therefore, it is inferred that the fluctuations in the reaction rate are associated with this precipitation phenomena.

Measurements made on specimens after completion of the oxidation tests suggested that the interface between the wustite and conglomerate represents the original alloy surface. A comparison between the original specimen thickness and the distance between the wustite-conglomerate interfaces on either side was made and the results are listed in Table VII-4. In the case of all specimens at 890°C, the net shift observed was zero within the experimental error of the measurement. At 1000°C, the results indicate that in atmospheres of low oxidizing potential, namely, $P_{CO_2} \leqslant 0.5$, the shift in the interface is also small and within the experimental error of the measurement. At high oxidizing potential, however, shifts as much as 37.5% of the original thickness were observed. Since the oscillatory reaction mode does not occur in the latter experiments (i.e. at high potential at 1000°C) it can be assumed that the conglomerate-wustite interface is the original metal interface in that mode.

Microscopic examination revealed large amounts of porosity at the wustite-conglomerate interface which could arise from the dissociation reaction which supplies the oxygen for the growth of the conglomerate layer, (Fig. VII-19). There is also considerable porosity in the conglomerate layer, largely surrounding the massive fayalite precipitates (Fig. VII-19). The density of the fayalite precipitates is observed to be a function of the oxidizing potential, reaching the stage of a continuous band at high potentials, (Figs. VI-27, VI-34, VI-36).

TABLE VII-4

Net Shift of Wustite-Conglomerate Interface Under Different Experimental Conditions at the End of Oxidation Test

Reaction Temperature 1000°C

Partial Pressure of Reaction Gas $P_{CO_2} + P_{CO}$	Mole Fraction of CO_2 in Reaction Gas N'_{CO_2}	Initial Thickness d of Specimen in mm.	Distance δ Between the Wustite-Conglomerate Interfaces on Either Side, in mm.	Net Shift 1/2 (d-δ) of the Wustite-Conglomerate Interface in mm.
1.0	0.4	1.28	1.25	0.015
"	0.5	1.29	1.23	0.03
"	0.6	1.28	1.27	0.005
"	0.7	1.22	1.12	0.05
"	0.8	1.30	1.05	0.125
"	0.9	1.28	0.98	0.15
"	1.0	1.28	0.80	0.24
0.7	0.43	1.20	1.16	0.02
"	0.57	1.22	1.08	0.07
"	0.71	1.23	1.07	0.08
"	0.86	1.21	1.18	0.015
0.5	0.40	1.28	1.37	-0.045
"	0.50	1.29	1.33	-0.02
"	0.70	1.28	1.11	0.085
"	0.80	1.32	1.24	0.04
Reaction Temperature 890°C				
1.0	0.40	1.33	1.30	0.015
"	0.50	1.31	1.29	0.01
"	0.70	1.30	1.34	-0.02
"	0.80	1.30	1.25	0.025
"	0.90	1.21	1.20	0.005
"	1.00	1.25	1.21	0.02

Since the only means of oxygen transfer from the atmosphere to the oxidizing specimen in the presence of a compact wustite scale is by reaction with iron at the outer wustite surface, fluctuations in the reaction rate must be associated with changes in the iron flux through the scales and alloy. These fluctuations arise because two competing processes are taking place during this stage of oxidation. This stage consists of the further oxidation of the internally oxidized metal zone into oxide, thereby causing the oxide-alloy interface to move inward.

One of the two processes is the oxidation of iron to wustite. This increases the reaction rate since wustite is a low resistance path for iron as compared to its original path through the alloy. The second process involves growth of the conglomerate layer by inward diffusion of oxygen as indicated by the marker experiments, Fig. VII-9. As a consequence of the latter, the formation of wustite decreases the inward flux of oxygen from the wustite-conglomerate interface, because wustite is a high resistance path for oxygen. The result of the inhibited inflow of oxygen and the enhanced outflow of iron is to supersaturate the conglomerate layer in silicon. To relieve this supersaturation, massive precipitation of fayalite takes place. This fayalite serves as well to reduce the outward iron flux, hence moderating the overall reaction in a kind of Le Chatelier principle.

The 'virtual path' for a specimen, as defined by Kirkaldy and coworkers(48), may be inferred from diffusion data and the metallography and is plotted on a schematic 1000°C section of the Fe-Si-0 phase diagram. This is shown for two cases in Fig. VII-20. The path ABCDEFGHI corresponding to low oxygen potential shows two regions of virtual supersaturation, FGH and DCB. The first

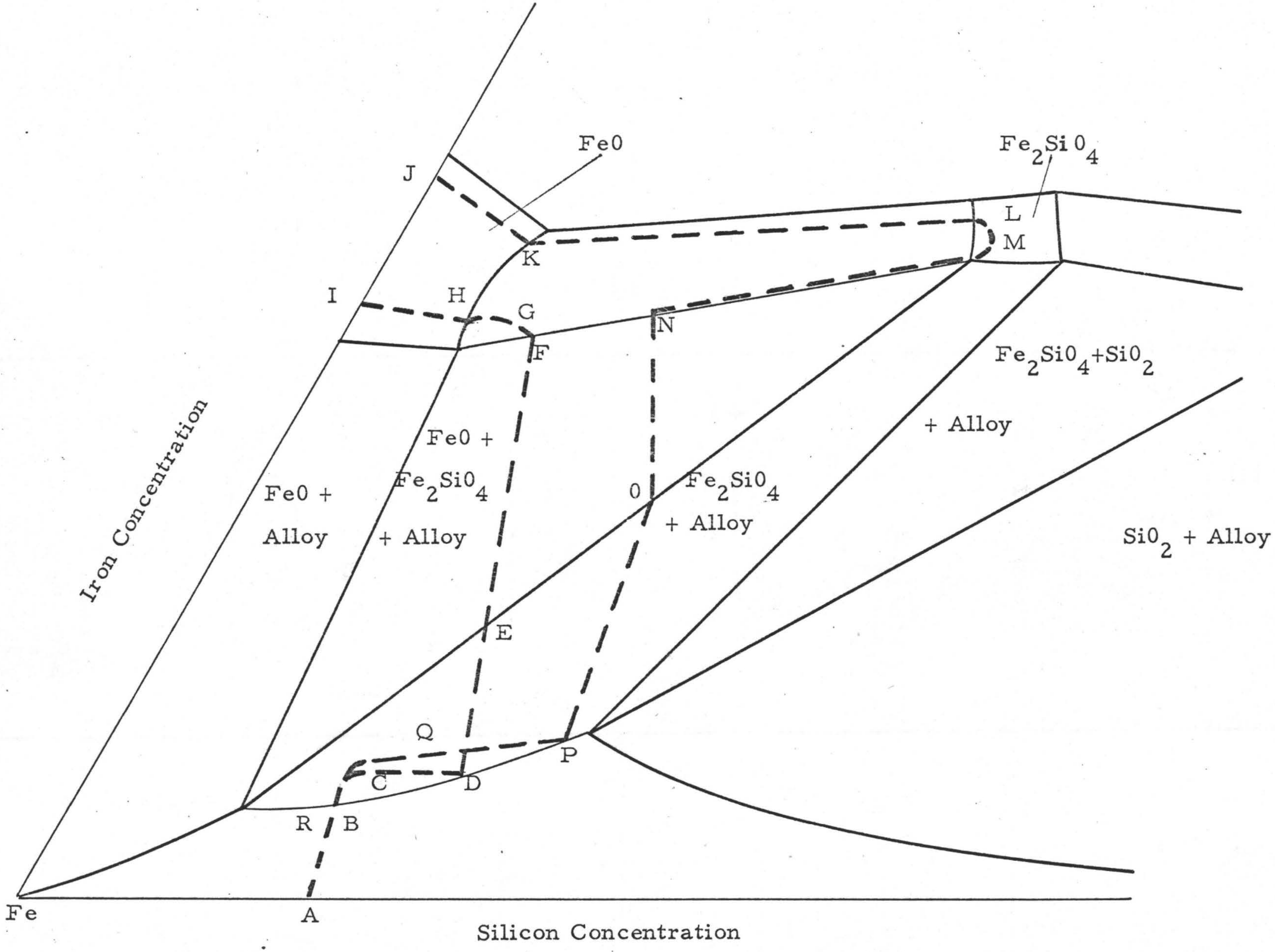

Fig. VII-20: Schematic representation of the virtual paths for an oxidized specimen in the 1000°C isotherm of the Fe-Si-0 diagram.

region of supersaturation FGH is associated with the wustite phase and leads to the formation of massive fayalite as discussed above. Because the virtually supersaturated regions are unstable, the actual path must dip in and out of the fayalite phase along tie lines GX and HY to form a discontinuous precipitate layer or periodic layers of fayalite as shown in Fig. VII-21. The second region DCB leads to the fine precipitate of fayalite found in the alloy phase as an internal precipitate, with a preference for formation at grain boundaries. This is shown in Fig. VII-22. The actual path in this region is shown as a solid line DB in Fig. VII-21 and closely approximates to the tie lines in the region DBA, after the precipitation has taken place.

As noted in section 6.5b, at high oxygen potentials only one continuous layer of fayalite was formed between the wustite and the conglomerate layers along with the usual zone of internal oxidation within the alloy. Although this case is not here classified as a oscillatory reaction mode, it is closely related, so the paths for this case has also been plotted in Fig. VII-20 (line JKLMNOPQRA). Here there is one region of virtual supersaturation and that is at PQR, which leads to internal precipitation of the fayalite within the alloy.

It is possible to determine the distance versus time plots of the fayalite bands by assuming that the bands originate at the conglomerate-alloy interface and thence remain stationary, and the corresponding times are given by the minima in the reaction rate curve. Furthermore, the growth curves of the conglomerate layer can also be obtained, since the fayalite precipitate bands serve as markers in this layer. The distance-time plots for the fayalite bands are shown in Fig. VII-10 and tend to obey a parabolic relationship at 1000°C and a linear relationship at 890°C. Hence the precipitation kinetics show a trend

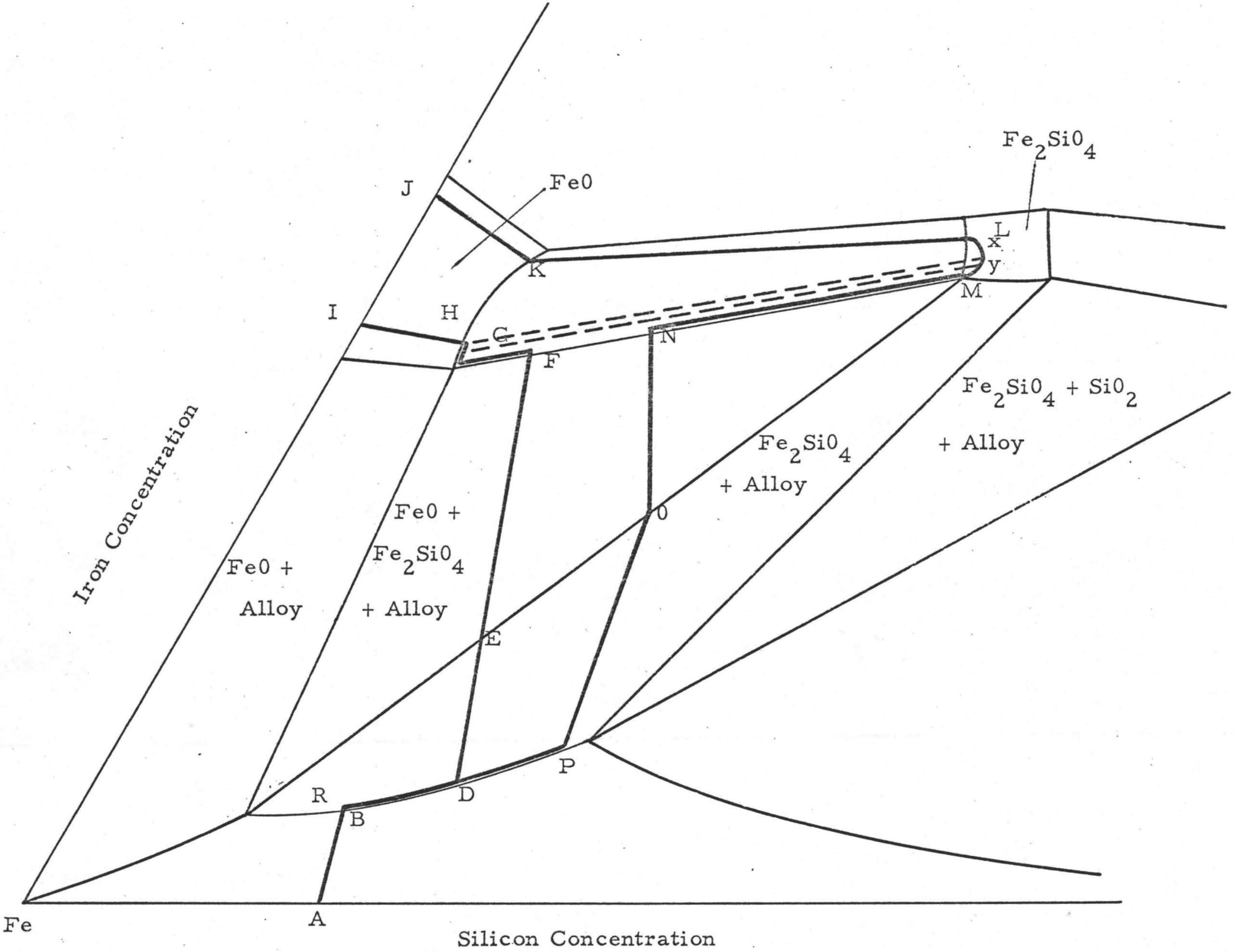

Fig. VII-21: Schematic representation of the actual paths for an oxidized specimen in the 1000°C isotherm of the Fe-Si-0 diagram.

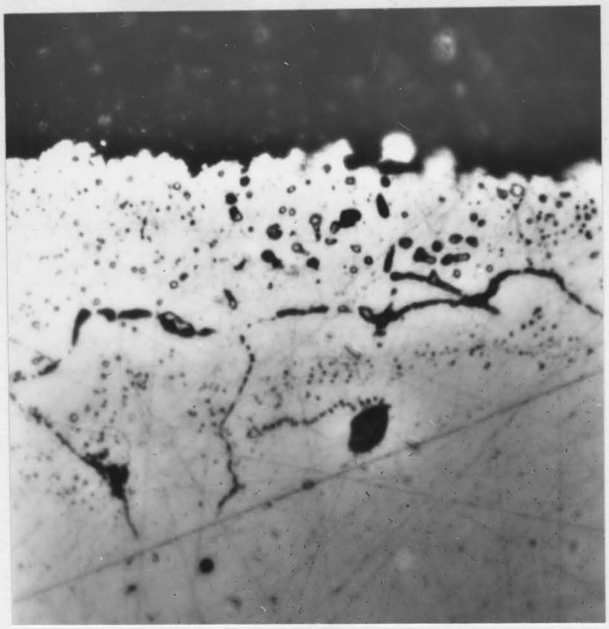

(a)

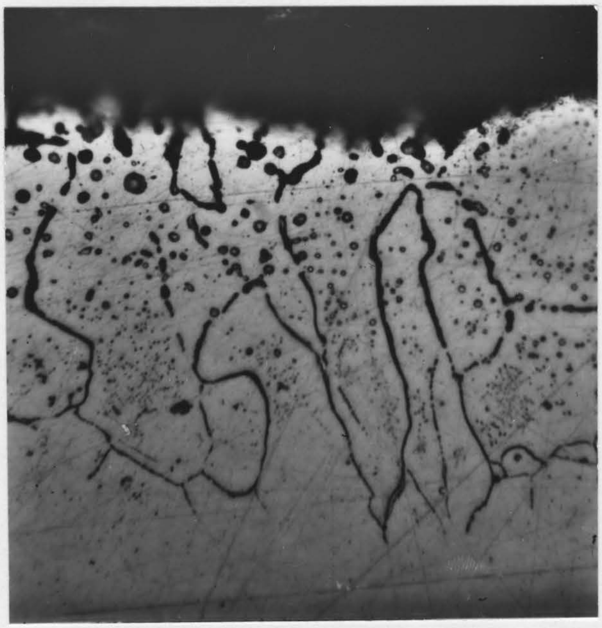

(b)

Fig. VII-22: Detail of internal oxidation zone within the alloy under different oxidizing conditions.

(a) $P_{CO_2} = 0.7$ atm., total pressure 1 atm. X1600

(b) $P_{CO_2} = 1.0$ atm., total pressure 1 atm. X1000 towards diffusion control at 1000°C and interface reaction control at 890°C.

The periodic precipitation reaction observed here is qualitatively very similar to the well-known Liesegang phenomena, although our observed kinetics do not conform very well to the predictions of Wagner's theory for that phenomenon(125). Our observations are also quite similar to those of Klueh and Mullins(126), who, in a recent study, report the occurrence of Liesegang precipitation of water vapour bubbles in solid silver at 800°C.

Another interesting aspect of our observations is the non-planar interface formed at the conglomerate-alloy interface. This non-planar nature of the interface is not marked at short times but becomes quite pronounced at long times. A few examples of the interface morphology are shown in Fig. VII-23. Note that most of the massive fayalite precipitates composing the precipitation bands lie on lines ahead of the metal projections into the conglomerate layer. It appears that even after silicon supersaturation is relieved by massive fayalite formation and internal oxidation, there remains sufficient instability within the system to promote the formation of a non-planar interface between the conglomerate layer and alloy. As with the periodic instability this phenomenon can be associated with the system's attempt to abet the outward flux of silicon by shortening the diffusion paths. Indeed, the silicon concentration at the tip of the metal projections and that at the flat portion of the interface were measured and found to be about 1.0 w/o and 4.5 w/o silicon, respectively, in agreement with the diffusion directions required by the foregoing hypothesis.

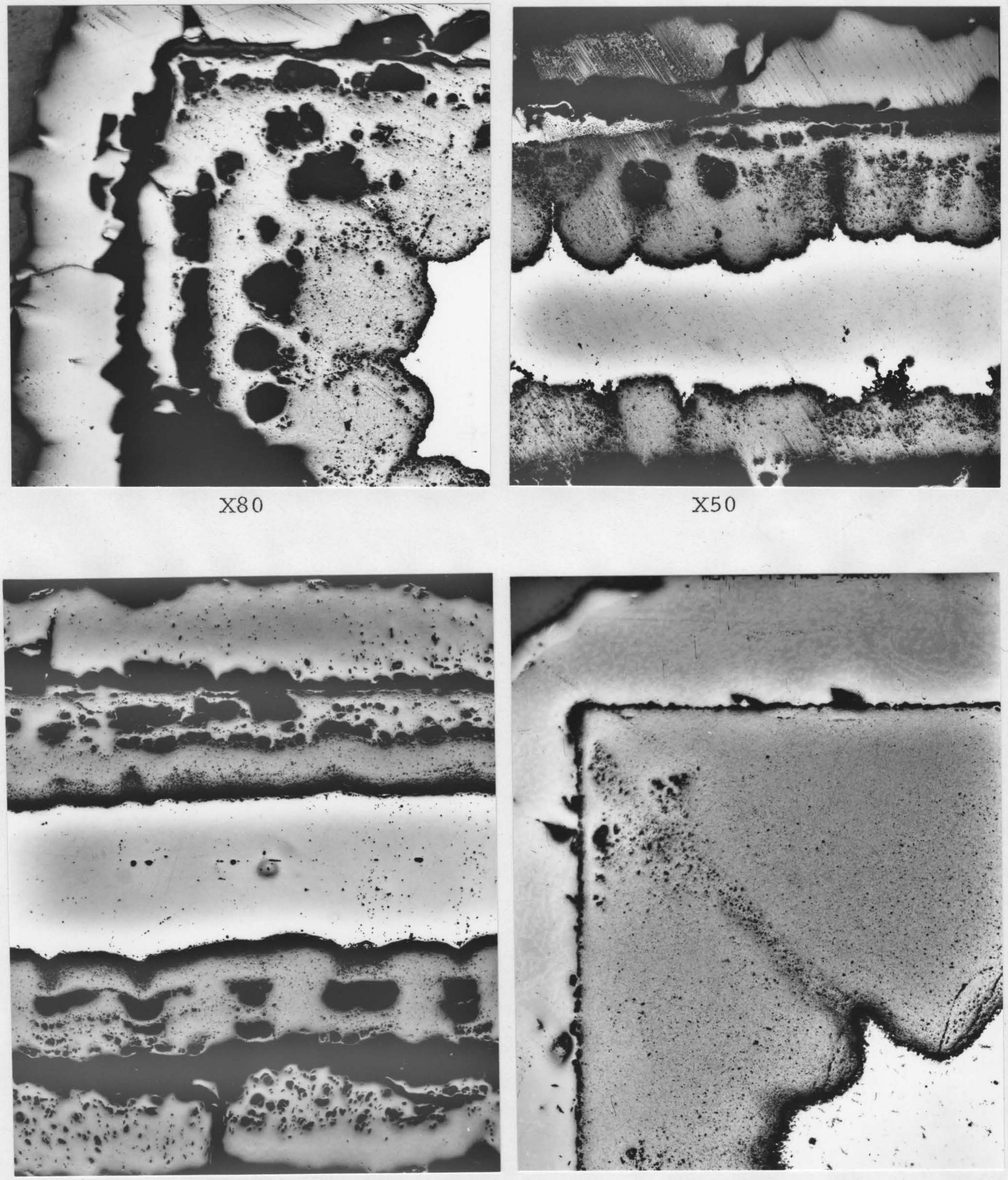

X80

X50

X40

X160

Fig. VII-2^3: Instabilities in the ternary Fe-Si-0 system exhibited as a non-planar interface between conglomerate and alloy.

CHAPTER VIII

CONCLUSIONS

1) The oxidation kinetics of the iron-1.5 $^{w}/o$ silicon alloy in the thick scale region at 890^{o} and 1000^{o}C obey linear relationships.

2) The above kinetics are consistent with the model based on gas-oxide interface reaction control, the two important steps being the dissociation of carbon dioxide and incorporation of chemisorbed oxygen into the wustite lattice. This model predicts the observed dependence of the linear reaction rate constant on the partial pressure of carbon dioxide.

3) In the initial stages, the reaction proceeds by the nucleation and growth of nodules containing fayalite and wustite. These nodules grow both laterally and vertically, whilst the rest of the specimen is covered with an amorphous silica film which grows vertically. Wustite and silica react at the nodule edge to form fayalite.

4) The oxidation kinetics in the initial stages can be explained by a nucleation and growth model for the oxide nodules, the lateral wustite growth rate being determined by a surface diffusion mechanism forthe reacting species. The dependence of the reaction rate constants on the partial pressure of carbon dioxide is consistent with predictions from the model.

5) The fluctuations in reaction rates observed at intermediate times in atmospheres of low oxidizing potential were found to be associated with the formation of massive fayalite precipitation bands in the inner conglomerate oxide layer of the scale.

6) The precipitation kinetics of the fayalite bands, which obeyed a parabolic relationship at 1000°C and a linear relationship at 890°C, appeared to be associated with instabilities created by counterdiffusion in this ternary iron-silicon oxygen system.

APPENDIX I

ELECTRON MICROPROBE ANALYSIS

Consider the analysis for element A in an alloy. The intensity of a suitable characteristic X-ray line from element A was used as a measure of the concentration of A in the alloy. The quantity K_A^m was the measured ratio of intensity obtained from the alloy to that obtained from pure A, where intensities have been corrected for instrumental drift, background and loss in count rate due to dead time of counter.

To a rough approximation K_A^m equals C_A, the weight fraction of A in the alloy. The aim of the correction process was to calculate C_A more accurately from the measured intensity ratio K_A^m.

Following Philibert(128), the total correction may be divided into three separate factors, flourescence, absorption and atomic number. In principle the absorption and atomic number effects can be combined and included in one calculation, but in practice no satisfactory combined correction has been produced.

A flow chart for the procedure used indicates the various steps which must be taken in the sequence shown.

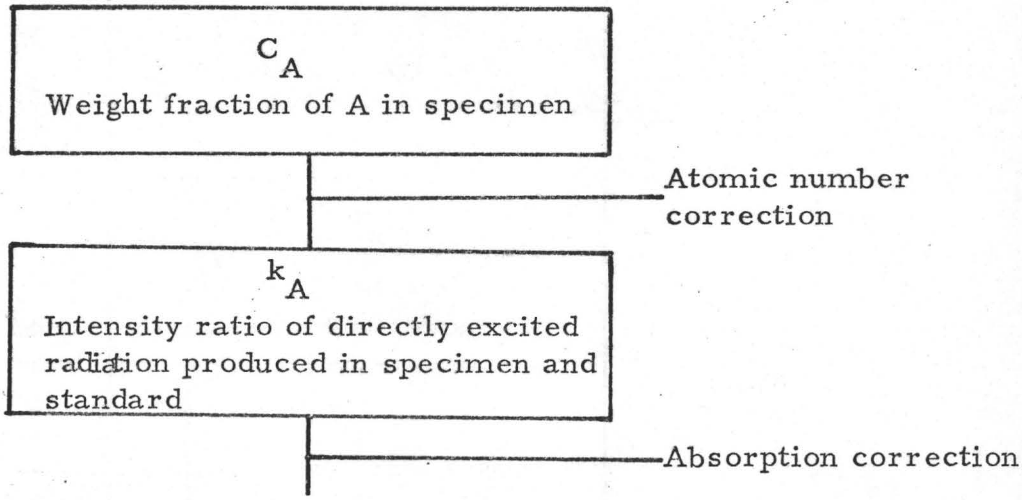

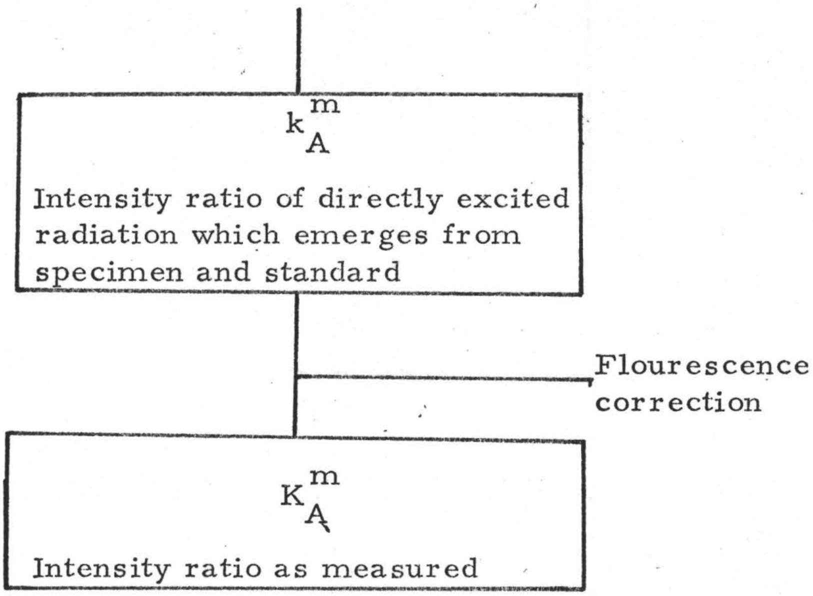

The calculation is simpler if worked from top to bottom rather than bottom to top, since C_A is required at various steps in the calculation. Hence working in this sense avoids the need for iteration; it is convenient if a table of C_A versus K_A^m is compiled to cover the concentration range of interest.

Atomic Number Correction

This correction takes into account the non-linearity in the relationship between C_A and k_A. The ratio of the generated intensity is calculated from the formula:

$$k_A = C_A \frac{R_{Alloy}}{R_A} \frac{S_A}{S_{Alloy}} \qquad (1)$$

where values of R and S depend upon the mean electron energy and the atomic number of the specimen, and are calculated for alloys according to the relationships:

$$R_{Alloy} = \sum_i C_i R_{Ai} \qquad (2)$$

$$S_{Alloy} = \sum_i C_i S_{Ai} \qquad (3)$$

where C_i is the true mass concentration of element i in the alloy and subscript A_i signifies values appropriate to the constituent element i when element A is being analysed at a given value of incident electron energy.

Values of R vary from R=1 if no electrons are backscattered to about R=0.6 for heavier elements, and are obtained from the work of Duncumb and Reed(129).

The electron stopping power $S = \frac{1}{\rho} \frac{dE}{dx}$ gives the rate at which electrons lose energy E measured along their path length in a specimen of density ρ. Values for S are based on Bethe's formula,

$$S = \text{constant} \frac{Z}{A} \frac{1}{E} \ln \left(\frac{1.166E}{J}\right) \tag{4}$$

where Z, A and J are the atomic number, atomic weight and mean ionization potential for that element. In the absence of good theoretical or direct experimental values for J, values calculated by Duncumb are used(129).

Absorption Correction

In this correction, we make allowance for absorption of the directly excited radiation as it emerges from both specimen and pure metal standard. The procedure followed is that due to Philibert(130) but with a modified value for the electron penetration coefficient due to Duncumb and Shields(131). The relation relating the intensity ratio for the emerging radiation k_A^m with the corresponding ratio for the directly excited radiation generated in the specimen k_A is

$$k_A^m = k_A \frac{f(X_{Alloy})}{f(X_A)} \tag{5}$$

where $f(X) = \frac{F(X)}{F(0)}$ (6)

F(X) is the intensity of emerging radiation and X is a parameter measuring the absorption in specimen or standard. When $X = 0$ there is no absorption of X-rays and thus F(0) gives in principle a measure of the atomic number effect (but as explained, the use of this atomic number correction is inadequate in practice), and the use of f(x) cancels out this atomic number correction and enables us to make a correction for absorption alone.

The parameter $$X = \left(\sum_i C_i \left(\frac{\mu}{\rho}\right)_i^A\right) \operatorname{cosec}\theta \qquad (7)$$

where θ is the take off angle for emerging radiation and $\left(\frac{\mu}{\rho}\right)_i^A$ is the mass absorption coefficient of element i for A characteristic radiation.

An approximate analytical expression derived by Philibert for F(x) is,

$$\frac{1}{F(X)} = \left(1 + \frac{X}{\sigma}\right)\left\{1 + h\left(1 + \frac{X}{\sigma}\right)\right\} \qquad (8)$$

The electron retardation coefficient σ was calculated by Philibert as a function of incident electron energy, E_o, alone. More recently the expression

$$\sigma = \frac{2.39 \times 10^5}{E_o^{1.5} - E_c^{1.5}} \qquad (9)$$

has been proposed(131), where E_c is the critical absorption energy for the radiation being used. This latter expression has a better theoretical basis and is also proving more satisfactory experimentally.

The parameter h is a function of atomic number alone, and Philibert's expression is used,

$$h = 1.2\,\frac{A}{Z^2} \qquad (10)$$

The value of h for an alloy is calculated according to

$$h = 1.2 \frac{\sum_i N_i A_i}{(\sum_i N_i Z_i)^2} \tag{11}$$

where N_i is the atomic fraction of the ith component in the alloy. Substituting the expression for F(X) in equation 6 enables us to calculate f(X):

$$\frac{1}{f(X)} = (1 + \frac{X}{\sigma}) \left\{ 1 + \frac{h}{1+h} \quad \frac{X}{\sigma} \right\} \quad . \tag{12}$$

and thus use equation 5 to correct for absorption effects.

Flourescence Correction

Here the component of the measured intensity (I^f_{Ai}) which is caused by absorption by element A of the characteristic radiation or radiations of one or more of the other constituent elements of the alloy is considered. If the measured intensity ratio for the directly excited radiation is written as,

$$k^m_A = I^m_{Ai}/I^m_A \tag{13}$$

then the inclusion of the flourescence contribution leads to a measured ratio

$$K^m_A = (I^m_{Ai} + I^f_{Ai})/ I^m_A = (1 + \frac{I^f_{Ai}}{I^m_{Ai}}) k^m_A \tag{14}$$

To make allowance for this contribution, the ratio I^f_{Ai}/I^m_{Ai} is calculated for each and every X-ray line from the other constituents in the alloy other than A, which might cause a significant fluorescence effect. Constituents giving an intensity I_i, having a wavelength just shorter than the A absorption edge, will be most important.

To calculate the flourescence contribution the equation of Castaing$^{(116)}$, slightly modified by Green$^{(132)}$ was used:

$$\phi_i = \frac{I^{f}_{Ai}}{I^{m}_{Ai}} = \frac{\Omega_{ik}\, w_i}{2} \left(\frac{r-1}{r}\right) \left(\frac{U_i-1}{U_A-1}\right)^{5/3} \frac{W_A}{W_i}\, u^{i}_{A}\, C_i \times \left[\frac{\ln\left\{1+\dfrac{\sum_j u^{A}_{j} C_j}{\sum_j u^{i}_{j} C_j}\operatorname{cosec}\theta\right\}}{\left(\sum_j u^{A}_{j} C_j\right)\operatorname{cosec}\theta} + \frac{\ln\left\{1+\dfrac{\sigma}{\sum_j u^{i}_{j} C_j}\right\}}{\sigma} \right] \qquad (15)$$

where

i) w_i is flourescence yield for relevant ionization level for element i and values used are from data of Kaye and Laby, which in turn relied on the work of Burhop.$^{(134)}$ Ω_{ik} is the weighting of each line associated with the level, such that $\sum_k \Omega_{ik} = 1$.

ii) r is the ratio of mass absorption coefficients for element A on either side of the relevant absorption edge. It is a measure of the fraction of absorbed radiation of element i, that causes ionization of A atoms. For K absorption edges, values of r were obtained from data of Victoreen$^{(134)}$, and Compton and Allison$^{(135)}$.

iii) $U = E_o/E_c$, and is the overvoltage ratio for absorption edges of the different elements.

iv) W is the atomic weight of element i.

v) u^{i}_{j} is the mass absorption coefficient for the characteristic line of element i in element j.

Combining the equations 1, 5 and 14, the combined expression relating measured relative intensity K^{m}_{A} to concentration C_A is,

$$K_A^m = (1 + \sum_i \phi_i) \quad \frac{f(X_{Alloy})}{f(X_A)} \quad \frac{R_{Alloy}}{R_A} \quad \frac{S_A}{S_{Alloy}} \qquad (16)$$

Using equation 16, tables of measured relative intensities versus concentration were constructed for the iron-silicon and the ternary iron-silicon-oxygen system for an operating voltage of 15 kV and take off angle of 18°.

The agreement between the calculated values and experimental results is excellent in the case of iron-slicon alloy, Fig. V-4. The line is the calculated curve whilst the points are experimental data.

In the case of the iron-silicon-oxygen alloy, the assumption is made in the calculations that the specimen is homogenous. In practice, however, it consists of various phases in different states of inter-distribution. For the conglomerate phase, which consists of a fine dispersion of silicate particles in a wustite matrix, the above assumption may be a fair approximation. The size of the silicate particles ranges from 0.02 - 14 μ^3. Since the spot size of the electron beam is about 2μ, the excited volume would be approximately 32 μ^3. Hence at the lower end of the silicate particle size range, the assumption of a homogenous material is reasonable.

APPENDIX II

DETERMINATION OF REACTION RATE FROM WEIGHT GAIN DATA BY NUMERICAL DIFFERENTIATION

To determine the reaction rate from the weight gain data numerical differentiation was found to be most suitable, since graphical methods have very poor accuracy and are cumbersome. All numerical differentiation methods are based on the fact that an interpolation function $\emptyset(x)$ can be used instead of $f(x)$ and that the derivative of $\emptyset(x)$ is approximately equal to the derivative of $f(x)$. Hence, there is a certain degree of error in the derivative of $f(x)$.

The function $f(x)$ can be written in the form

$$f(x) = \emptyset(x) + R(x) \tag{1}$$

where $\emptyset(x)$ is the interpolating function and $R(x)$ the residual term of an interpolation formula. Since the function values were available, rather than differences, it was decided to use Lagrange's interpolation formula for equal intervals to represent $\emptyset(x)$.

The Lagrange interpolation polynominal of degree n can be expressed in the form,(136)

$$f(x) = (-1)^n \frac{t\,(t-1).....(t-n)}{n!} \sum_{i=0}^{n} (-1)^i \frac{C_n^i\, y^i}{t-i}$$

$$+ h^{n+1}\, t(t-1)\,(t-2)\,....(t-n)\, f\,(x;\ x_o;\ .....x_n) \tag{2}$$

where $x_n - x_{n-1} = h$ and $t = \frac{x-x_o}{h}$ (3)

Differentiating once we get,

$$h\,f'(x) = \sum_{i=0}^{n} (-1)^{n+i}\, C_n^{\,i}\, yi\, \frac{d}{dt}\left\{ \frac{t\,(t-1)\,\ldots\ldots(t-n)}{(t-i)} \right\}$$

$$+\, h^{n+1} f(x;\ x_o;\ x_i;\ \ldots.x_n)\ \frac{d}{dt}\left\{t(t-1)\ldots(t-n)\right\}$$

$$+\, h^{n+2} f(x;\ x_o;\ \ldots X_n)\ t(t-1)\ldots(t-n) \qquad (4)$$

In particular, if $x = x_k$, we have

$$h\,f'(x_k) = \sum_{i=1}^{n} (-1)^{n+i}\, \frac{C_n^{\,i}\ yi}{n!}\ \frac{d}{dt}\left\{\frac{t(t-1)\ldots(t-n)}{t-i}\right\}_{t=k} +$$

$$h^{n+1}\, f\,(x;\ x_o;\ldots x_n)\,\frac{d}{dt}\left\{t\,(t-1)\ldots(t-n)\right\}_{t=k} \qquad (5)$$

Now the first derivatives for various values of n can be written down:

n = 2 (3 points)

$$y'_o = \frac{1}{2h}\left\{-\,3y_o + 4y_1 - y_2\right\} + \frac{h^2}{3}\ f'''\,(\xi) \qquad (6)$$

$$y'_1 = \frac{1}{2h}\left\{y_2 - y_o\right\} - \frac{h^2}{6}\ f'''\,(\xi) \qquad (7)$$

$$y'_2 = \frac{1}{2h}\left\{y_o - 4y_1 + 3y_2\right\} + \frac{h^2}{3}\ f'''\,(\xi) \qquad (8)$$

n = 3 (4 points)

$$y'_o = \frac{1}{6h}\left\{-11y_o + 18y_1 - 9y_2 + 2y_3\right\} - \frac{h^3}{4}\ f^{(iv)}\,(\xi) \qquad (9)$$

$$y'_1 = \frac{1}{6h}\left\{-2y_o - 3y_1 + 6y_2 - y_3\right\} + \frac{h^3}{12}\ f^{(iv)}\,(\xi) \qquad (10)$$

$$y'_2 = \frac{1}{6h}\left\{y_o - 6y_1 + 3y_2 + 2y_3\right\} - \frac{h^3}{12}\ f^{(iv)}\,(\xi) \qquad (11)$$

$$y'_3 = \frac{1}{6h}\left\{-2y_o + 9y_1 - 18y_2 + 11y_3\right\} + \frac{h^3}{4}\ f^{(iv)}\,(\xi) \qquad (12)$$

n = 4 (five points)

$$y'_o = \frac{1}{12h} \left\{ -25y_o + 48y_1 - 36y_2 + 16y_3 - 3y_4 \right\} + \frac{h^4}{5} \; f^{(v)}(\xi) \qquad (13)$$

$$y'_1 = \frac{1}{12h} \left\{ -3y_o - 10y1 + 18y_2 - 6y_3 + y_4 \right\} - \frac{h^4}{20} \; f^{(v)}(\xi) \qquad (14)$$

$$y'_2 = \frac{1}{12h} \left\{ y_o - 8y_1 + 8y_2 - y_3 \right\} + \frac{h^4}{30} \; f^{(v)}(\xi) \qquad (15)$$

$$y'_3 = \frac{1}{12h} \left\{ -y_o + 6y_1 - 18y_2 + 10y_3 + 3y_4 \right\} + \frac{h^4}{20} \; f^{(v)}(\xi) \qquad (16)$$

$$y'_4 = \frac{1}{12h} \left\{ 3y_o - 16y_1 + 36y_2 - 48y_3 + 25y_4 \right\} + \frac{h^4}{5} \; f^{(v)}(\xi) \qquad (17)$$

where $y = f(x)$ and $y' = \frac{d}{dx} \, (f(x))$

It can be seen by comparing the various formulae that the simplest expressions are obtained for even n at the middle points, that is, equation (7) and (15). The coefficients of the derivatives in the residual terms (those outside the curved brackets) are also the smallest here. Therefore, these formulae will contain the smallest error and hence were used as much as possible. It should also be observed that the error due to the residual term decreases as n increases if h is less than 1.

A computer program was written to use the above formulae and calculate the reaction rate from the weight gain data. The basic scheme used is outlined below:

In our case the independent variable x is time and the dependent variable is the weight gain w. Let us consider a table of w and t values as shown

t_o	w_o
t_1	w_1

t_2	$w_2 \longleftarrow$
t_3	w_3
t_4	w_4
t_5	w_5
t_6	w_6

If it is decided to use the five point formulae, then the derivative of w at t_2 marked by the arrow, can be readily calculated using equation (15) to good accuracy since it is the mid point of the first five points. The derivatives for t_o, t_1 can also be calculated using the corresponding formulae, equations (13) and (14), to a lesser degree of accuracy. To calculate the derivative at t_3, one uses the five points w_1, w_2, w_3, w_4, w_5 and calculates the derivative using the mid point formula. This procedure is continued to calculate the derivatives at successive points until the end of the table is reached. Here again as at the start, one has to use formulae other than midpoint formula to calculate the derivatives at the last two points. Therefore, the accuracy of the derivatives at the top and bottom of the table is necessarily lower than those calculated using the midpoint formula. An error of the order of 1% is made at the top and bottom of the table, whilst derivatives calculated by the midpoint formula have an error of order of 0.2% due to the residual term, when the five point formulae are used.

APPENDIX III

INDEXING SINGLE CRYSTAL ELECTRON DIFFRACTION PATTERNS

The diffraction pattern is a plane through the reciprocal lattice which is perpendicular to the incident electron beam and each spot in the pattern represents a particular set of reflecting planes. Since Bragg angles are very small, the zone axis of the reflecting planes is nearly parallel to the specimen normal. The distance from the centre bright spot to a diffraction spot is proportional to the reciprocal of the d-spacing of the reflecting plane normal in the real crystal and thus can be used to assign directions in the real crystal. Not all of the points in a particular reciprocal lattice plane will appear in the diffraction pattern because of interference between waves scattered from different scattering points in each unit cell (i.e. certain reflections are disallowed by the structure factor).

To illustrate how the diffraction pattern can be indexed, let us consider the spot pattern in Fig. VI-20. This diffraction pattern was obtained from the area marked A on the accompanying micrograph, that is, from the region at the interface between the wustite nodule and the amorphous silica. In the case of cubic crystals indexing can be done without a knowledge of the camera constant but for other more complex crystals, a knowledge of the camera constant is necessary to enable d-spacings to be calculated using the formula(119),

$$d_{hkl} = \frac{L\lambda}{R} \qquad (1)$$

where d_{hkl} is the d-spacing of the reflecting plane, R is the distance from central bright spot to any diffraction spot and $L\lambda$ is the camera constant. The camera constant for the particular operating conditions was determined to be 18.6 Å - mm.

Lists of the d-spacings of the various oxides, wustite, silica and fayalite were calculated from the known lattice parameters. For the case of wustite and some forms of SiO_2, which are cubic, lists of the interplanar angles were obtained from standard texts$^{(137)}$. For the case of fayalite, a list of the interplanar angles was calculated to aid in the analysis of the diffraction patterns.

The lengths OA, OB, OC are measured from the plate, as shown in Fig. A-1. From these values of R, the corresponding d-spacings of the reflecting planes may be calculated using equation (1). The d-spacings calculated are next checked against the lists of d-spacings of the various oxides. In this particular case, the measured d-spacings can only be accounted for by fayalite and the spots A, B, C are probably of the (011), (012), (021) form respectively. The exact indices of the first two spots can be arbitrarily selected provided they give the correct angle between the two planes. In practice, the indices of the three planes have to be chosen in such a manner as to satisfy the condition that the correct interplanar angles are given by these indices.

The measured R-values, the measured and calculated d-spacings and interplanar angles are listed in Table V-2. The diffraction pattern indexed in this appendix is that corresponding to plate no. 2254. It is observed that there is a good correspondence between the calculated and measured values, meaning that the correct indices have been assigned.

From the zone law, the zone axis is the cross-product of the two lattice vectors, namely,

$$ZA = [011] \times [0\bar{1}2] = [300] = [100]$$

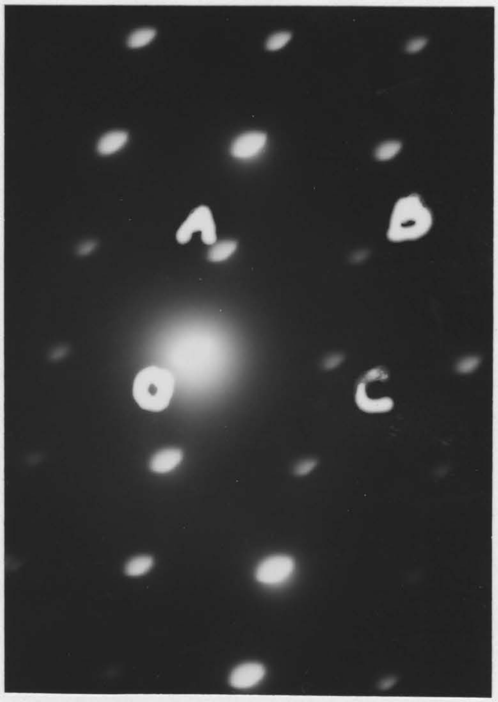

Fig. A-1: Selected area diffraction pattern corresponding to Fig. VI-20.

APPENDIX IV

If gaseous diffusion of carbon dioxide is rate controlling, the oxidation rate will be given by the rate of transfer of gas to the oxide surface. Consider the largest observed oxidation rate, namely, for oxidation of alloy in pure carbon dioxide. From the linear rate constant, the oxygen uptake is 1.24 gm-atom $0/cm^2$-sec. One gm-molecule of carbon dioxide supplies one gram-atom of oxygen according to

$$CO_2 \longrightarrow CO + 0 \qquad (1)$$

The rate of carbon dioxide diffusion to the surface is given by$^{(112, 113)}$,

$$N_{CO_2} = \frac{D}{RTl} N_V (P_{CO_2} - P_{CO_2}{*})$$

where

$$N_V = 0.664 \left(\frac{lv\rho}{\mu}\right)^{0.5} \left(\frac{\mu}{D}\right)^{0.33}$$

and v, ρ, u are the gas velocity, density and viscosity respectively, D is the gaseous diffusion coefficient and l is the specimen length. Substituting appropriate values,

$$N_V = 0.664 \left(\frac{1.5 \times 0.52 \times 0.43 \times 10^{-3}}{450 \times 10^{-6}}\right)^{0.5} \left(\frac{450 \times 10^{-6}}{.43 \times 10^{-3} \times 1.5}\right)^{0.33}$$

$$= 0.505$$

where $V_{max} = 2V_{average}$ has been substituted for the gas velocity.

Therefore

$$N_{CO_2} = \frac{1.5 \times 0.505 \times 0.71}{82.05 \times 1273 \times 1.5} = 3.5 \times 10^{-6} \text{ gm-atms.0/cm}^2\text{-sec}$$

The oxidation rate should be 28 times faster than the observed rate if the reaction rate is determined by gaseous diffusion of carbon dioxide across a boundary layer.

Bibliography

1. Hauffe, K., 'Oxidation of Metals', New York: Plenum Press, 1965.
2. Kubaschewski, O., and Hopkins, B. E., 'Oxidation of Metals and Alloys', London: Butterworths, 1962.
3. Evans, U. R., 'The Corrosion and Oxidation of Metals', London: Edwin Arnold, 1960.
4. Benard, J., 'Oxydation des Metaux', Paris: Gauthier-Villiars, 1962-4 (2 vol.).
5. Kofstad, P., 'High Temperature Oxidation of Metals', New York: John Wiley and Sons, 1966.
6. Metal Surfaces: Structure, Energetics and Kinetics, ASM and Met. Soc. of AIME, 1963.
7. 'Conference on Clean Surfaces', Ann. N. Y. Acad. Sci., 101, Art. 3 (1963).
8. Hayward, D. O., and Trapnell, B.M.W., 'Chemisorption', London: Butterworths, 1964, p. 17.
9. Farnsworth, H. E., 'The Surface Chemisorption of Metals and Semiconductors', New York: John Wiley and Sons, 1960.
10. MacRae, A. U., and Germer, L. H., 'Conference on Clean Surfaces', Ann. N. Y. Acad. Sci., 101, 627 (1963).
11. Hayward, D. O., and Trapnell, B. M. W., 'Chemisorption', London: Butterworths, 1964, p. 71.
12. Young, D. M. and Crowell, A. D.; 'Physical Adsorption of Gases', London: Butterworths, 1962.
13. Ehrlich, G., 'Conference on Clean Surfaces', Ann. N. Y. Acad. Sci., 101, 722 (1963).
14. Ehrlich, G., 'Metal Surfaces', ASM and Met. Soc. of AIME, 1963, p. 221.
15. Schlier, R. E. and Farnsworth, H. E., J. Appl. Phys., 25, 1333 (1954).

16. Farnsworth, H. E. and Tuul. J., J. Phys. Chem. Solids, 1, 48 (1958).

17. Germer, L.H., MacRae, A.U., and Hartman, C.D., Phil. Mag., 5, 222 (1960).

18. Germer, L.H., and MacRae, A.U., J. Chem. Phys., 36, 1555 (1962).

19. MacRae, A.U., Science, 139, 379 (1963); Surface Science, 1, 319 (1964).

20. Lander, J.J., and Morrison, J., ref. 7, p. 605.

21. Lander, J.J., Surface Science, 1, 125 (1964).

22. Ramasubramanian, N., Sewell, P.B., and Cohen, M.,J. Electrochem. Soc., 115, 12 (1968).

23. Wagener, S., Brit. J. Appl. Phys., 1, 225 (1950); 2, 132 (1951).

24. Bloomer, R.N., Brit. J. Appl. Phys., 8, 40, 321 (1957).

25. Cohen, M.S., Acta. Met., 8, 356 (1960).

26. Orr, W.H., 'Oxide Nucleation and Growth', Cornell University, Microfilm Inc., Ann Arbor, Mich., ONR Rept. No. 5, (1962).

27. Bardolle, J., and Benard, J., Compt. rend., 232, 231 (1951).

28. Harris, W.W., Ball, F.W., and Gwathmey, A.T., Acta. Met. 5, 574 (1957).

29. Boggs, W.E., Kachik, R.H., and Pellissier, G.E., J. Electrochem. Soc., 112, 539 (1965).

30. Rhead, G.E., Trans. Faraday Soc., 61, 797 (1965).

31. Bartlett, R.W., J. Electrochem. Soc., 111, 903 (1964).

32. Dignam, M.J., Fawcett, W.R., and Bohni, H., J. Electrochem. Soc., 113, 657 (1966).

33. Dignam, M.J., and Fawcett, W.R., J. Electrochem, Soc., 113, 663 (1966).

34. Beck, A. F., Heine, M. A., Caule, E. J., and Pryor, M. J., Corros. Sci., 1, 1 (1967).

35. Wagner, C., 'Atom Movements,' ASM, Cleveland, p. 153 (1951).

36. Davies, D. E., Evans, U. R., and Agar, J. N., Proc. Roy. Soc. (London), A225, 443 (1954).

37. Harrison, P. L., J. Electrochem, Soc., 112, 235 (1965).

38. Smeltzer, W. W., Haering, R. R., and Kirkaldy, J. S., Acta. Met., 9, 880 (1961).

39. Perrow, J. M., Smeltzer, W. W., and Embury, J. D., Acta. Met., 16, 1206 (1968).

40. Fishbeck, K., Neundeubel, L., and Salzer, F., Z. Elektrochem., 40, 517 (1934).

41. Hauffe, K. and Pfeiffer, H., Z. Elektrochem., 56, 390 (1952); Z. Metallk., 44, 27 (1953).

42. Pettit, F. S., Yinger, R. and Wagner, J. B., Jr. Acta. Met., 8, 61 (1960).

43. Pettit, F. S., and Wagner, J. B. Jr., Acta Met., 12, 35 (1964).

44. Smeltzer, W. W., Acta Met., 8, 377 (1960).

45. Irving, B. A., Corros. Sci., 5, 471 (1965).

46. Morris, L. A. and Smeltzer, W. W., Acta Met., 15, 1591 (1967).

47. Clark, J. B., and Rhines, F. N., Trans. ASM, 51, 199 (1959).

48. Kirkaldy, J. S., and Brown, L. C., Can. Met. Quart., 1, 41 (1962).

49. Moreau, J., and Benard, J., Rev. Met., 59, 161 (1962).

50. Smeltzer, W. W., Trans. AIME, 218, 674 (1960).

51. Roth, W. L., J. Appl. Phys. Suppl., 30, 3028 (1959); Acta Cryst., 13, 140 (1960).

52. Wagner, C., J. Electrochem. Soc., 99, 369 (1952).

53. Wagner, C., J. Electrochem. Soc., 103, 627 (1956).

54. Wagner, C., Z. Elektrochem. Soc., 63, 773 (1959).

55. Rapp, R. A., Acta Met., 9, 730 (1961).

56. Maak, F., Z. Metallk., 52, 538 (1961).

57. Maak, F., Z. Metallk., 52, 545 (1961).

58. Maak, F., and Wagner, C., Werkstoffe Korrosion, 5, 273 (1961).

59. Schmalzried, H., and Wagner, C., Z. physik. Chem. (NF), 31, 198 (1962).

60. Birks, N., and Rickert, H., J. Inst. Metals, 91, 308 (1961-62).

61. Moreau, J., and Benard, J., Compt. rend., 237, 1417 (1953).

62. Rhines, F. N., Trans. AIME, 137, 246 (1940).

63. Rhines, F. N., Johnson, W. A., and Anderson, W. A., Trans. AIME, 147, 205 (1942).

64. Thomas, D. E., J. Metals, 3, 926 (1951).

65. Darken, L. S., Trans. AIME, 150, 157 (1942).

66. Meijering, J. L., and Druyvesteyn, M. J., Phillips Res. Rept., 2, 81, 260 (1947).

67. Armitage, J. W., and Rapp, R. A., SIAM Rev., 5, 67 (1963).

68. Rapp, R. A., Frank, D. F., and Armitage, J. W., Acta Met., 12, 505 (1964).

69. Bohm, G., and Kahlweit, M., Acta Met., 12, 641 (1964).

70. Rapp, R. A., and Colson, H. D., Trans. AIME, 236, 1616 (1966).

71. Kirkaldy, J. S., Private communication.

72. Paidassi, J., Trans. AIME, 197, 1570 (1953).

73. Davies, M.H., Simnad, M.T., and Birchenall, C.E., J. Metals, N.Y., 3, 889 (1951).

74. Davies, M.H., Simnad, M.T., and Birchenall, C.E., J. Metals, N.Y., 5, 1250 (1953).

75. Himmel, L., Mehl, R.F., and Birchenall, C.E., J. Metals, N.Y., 5, 827 (1953).

76. Kobayashi, H., and Wagner, C., J. Chem. Phys., 26, 1609 (1957).

77. Turkdogan, E.T., McKewan, W.M., and Zwell, L., J. Phys. Chem., 69, 327 (1965).

78. Wagner, C., J. Appl. Phys., 29, 1295 (1958).

79. Kaiser, W., and Breslin, J., J. Appl. Phys., 29, 1292 (1958).

80. Gulbransen, E.A., Andrew, K.F., and Brassart, F.A., 113, 834 (1966).

81. Deal, B.E., and Grove, A.S., J. Appl. Phys., 36, 3770 (1965).

82. Nakayama, T., and Collins, F.C., 113, 706 (1966).

83. Burkardt, P.J., and Gregor, L.V., Trans. AIME, 236, 299 (1966).

84. Seybolt, A.U., and Alessandrini, E.I., Trans. AIME, 212, 507 (1958).

85. Sugiyama, M. and Nakayama, T., Japan Inst. Metals, Journal, 23, 534 (1959).

86. Bohenkamp, K. and Engell, H.J., Arch. Eisenhuttenw., 35, 1011 (1964).

87. Schenck, H., Schmidtmann, E., and Muller, H., Arch. Eisenhuttenw., 31, 121 (1960).

88. Ipatyev, V.V., and Orlova, G.M., J. Appl. Chem., U.S.S.R., 29, 981 (1956).

89. Schmahl, N.G., Baumann, H., and Schenck, H., Arch. Eisenhuttenw., 30, 269 (1959).

90. Schmahl, N. G., Baumann, H., and Schenck, H., Arch. Eisenhuttenw., 30, 415 (1959).

91. Schmahl, N. G., Kupperbusch, and Schenck, H., Arch. Eisenhuttenw., 34, 115 (1963).

92. Evans, J. W., and Chaterjee, S. K., J. Electrochem, Soc., 106, 860 (1959).

93. Tuck, C. W., Proc. First Int. Corr. Congress, London, Butterworths, 221 (1961).

94. Tuck, C. W., Corros. Science, 5, 63 (1965).

95. Rahmel, A., and Tobolski, J., Werkstoffe Korrosion, 16, 662 (1965).

96. Rahmel, A., Z. Elektrochem, 66, 363 (1962).

97. Rahmel, A., Werkstoffe Korrosion, 16, 837 (1965).

98. Darken, L. S., Trans. AIME, 150, 157 (1942).

99. Ward, R., Trans. AIME, 162, 141 (1945).

100. Pettit, F. S., Trans. AIME, 239, 1296 (1967).

101. Moreau, J., and Benard, J., Compt. rend., 237, 1417 (1953).

102. Moreau, J., and Benard, J., J. Inst. Metals, 83, 87 (1954-55).

103. Moreau, J., and Benard, J., Compt. rend., 236, 85 (1953).

104. Perrow, J., and Smeltzer, W. W., J. Electrochem. Soc., 109, 1023 (1962).

105. Darken, L. S., J. Am. Chem. Soc., 70, 2046 (1948).

106. White, J., J. Iron and Steel Institute, 148, 579 (1943).

107. Kanz, F., Scheil, E., and Schulz, E. H., Arch. Eisenhuttenw., 8, 67 (1934).

108. Elliot, J. F., and Gleiser, M., 'Thermochemistry for Steelmaking', vol. 1, Reading, Addison-Wesley Publishing Co., (1960).

109. Taylor, R. W., and Schmalzried, J. Phys. Chem., 68, 2444 (1964).

110. Samuels, L. E., J. Inst. Metals, 81, 471 (1952-1953), 85, 51, (1956-57).

111. Darken, L. S., and Gurry, R. W., J. Am. Chem. Soc., 67, 1398 (1945).

112. Schlichting, H., 'Boundary Layer Theory', London, Pergamon Press, 1955.

113. Bird, R. B., Stewart, W. E., and Lighfoot, E. N., 'Transport Phenomena', New York, John Wiley and Sons, Inc., 1966.

114. Birks, L. S., 'Electron Probe Microanalysis', New York, Interscience, 1963.

115. Theisen, R., 'Quantitative Electron Microprobe Analysis', Berlin, Springer-Verleg, 1965.

116. Castaing, R., Ph. D. Thesis, Univ. of Paris (1951).

117. 'The Electron Microprobe', Proc. Symp. Electrochem. Soc., Washington, New York, John Wiley and Sons, 1966.

118. Hirsch, P. B., Howie, A., Nicholson, R. B., Pashley, D. W., and Whelan, M. J., 'Electron Microscopy of Thin Crystals', London: Butterworths, 1965.

119. Thomas, G., 'Transmission Electron Microscopy of Metals', New York, John Wiley and Sons, Inc., 1966.

120. Sosman, R. B., 'The Phases of Silica', New Brunswick, Rutgers University Press, 1965, p. 316.

121. Fujii, C. T. and Meussner, R. A., J. Electrochem. Soc., 110, 1195 (1963).

122. Fujii, C. T. and Meussner, R. A., J. Electrochem. Soc., 111, 1215 (1964).

123. Kingery, W. D., 'Introduction to Ceramics', New York, John Wiley and Sons, Inc., 1960, p. 252.

124. Avrami, M., J. Chem. Phys., 8, 212 (1940).

125. Wagner, C., J. Colloid Sci., 5, 85 (1950).

126. Klueh, R.L., and Mullins, W.W., Acta Met., 17, 59, 69 (1969).

127. Geiger, G.H., and Wagner, J.B., Jr., Corrosion, 23, 185 (1967).

128. Philibert, J., Met. Corr. Ind., 40, 157, 216, 325 (1964).

129. Duncumb, P., and Reed, S.J.B., 'Summer School in Electron Microscopy and Microprobe Analysis', McMaster University, Hamilton (1968).

130. Philibert, J., X-ray Optics and X-ray Microanalysis, Proc. of 3rd. Int. Symp., Stanford, (1962).

131. Duncumb, P., and Shields, P.K., 'The Electron Microprobe', Proc. of Symp., Washington (1964).

132. Green, M. and V.E. Cosslett, Proc. Phys. Soc. (London), 78, 1206 (1961).

133. Burhop, E.H.S., 'The Auger Effect', Cambridge,University Press, (1952).

134. Victoreen, J.A., J. Appl. Phys. 20, 1141 (1949).

135. Compton, A.H. and Allison, S.K., 'X-rays in Theory and Experiment'; New York, D. Van Nostrand Company, 1935.

136. Scarborough, J.B., 'Numerical Mathematical Analysis', Baltimore, John Hopkins Press, 1959, p.86.

137. Barrett, C.S., 'Structure of Metals', New York, McGraw-Hill Book Co. Inc., 1952.

138. Garner, W.E., 'Chemisorption', London: Butterworths, 1957, p.212.